Technical University of Munich
TUM School of Engineering and Design

Mechanical surrogate models for hybrid material joints in crashworthiness simulation

Michael Fridolin Richter

Vollständiger Abdruck der von der TUM School of Engineering and Design der Technischen Universität München zur Erlangung eines

Doktors der Ingenieurwissenschaften (Dr.-Ing.)

genehmigten Dissertation.

Vorsitz: Prof. Dr-Ing. Kai-Uwe Bletzinger

Prüfer*innen der Dissertation:

1. Prof. Dr.-Ing. habil. Fabian Duddeck

2. Prof. Dr.-Ing. Peter Middendorf

Die Dissertation wurde am 27.12.2022 bei der Technischen Universität München eingereicht und durch die TUM School of Engineering and Design am 11.04.2023 angenommen.

Acknowledgement

I wrote the present work as an external doctoral candidate at the Chair of Computational Mechanics of the Technical University of Munich while working as a computational engineer at MATFEM.

I'd like to thank my supervisor Prof. Fabian Duddeck for making this endeavor possible. He always gave me a fast feedback, provided valuable expertise and created a nice working atmosphere at the Chair of Computational Mechanics at the Technical University of Munich.
Further, my gratitude goes to my second examiner Prof. Peter Middendorf, head of the *Insitut für Flugzeugbau* (IFB) at the Technical University of Stuttgart, for expressing his interest in my research topic and providing valuable input during our discussions as well as to Prof. Kai-Uwe Bletzinger for acting as chairperson of the examination board.

I carried out most of my work at MATFEM in Munich. I am grateful for the innovative work environment and friendly atmosphere there. First and foremost, my appreciation and sincerest thanks to Dr. Helmut Gese for initiating this research topic and preciously supporting my endeavor with his technical expertise, clear guidance, interest in my research and patience while conducting it. Prof. Harry Dell for his help and support in the material characterization as well as his humorous, cherished comments. Gernot Oberhofer for his interest and allowing me to take some time off during very busy times. I am deeply in debt to Felix Brenner and Martin Oehm for their support as well as to my other colleagues, who suspected me to sneak off to beer garden during summer while in reality I spend time at the university.

My research could not have been done without the results of the partners in the *Laser-Leichter* research project, which was publicly funded by the *German Federal Ministry of Education and Research* (BMBF) under Grant No. 13N12877. Thank you to all who participated: Dr. Philipp Schreiner as the project leader and the coordination of 13 consortium partners, but also granting me the access to material data and Dr. Udo Hartel both from *Robert Bosch GmbH*, Daniel Lezock from *Scherdel* for the interest in this work and discussions on material modelling, Oliver Seffer from the *Laser Zentrum Hannover* (LZH) for his support, Ralf Ossenbrink for conducting ct-Scans, Dr. Axel Jahn and Dr. Frieder Zimmermann from Fraunhofer *Insitut für Werkstoff- und Strahlentechnik* (IWS) in Dresden for the support in manufacturing and testing of hybrid specimens and as well

as Dr. Jens Standfuß for mentoring me during this time and humorous support for this doctorate.

I'd like to thank my colleagues from the chair and from the material groups for the open discussions and vivid exchange during our workshops and meetings, most notably Duo Zeng, Koushyar Komeylizadeh, Felizitas Lanzl and Ani Sarnaghi, and to the students who contributed to this thesis in the scope of their theses and software labs.

Lastly, I would express my deep gratitude for their endless love and support to my parents. I know I can always count on you and that you had the very best intentions for me since the beginning. My siblings David and Christiane for providing me the with culinary and sportive distractions - my apologies for being stubborn on your feedback and many thanks for letting me successfully urge you to proofread this manuscript. Also, a special and warm thanks goes to my Stammtisch crew from high school for enriching my life outside research. Lastly, to my love Cathrina for her endless patience and loving support during the conferral of this doctorate, when I cannot always have been the best company.

Abstract

In the precise exploitation of different materials benefiting from their local best properties, the multi-material design bears a huge lightweight potential to develop a safer and less pollutant individual passenger transport in the future. To pave the way for a consistent implementation of this composite design including new materials, novel joining techniques need to be developed. To include these hybrid joints efficiently in the virtual product development with simulation-assisted design of lightweight structures requires mechanical surrogate models. This thesis contributes to this research field and proposes a systematic development of mechanical surrogate models for dissimilar material pairings.
The objective of these surrogate models is to depict the initial stiffness as well as the deformation and failure behavior of the hybrid material pairing correctly in a simulation. Furthermore, these surrogate models need to be robust and reliable without hampering the computational efficiency. Special consideration is given for the surrogate models in crashworthiness simulation, because here not only the nonlinear material behavior but also dependencies on the orientation, strain-rate and multi-axial stress states pose a challenge. This thesis is therefore divided into two main parts, the characterization of base materials and the development of low-fidelity surrogate models for hybrid material joints. The basis of the development of surrogate models is constituted by a comprehensive material characterization of the base materials to be joint. Besides the phenomenological material modeling of the elasto-plastic behavior of monolithic steel and aluminum sheets, the macroscopically smeared description of textile reinforced thermoplastics, so-called organic sheets, represents an innovation. In particular by exploiting the separate description with two independent failure criteria for the thermoplastic matrix and the endless glassfibers, an opposing trend in the strain-rate dependency of failure can be captured. In the second part, with the use of the material cards from the first part, experimental characterization and metallurgical analysis of the hybrid material joints, a high-fidelity detail and a low-fidelity surrogate model are developed for two different, slender joints. The latter is joint with the direct or indirect use of a remote laser beam welding. Finally at the end of the second part, a surrogate model for a steel-aluminum weld line is validated on component level with a generic structure of a hat profile.

Keywords: Crashworthiness, material modeling, hybrid material joints, textiles, organic sheets, surrogate models

Kurzfassung

Mit dem gezielten Einsatz unterschiedlicher Materialien, die lokal ihre jeweiligen Stärken einbringen können, bietet die Multi-Material Bauweise ein großes Leichtbaupotential, um zukünftig den individuellen Personenverkehr in der Luftfahrt und im Automobilbau sicherer und emissionsärmer zu gestalten. Für die konsequente Umsetzung der Mischbauweise und bei der Anwendung neuer Materialien müssen neue Fügetechnologien entwickelt werden. Um hybride Materialkombinationen zukünftig auch im virtuellen Produktentwicklungsprozess für die simulative Auslegung von Leichtbaustrukturen berücksichtigen zu können, bedarf es sogenannter mechanischer Ersatzmodelle. In diesem Forschungsfeld leistet die vorliegende Arbeit einen Beitrag mit dem Ziel der systematischen Entwicklung mechanischer Ersatzmodelle für hybride Materialpaarungen.
Ziel dieser Ersatzmodelle ist es, sowohl die Steifigkeit, als auch das Deformations- und Versagensverhalten von hybriden Verbindungen in der Simulation korrekt wiederzugeben. Diese Surrogat-modelle sollen robust und zuverlässig sein, ohne dabei die Rechenzeit negativ zu beeinflussen. Spezielles Augenmerk liegt hierbei auf Ersatzmodellen für die Crashsimulation, weil diese, bedingt durch materielle Nichtlinearitäten und Abhängigkeit des Materialverhaltens von den Orientierungen, Dehnraten und mehrachsigen Spannungszuständen, eine große Herausforderung darstellt. Diese Arbeit ist hierfür in zwei Teile untergliedert, die Charakterisierung der Grundwerkstoffe und die Entwicklung von Ersatzmodellen für hybride Materialpaarungen. Ausgangspunkt für die Ersatzmodellentwicklung stellt eine umfangreiche Materialcharakterisierung der zu fügenden Grundwerkstoffe dar. Neben der phänomenologischen Materialmodellierung des elasto-plastischen Materialverhaltens von monolithischen Stahl- und Aluminium-Blechen, stellt die makroskopisch verschmierte Beschreibung von textilverstärkten Thermoplasten, sogenannter Organobleche, eine besondere Neuerung dar. Dies ist insbesondere relevant, weil durch eine separate Beschreibung des Versagensverhalten von thermoplastischer Matrix und Endlos-Glasfaser eine entgegengesetzte Dehnratenabhängigkeit des Versagens abgebildet werden kann. Im zweiten Abschnitt werden unter Einsatz der Materialkarten, experimentellen Charakterisierung und metallurgischen Untersuchungen der hybriden Materialpaarungen Detail- und Ersatzmodelle für zwei unterschiedliche, längliche Verbindungen entwickelt. Letztere wurden durch direkten bzw. indirekten Einsatz von Remote-Laserstrahlschweißen gefügt. Zum Abschluss des zweiten Teils wird ein Ersatzmodell für eine Stahl-Aluminium Schweißnaht auf Komponentenebene einer generischen Hutprofilstruktur validiert.

Stichwörter: Crashverhalten, Materialmodellierung, hybride Materialpaarungen, Textil, Organoblech, Ersatzmodel

Contents

List of Abbreviations

1D	one-dimensional
2D	two-dimensional
3D	three-dimensional
AR	Aspect Ratio
ASCII	American Standard Code for Information Interchange
BBA	Building Block Approach
BIP	Brittle Intermetallic Phase
BIW	Body-in-white
BM	Base Material
BMC	Bulk Molded Compound
CAE	Computer Aided Engineering
CDP	Cathodic Dip Painting
CFRP	Carbon Fiber Reinforced Polymers
CPU	Central Processing Unit
CT	Computed Tomography
CTF	Connector Force
CZM	Cohesive Zone Model
DIC	Digital Image Correlation
DIN	Deutsches Institut für Normung
DNF	Ductile Normal Fracture
DP	Dual Phase
DSF	Ductile Shear Fracture
EDX	Energy Dispersive X-ray Spectroscopy
EFRT	Endless Fiber Reinforced Thermoplastics

EN	Europäische Norm
FE	Finite Element
FEM	Finite Element Method
FF	Fiber Failure
FKA	Forschungsgesellschaft Kraftfahrtwesen Aachen
FLC	Forming Limit Curve
FMC	Failure Mode Concept
FRP	Fiber Reinforced Plastic
GOM	Gesellschaft für Optische Messtechnik
HAZ	Heat Affected Zone
HPDC	High Pressure Die Cast
HV	History Variable
IDS	Instability Ductile Shear
IFF	Interfiber Fiber Failure
IMA	In-molding Assembly
IP	Integration Point
ISO	Internationale Organisation für Normung
IWS	Fraunhofer Institut für Werkstoff- und Strahltechnik
KS2	Kopfzug-Schälzuggeometrie der 2. Generation
LBW	Laser Beam Welding
LFRT	Long Fiber Reinforced Thermoplastics
LFT	Lehrstuhl für Fertigungstechnologie
LSM	Least Square Method
LZH	Laser Zentrum Hannover e.V.
MH	Micro Hardness
NCAP	New Car Assessment Program
NFRT	Non Fiber Reinforced Thermoplastic
NVH	Noise Vibration Harshness
ODE	Ordinary Differential Equation
PA	Polyamide

PDP	Product Development Process
PIS	Post Instability Strain Model for Shell Elements
PMA	Post Molding Assembly
PP	Polypropylene
RD	Rolling direction
RT	Room Temperature
RUC	Representative Unit Cell
RVE	Representative Volume Element
SDV	Solution Dependent Variable
SEA	Specific Energy Absorption
SFRT	Short Fiber Reinforced Thermoplastics
SLM	Selective Laser Melting
SMC	Sheet Molded Compound
SP	Section Point
SPR	Self-Piercing Rivet
SW	Spot Weld
T4	Heat treatment condition: solution annealed and naturally aged
T6	Heat treatment condition: solution annealed and artificially aged
TAPO	Toughend Adhesive Polymer
TWIP	Twinning Induced Plasticity
UD	Unidirectional
UTS	Ultimate Tensile Strength
VNRS	V-notched Rail Shear
VW	Volkswagen AG
WWFE	Worldwide Failure Exercise
Al	Aluminum
C	Carbon
Cu	Copper
Fe	Iron
Mg	Magnesium

Mn	Manganese
N	Nitrogen
P	Phosphorus
S	Sulfur
Si	Silicone

List of Symbols

Latin letters and symbols

Symbol	***Unit***	***Description***
A_0	mm^2	Initial cross-sectional area
A	mm^2	Cross-sectional area
$C_1 - C_4$	–	Parameters for Xue-Wierzbicki failure model
E_0	MPa	Young's modulus in 0°-direction
E_{45}	MPa	Young's modulus in 45°-direction
E_{90}	MPa	Young's modulus in 90°-direction
F	N	Force
G	J	Energy for cohesive models
G	MPa	Shear modulus
H	–	Plastic flow potential
I_1, I_2, I_3	–	1^{st}, 2^{nd} and 3^{3rd} invariant of the strain tensor
$J_1^{'}$	MPa	1^{st} invariant of the deviatoric stress tensor
$J_2^{'}$	MPa^2	2^{nd} invariant of the deviatoric stress tensor
$J_3^{'}$	MPa^3	3^{rd} invariant of the deviatoric stress tensor
J_1	MPa	1^{st} invariant of the Cauchy stress tensor
J_2	MPa^2	2^{nd} invariant of the Cauchy stress tensor
J_3	MPa^3	3^{rd} invariant of the Cauchy stress tensor
K	MPa	Initial stiffness for cohesive models
K	MPa	Bulk modulus
R_m	MPa	Ultimate tensile strength
$R_{p0.2}$	MPa	Yield strength for 0.2 % plastic strain
R	MPa	Failure strength for composites
T_g	°C	Glass transition temperature
T	°C	Temperature
V	mm^3	Volume
W	J	Work
$\mathbb{B}$	–	Tensor 3^{rd} order
$\mathbb{C}$	N/mm	Stiffness or elasticity matrix
$\mathbb{D}$	Ns/mm	Damping matrix
$\mathbb{M}$	kg	Mass matrix
$\mathbb{S}$	mm/N	Compliance matrix
$\mathbf{B}$	–	Tensor 2^{nd} order (Matrix)

Symbol	***Unit***	***Description***
ε^0	–	Strain threshold for cohesive models
$\vec{a}$	mm^2/s	Acceleration
$\vec{b}$	–	Tensor 1^{st} order (Vector)
$\vec{u}$	mm	Displacement
$\vec{v}$	mm/s	Velocity
a	–	Orthotropy coefficient for Hill1948
b	–	Tensor 0^{th} order (Scalar)
c	mm/s	Effective dilatational wave speed
$d\vec{s}, d\vec{S}$	–	Line element
da, dA	–	Area element
dv, dV	–	Volume element
d	–	Parameter for ductile normal fracturel
d	mm	Distance
f	–	Parameter for ductile shear fracture
k_{SF}	–	Weighting factor of stress triaxiality for CrachFEM DSF model
l_0	mm	Initial gauge length
l_c	mm	Length of critical element
l	mm	Actual length
m	kg	Mass
m	–	Strain-rate sensitivity exponent
n	–	Hardening exponent
p	MPa	Hydrostatic pressure
q	–	Parameter for ductile normal fracture
q	MPa	von Mises equivalent stress
r_0	–	r-value along rolling direction
r_{45}	–	r-value in 45° to rolling direction
r_{90}	–	r-value in 90° to rolling direction
r	mm	Radius
s_{NF}	–	Weighting factor of stress triaxiality for CrachFEM DNF model
t^0	MPa	Stress threshold for cohesive models
t_c	s	Critical time step
t	mm	Thickness
u	mm	Displacement
w	–	Anisotropy function for ductile fracture
w	mm	Width
e	%	Engineering strain
s	MPa	Engineering stress

Greek letters and symbols

Symbol	***Unit***	***Description***
Γ	–	Boundary

Symbol	***Unit***	***Description***
Ω	–	Region
Ψ	–	Failure risk in CrachFEM
α_{th}	K^{-1}	Thermal expansion coefficient
α	$^\circ$	In-plane off-axis orientation
α	–	Strain-rate ratio
β	–	Stress state parameter for ductile normal fracture
δ	–	Inhomogeneity parameter for Crach
$\dot{\varepsilon}$	1/s	Strain-rate
η_{MF}	–	Stress triaxiality normalized by uniaxial tension
η	–	Stress triaxiality
γ	$^\circ$	Orientation angle for Crach-algorithm
γ	–	Shear deformation
λ	W/mK	Thermal conductivity
μ	–	Coefficient of friction
ν	–	Poisson's ratio
ω_{max}	Hz	Largest eigenfrequency
$\sigma_1, \sigma_2, \sigma_3$	MPa	1^{st}, 2^{nd} and 3^{3rd} principal stress
σ_m	MPa	Average stress
σ_{vM}	MPa	von Mises equivalent stress
σ	MPa	Stress
τ_{max}	MPa	Maximal shear stress
τ	MPa	Shear stress
θ_{MP}	$^\circ$C	Melting point
θ	–	Lode angle $\in [0; \frac{\pi}{3}]$
θ	–	Stress state parameter for ductile shear fracture
ε^{+}_{SF}	–	Parameter for ductile shear fracture
ε^{-}_{SF}	–	Parameter for ductile shear fracture
ε^{el}	–	Elastic strain
ε^{pl}	–	Plastic strain
ε^{tot}	–	Total strain
$\varepsilon_1, \varepsilon_2, \varepsilon_3$	–	1^{st}, 2^{nd} and 3^{3rd} principal strain
ε_{vM}	–	von Mises equivalent strain
ε	–	Strain
ϱ	$\mathrm{kg/m}^3$	Mass density
ξ	–	Parameter of the Lode angle $\in [-1; 1]$

Indices

$**$	Fracture.
$*$	Instability.
0	Initial configuration.
1, 2, 3	Directions of coordinate system.
1, 2, 3	Principal axis.

Al	Aluminum.
St	Steel.
$0°, 22.5°, 45°, 90°$	Material orientation.
$\parallel$	Parallel to fibers.
$\perp$	Perpendicular to fibers.
bC	Biaxial compression.
bT	Biaxial tension.
$crit$	Critical.
c	Critical.
dyn	Dynamic.
el	Elastic.
eng	Engineering.
eq	Equivalent.
i, j	Auxiliary variables.
log	Logarithmic.
lo	Longitudinal.
max	Maximal.
min	Minimal.
m	Mean.
n, t, s	Loading mode: normal, tearing, sliding.
nf	Normal Fracture.
pS	Plane strain.
pl	Plastic.
p	Punch.
qs	Quasi-static.
red	Reduced.
ref	Reference.
sH	Shearing.
sf	Shear Fracture.
s	Support.
tC	Hydrostatic compression.
tT	Hydrostatic tension.
tot	Total.
$true$	True.
tr	Transversal.
t	Thickness direction.
uC	Uniaxial compression.
uT	Uniaxial tension.
vM	von Mises.
w	Width direction.
x, y, z	Directions of Cartesian coordinate system.

„There is nothing more practical than a good theory."

Kurt Lewin

1. Introduction

The steadily growing demand for personal mobility, the increasing shortage of fossil fuels and the impact of climate change pose a major challenge for the automotive as well as aerospace sector. One approach to solve this issue while meeting the need of increasingly stringent legal requirements on emissions and safety regulations is the sustainable development of alternative propulsion concepts paired with efficient lightweight structures. In order to exploit the full lightweight potential, a symbiosis of a consistent realization of an appropriate shape and the application of locally demanded materials is required. From the range of application oriented materials - as e.g. fiber reinforced composites, lightweight materials such as aluminum, sandwich materials but also high-tensile steels such as boron steel - the material for its locally demanded properties needs to be chosen and optimally combined with the surrounding components. In such a material mix, the joint of the dissimilar material pairing often turns out to be the bottleneck of the hybrid structure. Due to the variety of different applications and material combinations, the current state of the art of production, process assurance as well as simulation of hybrid material pairings is not satisfying and currently subject to many research projects. For example adhesion of components needs long process cycles with restricted flexibility; furthermore adding additional joining elements such as bolts or screws contradicts the actual overall goal of weight reduction. To overcome these drawbacks, the application of photonic lasers for preparatory treatment of the joining surface or for the direct joining by remote melting represents a promising and flexible joining tool.

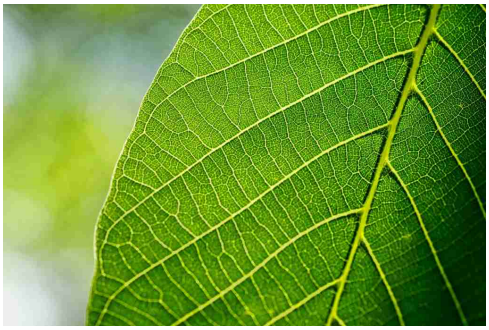

Figure 1.1.: Reinforcement structure of a leaf [1]

Textile reinforced thermoplastics, so-called organic sheets, offer a huge potential of weight savings and subsequently the reduction of pollutant emissions. However, a large share of structural parts in vehicles is still designed with monolithic metallic structures which

are frequently over-sized for their purpose. Various examples of load adapted lightweight structures can be found in nature as displayed in Figure 1.1, where evolution led to a fiber reinforced leaf structure as optimum regarding weight and structural resistance.

Similarly to the evolved design by nature, local reinforcements of structures are most often the outcome of either a topology or structural shape optimization for a given load spectrum. Its realization is mostly limited by manufacturing constraints as well as elevated manufacturing expenses compared to conventional methods. Tailor welded blanks or tailor rolled blanks are an example of including local reinforcement in monolithic steel sheets. In this context, the application of short and endless fiber reinforced thermoplastic composites bear a huge lightweight potential for both the automotive and aerospace industry.

1.1. Organic sheets in the automotive industry

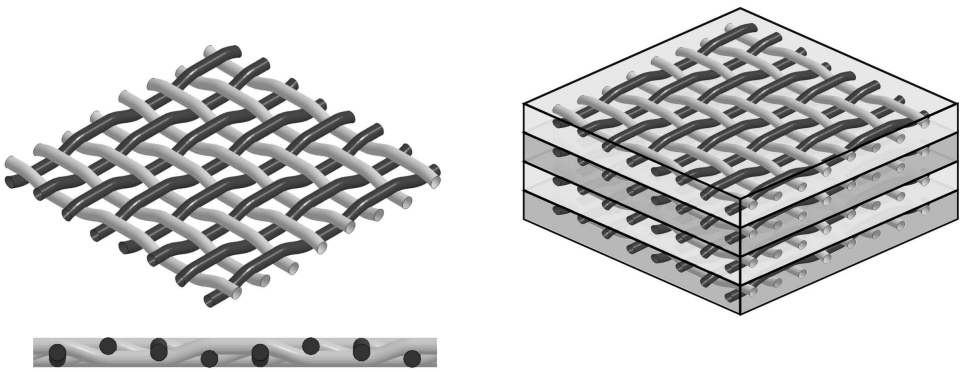

Figure 1.2.: Left: Isometric and side view of the bi-directional twill-weave architecture; right: example of a layered composite made from twill-weave layers

Textile reinforced thermoplastics - so-called organic sheets - are an example of endless glass or carbon fiber reinforced thermoplastics (EFRT). They are an impregnated and preconsolidated semi-finished product which is normally made of multiple layers as displayed on the right-hand side of Figure 1.2. Here, the architecture of the endless fibers is equally balanced in warp and weft direction with twill-weave bindings (see left side in Figure 1.2) without any additional reinforcement in the thickness direction. Via this architecture, a 47% fiber volume fraction of fibers [2] can be obtained. Whereas organic sheet exist with endless carbon as well as glass fibers, this thesis focus on glass fibers. Various advantages of the material lead to an increased interest for this material rendering it suitable for the application in the automotive industry and hence substituting metallic material for semi-structural parts. Main advantages of the organic sheet are:

- Good specific material properties: high strength and fracture toughness resulting in an increased capacity of energy absorption;
- Good manufacturability, e.g. thermoforming;
- Short cycle times for thermoforming of $< 1\,\text{min}$ [3];
- Remelting of the thermoplastic matrix allows welding and combining thermoforming and back-injection in the same injection mold;
- Shorter design and production cycle times combined with a high flexibility.

In Figure 1.3 the mechanical properties of a steel, an aluminum and textile reinforced thermoplastic sheet are compared in form of a spider diagram normalized to the properties of the steel alloy. Especially the elevated specific energy absorption (SEA) for the organic sheet compared to its low mass density is remarkable for this material.

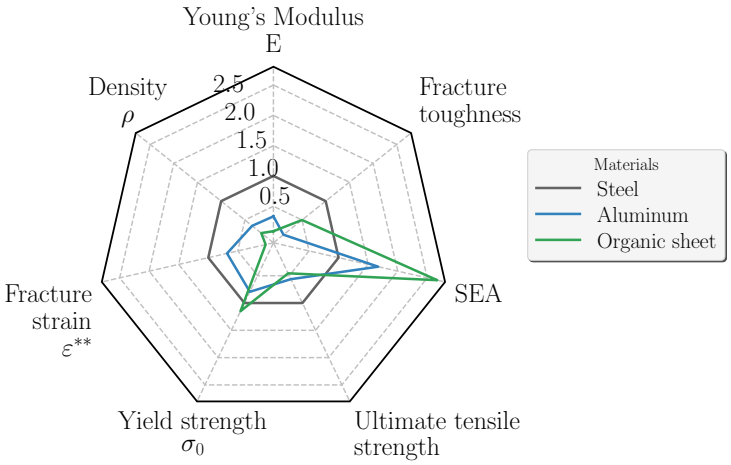

Figure 1.3.: Comparison of material properties for a steel- (S355JR), aluminum (EN AW-6082 T6) and organic sheet (Tepex® dynalite 102-RG600) normalized to the steel properties

The increasing interest in further analyzing textile reinforced thermoplastics and exploiting their full lightweight potential is substantiated by the number of research projects in this area, e.g. [4, 5]. Earlier interest in textile reinforced thermoplastics is treated in the theses of Breuer [6] focusing on industrial manufacturing and Dehn [7] for the CAE-design of crashworthiness load cases. Further, the combination of thermoforming and back-injection was analyzed in the joint research project *SpriForm* [8]. Special attention for the material modeling of organic sheet also for crashworthiness applications is addressed in the work by Vogler [9, 10].

1.2. Hybrid structures

Steadily increasing requirements for structural parts in the automotive sector lead to applications of new materials facilitated by new manufacturing techniques. Especially in the context of electric mobility, where the range is strongly limited by the overall weight of a vehicle, complying with these requirements becomes even more stringent. Multi-material design allows to combine different materials for their locally demanded material properties enabling a design optimized for the specific functions and requirements.
Figure 1.4 displays a forecast of the application and distribution of different materials in a body-in-white (BIW) structure from 2010 to 2040. The distribution is forecasted to move from a design primarily dominated by mild steel and high strength alloys of 80% in 2010 to a more evenly distributed assembly across multiple materials, with aluminum and magnesium amounting to a total of 31 % and FRP Composite to 15 %. Further it is estimated that the strongest increase for relevant structural lightweight components is expected for reinforced thermo- and duroplastic composites [11]. For the virtual design and development of the BIW in the future, this trend entails the necessity for joining multiple hybrid material pairings. Not only the processes and procedures need to be developed for hybrid material pairings but also material models and sub-models for the simulation of hybrid structures including multiple dissimilar material joints have to be derived. Moreover, for the virtual simulation of such high number of different materials in 2040, a structured and consistent material description is needed, helping the CAE-engineer to easily fathom and comprehend the underlying material model [5, 12].

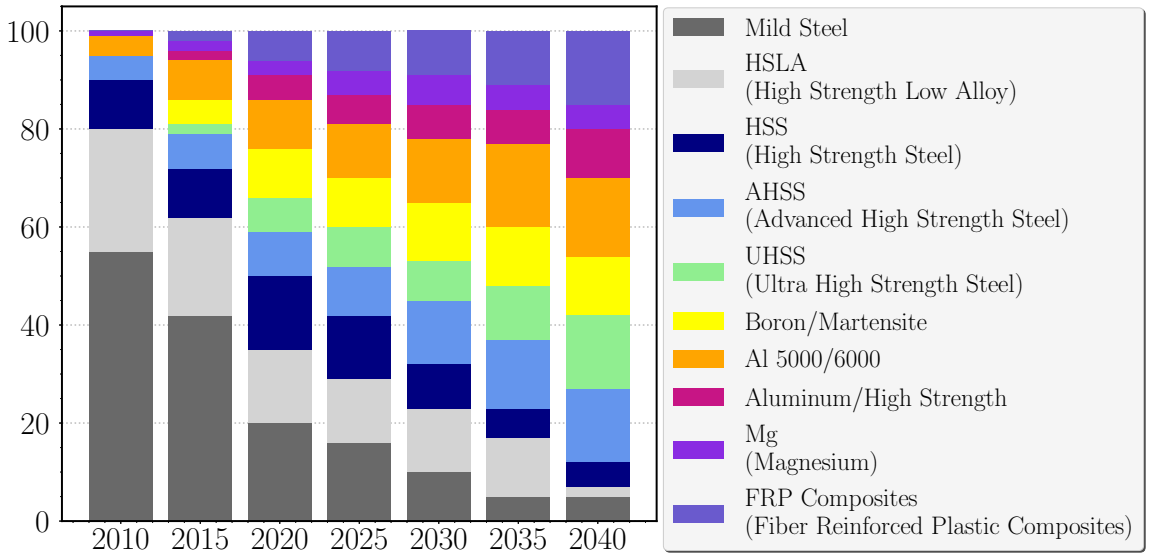

Figure 1.4.: Material distribution of the body-in-white from 2010 to 2040 [13]

For the application in crashworthiness simulation, one of the main criteria for engineering design is, besides initial local stiffness, strength and ductility, a more global characteristic, e.g. the capacity to absorb energy. Here, the mechanisms between ductile sheet metals

and composite materials like textile reinforced thermoplastics deviate significantly. Prior to failure initiation, ductile sheet metals exhibit a plastic strain hardening, composites however absorb energy via the so-called crushing, an accumulation of different micro-cracks of the fibers.

1.3. Motivation

The requirements on the design in the automotive industry stem from multiple disciplines. For an integration of hybrid material pairings in the construction of a body-in-white (BIW) requirements from the following fields must be met:

- Noise-Vibration-Harshness (NVH);
- Crashworthiness and passive safety;
- Impact;
- Structural durability;
- Vehicle dynamics and active safety;
- Acoustics (air- and structure-borne);
- Driving comfort;
- Aerodynamics.

A survey on the influence factors conducted by [5] displayed in Figure 1.5 predicts that material models and joining technology will together constitute 55% of the quality of simulation results concerning new BIW materials.

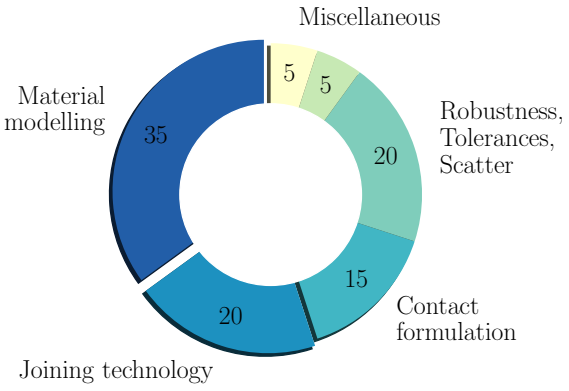

Figure 1.5.: Influence factors on the forecast quality of a simulation in % [5]

These two topics will be addressed throughout this thesis. Firstly, by a phenomenological material modeling of the two base materials to be joint. For hybrid material pairings by joining two dissimilar semi-finished products, the deformation and failure behavior of the joint is dominated by the weaker part of the two joining partners. It is hence essential to well capture the deformation and failure of the base materials to be joint in the simulation of hybrid joints. And secondly, by the development of mechanical surrogate models for hybrid material joints manufactured by a novel joining approach using a remote laser beam weld (LBW).

2. State of the art

The pre-requisite for mechanical surrogate models of hybrid material pairings including organic and metallic sheets is outlined in this chapter. Besides the fundamentals of mechanics, the experimental characterization and material modeling of both base materials and hybrid joints are addressed in Sections 2.1 and 2.2. The state of the art for the material modeling of textile reinforced thermoplastic and its limitations are discussed in Section 2.3. Capabilities of currently existing surrogate models and their short-comings for hybrid material pairings including reinforced thermoplastics are stated in Section 2.4. Focus lies here on structural simulation using the explicit code of *Abaqus* in combination with the user-defined material model *MF GenYld+CrachFEM*. The discussion of these aspects is concluded by the formulation of the research question of this thesis in Section 2.6. At last, the structure of this thesis is outlined in Section 2.7.

2.1. Mechanical fundamentals

Computational models are based on the theory and assumptions of continuum mechanics, whose fundamentals as far as relevant for this thesis are outlined in this section. For more detailed information the interested reader is referred to literature, e.g. [14, 15, 16]. For the virtual design of lightweight structures, the finite element simulation (FEM) is established in the structural calculation. Where analytical equations can no longer be used, FEM allows to solve partial differential equations with a discretization in space and time. It is a numerical approximation method for continuum problems based on discretization of the continuum, the so-called finite elements. Its application allows with the introduction of initial and boundary conditions to evaluate not only global structural responses such as force, displacement and energy, but also local quantities as strains and stresses.

Table 2.1.: Overview of tensor notation

b	Tensor 0^{th} order	Scalar
$\vec{b}$	Tensor 1^{st} order	Vector
$\mathbf{B}$	Tensor 2^{nd} order	Matrix
$\mathbb{B}$	Tensor 4^{th} order	-

Table 2.1 provides an overview of the relevant notation conventions in this context.

2.1.1. Continuum mechanics

The Tonti-diagram in Figure 2.1 illustrates the relation of the physical entities acting on the continuum Ω and its boundary $\Gamma = \partial\Omega$ stipulating the basic field equations of the boundary problem.

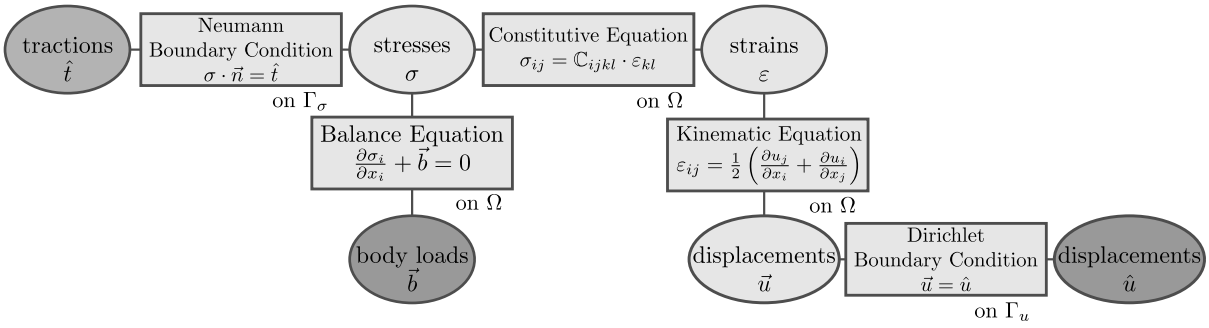

Figure 2.1.: Tonti-diagram for linear elasticity [17]

- *Balance condition:* For static problems an equilibrium of the forces is required. For dynamic problems the equations of motion replace the balance condition.
- *Kinematic equation:* The kinematic relation links the quantities for displacement $\vec{u}$ with deformation ε.
- *Constitutive equation:* The constitutive equations relate the deformation quantities ε with the inner stresses σ.

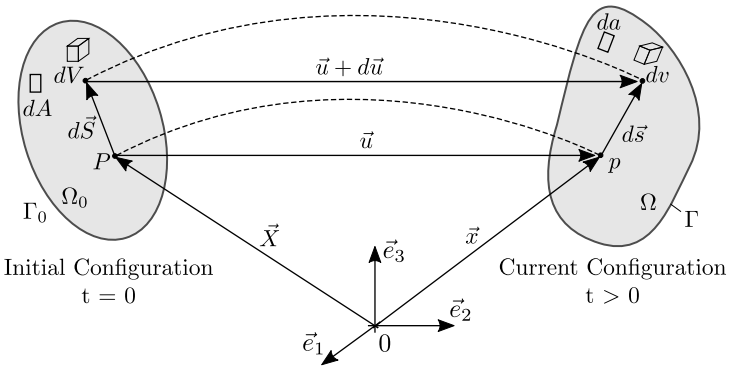

Figure 2.2.: Relation between initial and current configuration for the deformation of a continuum Ω

Figure 2.2 visualizes the transformation between an undeformed, initial reference configuration at $t = 0$ and the current, deformed configuration. An arbitrary material point P in the initial region Ω_0 is defined by the position vector $\vec{X}$. The displacement vector $\vec{u}$ for the displacement from point P to p is defined as $\vec{u} = \vec{x} - \vec{X}$. The equations are expressed in a orthogonal Cartesian coordinate system x_1, x_2, x_3 with unit base vectors

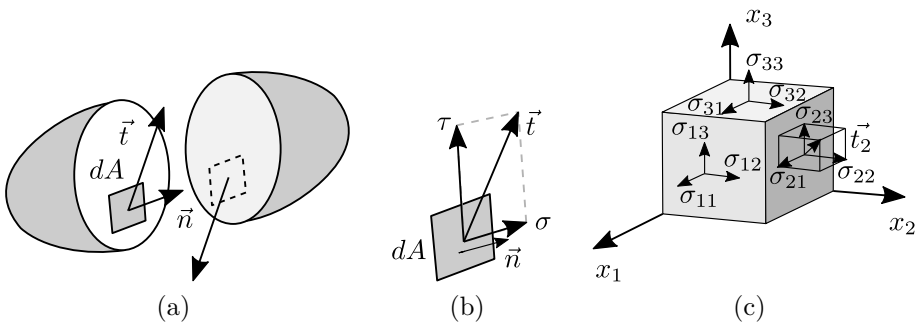

(a) (b) (c)

Figure 2.3.: Stress vector according to [18]

$\vec{e_1}$, $\vec{e_2}$, $\vec{e_3}$. A body or continuum subjected to a loading applied on a point, line, area or volume will result into inner forces or stresses. According to the Euler-Cauchy stress principle on the interface between two bodies or on a boundary surface with a surface area unit vector $\vec{n}(\vec{x}, t)$ there exists a vector field of stress vectors $\vec{t}(\vec{x}, \vec{n}, t)$ as displayed in Figure 2.3a. Based on the postulation of a local equilibrium of the momentum $\sigma_{ij} = \sigma_{ji}$, the Cauchy stress tensor can be reduced from nine to six independent stress components as displayed in Equation (2.3). This stress vector equates to the quotient of the acting force dF and the surface area dA as given in Equation (2.1).

$$\vec{t} = \lim_{\Delta A \to 0} \frac{\Delta \mathbf{F}}{\Delta A} = \frac{d\mathbf{F}}{dA}. \tag{2.1}$$

The stress component of $\vec{t}$ alongside the surface normal is referred to as normal stress σ. The components tangential to the surface element are described as shear stresses τ. These two stress types are visualized in Figure 2.3b. Technical stresses relate to the interface of the initial configuration dA, while true stresses relate to the current configuration da. Commonly, the following nomenclature is used for both stress types σ_{ij} and τ_{ij} with i, j = 1, 2, 3. Here, the first index denotes the orientation of the direction alongside the surface normal and the second index the operating direction of the stress as shown in Figure 2.3c. Cauchy theorem relates the stress vector $\vec{t}$ and the normal vector $\vec{n}$ with the Cauchy stress tensor σ (see Figure 2.3).

$$\vec{t} = \boldsymbol{\sigma} \cdot \vec{n}. \tag{2.2}$$

$$\boldsymbol{\sigma} = \begin{pmatrix} \sigma_{11} & \sigma_{12} & \sigma_{13} \\ \sigma_{21} & \sigma_{22} & \sigma_{23} \\ \sigma_{31} & \sigma_{32} & \sigma_{33} \end{pmatrix} = \begin{pmatrix} \sigma_{11} & \tau_{12} & \tau_{13} \\ \tau_{12} & \sigma_{22} & \tau_{23} \\ \tau_{13} & \tau_{23} & \sigma_{33} \end{pmatrix}. \tag{2.3}$$

This is the stress state of a point in Cartesian coordinates, where σ_{ij} denotes the normal stresses and τ_{ij} the shear stresses (i,j=1,2,3). For every material point, three normal stresses exist, such that the corresponding shear stresses vanish, i.e. $\tau_{ij} = 0$. These

particular normal stresses are the eigen values of the stress tensor and also referred to as principal stresses and given by Equation (2.4).

$$\boldsymbol{\sigma} = \begin{pmatrix} \sigma_1 & 0 & 0 \\ 0 & \sigma_2 & 0 \\ 0 & 0 & \sigma_3 \end{pmatrix}; \tag{2.4}$$

$$\sigma_1 \geq \sigma_2 \geq \sigma_3. \tag{2.5}$$

For the derivation of the principal stresses, the eigen value problem of the stress tensor (2.3) yields a cubic equation which contains coordinate-independent stress invariants J_1, J_2 and J_3 of the stress tensor (2.3) as coefficients.

$$\sigma^3 - J_1 \cdot \sigma^2 + J_2 \cdot \sigma - J_3 = 0. \tag{2.6}$$

The stress invariants, as indicated by the name, are independent of the used coordinate system. Using these invariants ensures that the material response is hence invariant towards arbitrary rotations around the axis. They can be expressed as

$$J_1 = tr\,(\boldsymbol{\sigma}) = \sigma_1 + \sigma_2 + \sigma_3; \tag{2.7}$$

$$J_2 = \frac{1}{2}\left(tr\left(\boldsymbol{\sigma}^2\right) - tr\,(\boldsymbol{\sigma})^2\right) = \sigma_1\sigma_2 + \sigma_2\sigma_3 + \sigma_1\sigma_3; \tag{2.8}$$

$$J_3 = det\,(\boldsymbol{\sigma}) = \sigma_1 \cdot \sigma_2 \cdot \sigma_3. \tag{2.9}$$

Further the Cauchy stress tensor can be disassembled into a hydrostatic and deviatoric component as displayed in Equation (2.10), where the first one describes the volumetric change (dilation) and the latter one the dimensional change (distortion).

$$\boldsymbol{\sigma} = \sigma_m \mathbf{I} + \boldsymbol{\sigma'} = \begin{pmatrix} \sigma_m & 0 & 0 \\ 0 & \sigma_m & 0 \\ 0 & 0 & \sigma_m \end{pmatrix} + \begin{pmatrix} \sigma'_1 & 0 & 0 \\ 0 & \sigma'_2 & 0 \\ 0 & 0 & \sigma'_3 \end{pmatrix}. \tag{2.10}$$

In addition, we define the hydrostatic pressure p as the average of the principal stresses, which is equivalent to $J_1/3$ (see Equation (2.11)). The name for hydrostatic pressure is inspired by fluiddynamics. Subtracting this on the diagonal of the stress tensor $\sigma_m \mathbf{I}$ leads to the deviatoric stresses σ'_{ij} and $\mathbf{I}$ representing the identity matrix.

$$\sigma_m = \frac{1}{3} J_1 = \frac{1}{3}\left(\sigma_1 + \sigma_2 + \sigma_3\right) = -p. \tag{2.11}$$

The corresponding deviatoric stress invariants are called J'_1, J'_2, and J'_3.

$$J'_1 = tr\left(\boldsymbol{\sigma'}\right) = \sigma'_1 + \sigma'_2 + \sigma'_3; \tag{2.12}$$

$$J'_2 = \frac{1}{2}\left(tr\left(\boldsymbol{\sigma'}^2\right) - tr\left(\boldsymbol{\sigma'}\right)^2\right) = \sigma'_1\sigma'_2 + \sigma'_2\sigma'_3 + \sigma'_1\sigma'_3; \tag{2.13}$$

$$J'_3 = det\left(\boldsymbol{\sigma'}\right) = \sigma'_1 \cdot \sigma'_2 \cdot \sigma'_3. \tag{2.14}$$

Especially the second invariant, J_2' is important for plasticity; it is related to the equivalent stress according to vonMises. For incompressible plasticity models we assume that the hydrostatic pressure causes only an elastic change of volume and that only shear stresses evoke a plastic deformation without a change in volume.

$$\sigma_{vM} = \sqrt{3J_2'} = \sqrt{\frac{1}{2}\left[(\sigma_1-\sigma_2)^2+(\sigma_2-\sigma_3)^2+(\sigma_1-\sigma_3)^2\right]}. \tag{2.15}$$

Based on the components of the stress tensor σ_1, σ_2, and σ_3, the equivalent stress in accordance with von Mises can be defined reducing the stress tensor to a scalar value representing a quantitative measure for a multi-axial stress state. To differentiate the type of stress state for multi-axial loading the stress triaxiality η (Equation (2.16)) and parameter of the Lode angle ξ (Equation (2.18)) which are based on the stress invariants will be used in the following. Peshekhodov distinguishes their meaning in his thesis as the following [19]:

- Stress triaxiality η: Ratio of averaged principal stresses σ_m and the equivalent stress according to von Mises σ_{vM}.
- Parameter of the Lode-angle ξ: measure how the principal stress σ_i is dominated by the other two components σ_j and σ_k.

$$\eta = \frac{J_1}{\sqrt{27|J_2'|}} = \frac{\sigma_m}{\sigma_{vM}} = \frac{1/3\cdot(\sigma_1+\sigma_2+\sigma_3)}{\sqrt{\frac{1}{2}\left[(\sigma_1-\sigma_2)^2+(\sigma_2-\sigma_3)^2+(\sigma_1-\sigma_3)^2\right]}} \in [-\infty;+\infty]\,; \tag{2.16}$$

$$\theta = \frac{1}{3}\arccos(\xi) \in \left[0;\frac{\pi}{3}\right]; \tag{2.17}$$

$$\xi = \frac{3\sqrt{3}J_3'}{2J_2'^{3/2}} = \frac{27(\sigma_1-\sigma_m)(\sigma_2-\sigma_m)(\sigma_3-\sigma_m)}{2\left(\frac{1}{2}\left[(\sigma_1-\sigma_2)^2+(\sigma_2-\sigma_3)^2+(\sigma_1-\sigma_3)^2\right]\right)^{3/2}} \in [-1;1]\,. \tag{2.18}$$

With regard to the representation of the yield locus in 3D stress space as displayed in

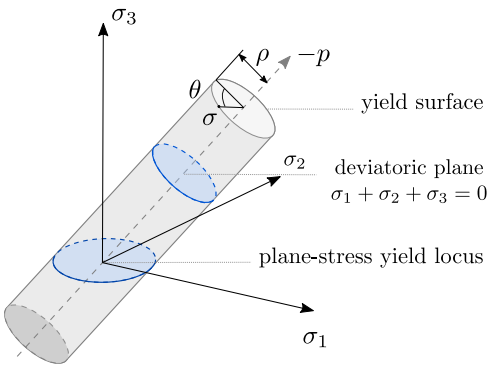

Figure 2.4.: vonMises yield surface in 3D stress space based on the principal stresses

Figure 2.4, these two stress invariants allow to describe a point in the vonMises-cylinder similar to cylinder coordinates. In the deviatoric plane the Lode angle θ is the angle which allows to orbit around the axis of hydrostatic pressure with the radius $\rho = \sqrt{2J_2'}$ of the yield surface. With the help of the Lode angle as a measure it is possible to distinguish if a certain stress state, e.g. uniaxial tension, is derived from a flat dog-bone specimen or a rotational symmetric round bar specimen.

Table 2.2.: Overview of characteristic stress states defined by the stress triaxiality η_{MF} and the corresponding experimental specimens

Stress state	Nomenclature	Stress triaxiality η_{MF} in -	Specimen
Hydrostatic pressure	tC	$-\infty$	-
Biaxial compression	bC	-2.0	Biaxial compression test
Uniaxial compression	uC	-1.0	Uniaxial compression test
Shearing	sH	0.0	ASTM-shear specimen
Uniaxial tension	uT	$+1.0$	Uniaxial tensile test
Plane strain	pS	$\frac{3}{\sqrt{3}} = +1.73$	Waisted tensile test
Biaxial tension	bT	$+2.0$	Biaxial or notched tensile test
Hydrostatic tension	tT	$+\infty$	-

η_{MF} denotes here the stress triaxiality normalized by the uniaxial tension so that $\eta_{MF} = 1.00$ following $\eta_{MF} = 3 \cdot \eta$ is valid. For more detailed information on the stress states and how they can be obtained from specimens of different shapes the interested reader is referred to Appendix A.1.

Alternatively, a stress state can also be described for the plane stress situation using a strain-rate ratio α, which is defined as the ratio of the strain-rate in the second principal direction to the strain-rate in the first principal direction (see Equation (2.19)). As a first approximation, the strain-rate ratio α can be approximated by the ratio of principle strains in respective directions.

$$\alpha = \frac{\dot{\varepsilon_2}}{\dot{\varepsilon_1}} \approx \frac{\varepsilon_2}{\varepsilon_1}. \tag{2.19}$$

Direct transformation of the stress-space parameter stress triaxiality η_{MF} into the strain-rate parameter α is only feasible for isotropic materials and linear strain paths using Equation (2.20) for the special case of plane stress state for $-2.0 \leq \eta_{MF} \leq +2.0$ [20]. An overview of the ratio of principal strains and corresponding values of α is given in Table 2.3.

$$\varepsilon_{vM} = \frac{2}{\sqrt{3}} \varepsilon_1 \sqrt{1 + \alpha + \alpha^2}. \tag{2.20}$$

$$\varepsilon_{ij} = \frac{1}{2}\left(\frac{\partial u_j}{\partial x_i} + \frac{\partial u_i}{\partial x_j}\right) = \begin{pmatrix} \varepsilon_{11} & \varepsilon_{12} & \varepsilon_{13} \\ \varepsilon_{21} & \varepsilon_{22} & \varepsilon_{23} \\ \varepsilon_{31} & \varepsilon_{32} & \varepsilon_{33} \end{pmatrix} = \begin{pmatrix} \varepsilon_{11} & \varepsilon_{12} & \varepsilon_{31} \\ \varepsilon_{12} & \varepsilon_{22} & \varepsilon_{23} \\ \varepsilon_{13} & \varepsilon_{23} & \varepsilon_{33} \end{pmatrix}. \tag{2.21}$$

Table 2.3.: Overview of characteristic stress states defined by the strain-rate ratio α

Ratio of principal strains ε_2 / ε_1	Strain-rate ratio α in -	Description of stress state
$-2/1$	- 2.0	Uniaxial compression
$-1/1$	- 1.0	Shearing
$-0.5/1$	- 0.5	Uniaxial tension
$0/1$	0.0	Plane strain
$1/1$	+ 1.0	Biaxial tension

Equation (2.21) represents the linearized strain tensor derived from the Green-Lagrange-deformation tensor under the assumption of small strains. The entries in the main diagonal represent normal strains and non-diagonal entries correspond to shearing. We further use

$$\varepsilon_{ij} = \frac{\gamma_{ij}}{2} \text{ with } i \neq j. \tag{2.22}$$

Analogously to the definition of the equivalent vonMises stress the equivalent vonMises strain can be defined using the principle strain components as stated in Equation (2.23).

$$\varepsilon_{vM} = \frac{1}{\sqrt{2}\,(1+\nu)} \sqrt{(\varepsilon_1 - \varepsilon_2)^2 + (\varepsilon_2 - \varepsilon_3)^2 + (\varepsilon_3 - \varepsilon_1)^2}. \tag{2.23}$$

The first principal strain components are defined in the system of principal axis which has an orientation for which the sections orthogonal to the axis shear strains vanish and only principal strains remains as in Equation (2.24).

$$\boldsymbol{\varepsilon} = \begin{pmatrix} \varepsilon_1 & 0 & 0 \\ 0 & \varepsilon_2 & 0 \\ 0 & 0 & \varepsilon_3 \end{pmatrix}; \tag{2.24}$$

The principal strains are orthogonal to one another following the nomenclature of Equation (2.25):

$$\varepsilon_1 \geq \varepsilon_2 \geq \varepsilon_3. \tag{2.25}$$

The invariants of the strain matrix are defined as the following in Equation (2.26).

$$I_1 = tr\,(\boldsymbol{\varepsilon}) = \varepsilon_1 + \varepsilon_2 + \varepsilon_3; \tag{2.26}$$

$$I_2 = \frac{1}{2}\left(tr\left(\boldsymbol{\varepsilon}^2\right) - tr\,(\boldsymbol{\varepsilon})^2\right) = \varepsilon_1\varepsilon_2 + \varepsilon_2\varepsilon_3 + \varepsilon_1\varepsilon_3; \tag{2.27}$$

$$I_3 = det\,(\boldsymbol{\varepsilon}) = \varepsilon_1 \cdot \varepsilon_2 \cdot \varepsilon_3. \tag{2.28}$$

The first strain invariant I_1 represents the length change of a the diagonal of a cube, the second strain invariant I_2 change of the surface and the third I_3 the change of volume of a cube [21].

2.1.2. Explicit time integration scheme

In continuum mechanics, three different types of non-linearities exist. They are either related to geometry (e.g. large deformations), material (e.g. plastic yielding) or structure (e.g. contact). Based on shape functions, the FEM provides a spatial discretization of a structure. For the additional time discretization, different integration schemes are established. While in an implicit time integration scheme a system of equations set up for a future time step has to be solved, this is not the case for the explicit approach. The equations for the implicit time integration scheme use only the unknown quantities in the future and will be hence solved iteratively while respecting convergence criteria. If these cannot be met, the time step is reduced until a solution can be found respecting the convergence criteria. Nevertheless, due to the unconditional stability of the implicit methods, the implicit time integration scheme normally allows big time steps reducing the total number of time steps.
In the explicit time integration scheme however, the system of equations is assumed to be constant for a comparably small time step and therefore can be extrapolated for the next time step. In order to ensure numerical stability and to keep the numerical error as small as possible, the time step size needs to be very small, resulting in a huge number of time steps. Because of non-linearities mentioned above, which are crucial to respect in a crashsimulation, convergence is challenging for implicit methods such that we often end up with at least the same number of time steps like in explicit schemes. Resolving the system of equations in an implicit time step is more costly (e.g. conversion of the stiffness matrix $\mathbb{C}^{-1}$) than for the explicit time step. The computational cost in an implicit finite element method is approximately proportional to the square of the number of degrees of freedom of the model, whereas that of the explicit finite element method is directly proportional to the number of degrees of freedom. This means the explicit time integration scheme is the standard approach for virtual development concerning crashworthiness. In the following, the theory is summarized for linear systems because this is sufficient to demonstrate the time-step approach.

After spatial discretization via FEM shape functions, we obtain the following non-linear ordinary differential equation (ODE):

$$\mathbb{M}\vec{a} + \mathbb{D}\vec{v} + \mathbb{C}\vec{u} = \vec{F}(t); \tag{2.29}$$

$$\mathbb{M}\frac{d^2\vec{u}}{dt^2} + \mathbb{D}\frac{d\vec{u}}{dt} + \mathbb{C}\vec{u} = \vec{F}(t). \tag{2.30}$$

Here $\mathbb{M}$ denotes the mass matrix, $\mathbb{D}$ the damping, and $\mathbb{C}$ the stiffness matrix. For the explicit scheme, we use a central differences approach, which is here defined for the velocities at half time step via [22]:

$$\dot{\vec{u}}^{(i+\frac{1}{2})} = \dot{\vec{u}}^{(i-\frac{1}{2})} + \frac{\Delta t^{(i+1)} + \Delta t^{(i)}}{2}\ddot{\vec{u}}^{(i)}. \tag{2.31}$$

$$\vec{u}^{(i+1)} = \vec{u}^{(i)} + \Delta t^{(i+1)} \dot{\vec{u}}^{(i+\frac{1}{2})}. \tag{2.32}$$

The available explicit FE solver use the central difference rule to integrate the motion explicitly through time (see Equation (2.31). Since the explicit procedure normally uses a diagonal, i.e. lumped mass matrix, $\mathbb{M}$, solving for the accelerations is trivial. Because of this decoupling, the explicit time integration requires neither iterations nor the assembly of the tangent stiffness matrix [22]. As shown in literature, this approach is only conditionally stable, i.e. the smallest stable time step is defined by the Courant-criterion as the solution of an eigenvalue problem [23]:

$$\Delta t_c \leq \frac{2}{\omega_{max}} \left(\sqrt{1 + \xi^2} - \xi \right); \tag{2.33}$$

where ξ denotes the fraction of critical damping for the highest eigenmode and ω_{max} the largest eigenfrequency. Using FEM, the critical time step Δt_c is defined by the ratio of the critical element length to the current effective dilatational wave speed c of the material as displayed in Equation (2.34). The latter is defined in a one-dimensional case using linear isotropic elasticity by the ratio of the Young's modulus E and mass density ρ of the material, $c = \sqrt{E/\rho}$. For FEM with linear shape functions, the critical element length l_c represents the minimal distance between two nodes in a single element over all elements in the corresponding mesh. For linear problems, the definition can be used as stated in Equation (2.34), but for non-linear problems and to avoid stability problems when using damping, an additional safety margin for the critical time step needs to be defined ranging from 0.67-0.90.

$$\Delta t_c = \frac{l_c}{c} = l_c \sqrt{\frac{\rho}{E}}; \tag{2.34}$$

$$l_c = \min\left(l_e\right). \tag{2.35}$$

For the explicit time integration scheme, the relation in Equation (2.35) implies that the overall critical time step for a simulation run is determined by the smallest element of the entire FEM mesh. To ensure a low computational cost of a model it is therefore desirable to have a homogeneous discretization throughout the entire model. As this is hardly feasibly for some parts with e.g. geometrical details which cannot be neglected in the modeling, a selective mass scaling can be used to compensate the effect of the critical elements. For the selective mass scaling, the mass density of the critical elements is artificially augmented which increases the critical time step of these elements.

2.2. Material modeling of ductile metals

With the mechanical and computational fundamentals stated, the material modeling of the first base material, ductile metals, is outlined throughout the following chapter. The constitutive equations relating the inner stresses with strains as displayed in the Tonti-diagram in Figure 2.1 up to the point of failure initiation will be explained. After surpassing the linear elastic regime with direct proportional Hooke's law, non-reversible, plastic deformation commence to occur which are characterized by a non-linear degressive characteristic of the stress-strain curve. In order to account for the plastic deformation in a material model, a general yield criterion is needed as well as a hardening law relating the stresses to the plastic strain. For metallic material models to describe the behavior along the loading history on a macroscopic scale the following components are required:

1. Linear elasticity;
2. Yield criterion;
3. Plastic hardening law;
4. Flow rule associativeness;
5. Failure envelope.

For ductile metals, material parameters are obtained in an experimental characterization program. For ductile thin-walled sheet metals, this experimental characterization is mainly done in the plane of the sheet metal covering the anisotropy induced by the rolling process.

2.2.1. Linear elasticity

In this section, the modeling for linear elasticity for ductile metals is summarized addressing isotropic and anisotropic cases. Because they can also be used for other materials discussed in this thesis, the description given here is kept general; i.e. it can be transferred to the modeling of an uni-directional layer of fiber reinforced plastic (FRP). In linear-elastic regime, the stresses and strains are coupled by Hooke's law over the following constitutive Equations (2.36) and (2.38) for the 1D and a general 3D stress state, respectively. Where $\mathbb{C}$ denotes the stiffness or elasticity tensor and $\mathbb{S}$ the compliance tensor, which can be derived as the inverse of the elasticity tensor $\mathbb{S} = \mathbb{C}^{-1}$. Both tensors are symmetrical and of fourth order.

$$\sigma_{ij} = \mathbb{C}_{ijkl} \cdot \varepsilon_{kl}; \tag{2.36}$$

$$\begin{pmatrix}\sigma_{11}\\ \sigma_{22}\\ \sigma_{33}\\ \sigma_{12}\\ \sigma_{13}\\ \sigma_{23}\end{pmatrix} = \begin{bmatrix} C_{1111} & C_{1122} & C_{1133} & C_{1112} & C_{1113} & C_{1123} \\ & C_{2222} & C_{2233} & C_{2212} & C_{2213} & C_{2223} \\ & & C_{3333} & C_{3312} & C_{3313} & C_{3323} \\ & & & C_{1212} & C_{1213} & C_{1223} \\ & sym. & & & C_{1313} & C_{1323} \\ & & & & & C_{2323} \end{bmatrix} \cdot \begin{pmatrix}\varepsilon_{11}\\ \varepsilon_{22}\\ \varepsilon_{33}\\ \varepsilon_{12}\\ \varepsilon_{13}\\ \varepsilon_{23}\end{pmatrix}. \tag{2.37}$$

$$\varepsilon_{ij} = \mathbb{C}^{-1}_{ijkl} \cdot \sigma_{kl} = \mathbb{S}_{ijkl} \cdot \sigma_{kl}. \tag{2.38}$$

Because of the symmetry of the elasticity tensor for the general case, 21 independent variables remain for the description of the tensor of fourth order. If symmetry planes can be found for the continuum of a material these symmetries can be used to further reduce the number of independent variables to describe the material (see Figure (2.5)).
While in the linear-elastic range, the following material parameters are needed

- **Young's modulus E:**
  The Young's modulus E_i represents the slope of the stress-strain-curves in the linear-elastic regime for loading in i-direction
  $$E_i = \frac{\Delta\sigma_{ii}}{\Delta\varepsilon_{ii}}. \tag{2.39}$$

- **Shear modulus G:**
  The shear modulus G_{ij} describes the linear elastic deformation of the materials under shear loading
  $$G_{ij} = \frac{\tau_{ij}}{\tan(\gamma_{ij})} \approx \frac{\tau_{ij}}{\gamma_{ij}}. \tag{2.40}$$

- **Poisson's ratio ν:**
  Lateral strain or transversal contraction of a material perpendicular to loading direction can be calculated using the Poisson's ratio ν_{ij}. It is defined as the ratio of the longitudinal ε_{jj} to the lateral strain ε_{ii}
  $$\nu_{ij} = -\frac{\varepsilon_{jj}}{\varepsilon_{ii}}. \tag{2.41}$$
  For isotropic materials the definition of the Poisson's ratio lays in the range of
  $$\nu_{ij} \in [-1.0; 0.5[\,. \tag{2.42}$$
  A value of $\nu = 0.0$ indicates that a longitudinal strain will not evoke a length change in lateral direction. Whereas $\nu = 0.5$ denotes incompressible material behavior as it is typical e.g. for rubber. A negative Poisson's ratio will cause a transverse expansion and can be observed for highly anisotropic materials such as honeycomb structures and are also referred to as auxetic materials.

- **Bulk modulus K:**
  The bulk modulus K specifies the necessary variation of pressure for an elastic volume change of the material. This relations is given for an isotropic material by

$$K = -\frac{\Delta p}{\Delta V/V}. \tag{2.43}$$

As an incompressible behavior of $\nu = 0.50$ entails a numerical singularity, a slightly smaller value is used for the Poisson's ratio of $\nu = 0.499$. It is common practice to define the incompressibility with a sufficiently high ratio of the bulk modulus K to the shear modulus G [14]. As the shear and bulk modulus are usually not determined experimentally, at least for isotropic materials they can be calculated using the Young's modulus E and Poisson's ratio ν using Equations (2.44) and (2.45).

$$G = \frac{E}{2 \cdot (1+\nu)} \rightarrow \nu = \frac{E}{2 \cdot G} - 1; \tag{2.44}$$

$$K = \frac{E}{3 \cdot (1-2 \cdot \nu)}. \tag{2.45}$$

Figure 2.5 displays the application of material symmetry planes on a cube and provides some material samples. Transverse isotropy is defined with a single preferential direction and homogeneous material properties in the plane perpendicular to the preferential direction. This direction is defined in case of UD-laminates, short fibre reinforced thermoplastic (SFRT) along the fibers and for a cold rolled sheet normal to the sheet if the in-plane properties do not vary strongly. For a pronounced in-plane orthotropy cold rolled sheet need to be modeled as orthotropic as wood or textiles. With the use of the material symmetries the number of independent variables can be reduced significantly for the elasticity tensor $\mathbb{C}_{ijkl}$ as displayed in Table 2.4. This is also applicable to the plastic regime. Without the use of symmetry planes the number of variables increases together with the required experimental input.

Table 2.4.: Overview of the independent variables of the elasticity tensor for different material symmetries

Material description	Symmetry planes	Number of variable	Independent variables
anisotropic	0	21	$\mathbb{C}_{ijkl}$
orthotropic	3	9	$E_{11}, E_{22}, E_{33}, \nu_{12}, \nu_{23}, \nu_{31},, G_{12}, G_{23}, G_{31}$
transverse isotropic	∞	5	$E_{11}, E_{22}, \nu_{12}, \nu_{23}, G_{12}$
isotropic	∞	2	E_{11}, ν_{12}

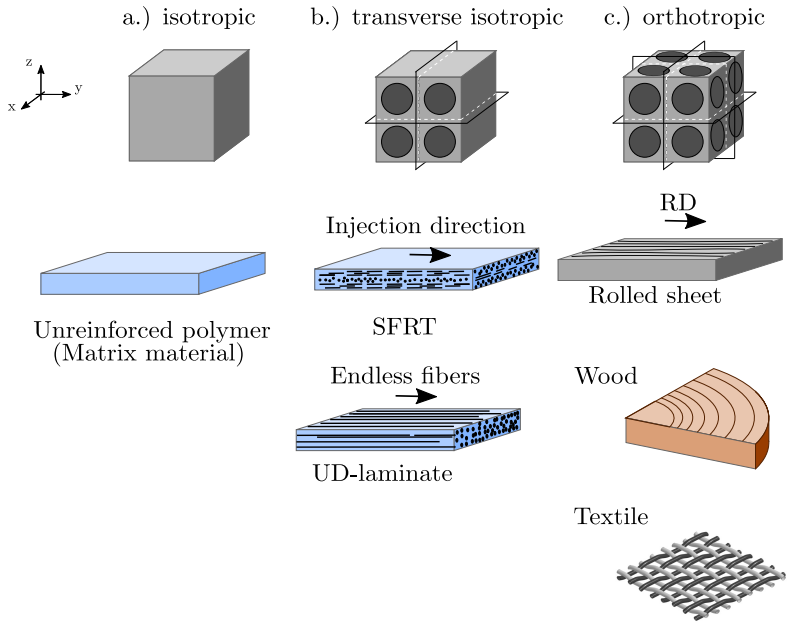

Figure 2.5.: Schematic sketch for the symmetry planes for a.) isotropic b.) transverse isotropic and c.) orthotropic material including examples

2.2.2. Plasticity

After the purely elastic deformation, plastic deformations will result in a permanent, non-reversible change of shape. In the context of ductile metals, the phenomenon of plastic yield originates from movement of dislocations in the crystal lattice structure under shear loading [24]. The plastic deformations are hence irreversible and deformation under yielding represents an isochoric process. In order to account for plastic yielding in a simulation, the material model needs to have a yield locus including a plastic flow rule as well as a plastic strain hardening law.

Yield locus:
Yield locus describes the onset of yielding in dependence on the stress state. All stress states within the yield locus show purely elastic behavior. Different formulation of yield loci are available ranging from an isotropic vonMises to an orthotropic Hill1948 or Barlat2000 and Dell2006. To reduce complexity and also computational cost it is best practice to use the simplest yield locus formulations with a good fit of all experiments. Figure 2.6 displays the trace of von Mises yield locus in the σ_1-σ_2-plane for the plane stress state. The points on the trace indicate yield strength for different stress states embodied with a loading on an infinitesimal volume element and icons for the respective physical experiment to derive the yield stresses for different stress states.

The trace of the vonMises cylinder representing the plane stress state can also be seen in Figure **??**, where the von Mises cylinder is displayed in the 3D stress space. It is the

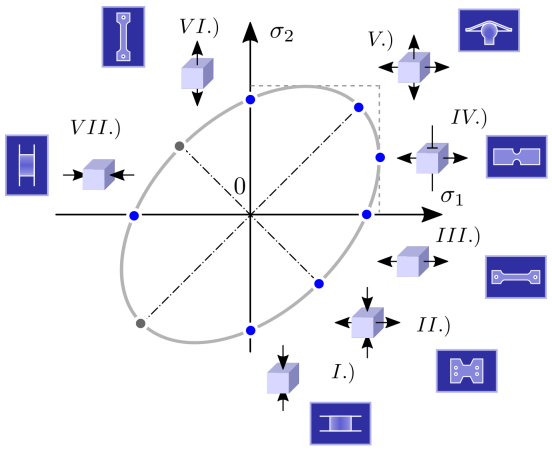

Figure 2.6.: Yield locus with yield strength for different stress states I.-VII. derived from experiments for plane stress state ($\sigma_3 = 0$)

projection onto the $\sigma_3 = 0$-plane. Here, the space diagonal of the first in the first and seventh octant displayed in dotted gray lines represents the hydrostatic axis.

Further, these yield loci can be enhanced with one of the correction terms displayed

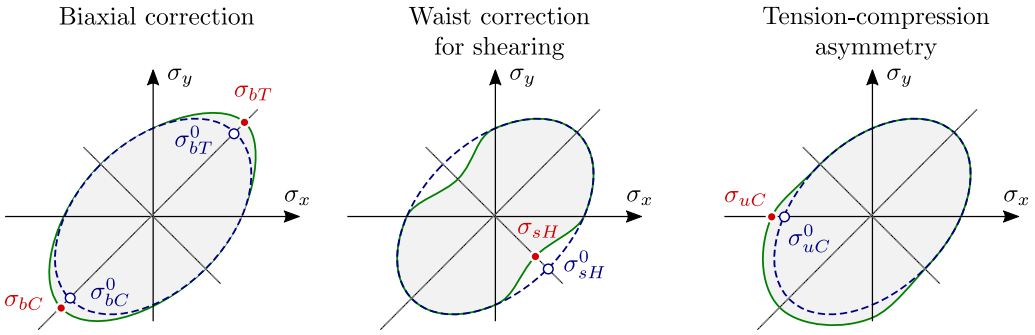

Figure 2.7.: Comparison of different yield locus correction terms with respect to an orthotropic yield locus Hill1948

in Figure 2.7. In terms of computational time it is more favorable to choose a model with fewer parameters, i.e. with rather a simpler correction term than a more complex functional description. These yield locus correction terms can also be a function of strain and strain-rate [25].

Using the correction terms for the yield locus, anisotropic plastic strain hardening of the material can be modeled in the simulation. In Figure 2.8 an example for anisotropic hardening for a twinning induced plasticity of an austenitic steel is presented. For the yield locus displayed on the left side of Figure 2.8 the dependency of correction terms for biaxial tension and waist are displayed for three different loading types uniaxial tension, biaxial tension and shearing together with the $\sigma_{eq} - \varepsilon_{eq}^{pl}$ curves for the corresponding stress states. While the original yield locus without any type of correction is displayed in dashed light green lines, the corrected yield locus is displayed in solid green lines. Comparing

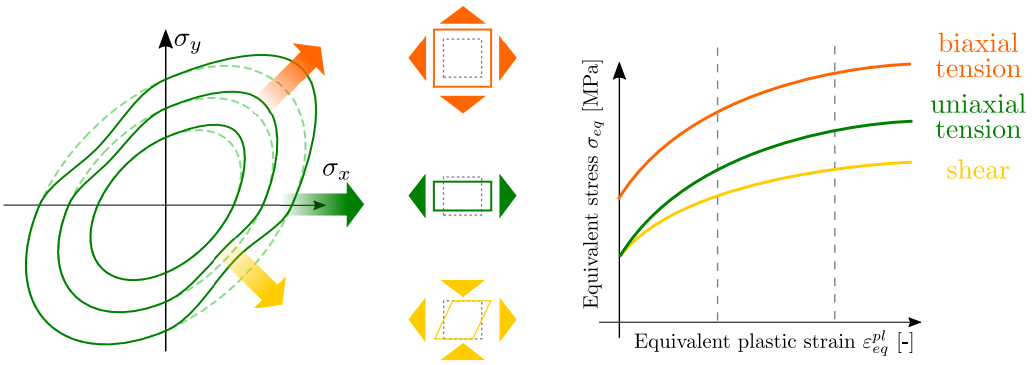

Figure 2.8.: Visualization of stress-state dependent, anisotropic hardening for an austenitic Twinning Induced Plasticity (TWIP) steel sheet

the yield loci for three different plastic strains exhibits the evolution of the yield locus with an increasing influence on the waist and biaxial correction term for higher strains.

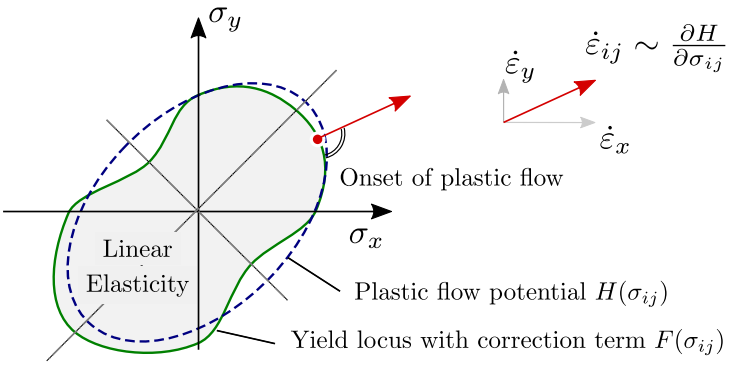

Figure 2.9.: Visualization of the plastic flow potential H and a yield locus F for a non-associative flow

$$F\left(\sigma_{ij}\right) = \sigma_{eq}. \tag{2.46}$$

The detriment of using these correction terms is that the corrected yield loci may lose their convexity. While the yield locus has a convex shape the plastic flow potential can be determined as the normal on the yield locus. This is referred to as associated plastic flow and means that the normal to the yield locus F can also serve to determine the plastic potential H [24]. Hence the plastic strain increments can be divided into components $\Delta\varepsilon_1$ and $\Delta\varepsilon_2$ according to the normal on the yield locus as displayed in Figure 2.9. Plastic associated flow stipulates a convex form of the yield locus for only a convex shaped potential allows to unambiguously determine the normal at any given point. In case that the yield locus is not taken as plastic potential, the plastic flow is defined independently with a non-associative model of the plastic flow [26].
Another important aspect while using the anisotropic hardening is to bear in mind that the plastic work hardening done upon loading is conserved independently of the type of

loading. The principle of equivalent plastic work is used when transferring the stress-strain curves from the reference plastic strain hardening curve to a different stress state or direction. The principle of equivalent plastic work stipulates that the energy of work defined as the area below the stress-strain curves will be conserved when changing form one stress state to another (see Equation (2.47)).

$$dW = \sigma_{eq} d\varepsilon_{eq} = \sigma_{vM} d\varepsilon_{vM}. \tag{2.47}$$

A drastic change from tension to compression can be observed for magnesium profile as displayed in Figure 2.10. Based on an initially orthotropic Hill1948 yield locus, a correction term for tension compression asymmetry is used which results in the shape of the yield locus depicted on the left side and a different characteristic in the stress-strain curves for tension and compression on the right side normalized by the yield stress under uniaxial tension. The areas below the plastic strain hardening curves represent the same amount of plastic strain hardening work under tension and compression. Based on the equivalent vonMises strain, the reference plastic strain hardening work under tension would be transformed to compression regime based solely on the strain value of $\varepsilon_{eq}^{pl} = 0.22$, which would reduce the initially green area to the intersecting area of gray and green, neglecting almost half of the remaining areas in between the compression curve in dashed gray lines and the tension curve in solid green lines. The principle of equivalent plastic work is hence used for transferring the stress strain curves from one stress state to another in the material model, but it is also used when using flow stress curves from other stress states or experiment for an elongation of the reference hardening curve in rolling direction (RD).

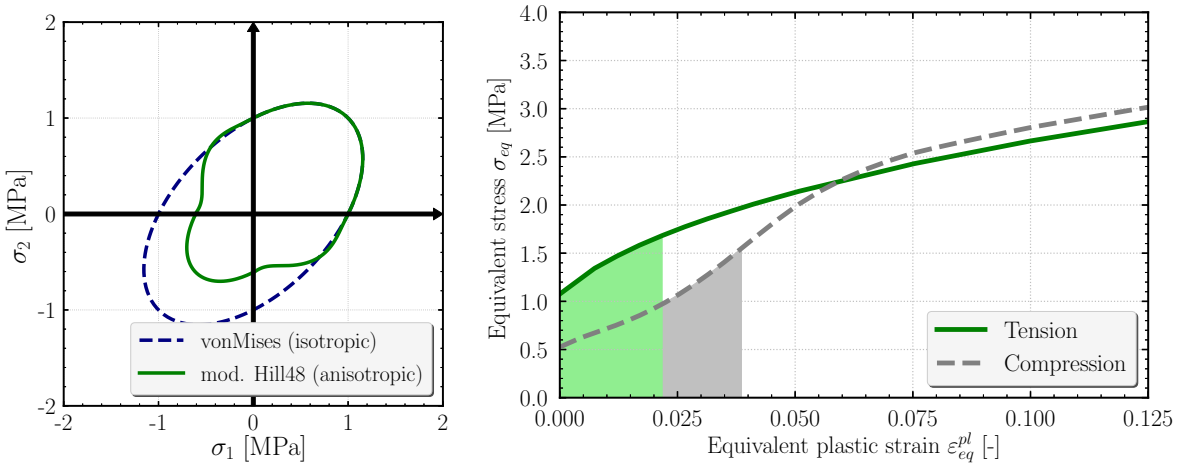

(a) Yield locus correction

(b) Plastic strain hardening

Figure 2.10.: Yield locus on the left and plastic strain hardening behavior in tension and compression on the right for a Magnesium MnE21 profile [27, 28]

In this context with the use of the anisotropic hardening the influence of the stress state on the plastic strain hardening can be accounted for. In other words the anisotropic

hardening allows to differentiate the type of loading while the in-plane orthotropy is described by the yield locus formulation.

R-value:
The in-plane orthotropy is described using the r-values, also referred to as Lankford coefficients. It is a measure from which direction the material tends to flow and is commonly used in deep-drawing simulations. The r-values are defined as the ratio of the plastic strain in thickness direction ε_t^{pl} and the plastic strain in width direction ε_w^{pl} (See also Equation (2.48)). For thin-walled metals the r-value is measured in parallel to the rolling direction (RD) for r_0, diagonal for r_{45} and transversal for r_{90} in a uniaxial tensile test. A high Lankford coefficient characterizes good deep-drawing properties of the material because most of the plastic flow originates from the width direction and less from the thickness direction. This means that the material is less prone to necking in the deep-drawing process. An r-value $r = 1.0$ is typical for an isotropic material.

$$r_i = \frac{\varepsilon_w^{pl}}{\varepsilon_t^{pl}}. \tag{2.48}$$

Plastic hardening law:
Basis for the plastic hardening law is the experimental input from e.g. a uniaxial tensile test. The experimentally measured data, engineering stress s and engineering strain e allow to compare materials among one another but do not provide a true information on the deformation characteristics. This is due to the fact that they are based entirely on the original dimensions such as initial cross-section A_0 or initial length l_0 of the specimens, which change continuously throughout the experiment. Therefore, these measurements can be converted into true stress σ, based on the actual cross-sectional area of the specimen A, and true strain ε also referred to as logarithmic strain with Equation (2.50). Equations (2.50) and (2.53) show how the true stress and strains can be derived from the engineering stresses and strains based on stipulating volume constancy as expressed in Equation (2.52). The limits of the integral in Equation (2.50) are applicable for uniaxial tension. For uniaxial compression, these integral limits are inversed resulting in a $1 - \mathrm{e}$ term as the argument of the natural logarithm. This argument reflects that the true stress σ is bigger than the engineering stress s for uniaxial tension as the stress increases with an increasing cross-section and vice versa for compression. Engineering stress s and true stress σ as well as engineering strain e and true strain ε respectively deviate from one another from the onset of yielding, the most pronounced deviation, however, takes place after the point of uniform elongation, when the cross section of the specimen decreases drastically.

$$\mathrm{e} = \frac{\Delta l}{l_0} = \frac{l - l_0}{l_0} \rightarrow \frac{l}{l_0} = \mathrm{e} + 1; \tag{2.49}$$

$$\varepsilon = \int_{l_0}^{l} \frac{dl}{l} = \ln\left(\frac{l}{l_0}\right) = \ln\left(\mathrm{e} + 1\right); \tag{2.50}$$

$$\mathrm{s} = \frac{F}{A_0}; \tag{2.51}$$

$$A_0 \cdot l_0 = A \cdot l \rightarrow \frac{A_0}{A} = \frac{l}{l_0}; \tag{2.52}$$

$$\sigma = \frac{F}{A} = s \cdot \frac{A_0}{A} = \mathrm{s} \cdot \frac{l}{l_0} = \mathrm{s}\,(\mathrm{e}+1)\,. \tag{2.53}$$

The true strain ε obtained from Equation (2.50) represents the total strain ε^{tot} including both the elastic ε^{el} and plastic ε^{pl} part. For the strain hardening behavior only plastic, permanent strains are considered, the elastic portion is deducted in accordance with Equation (2.54) for the 1D case leaving the remaining degressive branch (black) of the strain hardening behavior in Figure 2.11. A comparison between the engineering stress-strain curves measured in the experiment and the plastic flow curve deducted for uniaxial tension until the point of uniform elongation is given in solid black and red lines in Figure 2.15.

$$\varepsilon^{tot} = \varepsilon^{el} + \varepsilon^{pl} \rightarrow \varepsilon^{pl} = \varepsilon^{tot} - \frac{\sigma_{true}}{E}. \tag{2.54}$$

Figure 2.11 provides an overview of the different types of plasticity. For ductile sheet metals the degressive curve, i.e. the black curve is characteristic. From the uniaxial tensile tests the plastic hardening behavior can be used until the point of uniform elongation. After the point of maximal force $dF = 0$ diffuse necking starts and the stress state starts to change from uniaxial tension to plane strain. Larour discussed in his thesis the effect of the use of different analytical functions for the approximation of the plastic strain hardening behavior for ductile sheet metals (see Figure 2.12) [29, 30]. To choose which analytical law describes the plastic strain hardening behavior best at higher deformation, an additional experiment can be used. A hydraulic bulge test, a compression test with layered stack of circular plates or an in-plane torsion test allow to record the plastic strain hardening beyond the point of uniform elongation at a different stress state [5, 31]. However, for metals who exhibit an anisotropic hardening behavior, a different stress level will be recorded. Following the principle of plastic work, which stipulates a constant area below the plastic hardening curve for different stress states, the additional experimental data can be scaled to the stress level from uniaxial tension. Therefore, the combined plastic strain hardening curve can be used for the approximation of the analytical plastic hardening law [32].

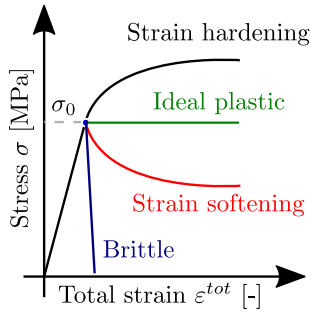

Figure 2.11.: Different types of plasticity

In Figure 2.12, the extrapolated plastic hardening behavior is displayed for different an-

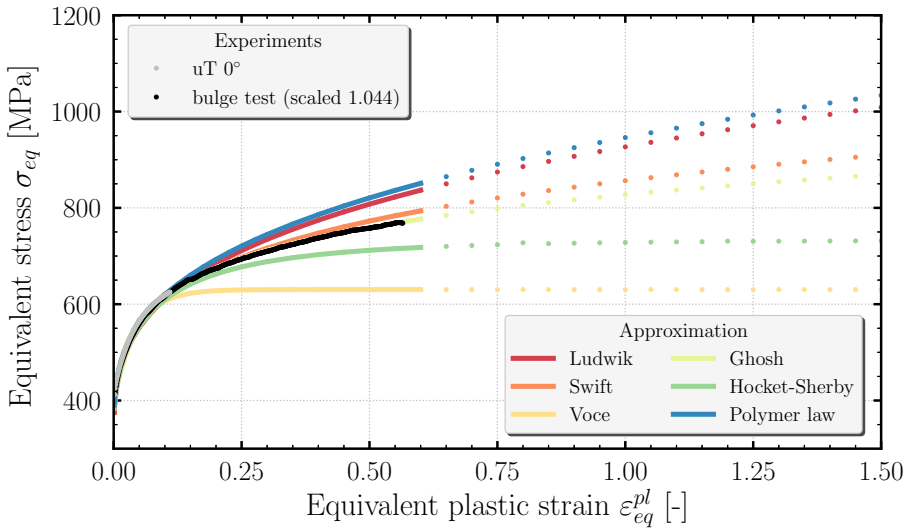

Figure 2.12.: Extrapolation results of analytical hardening laws for quasi-static experiments for S355JR (fit-range between $R_{p0.2}$ and R_m)

alytical laws together with the averaged experimental curves for a uniaxial tension (gray dots) and plane bulge test (black dots). The fitting of the analytical laws is done solely with the uniaxial tension data and no additional information from the bulge test is used. The material characterization of the S355JR will be discussed in detail in Chapter 4.2 and the more interested reader is referred to the work of Ghosh [33] and Larour [29, 30].

Ludwik	$\sigma_{eq}(\varepsilon_{eq}) = a + b\varepsilon_{eq}^{n}.$	(2.55)
Swift	$\sigma_{eq}(\varepsilon_{eq}) = a\,(\varepsilon_0 + \varepsilon_{eq})^{n}\,;$	(2.56)
Voce	$\sigma_{eq}(\varepsilon_{eq}) = a\,(1 - b \cdot \exp(-c\varepsilon_{eq}))\,;$	(2.57)
Ghosh	$\sigma_{eq}(\varepsilon_{eq}) = a \cdot (\varepsilon_0 + \varepsilon_{eq})^{n} + k;$	(2.58)
Hocket-Sherby	$\sigma_{eq}(\varepsilon_{eq}) = a - (a - \sigma_0) \cdot \exp(-c\varepsilon_{eq}^{n});$	(2.59)
Polymer law	$\sigma_{eq}(\varepsilon_{eq}) = a_0 + a_1 \cdot \varepsilon_{eq}^{n1} + a_2 \cdot \varepsilon_{eq}^{n2} \cdot exp(-c\varepsilon_{eq}).$	(2.60)

With Equations (2.55)-(2.60), analytical functions $\sigma_{eq}(\varepsilon_{eq})$ for the relationship between equivalent stress and equivalent plastic strains ε_{eq}^{pl} are outlined. ε_{eq} relates for all Equations (2.55)-(2.60) to the plastic true strain. The best parameter fit for the experimental input of the S355JR for some of these functions is plotted in Figure 2.12. In Figure 2.13 different types of plasticity are displayed with their influence on the yield locus as well as stress-strain curves for a load reversal from tension to compression. The colored dots on the yield surface in Figure 2.13 represent the yield stress under tension for the first loading in light blue, the yield stress under uniaxial tension in dark blue, and, under compression in green after some plastic deformations. If a material possesses isotropic hardening the yield strength is increasing identically for tension and compression after some initial plastic deformation. This behavior is captured by enlarging the yield lo-

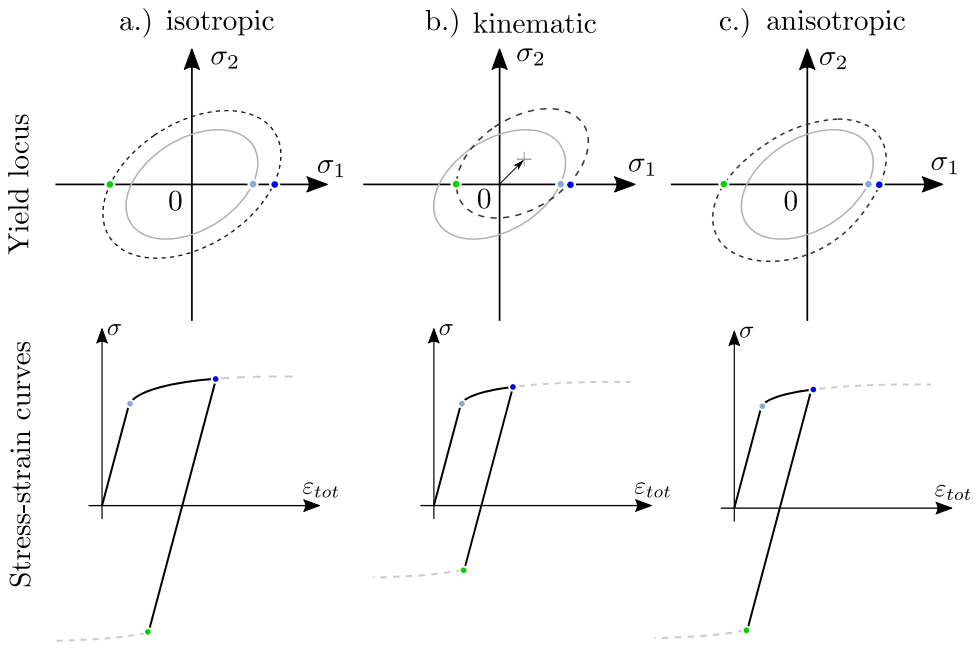

Figure 2.13.: Different types of plastic strain hardening for a load reversal from tension to compression: a.) isotropic, b.) kinematic and c.) anisotropic [26, 34]

cus after the initial plastic deformation as displayed with the two concentric yield loci in the top left of Figure 2.13. Some materials show an influence on the yield strength after a load reversal. After a loading under tension the very same specimen may show a reduced yield strength under compression. In this case the yield surface maintains the shape but is translated with respect to the origin named kinematic hardening (see middle column of diagrams in Figure 2.13). Almost all metals show a combination of isotropic and kinematic hardening. To account for such a combined isotropic-kinematic hardening, multiple tension-compression tests with load-reversal at different plastic deformations need to be conducted to differentiate between the isotropic and kinematic proportion. Lastly, anisotropic hardening may exist which is the case for e.g. Magnesium (Mn) profiles or some plastic materials. For anisotropic hardening the material deforms differently pronounced under tension and compression, which is why the shape of the yield locus evolves from its original shape as displayed on the right column of Figure 2.13. Besides the analytical equations represented above some rheological analogous or substitute models exist for modeling the plastic strain hardening, e.g. the Maxwell equation.

Strain-rate sensitivity:
In the simulation, logarithmic interpolation between defined strain-rates is performed. The strain-rate $\dot{\varepsilon}$ is defined as the derivative of the strain ε w.r.t. time as given in Equation (2.61).

$$\dot{\varepsilon} = \frac{d\varepsilon}{dt}; \tag{2.61}$$

$$\dot{\varepsilon}^{tot} = \dot{\varepsilon}^{el} + \dot{\varepsilon}^{pl}. \tag{2.62}$$

In order not to limit the generality of the strain-rate description $\dot{\varepsilon}$, the total strain-rate is considered to be composed of the elastic and plastic part as outlined in Equation (2.62). Especially for unreinforced thermoplastics, the elastic strain-rate $\dot{\varepsilon}_{el}$ can amount to a significant amount of the total strain-rate which cannot be neglected.
For metallic materials a pronounced strain-rate sensitivity behavior can be observed in experiments. To take the strain-rate sensitivity of the plastic strain hardening into account, experiments are performed at different strain-rates. A reference plastic hardening curve in the quasi-static range as described in the previous section is complemented for the strain-rate effect using an additional law from Equations (2.63) and (2.66).

- Cowper-Symonds:

$$\sigma_{eq}\left(\varepsilon, \dot{\varepsilon}\right) = \sigma_{ref}\left(\varepsilon\right) \cdot \left(1 + \left(\frac{\dot{\varepsilon}_{ref}}{D}\right)^{\frac{1}{p}}\right). \tag{2.63}$$

- Natural logarithmic m [29]:

$$\sigma_{eq}\left(\varepsilon, \dot{\varepsilon}\right) = \sigma_{ref}\left(\varepsilon\right) \cdot \left(\frac{\dot{\varepsilon}}{\dot{\varepsilon_{ref}}}\right)^{m}. \tag{2.64}$$

- tanhyp:

$$\sigma\left(\varepsilon, \dot{\varepsilon}\right) = \sigma_{ref}\left(\varepsilon\right)\left\{a_1 + a_2 \text{tanhyp}\left(a_3\left(\dot{\varepsilon} - a_4\right)\right)\right\}. \tag{2.65}$$

- Normal distribution:

$$\sigma\left(\varepsilon, \dot{\varepsilon}\right) = \sigma_{ref}\left(\varepsilon\right)\left\{1 + b\left[\exp(-f\left(\log\frac{\dot{\varepsilon}}{\dot{\varepsilon}_{ref}} - x\right)^2\right) - \exp(-fx^2)\right]\left(1 + c\exp(r\varepsilon)\right)\right\}. \tag{2.66}$$

$\dot{\varepsilon}_{ref}$ represents the quasi-state reference strain-rate for which a good approximation of the hardening behavior is found. Equations (2.63) to (2.65) multiply this quasi-static reference stress-strain curves to a different level in dependence on the formulation while keeping the same characteristic. More elaborate models for strain-rate dependency are based on the formulation of tanhyp, i.e. Equation (2.65), to account for a non-equidistant, logarithmic dependency. The last model using a normal distribution combines the aforementioned non equidistant, logarithmic dependency with a dependency of the strain ε which allows to change the characteristic of the hardening curve with its second term depending on the strain ε [25].
For a material with a pronounced positive strain-rate dependency on the plastic strain

hardening behavior, such as mild steels or polypropylene, including the strain-rate effect is crucial and can have an impact which is no longer negligible even for the simulation of a quasi-static tensile tests. After the onset of localized necking the strain-rate within the necking zone rises drastically. Including a positive strain-rate in the simulation can stabilize the simulation because for elevated strain-rates higher stresses can be reached. A comparative study on the influence of strain-rate sensitivity for crashworthiness using Euro NCAP load cases with and without considering strain-rate effect [35]. For the investigation of ductile, mild steel grades with a pronounced strain-rate dependency, it was found to have an significant influence on criteria such as global deformation or intrusion from 110% to close to 200%. Furthermore, negative strain-rate effects on the plastic strain hardening behavior can be observed for aluminum alloys originating in adiabatic softening as discussed in [20].

2.2.3. Failure criteria for ductile metals

Figure 2.14 summarizes the main failure modes which can be observed for ductile sheet metals. The predominant failure mode for ductile metal sheets, which exhibit plastic strain hardening prior to fracture, is necking [36]. Necking is an instability occurring under in-plane tensile loading for plastic deformation where relatively large amounts of strain localize disproportionately in a small region [37].

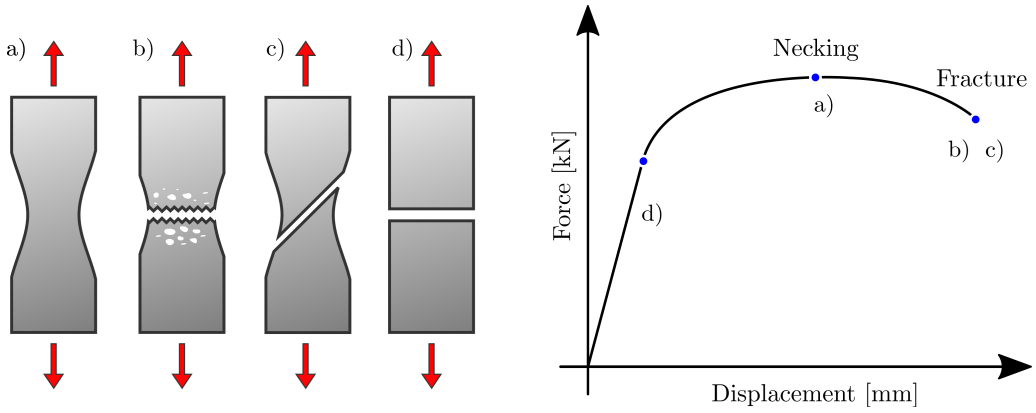

Figure 2.14.: Failure modes for ductile metals a) necking b) ductile normal fracture (DNF) c) ductile shear fracture (DSF) and d) brittle fracture

The ductile normal fracture (DNF) is caused by the growth and coalescence of pores and voids on a microscopic level until they eventually form a fracture on a macroscopic level. Due to these voids a rough fracture surface perpendicular to the loading direction characterizes this failure mode. Ductile shear fracture (DSF) is caused by shear band localization under plastic strain hardening. A smooth fracture surface under 45° to loading is characteristic. Hence, the failure modes can well be differentiated in the experiments

based on the physical appearance of the fracture specimens. Lastly, brittle fracture mode can occur for ductile metals under very low temperatures due to transgranular or intergranular cleavage.
Necking can be considered as a local instability when the geometrical softening can no longer be compensated by the plastic strain hardening of the material. This phenomenon of geometrical softening can be captured in a FEM simulation with solid elements accounting for stresses in thickness direction. The forming limit curve (FLC) represents an auxiliary mean to remedy that shell elements account only for membrane strains to assess the instability risk caused by necking. For thin sheet metals, necking often is the predominant failure mechanism which leads to local neck zones in which then either the ductile normal or shear fracture will occur [38].

How these mechanisms work can be explained with the use of the force-displacement curves of the uniaxial tensile tests under monotonous uniaxial loading as depicted in Figure 2.15 for a flat dogbone specimen made of a steel sheet. After trespassing the elastic range, plastic strain hardening commences in the zone of parallel length (Point I) in Figure 2.15). At the force peak, when the point of uniform elongation is reached, diffuse necking starts. It is triggered by a geometrical imperfection like a slight variation of the width due to the milling of the specimen. The onset of diffuse necking coincides with the force peak at Point II and is characterized by instability from width direction. At a certain point, the thinning can no longer be compensated by the increase of stress, which means that the force for a local element is no longer in equilibrium and local necking starts. As long as the increase in stress is able to compensate the reduction of the cross-section the force increases. In which degree the plastic hardening takes place from the width or thickness is described with the use of r-values. At approximately 2/3 of the way from the point of uniform elongation until the fracture, local necking commences at Point III in Figure 2.15). The effect of local necking is triggered by some inhomogeneity in the microscopic texture. After the onset of local necking the strains start to localize very quickly. Two mechanisms help to stabilize the area of the local neck while the force is monotonously decreasing. At the beginning the local Poisson's ratio ν impedes the transversal contractions which forces the stress state within the region of local necking to change from uniaxial tension $\eta_{MF} = 1.0$ to plane strain $\eta_{MF} = 1.73$. This results in an increase of stress. The second supporting effect is the strain-rate dependency of the material. After the strains start to localize, the strain-rate increases in the area of the local neck. With a positive strain-rate effect, the plastic hardening behavior jumps to a higher stress level. This is why it is important also to model the strain-rate dependency of the material behavior for quasi-static tests. Eventually failure of the metallic material occurs (Point IV) in Figure 2.15). An analysis of the fracture surface after the experiment can clarifiy whether the specimen failed by ductile shear or ductile normal fracture. Whereas for ductile shear fracture a smooth surface occurs, which is due to shear band localization under 45° w.r.t. the loading direction, the ductile normal fracture is characterized by a rough fracture surface normal to the loading direction due to the growth and coalescence of micro-voids prior to the macroscopic rupture.

In the context of metallic materials, three types of failure criteria exist which can

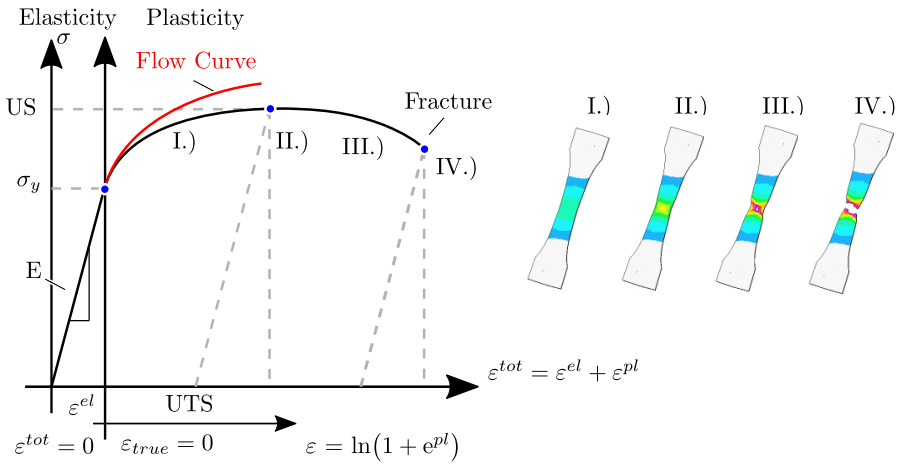

Figure 2.15.: Stress-strain curves with material characteristic values and different phases of plastic hardening for the uniaxial tension loading of a flat dogbone specimen [32]

be differentiated by the metric: strain-based, stress-based and energy-based fracture criteria. The state of the art of the most common fracture models was compared and benchmarked by [39] regarding their applicability, their calibration effort and predictive quality in simulation. This thorough and comprehensive study includes seven fracture models ranging from simple approaches as a constant fracture strain or a maximum shear stress to functions of the strain based threshold depending on two stress invariants.
Following the conclusions of Wierzbicki, the two failure models of Xue-Wierzbicki as well as CrachFEM will be represented in the following [39, 20].

Xue-Wierzbicki:
For the description of fracture in 3D, the stress triaxiality η is no longer unique. Hence, two stress invariants are needed, whereas for plane strain states for shell elements only a single invariant is sufficient [39]. In Figure 2.16 the fracture surface is displayed over the stress triaxiality η and parameter of the Lode angle ξ, both introduced in Section 2.1.1. For sake of simplicity the parameter of the Lode angle ξ is abbreviated as Lode parameter ξ. This criterion is able to predict fracture generally for all stress states as long as the deformation follows a linear strain path as stated in Equation (2.67).

$$\int_0^{\varepsilon_{eq}^{**}} \frac{d\varepsilon_{eq}}{f(\eta, \xi)}. \tag{2.67}$$

The fracture criterion of Xue-Wierzbicki is given by Equation (2.68). For this formulation four parameters $C_i, i = 1...4$ need to be derived from four independent experiments. Additionally to the 3D-fracture surface in Figure 2.16, the trace for the plane stress condition is marked in red on the surface and projected on the right, yielding the characteristic of $\varepsilon_{eq}^{**}(\eta)$. This failure model does not distinguish the failure mode.

$$f(\eta, \xi) = \varepsilon_{eq}^{**}(\eta, \xi) = C_1 \exp(C_2 \eta) - [C_1 \exp(C_2 \eta) - C_3 \exp(C_4 \eta)] \left(1 - \xi^{1/n}\right)^n. \tag{2.68}$$

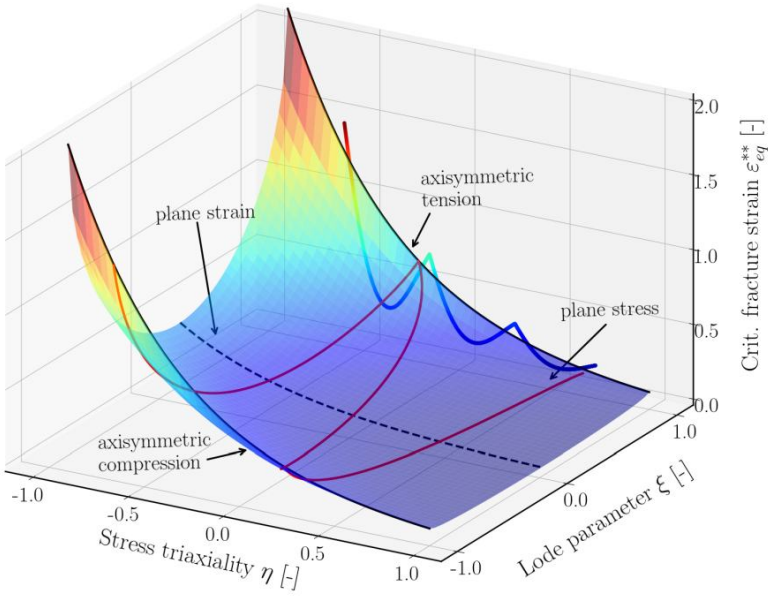

Figure 2.16.: Symmetric fracture surface according to Xue-Wierzbicki in dependence on two stress invariants [39]

CrachFEM:
The *CrachFEM* failure model comprises two different failure modes for ductile normal and shear fracture as well as necking by a transient calculation of the FLC based on the *Crach*-algorithm [20, 31]; this is explained in the following.

Ductile normal fracture (DNF):
A general relation for the non-monotonic behavior of equivalent fracture strain ε_{eq}^{**} with increasing stress triaxiality η is given with Equation (2.69)

$$\varepsilon_{eq}^{**} = d_0 e^{-c\eta_{MF}} + d_1 e^{c\eta_{MF}}. \tag{2.69}$$

In Equation (2.69), d_0 and d_1 are material dependent parameters and c describes the in-plane orthotropy of the material. As this general form must also be applicable to the specific loading for equibiaxial tension and compression, which are both theoretically independent of the orientation, the following conditions stated below must be fulfilled:

$$\varepsilon_{NF}^{+} = \varepsilon_{eq}^{**}\left(\eta_{MF} = \eta^{+}\right), \varepsilon_{NF}^{-} = \varepsilon_{eq}^{**}\left(\eta_{MF} = \eta^{-}\right), \tag{2.70}$$

where ε_{NF}^{+} and ε_{NF}^{-} represent the equivalent fracture strain ε_{eq}^{**} for equibiaxial tension and compression occurring under normal fracture, and η^{+} and η^{-} the corresponding stress

triaxialities η. Substituting the conditions in Equation (2.70) for the material parameters d_0 and d_1 in Equation (2.69) yields

$$\varepsilon^{**}_{eq,NF}\left(\eta_{MF},\alpha\right) = \frac{\varepsilon^{+}_{NF}\cdot\sinh[c(\eta^{-}-\eta_{MF})]+\varepsilon^{-}_{NF}\cdot\sinh[c(\eta_{MF}-\eta^{+})]}{\sinh[c(\eta^{-}-\eta_{MF})]}. \tag{2.71}$$

In Equation (2.71) introducing the orientation variable $c(\alpha)$ allows to describe the planar orthotropy of the fracture strain in dependence on the off-axis angle α.

Ductile shear fracture (DSF):
For the ductile shear fracture, the shear fracture parameter θ is introduced with Equation (2.72). Here k_{SF} represents a material parameter and φ the ratio of the maximum shear stress τ_{max} to the equivalent stress according to vonMises σ_{vM}. Since the shear fracture parameter θ combines two stress invariants, the stress triaxiality η_{MF} and the ratio τ_{max}/σ_{vM}, it is applicable to both plane stress and general 3D stress state. Hence, the equivalent plastic strain for shear fracture can be formulated w.r.t. θ as given in Equation (2.73).

$$\theta = \frac{1-k_{SF}\eta_{MF}}{\varphi} \text{ with } \varphi = \frac{\tau_{max}}{\sigma_{vM}} \text{ where } \tau_{max} = \frac{\sigma_I-\sigma_{III}}{2}; \tag{2.72}$$

$$\varepsilon^{**}_{eq,SF}\left(\eta_{MF},\alpha\right) = \frac{\varepsilon^{+}_{SF}\cdot\sinh[f(\theta^{-}-\theta)]+\varepsilon^{-}_{SF}\cdot\sinh[f(\theta-\theta^{+})]}{\sinh[f(\theta^{+}-\theta^{-})]}. \tag{2.73}$$

Where θ^{+} and θ^{-} represent the values for θ for the stress state of equibiaxial tension and compression and ε^{+}_{SF} and ε^{-}_{SF} denote the equivalent plastic strains at fracture for equibiaxial tension (+) and equibiaxial compression (-). Besides ε^{+}_{SF} and ε^{-}_{SF}, f is the third material parameter in Equation (2.73).

$$\varepsilon^{+}_{SF} = \varepsilon^{**}_{eq}\left(\theta=\theta^{+}\right), \varepsilon^{-}_{SF} = \varepsilon^{**}_{eq}\left(\theta=\theta^{-}\right). \tag{2.74}$$

Even though a planar orthotropy of the shear fracture can be included with the orientation variable $f(\alpha)$, the orthotropy shows no significant influence on the shear fracture and therefore assuming a constant f is accepted [36].

Figures 2.17a and 2.17b display the fracture limit surface, for fracture criteria of ductile normal (DNF) and ductile shear fracture (DSF) exemplarily for the dual phase steel DP600. These fracture surfaces are displayed in an isometric view over the stress triaxiality η_{MF} and Lode parameter ξ which are needed for a generalized 3D failure description for solid element formulation. For shell elements, these surfaces are based on the assumption that the stress component in thickness direction is negligible ($\sigma_3 = 0$). This assumption of the plane stress is displayed in Figures 2.17a to 2.17b as the trace in a solid line. The failure description of shell elements based on plane stress depends only on stress triaxiality η_{MF} as shown in Figures 2.17c and 2.17d. Note that Figures 2.17c and 2.17d display a rotation of the view from Figures 2.17a and 2.17b. In this representation of Figure 2.17a the trace for ductile shear fracture, which resembles a garland, lays well in

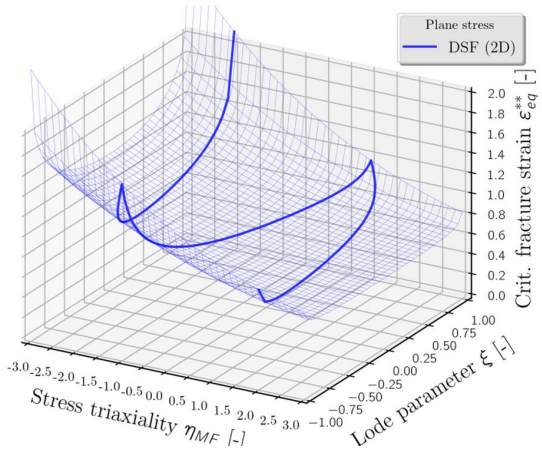

(a) Isometric view on DSF-fracture surface over stress triaxiality η_{MF} and Lode parameter ξ (3D)

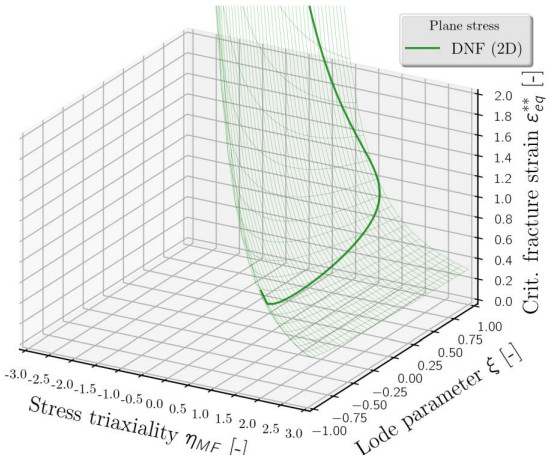

(b) Isometric view on DNF-fracture surface over stress triaxiality η_{MF} and Lode parameter ξ (3D)

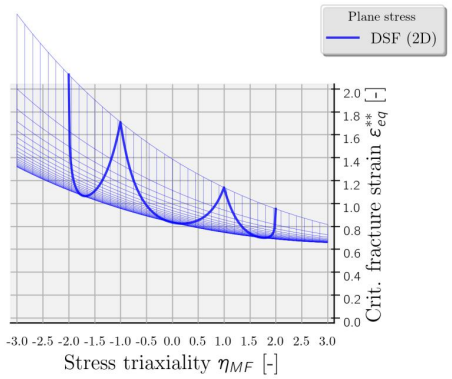

(c) DSF over stress triaxiality η_{MF} (2D)

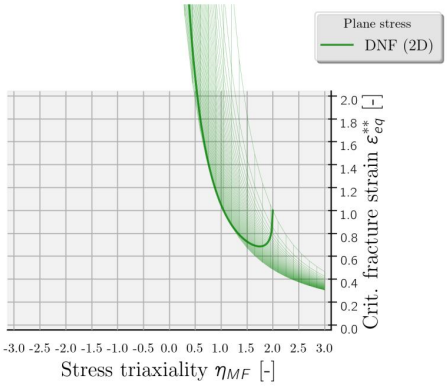

(d) DNF over stress triaxiality η_{MF} (2D)

Figure 2.17.: 3D fracture surface depending on stress triaxiality η_{MF} and Lode parameter ξ separating between ductile normal (DNF) and ductile shear fracture (DSF) for DP600. The solid lines show the fracture curves for plane stress.

the valid range between biaxial compression $\eta_{MF} = -2.0$ and biaxial tension $\eta_{MF} = +2.0$. The information of Figures 2.17c and 2.17d can be merged in a single plot for both fracture criteria DNF and DSF in as given Figures 2.18a and 2.18b over the stress triaxiality η_{MF} and strain-rate ratio α. These fracture diagrams allow to determine the critical fracture strain ε_{eq}^{**} for different stress states and are shown for the quasi-static regime exemplarily for the dual-phase steel DP600. Instead of the commonly used stress triaxiality η the fracture diagrams are shown over the stress triaxiality η_{MF} normalized by uniaxial tension as in Figure 2.18a. Note that the ductile normal fracture (DNF) curve is the critical mechanism in the range between uniaxial $\eta_{MF} = +1.0$ and biaxial tension $\eta_{MF} = +2.0$. Further, the most critical state is plane strain which represents the minimum value of the

DNF curve which is significantly lower value than for uniaxial or biaxial tension. The DNF curve rises for lower values of η_{MF} asymptotically to infinity, which is also physically meaningful since the underlying mechanisms of growth and coalescence of micro-voids for the normal fracture can only occur in tension dominated loadings. Following the η_{MF} further down to even smaller values from uniaxial tension, i.e. from $\eta_{MF} = +1.0$ to biaxial compression $\eta_{MF} = -2.0$, only the ductile shear fracture (DSF) is relevant for the failure initiation. Therefore, the slope of the DSF failure curve representing the critical fracture strain ε_{eq}^{**} increases for lower values of η_{MF}.

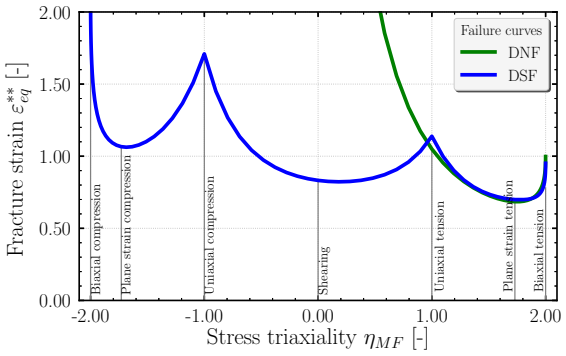

(a) Fracture curves for ductile normal (DNF) and ductile shear fracture (DSF) as a function of the stress triaxiality η_{MF} including characteristic stress states

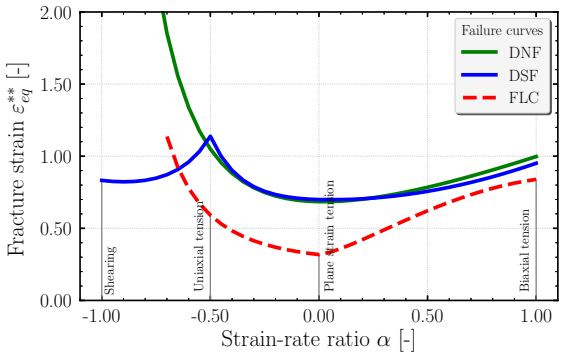

(b) Fracture curves for ductile normal (DNF) and ductile shear fracture (DSF) as a function of the strain-rate ratio α including the forming limit curve (FLC) for the plane stress state

Figure 2.18.: Fracture diagrams for the dual-phase steel DP600 over the stress triaxiality η_{MF} on the left and strain-rate ratio α on the right

Additionally to the fracture limit curves, the forming limit curve (FLC) is also displayed in Figure 2.18b. With the help of the FLC the critical fracture strain ε^* can be predicted for shell elements when localized necking occurs. It is therefore valid only for the plane stress state between uniaxial to biaxial tension [19]. The FLC lays below the fracture curves and hence is more critical meaning the underlying DP600 material is more prone to failure initiated by necking than a pure ductile normal or shear fracture.
In the context of a FEM simulation the fracture limit curve represents a threshold. As long as the strain in any arbitrary element lays below these curves, they are intact. Fracture risks for all three mechanisms can be outputted to the result file and post-processed in order to identify critical regions close to failure in a structural analysis. As soon as an element surpasses the fracture limit curves the element will be eliminated representing a failure initiation of a macroscopic fracture.

Instability:
Whereas the previously described phenomenon of necking can be captured with solid elements, the concept of a forming limit curve (FLC) allows to describe the onset of localized necking for shell elements [36, 25]. Hence the FLC represents a stress-state

dependent envelope embodying the limit strain for the plane stress state. The FLC

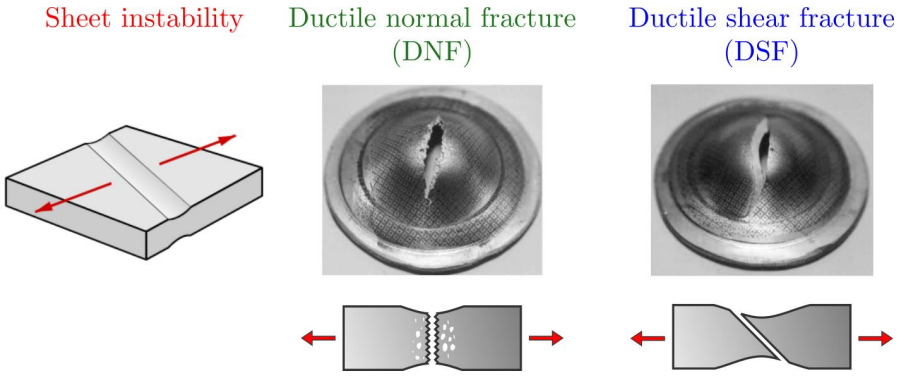

Figure 2.19.: Visualization of the sheet instability (localized necking), normal fracture and shear fracture [36]

can be determined experimentally using the Nakajima test by loading of a metal sheet with varying bridge widths by a spherical punch until failure initiation. The varying bridge widths allow to record the limit strain under different stress states. The use of of Nakajima tests however is laborious, time consuming and cannot be conducted for high-strength steels [38]. The numerical algorithm Crach can predict the FLC based on the following input [25]:

- Plastic strain hardening exponent n in accordance with Swift;
- r-values for the orthotropy of Hill1948 r_{00}, r_{45} and r_{90};
- Strain-rate sensitivity parameter m;
- Inhomogeneity parameter δ.

The inhomogeneity parameter δ represents a small initial imperfection reducing the initial thickness of the metallic sheet t_0, where tilde ($\tilde{}$) denotes the variables inside the neck.

$$\tilde{t_0} = t_0 \, (1 - \delta) \, ; \tag{2.75}$$

$$d\tilde{\varepsilon}_{y'} = d\varepsilon_{y'}. \tag{2.76}$$

For the neck, small strains in parallel direction to the neck denoted by y' are identical in- and outside of the neck as given in Equation (2.76). This model is applicable for linear strain paths with $\varepsilon_2 < 0$ with the principal strains $\varepsilon_2 \leq \varepsilon_1$ where the neck is very small [20]. For $\varepsilon_2 > 0$ and in particular for biaxial tension, the neck has a significant width and Equation (2.76) is no longer appropriate to describe the strain evolution. Therefore, the cross-section of the neck is approximated by [36]:

$$\tilde{t_0} = t_0 \left(1 - \delta \, \cos \left(\frac{\pi x'}{l} \right) \right). \tag{2.77}$$

The force equilibrium is checked by the Crach-algorithm in the vicinity of the neck during a steady increase of the strains. If a common solution for this plastic flow problem in- and outside the neck can no longer be found, it is an indication for instability and the onset of localized necking [36]. The force equilibrium needs to be solved for various orientations w.r.t. the rolling direction (RD) denoted by the rotation angle for Crach-algorithm γ. The overall limit strain is derived via an optimization given in Equation (2.78):

$$\varepsilon^*_{eq} = \min_{\gamma} \left(\varepsilon^{\gamma}_{eq} (\gamma) \right). \tag{2.78}$$

2.2.4. Orthotropic fracture for strain-based criteria

In order to further account for the direction dependency of fracture, both models for ductile normal and shear fracture can be enhanced by an orthotropic fracture model. The fracture surface is defined by the normal of an orientation vector as displayed in Fig-

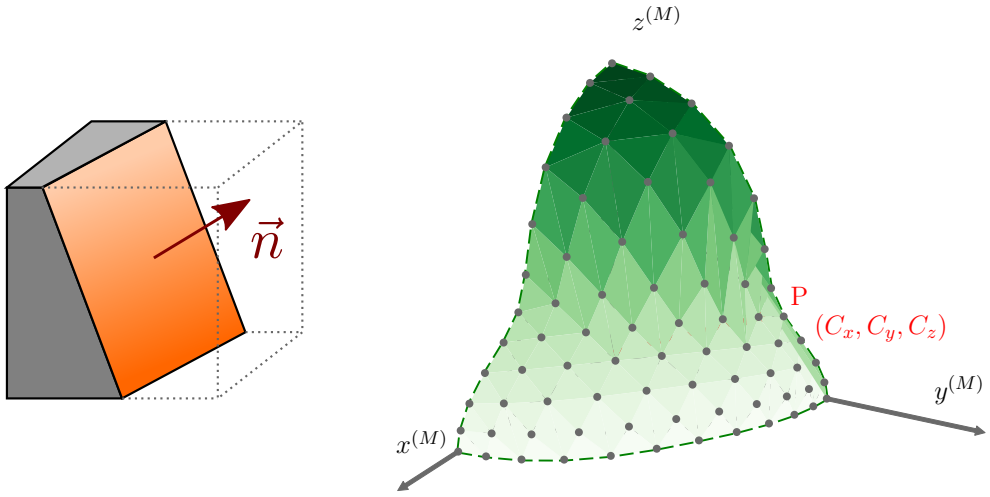

(a) Fracture surface defined by a discrete direction determined by the normal

(b) Triangulation of the fracture plane for one of four octants

Figure 2.20.: Visualization of the orthotropic fracture model coordinates on the right denote material coordinates

ure 2.20a. Because not all arbitrary directions can be considered in the evaluation of the anisotropic fracture risk, some discrete orientations are used. These discrete directions are obtained by spanning a surface of triangles with regular, equidistant intervals over one octant as displayed in Figure 2.20b. Directions for the other octants are obtained by symmetry and the user can refine the number of triangles by a higher number of subdivisions.

The previously introduced fracture surface in dependency of the stress state is complimented with an anisotropy function $w\left(C_x, C_y, C_z\right)$. ε_x^{**} denotes the stress state dependent fracture strain of the x-axis serving as the reference direction. The anisotropy function $w\left(C_x, C_y, C_z\right)$ which is defined as the ratio of the fracture strain in direction (C_x, C_y, C_z) to the reference orientation x, where $\vec{C}$ represents the orientation vector normal to the fracture surface as displayed in Figure 2.20a. For the numerical model it can be expressed as the product of two functions as stated in Equation (2.79).

$$\varepsilon^{**} = \varepsilon_x^{**} w\left(C_x, C_y, C_z\right). \tag{2.79}$$

The minimum fracture curve is used as reference and ε_{min}^{**} is derived either from the beta-model for DNF $\varepsilon_{min}^{**}(\beta)$ or from the theta-model for DSF $\varepsilon_{min}^{**}(\theta)$. w_{min} represents the minimum value of w which is not discussed here.

$$\varepsilon^{**} = \varepsilon_{min}^{**} \frac{w\left(C_x, C_y, C_z\right)}{w_{min}}. \tag{2.80}$$

The fracture risk will be hence evaluated in planes normal to each of the specified discrete directions yielding an individual fracture risk for every plane ψ_k. The relevant fracture risk ψ is finally obtained as the most critical one for the weakest direction in accordance with Equation (2.81). The weakest plane prone to fracture can be visualized in postprocessing.

$$\psi = \min_k \psi_k. \tag{2.81}$$

Exploiting possible geometrical symmetry planes the general orthotropic fracture model can be further reduced. The corresponding surfaces to the reduction are displayed in the Figures 2.21a-2.21c. However, in the simulation orthotropy of fracture is checked in four octants for the loading may change from tension to shearing or compression. For reasons of clarifications the traces in the first octant are also displayed additionally to the isotropic reference in Figures 2.21b and 2.21c. The model is valid for 3D stress states and

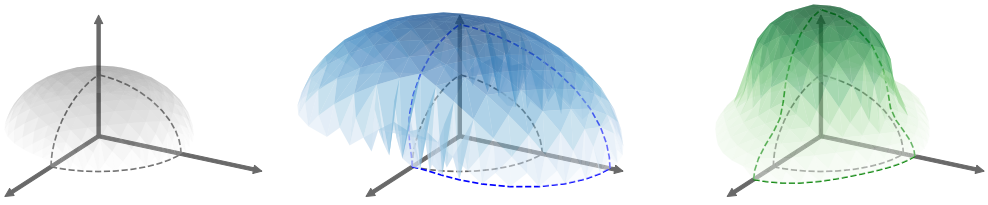

(a) isotropic (b) transverse isotropic (2D orthotropic) (c) orthotropic

Figure 2.21.: Display of fracture surfaces in four upper octants for different symmetries

can be used with shell and solid elements. For the application of thin-walled structure of e.g. sheet materials only the trace in the x-y plane is relevant.

2.3. Material modeling of endless textile-reinforced thermoplastics

Prerequisite for the simulation of joints with dissimilar material pairings is a comprehensive description of the base materials (BM). In the context of this thesis, this includes two semi-finished products of either steel or aluminum and organic sheet. The latter is a textile reinforced thermoplastic made of endless glassfibers embedded in a thermoplastic matrix. Because both its constituents, the fiber and the matrix, can show yielding, those two sources of material non-linearities need to be captured under multi-axial loading. Therefore in this section, the state of the art for material models applicable for textile reinforced thermoplastics is presented and discussed in the context of crashworthiness simulation. Firstly, some fundamentals of endless reinforced polymers are outlined, followed by a multiscale analysis of the predominant deformation and failure behavior. Lastly common material models are presented to model the material behavior in a phenomenological manner on a macroscopic scale. As there is currently no established material model for textile reinforced thermoplastic composites, applicable material models are discussed. Whereas yielding and plastic strain hardening is more established in material models for unreinforced polymers, failure criteria for endless glassfibers tend to be found in the context of stiff composites with endless carbon fibers embedded in a duroplastic matrix.

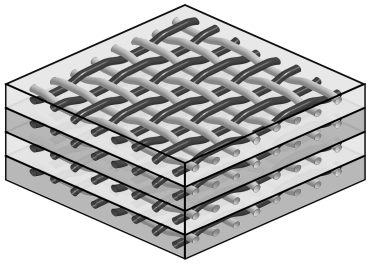

Figure 2.22.: Example of a twill-weave architecture for a textile

2.3.1. Fundamentals of textile reinforced thermoplastics

For the material characterization and modeling of bi-phase composite materials, it is important to have an in-depth understanding of its two constituents, fiber and matrix, and how they are arranged with respect to one another.

In the last line of Figure 2.23 the different molecule chain structures of partially regular cross links denoted as semi-crystalline and irregular wounded, amorphous thermoplastics are visualized. Whereas thermoplastics soften upon heating and are arbitrarily shapeable, neither elastomers nor thermosets can be melted or welded [41]. Due to their rigid network of cross links between the molecule chains thermosets, also referenced as duroplastics, are comparatively stiff and fail under a brittle mode. Also they show little visco-elasticity and low shrinkage and are therefore often modeled elastic. Elastomers like rubber for example on the other hand can undergo large elastic deformations [9, 21].

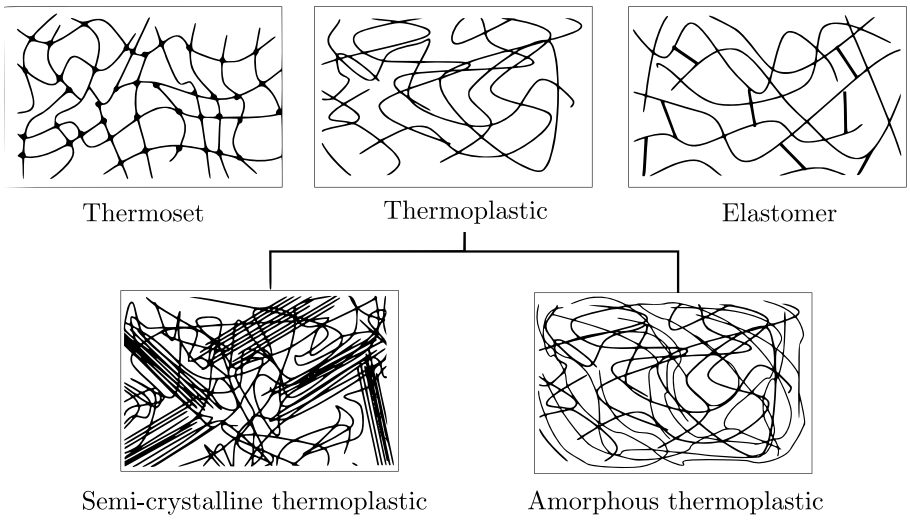

Figure 2.23.: Schematic representation of molecular chain structure of thermosets, elastomers and thermoplastics [40]

Table 2.5.: Classification of pre-impregnated semi-finished polymers based on the fiber length of their reinforcement [42]

Reinforcement		Unreinforced	Short fiber	Long fiber	Endless fiber
Fiber length l		-	0.1-1 mm	1-50 mm	50 mm
Matrix	Duroplastic			SMC/BMC	Laminates
	Thermoplastic	NFRT PA, PP	SFRT PA6-GF30	LFRT PP-LGF40	EFRT organic sheet

In Table 2.5, examples for un- and fiber reinforced materials are listed in dependence on the matrix and distinguished by their fiber length. Whereas duroplastic composites are mainly of interest for aerospace application, the use of thermoplastics enjoys a steadily growing interest in the automotive industry. Arbitrary lay-ups of UD-material resulting in a laminate sheet molded compound (SMC) or bulk molded compound (BMC) are an example of long fibers in a duroplastic matrix of a semi-finished product. Containing already both the endless fibres and the matrix the material will be formed in a compression molding process to a near net shape geometry.
Non fiber reinforced thermoplastic as pure polyamide (PA) or polypropylene (PP) may be used for panels in the interior. Short-fiber reinforced thermoplastics (SFRT) and long-fiber reinforced thermoplastics (LFRT) are used for parts with complex geometries by mold injection when superior mechanical properties are needed. LFRT are chosen over SFRT for the elevated fracture toughness. Lastly, endless fiber reinforced thermoplastics (EFRT) can be used for semi-structural parts. Due to elevated mechanical performance, the focus of application in the automotive sector lies on reinforced thermoplastics. Figure 2.24b displays the principal dependence of mechanical properties on the fiber length

for a fiber diameter of 20 µm. Whereas the diameter of the fiber is fixed by the manufacturing and we have 9-24 µm as typical value for glass fibers and 6 µm for carbon fibers [43]. The diameter of a human hair is about 50 µm for exemplary illustration [42]. The lateral surface of fibers has a positive effect for it can transfer shear stress (see Figure 2.24a). However, at the two ends of the fibers cavities form which can be treated as a micro-notch in the matrix material. Choosing the right fiber length is hence a trade-off between the beneficial lateral surface of the fiber which is directly linked to the fiber length and the malfunction of the micro-notches in the matrix. In general terms it can be stated that the longer the fiber the better its reinforcement. However, during the production slender brittle fibers can easily brake. For the reshaping of endless fiber reinforced thermoplastics (EFRT), the fibers might easily brake under higher deformation especially if the bending radius is too small. This also applies for long fiber reinforced thermoplastics (LFRT) which are molded from granulate to the final shape. In the mold injection process under the influence of temperature and pressure the fibers can be shredded down to 10-20% of their original length.

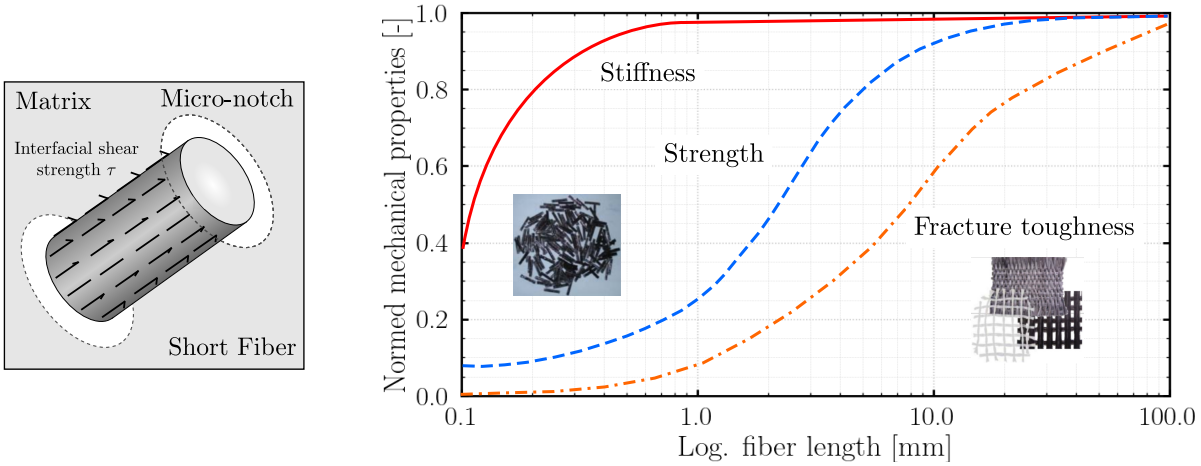

(a) Reinforcement of a short fiber

(b) Influence of the fiber length on mechanical properties [44]

Figure 2.24.: Scheme for the mechanism of action of a fiber reinforcement on the left and influence of fiber length on normalized mechanical properties on the right

For the production of textile reinforced composites, endless glassfibers are woven and embedded in a thermoplastic matrix. In the last line of Figure 2.25 different architectures for a perpendicular alignment of fibers in weft- and warp-direction are displayed. Endless glassfibers are more suitable for the weaving process and the thermoplastic matrix is advantageous because it allows to be re-formed and welded [6, 45]. On the downside, the thermoplastic matrix starts to soften at elevated temperature. Duroplastic matrixes possess a higher operating temperature range but can no longer be formed after curing. Important for the mechanical point is the constitution of fibers, their architecture as

well as the fiber-matrix interface. The sizing of fibers, with e.g. the use of an adhesion promoter, can improve the interface of thermoplastic matrix and fibers and is especially important for glassfibers [43].

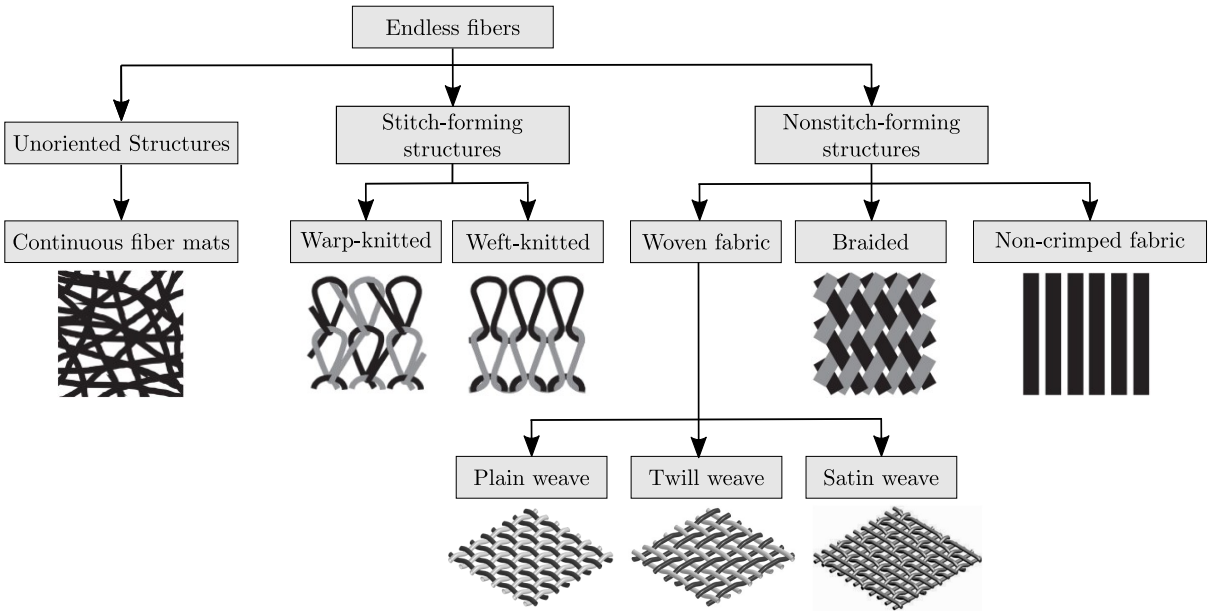

Figure 2.25.: Classification of different endless fiber reinforced thermoplastics based on their architecture [46, 47]

For further information on the characterization and mechanical behavior of unreinforced thermoplastic in crashworthiness simulation, the interested reader is referred to the work of Junginger [40] and Becker [48] for unreinforced thermoplastics and to Peter [49], Kryvachi [50], Schöpfer [51] or Vogler [9] for short-fiber reinforced thermoplastics.

2.3.2. Multiscale material modeling

Due to the heterogeneous structure of textile-reinforced thermoplastics they should be analyzed on different scales. Which scale is the most appropriate to use depends on the exigencies and application of the simulation [52].
In Figure 2.26, different scales are analyzed in accordance with [53, 54]. Figure 2.26 illustrates the different scales in the context of textile reinforced polymers. The smallest scale with the highest resolution is the micro-scale which allows to model a single fiber, its interface to the surrounding matrix, and the matrix itself. Moving up one level, the mesoscopic scale comes next. Here, the fiber architecture can be represented by using tows including a bundle of fibers. The last scale is the macroscopic scale where the properties of two constituents, i.e. fiber and matrix blend to a homogeneous, textile layer. For a process

simulation of a deep drawing process where the fiber re-alignment and wrinkling throughout the process are of interest, the micro-scale can be the suitable scale. For structural simulation on component level or even bigger structures the high resolution of the smaller scales entails very high computational cost and cumbersome model preparation. Whereas the detailed information about the sliding of fibers in the matrix might not be so relevant.

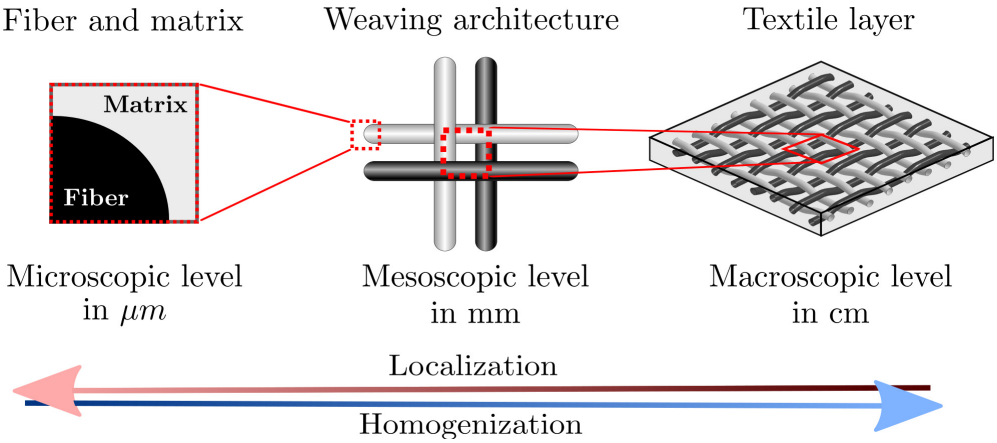

Figure 2.26.: Scheme of textile reinforced polymers on a multi-scale levels

The lower scales can also be used to determine mechanical properties of a composite on a macroscopic scale based on the material properties of its two constituents, fiber and matrix and its architecture. The process of deriving properties on lower level for the higher level is called homogenization and localization vice-versa. In order to relate these scales with one another so-called unit cells, indicated as the red squares in Figure 2.26, are needed. More precisely, for material with randomly distributed material properties on a microscopic scale a unit cell is the smallest volume which is large enough to yield a value representative for the whole. Therefore, it is also referred to as representative volume element (RVE). For composites with repetitive patterns which can be used to set-up the structure of the composite the unit cell is referred to as representative unit cell (RUC).

Doebrich generated a RUC for woven fabrics with the use of simplified beam elements (digital elements) on micro-scale level [53]. Maron analyzed in his thesis the phenomenological deformation mechanisms and could show stochastic relations across the scales in the context of thermoforming simulation of textile reinforced thermoplastics [55]. Kaiser proposed in his thesis a coupling of a unit cell model consisting of 1D elements such as beams and bars to a macroscopic model for the context of deep-drawing simulation [52, 56]. Roesner showed in his PhD thesis some means for homogenizing the material micro-structure of textiles considering the visco-elastic and visco-plastic material behavior [57].

Recent research in the field of homogenization schemes for derivation of macroscopic material properties of composites is conducted based on a micro-mechanical approach

[54, 58]. Even though the idea of virtual determination of material properties might seem very appealing and attractive at first glance, there are currently still some drawbacks of this approach. This is true especially in the context of crashworthiness simulation where the entire loading history until fracture initiation needs to be captured. Firstly, it is a laborious task to create a unit cell on microscopic level with repetitive boundary conditions and then, this unit cell is solely applicable for a certain fiber architecture, e.g. 3D-braided composites. Further, the characterization of the fiber-matrix interface is difficult and the so obtained values for the interface description are burdened with scatter. Lastly in the context of organic sheets, where both, the thermoplastic matrix and the endless glass fibers are sources of material non-linearities it is very difficult to separate different phenomena occurring at the same time on different scales.

In the context of this thesis, the material modeling shall be applied for crashworthiness load-cases on coupon as well as on component level and lays out the pre-requisite for surrogate modeling of hybrid joints. Therefore, the smeared material modeling of the effective material behavior on a macroscopic scale is the most suitable scale.

2.3.3. Plastic hardening

For fiber reinforced thermoplastic composites plastic strain hardening originates from the matrix. Besides non-linear elasticity can be observed for thermoplastics as represented in the stress-strain response in Figure 2.27 followed by a pronounced non-linear plastic deformation. For plastic deformation, *crazing* and shear band formation deformation are two concurring mechanisms [40]. The initiation and evolution of crazes occurs mostly under uni- or biaxial tension and originates from micro-voids. Macroscopically, it manifests in an increase of volume, superficial white coloration (stress whitening) on the specimen, and a reduction of the yield strength [40]. In contrast, the shear band deformation can be observed under arbitrary stress states due to orientation inhomogeneities under 45° to the loading direction resulting in a necking.

In metallic materials, plasticity is due to the movements of dislocations in the crystal lattice induced by shear loading. These deformations are irreversible, isochoric and independent of hydrostatic pressure (see red vonMises line in Figure 2.28). In contrast to metals the yielding behavior of polymers does not represent an isochoric process and volumetric strain occur requiring a pressure dependent yield formulation [10]. The yielding behavior for thermoplastic depends on the prevailing stress state and can be completely different for different loading types as uniaxial tension, uniaxial compression, shearing, and biaxial tension [9]. For most composites composed of carbon fibers in a duroplastic matrix, plastic strain hardening plays a minor role and is predominantly observed in transverse compression or shear dominated loadings. Therefore, it plays only a subordinate role in material models for composites [59].

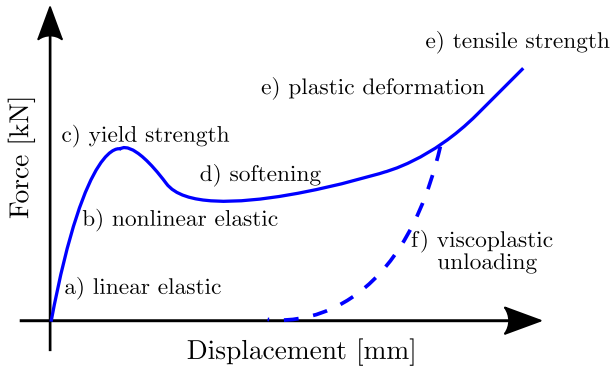

Figure 2.27.: Typical force-displacement response of a thermoplastic submitted to uniaxial loading [9]

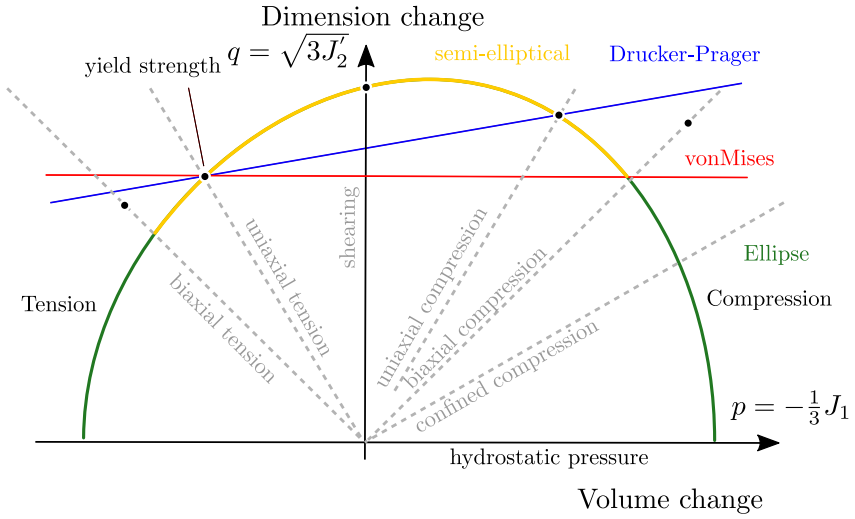

Figure 2.28.: Yield criteria for plastics displayed in the p-q-space with yield strength for different stress states

Figure 2.28 gives an overview of available yield locus formulations suitable for modeling plastic materials displayed in the p-q-space. Here q represents the equivalent stress in accordance with vonMises and p the hydrostatic pressure; different stress states can be represented by straight lines from the origin. The normal on the yield surface represents the plastic Poisson's ratio ν^{pl} which is defined as the saturated transversal contraction in a monotonous plastic loading [60, 61]. For thermoplastic materials under tensile loading, volume change may occur and they are no longer isochoric, plastic incompressible ($\nu^{pl} = 0.5$). Whereas the r-values are a measure whether the plastic material is more prone for thinning out of the thickness ($r < 1.0$) or width ($r > 1.0$), the plastic Poisson's ratio ν^{pl} serves as a measure indicating plastic volume change ($\nu^{pl} < 0.5$) or if the material behaves isochoric and plastic incompressible ($\nu^{pl} = 0.5$). Commercially available is the *Semi-Analytical Model for polymers* (SAMP-1) model of a semi-elliptical yield locus in p-q-space valid for the plane stress state available in *LS-Dyna* under **MAT_187* [62,

63]. Due to its three parameters of the elliptical equation the yielding points of only three stress states can be met. Whereas plastic compressibility is predominant for unreinforced thermoplastics, for fiber reinforced thermoplastics compressibility of the matrix is negligible in the compound.

Non-linear plastic strain hardening of textile reinforced thermoplastics is discussed in detail by Vogler [9, 10]. He proposed an invariant-based plastic hardening approach enabling to move from an originally orthotropic configuration to a universal anisotropic one by covering the misalignments from a previous draping process or induced by loading (fiber migration). The influence of temperature and strain-rate dependency on the plastic strain hardening of textiles is outlined for example by [64]. The inelasticity of the effective material behavior is addressed in the work of Kästner for textile-reinforced polypropylene [65]. A pronounced non-linear strain hardening effect for textiles in the context of crashworthiness simulation is discussed by [66] and [67].

2.3.4. Fracture criteria for organic sheets

The difference of the mechanical properties for the two constituents, endless glassfibers and thermoplastic matrix results in manifold fracture types. In accordance with [42], Figure 2.29 categorizes the fracture types in dependence on the type and direction of loading and distinguishes two main failure types: fiber failure (FF) and interfiber failure (IFF). Whereas the shear stresses culminate solely in IFF dominated by a comparatively softer matrix, normal stresses may result into a FF or IFF dependent if the loading is applied longitudinal to the fibers or transversal. Whereas two out of the six failure types fail by FF, it is worth noting that for the four IFF types failure originates in the matrix.

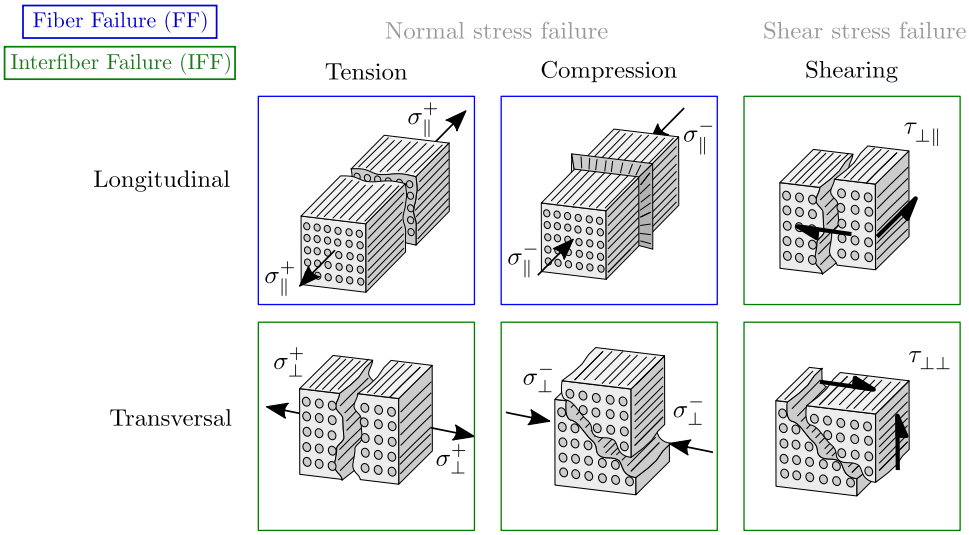

Figure 2.29.: Basic strength and failure types for composites in accordance with [42]

In a similar manner as Wierzbicki conducted a comparative analysis of different failure criteria applicable to ductile sheet metals [39], Cuntze realized a comparative study on brittle fracture criteria for composites whose results are integrated in the world wide failure exercise (WWFE-II) [68]. Here, a comparison of the 19 most established fracture criteria is given for the stress space defined by $\sigma_2 - \sigma_3$. Based on a smeared or homogenized stress value of the composites failure, assessment can be done with these criteria [69]. Analogously, to yield surface for the onset of yielding for ductile metals, these fracture criteria represent a failure envelope in stress space representing the critical strength R for the initiation of brittle failure. These criteria include linear, non-interacting (max. stress or max. strain), quadratic, partially interacting (Hashin and Puck) and quadratic, fully interacting (Tsai-Wu) criteria [70, 71, 72, 73]. Although no universally applicable recommendation for a fracture criterion is found in the failure exercise, the physically motivated approaches of Puck and show the best predictive quality. The results of the WWFE are summarized by [74].
The idea of Puck's action plane failure criterion [75] was adapted for UD laminates resulting in the LaRC03 criterion including calculation of fracture angle under transverse compression and criteria for fiber kinking and transverse tensile cracking [69]. This criterion was later enhanced for 3D stress state, in LaRC04. Action plane based fracture criteria are capable to distinguish fracture risk for the different types of fracture modes [71]. Cuntze introduced the failure mode concept (FMC) based on the stress invariants of the transverse isotropy. Following the hypothesis of normal and shear stress failure from the categories in Figure 2.29 an overview of the common failure criteria for composites discussed above is displayed in Figure 2.30. These criteria have in common that the normal stresses in compression are higher than in tension as displayed on the right side of Figure 2.30. Here R represents the failure strength, the subscripts $\perp$ and $\parallel$ indicate a loading transverse or parallel to fiber direction, and the superscript, $+$ and $-$ a loading in tension and compression, respectively.

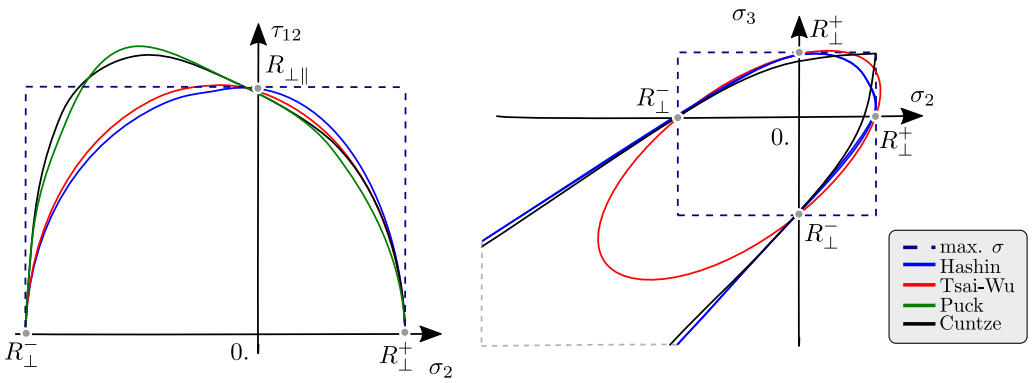

Figure 2.30.: Comparison of different stress-based failure criteria for composites in the $\sigma_2 - \tau_{12}$ on the left and $\sigma_2 - \sigma_3$ plane on the right [72]

The following paragraphs summarizes different material models applicable for textile reinforced thermoplastics, which are currently available, and discuss their advantages

and drawbacks in the context of material modeling of organic sheets. The need of a material model for organic sheets applicable to industrial simulation on component level is outlined by [76, 77].

Models based on continuum damage mechanics: One of the well-established approaches for modeling textile reinforced thermoplastics is based on ideas published by Ladevèze and Le Dantec for an elementary ply of a laminate composite [78]. This model is based on continuum damage mechanics where evolution of damage is related either to micro-cracking of the matrix or to fiber-matrix debonding. Tension and compression are treated differently. Strain-based thresholds are defined as yield conditions accounting for plasticity via an isotropic hardening law according to Ludwik. It is assumed that no plastic yield exists in fiber direction, i.e. thresholds are defined for shearing and compression. This Ladevèze model was, e.g., used by Greve and Pickett for non-crimp fabrics (NCF), complemented by a model for fracture in fiber direction [59]. Strain-based thresholds for failure initiation and evaluation for transverse and shear loading are combined with a modified Puck failure envelope for intra-laminar matrix failure. According to the authors, the approach, named 'Ladevèze-Puck' damage and failure model, can be used to capture (i) intra-ply failure modes in principal fiber directions for tension and compression, (ii) intra-ply shear failure, and (iii) the interaction of these modes. The work mentioned above has been implemented into the commercial finite element code PAM-Crash. Remaining drawbacks of this model for crashworthiness simulations are its limitations concerning strain-rate dependency as well as the incomplete failure assessment. The strain-rate dependency of five damage related parameters can be defined but not for the failure envelope defined as Puck cylinder. In general, the idea to have two different failure mechanisms for a bi-phase material is appropriate; however, the current implementation uses a strain-based threshold for fiber and a stress-based threshold for matrix related failure which may result in deviations.

Models based on failure modes: The failure mode concept (FMC) is a continuum mechanics based approach in which a threshold for damage and failure initiation is defined which is proposed by Cuntze et al. [79]. The first threshold separates the linear-elastic regime from damage evolution with a non-linear stress-strain relationship [80]. For the second threshold, nine independent scalar stress values are defining a failure envelope while a separation between tension and compression is possible. This bears the advantage that every stress value is characteristic for a failure mode as the name of the concept implies. However, the values are purely defined in stress-space, applicable for stiff and brittle composite structures, but not for the ductile intermediate in-plane off-axis angle of the organic sheet. Here, a strain related criterion is required. In addition, the differently pronounced strain-rate sensitivities for fiber and matrix of organic sheets cannot be addressed.

Phenomenological models: For crashworthiness simulation some internal material models are available in the explicit solvers which are applicable for modeling textile reinforced composites. The material model available in *Abaqus* under the keyword **FABRIC* also focuses on the cyclic loading and unloading of the fabric. A differentiation of the loading type is possible in tension, compression for the weft and warp direction as well as for shearing via a definition of separate loading curves. The plastic hardening behavior can be described including a strain-rate dependency. Special feature is the tracking of the re-alignment of the fibers. The fibers in higher deformation tend to shear relative to one another as it can be observed in the picture-frame test or uniaxial tensile test under 45° [47, 81]. Because of this fiber migration, the original assumption of an orthotropic material holds no longer true [22]. This material model shows relevant features for the forming simulation. However, for crash simulation it lacks an adequate description of failure modes for fiber and matrix.
Matzenmiller's work developed for elastic brittle composites can be adapted for textiles and offers a non-linear behavior until fracture initiation and a constant stress level afterwards [82]. The work of Pinho offers an orthotropic, linear elasticity followed by a 1D-plasticity for in-plane shear loading and a coupled, stress-based failure criteria differentiating between fiber and matrix tension and compression. Fracture toughness is based subsequently on a linear damage evolution [83, 84]. Camanho proposes only a linear hardening and a bi-linear damage evolution. Fracture in fiber tension is evaluated using a max. strain criterion [85, 86]. The following three approaches by Matzenmiller, Pinho and Camanho have been realized as orthotropic material models for composites in commercial FE code LS-Dyna and can be found as **MAT_058*, **MAT_261* and **MAT_162* respectively.
Cousigne et al. [66] proposed a numerical model for thin and thick shells representing the plasticity characteristics until failure for the in-plane material directions by a one-dimensional load curve or, alternatively by a Ramberg-Osgood equation. As failure criteria, they used either a maximal stress criterion or the quadratic Tsai-Wu criterion. Damage propagation post-failure is modeled for each principal in-plane material direction.

Concluding the sections on material modeling of ductile metals (Section 2.2) and organic sheets, (Section 2.3) both exhibit different mechanism for failure initiation and energy absorption. Whereas metals absorb a high amount of energy by ductile yielding, composites absorb energy via crushing which is dominated by the brittle failure of the fibers [87, 88]. Dehn scrutinized the mechanisms of textile reinforced thermoplastics to absorb energy [7]. However, none of the above discussed phenomenological, orthotropic material models is capable to capture visco-elasticity coupled with a general orthotropic, stress-state dependent plasticity to account for the pre-failure non-linearities under multiaxial loading conditions and triaxial stress states. Further for a physically sound material modeling, fracture criteria are necessary for the initiation originating from either fiber or matrix including a strain rate sensitivity which is differently pronounced for fiber and matrix. This is discussed in the next section.

2.4. Mechanical surrogate models for hybrid material pairings

Contrarily to joints with identical materials which are primarily created by thermal processes, mechanical joining and adhesive bonding are the current prevalent processes for hybrid material pairings. However, thermal joining processes bear a huge potential for dissimilar material pairings; they are currently subject to research and not as widespread in industrial applications [11]. An overview of joining techniques for dissimilar metal pairings is given by Wagner [89] and Meschut [90]. For the context of metal-polymer hybrid joints, Moldovan gives an overview and the potential of using the laser to manufacture hybrid material pairings [91] is outlined by Bergmann [92] and demonstrated by Heckert [93, 94] and Köckritz [95].

The transmission of force can act on one of the following physical operating principals with an exemplary joining type:

- *Force-fit*: e.g. screw or clamping;
- *Form-fit*: e.g. bolt or rivet;
- *Adhesion*: e.g. glueing or welding.

Joining methods for hybrid material pairings including thermoplastic materials with metals can be divided in In-molding assembly (IMA) and Post-molding assembly (PMA) in accordance to [92, 96]. Table 2.6 summarizes different joining PMA technologies clustered by their type which are applicable for dissimilar material pairings [92, 98, 97].

Table 2.6.: Joining technologies for dissimilar metal-plastic material pairings

PMA		
Mechanical joining	Adhesive bonding	Thermal joining
Screwing	chemical adhesion promoters	friction-based process
Riveting	micro-sized surface roughness	ultrasonic
Bolting	macro-sized mechanical interlocking	induction and
Snap joints	(pins, grooves, laser-structuring)	laser-based process

Different specimens for the experimental characterization of joints exist such as single lap joint test, bonded cross test or hollow torsion cylinders (see Figure 2.31). Even though the single lap joint test is commonly used for the strength analysis, e.g. in process analysis of joining processes for a relative comparison of different set-ups to one another, it is hardly possible to obtain an experimental characterization of displacement and strength at failure initiation for a defined loading. During the monotonous loading of a single lap joint, the loading changes from initially pure shear loading to a superimposed head tension when the joint starts to be bent out of plane. Different concepts as a two double

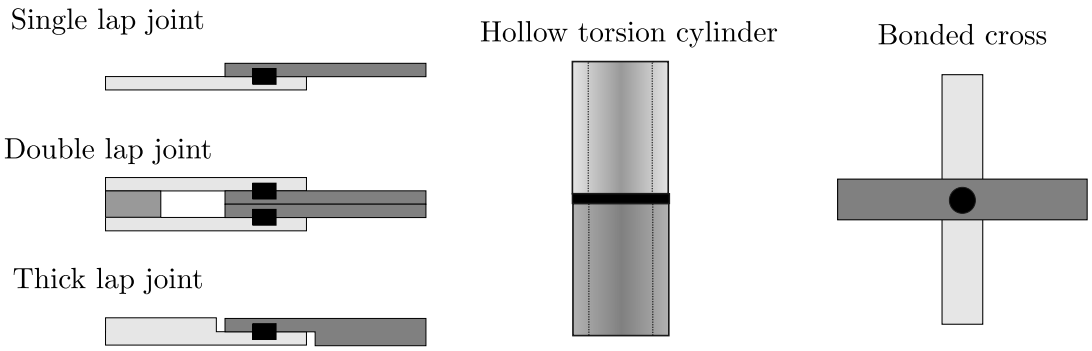

Figure 2.31.: Overview of different coupons for the experimental characterization of joints

lap joint or a thick single lap joint with thinner flanges for the joint can be used to circumvent the movement of the joint and assure a more constant shear loading.

For the experimental characterization of the deformation and failure behavior of joints the KS2-specimen and peeling are often regarded. For the KS2-specimens, two metallic sheets are formed into a u-shaped profile and connected with one another so that the joint constitutes the bottleneck of the specimen (see Figure 2.32). A flexible mounting allows the joint to be tested under various angles for pure shear loading under 0° or a head tension under 90° with little effort to change the orientation. The local displacement measure allows to capture the deformation only of the joint and record force-displacement curves during the experiment. Based on the characteristic of these force-displacement curves, the initial stiffness, load bearing strength of the joint, and displacement until failure initiation can be measured as well as the absorbed energy.

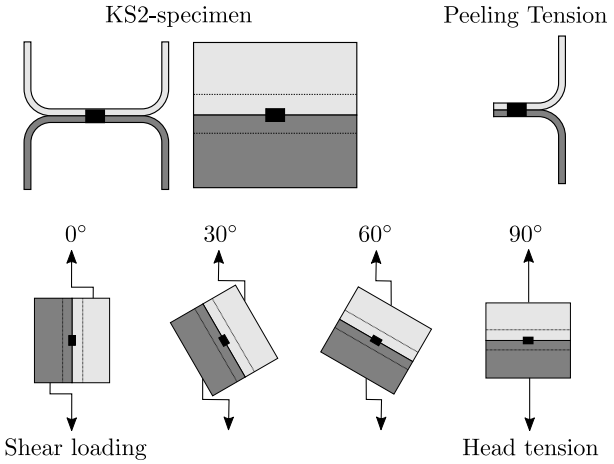

Figure 2.32.: KS2-specimens under various angles and peeling tension specimen for the experimental characterization of stiffness, load bearing strength, and displacement until failure of joints [99]

In this field of research, recent work focuses on the development of a joining process using a laser beam source for joining hybrid material pairings. Either directly for steel-aluminum

joints [100, 101] or indirectly by enhancing the topography for plastic metal hybrids [94, 97, 102]. For the simulation of joints, first contributions were made by Sommer for resistance spot welded joints of dual phase steel DP600 [103]. In the same year 2009 Schmeer published in his thesis process analysis and simulation of a hybrid material pairing between aluminum, magnesium (AlMg3) and polyamide 66 with carbon fiber reinforcement (PA6-CF) with endless carbon fibers woven in a twill-weave architecture by means of induction welding for a single lap joint [104]. Hybrid material pairings based on form-closure between steel sheets and aluminum pressure die casts were analyzed by Pasligh [105]. Research for the plastic-metal hybrid material pairings for LFRT was conducted by Paul et a. [96, 106, 107] in 2013 and later. The work of Burbulla treated the rate dependent elasto-viscoplastic material behavior of adhesives in 2015 [108]. In the same year, Burget published his thesis on deformation and failure behavior of spotwelds for dissimilar joints of micro-alloyed and press hardened steel [109]. Nelson and Reil analyzed a combination of form-fit and adhesion by combining tubular self-piercing rivets (SPR) with the use of adhesive hybrid material pairings of steel and aluminum [110, 111, 112]. Porsch contributed in his thesis to the surrogate modeling of notch induced failures under crash relevant loadings [113]. Lastly, Berntsen addressed in his thesis from 2020 the experimental characterization and numerical modeling of semi-structural two-component polyurethane and structural toughened epoxy adhesive for multi-material joints [114].

Because adhesives and self-piercing rivets are both suitable for series production of hybrid material pairings in automotive bodywork structures, a lot of research has been done in this field [5]. Their importance for lightweight design is reflected by the number of research works in this area as summarized in the chronological list above. While a lot of research focuses on surrogate models for the sole use or a combination of the two joining techniques, the current state of the art for the simulation of hybrid material pairings including long and endless fiber reinforced thermoplastics is not able to keep up with the pace of the process development.

In the following sections existing modeling techniques are presented which are also applicable to hybrid material joints. Firstly, cohesive zones or also cohesive elements can be used for planar interfaces also of larger scale. For them, a bi- or trilinear traction separation law can be calibrated to reproduce the deformation as well as the global energy absorbed in the joint. Connector elements are commonly used for point-wise connection and applicable to hybrid material pairings of spotwelds or SPR.

2.4.1. Cohesive zones

Cohesive zone contacts or elements are well suitable to model planar joints or interfaces, e.g. the interfaces of composites laminae Special purpose elements for large scale and very thin connections can be created, e.g. using gluing or a thermal direct joining techniques. To circumvent the requirement of strongly reducing the critical time step in a simulation,

cohesive zone models (CZM) can be used either in form of a cohesive element or contact. The following failure types can be distinguished for planar joints:

- *Cohesion*: Rupture of the adhesive layer;
- *Adhesion*: Interface debonding;
- *Adherend*: Rupture of the base material (BM).

Using the cohesive zone models (CZM) for flat, planar joints the first two failure types of co- and adhesion can be modeled. For the rupture of one of the adherends, an adequate material model for the BM needs to be used. Originating from the crack opening in fracture mechanics, the delamination modes of a flat, planar joint can be separated into mode I - head tension - and two shearing failure modes - sliding (mode II) and tearing mode (mode III) - as displayed in Figure 2.33.

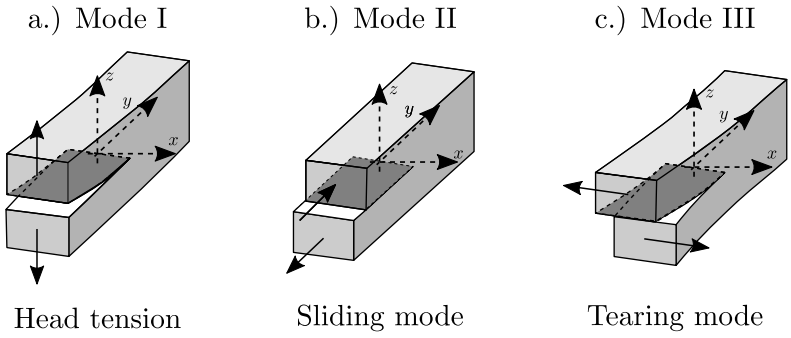

Figure 2.33.: Types of crack opening according to [18]

A simple exemplary case is a bi-linear material behavior with initial stiffness until failure initiation and a linear softening afterwards. The bi-linear traction-separation law is best suited for brittle materials or joints. For more ductile joints, the approach can be extended to an ideal plasticity or a trilinear or trapezoidal approach (see Figure 2.34). Failure initiation can be described based on a traction-separation law for which the separation initiation thresholds can be defined in different metrics with a maximal value in force or displacement as well as in stress or strain. These metrics are summarized in Table 2.7 for local metrics of stress- or strain-based criteria. There are two principal ways to define the thresholds as given by the two rows in Table 2.7.

Table 2.7.: Failure initiation criteria for traction-separation laws [115]

	Stress threshold	Strain threshold
maximal	$\max\left\{\left(\frac{t_n}{t_n^0}\right), \left(\frac{t_s}{t_s^0}\right), \left(\frac{t_t}{t_t^0}\right)\right\}$	$\max\left\{\left(\frac{\varepsilon_n}{\varepsilon_n^0}\right), \left(\frac{\varepsilon_s}{\varepsilon_s^0}\right), \left(\frac{\varepsilon_t}{\varepsilon_t^0}\right)\right\}$
interacting	$\left(\frac{t_n}{t_n^0}\right)^2 + \left(\frac{t_s}{t_s^0}\right)^2 + \left(\frac{t_t}{t_t^0}\right)^2$	$\left(\frac{\varepsilon_n}{\varepsilon_n^0}\right)^2 + \left(\frac{\varepsilon_s}{\varepsilon_s^0}\right)^2 + \left(\frac{\varepsilon_t}{\varepsilon_t^0}\right)^2$

Firstly, the maximal values supposing no interaction of the different failure modes and secondly the interacting types, which are based on the ellipsoid failure envelope defined by quadratic equations. The ellipsoid is hence a 3D representation of the failure initiation. A given stress- or strain state within this envelope represents a sound connection and a point on the surface represents failure initiation [22]. The failure initiation thresholds are defined in the denominator t_n^0, t_s^0, t_t^0 and ε_n^0, ε_s^0, ε_t^0 for stress and strain-thresholds, respectively.

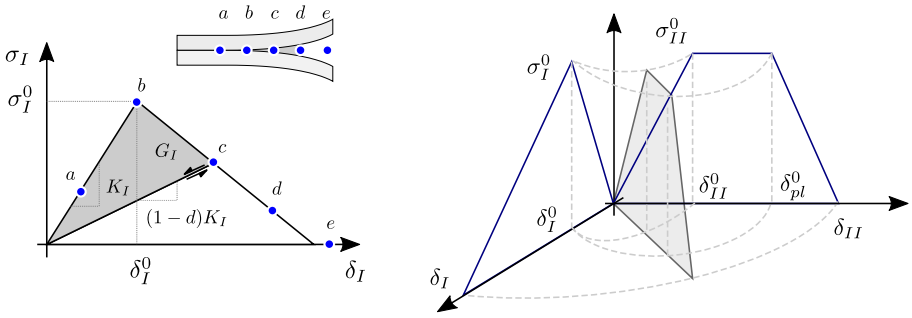

Figure 2.34.: Traction separation law for cohesive elements with a bi-linear approach for mode I on the left and a mixed-mode-separation for a tri-linear mode II on the right [87]

Based on the initial stiffness K_i and failure initiation criteria, the consumed energy G_i per mode can be calibrated with i denoting the mode I, II and III represented before in Figure 2.33. The trapezoidal rule with the vertical part in the traction separation law covers ideal plasticity, non-linear plastic hardening as it can be observed for most thermoplastic materials is not included here.
Formulations for both, cohesive elements and contacts are well established in commercial FEM solvers for planar joints. The drawback in the context of hybrid material pairings is that they are rate-independent; in addition, the multi-linear traction-separation law neglects pronounced non-linearities of joints which might originate from one of the BM and which are pronounced for reinforced thermoplastics.

2.4.2. Connector elements

To enable complex applications, surrogate models for the mechanical behavior of joints are already available in commercial FE solvers (*Abaqus, LS-Dyna, Radioss* and *Pam-Crash*).

Figure 2.35 displays the isometric and top view in the first and second line respectively of the different modeling strategies for joints with increasing complexity from the left to the right. For pointwise connections to model e.g. spotwelds or self-piercing rivets, surrogate models are for example beam element connections of simply two nodes or a

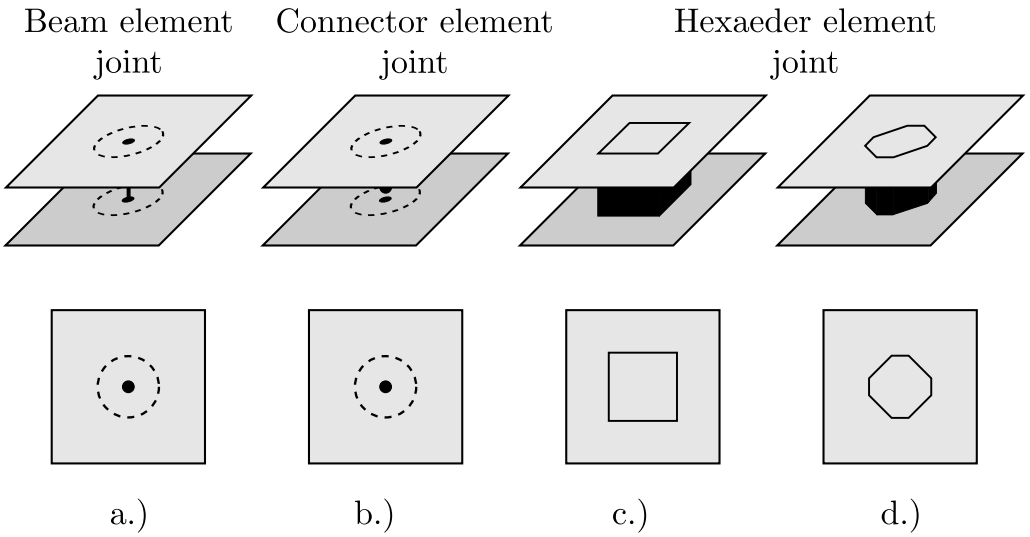

Figure 2.35.: Modeling strategies for joints according to [113]

coupled zone of multiple nodes For the hexaeder elements a full elasto-plastic material model with strain-rate dependent strain hardening and failure can be used.

The overview for joints presented in this section summarizes the current state of the art for modeling joints with a focus on point connections. Their applicability for hybrid joints is discussed in the succeeding section. To some extend, these models can also be extended to joints with longer geometrical dimensions as e.g. weld lines.

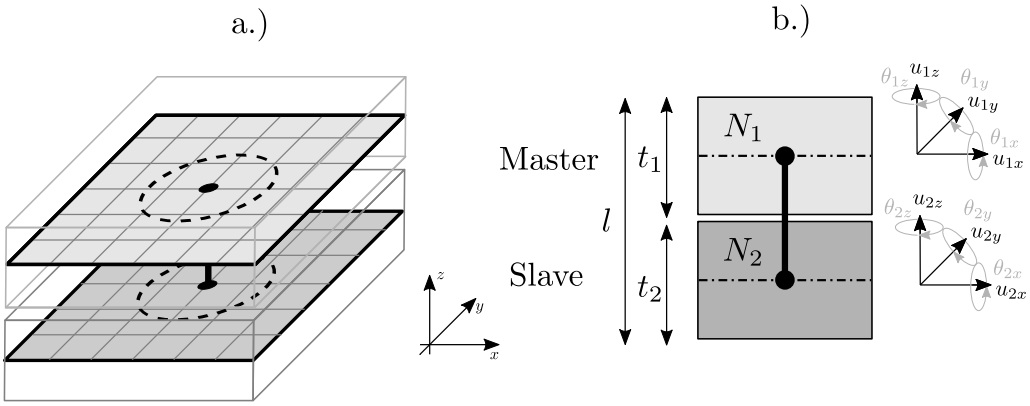

Figure 2.36.: Basic principle of surrogate model

Figure 2.36 represents the schematic basic working principle of a surrogate model for joints as there are available in, e.g., *PamCrash* by a Multi-PLINK between a surface and master node. Based on a spring-beam element a kinematic coupling of the master node N_1 to the slave node N_2 is achieved while the influence radius of the main nodes is realized by a spring element as displayed in dashed black lines on the left of Figure 2.36. A

local equilibrium of the indicated forces/momentums needs to be reached together with a failure envelope with forces f_{ij} or displacement u_{ij}. In *LS-Dyna* an comparable surrogate model is available under the keyword **Constrained_SPR2* stipulating a local equilibrium for forces and momentum between the master and slave node [116]. Additionally, we have **Constrained_Spotweld* to define massless nodes for non-contiguous nodes applicable for elements with a rotary inertia of shells or beams by coupling the nodal rotations and displacements [62]. For failure initiation both, a ductile and brittle mode can be used.

2.4.3. Direct discretization

The direct discretization uses the element formulation and material model of the respective FEM solver. For example, the toughened adhesive polymer (TAPO) model 3D continuum description is implemented as **MAT_252* in LS-Dyna as elasto-plastic material model taking into account an isotropic $J_1 - J_2^{'}$-plasticity the rate dependency of the structural response [62, 110, 117]. **MAT_240* can be used in LS-Dyna only for cohesive elements, rate dependent, elastic-ideally plastic models using a tri-linear traction-separation law with a quadratic yield and damage initiation formulation [62]. Surrogate

Table 2.8.: Overview of the common surrogate modeling techniques available in the explicit FEM Codes Abaqus explicit and LS-DYNA

Model	Application	Solver	Capabilities				
			Plasticity	Strain-rate	Stress state	Anisotropy	Failure
Cohesive Element	planar	-	●	○	●	○	●
Cohesive Contact	planar	-	●	○	●	○	●
**Constrained_SPR2*	point	LS-Dyna	◉	○	●	○	●
**Connector*	point	Abaqus	◉	○	●	○	●
**MAT_240*	-	LS-Dyna	Ideal-plasticity	●	●	○	●
**MAT_252*	-	LS-Dyna	$J_1 - J_2^{'}$	●	●	○	○
**Constrained_spotweld*	point	LS-Dyna	○	○	○	○	●

models serve as mechanical subsystems for joints substituting their deformation and failure behavior on a component or sub-system level. Even though the current state of the art of surrogate models includes a large set of approaches of connector elements in different solvers (see Table 2.8), not all of them are applicable to hybrid material pairings. In Table 2.8 black dot (●) represent available, gray dot (◉) partially available and white dot (○) not available. This is true especially for cases with a pronounced strain-rate sensitivity and direction dependency of the organic sheet. In addition, they are often developed for

point-wise connections such as self-piercing rivets (SPR) or spot-welds (SW); hence, they are not applicable for weld lines with long and slender geometrical dimensions. Whereas numerous research is done to analyze the joining process for hybrid material pairings for dissimilar pairings with metallic and reinforced polymers, the state of the art for mechanical surrogate models focuses more on hybrid steel-aluminum material pairings with the use of adhesives or mechanical joining techniques such as SPR.

2.5. Problem description

Even though numerous advantages of multi-material structures exist as outlined in Chapter 1, their design still bears various challenges. Besides a profound comprehension of the different materials to be joined, ranging from monolithic rolled sheets to bi-phase composite materials, these include namely the dimensioning of hybrid material joints. For the integration of hybrid material joints in the CAE process, robust and reliable models are needed. This thesis aims to contribute to the development of surrogate models for hybrid material pairings. For its high flexibility in joining hybrid material pairings, different processes are analyzed using directly or indirectly remote laser beam welding (LBW). Since these weld lines are of very long and slender geometries due to the nature of the thin laser beam, it is difficult or hardly feasible to model these joints or connections with an industrial mesh discretization of 3.00 - 5.00 mm.

2.6. Aims and objectives

The main objective of this thesis is the systematic development of mechanical surrogate models for hybrid material pairings. These surrogate models later serve as a substitute model on a component or full vehicle level and allow to correctly model the initial stiffness, deformation, and failure behavior of hybrid material pairings without compromising the overall critical time step in an explicit simulation run.

As the advantages of organic sheets for structural parts are laid out before, this thesis focuses on establishing the simulation of organic sheets in two aspects. Firstly, the phenomenological material modeling of the organic sheet to ensure reliable results under reasonable computational costs. Secondly, the development of surrogate models which can correctly depict the deformation and failure behavior of hybrid joints on a component level. Both developments will help to perform virtual tests in the CAE-driven design process. This enables the reliable virtual design and testing using simulations. Hence only for the most promising iterations of the development process physical hardware prototypes need to be manufactured and tested. This simulation-driven design process

helps to save energy and resources while meeting the requirements of an ever faster growing design process.

For the simulation of surrogate models as a substitute model for hybrid material joints it is a pre-requisite to describe the material behavior of both base materials correctly. This requires experiments on physical coupons of hybrid joints for the characterization of the deformation and failure behavior. In order to do so, a comprehensive experimental program is needed for the characterization of the base material as well as for the joint itself. Since there still is no standardized procedure for the characterization of the textile reinforced thermoplastics (organic sheets), the concept of the experimental matrix needs to be carefully designed to be able to deduct all necessary material parameters from it.

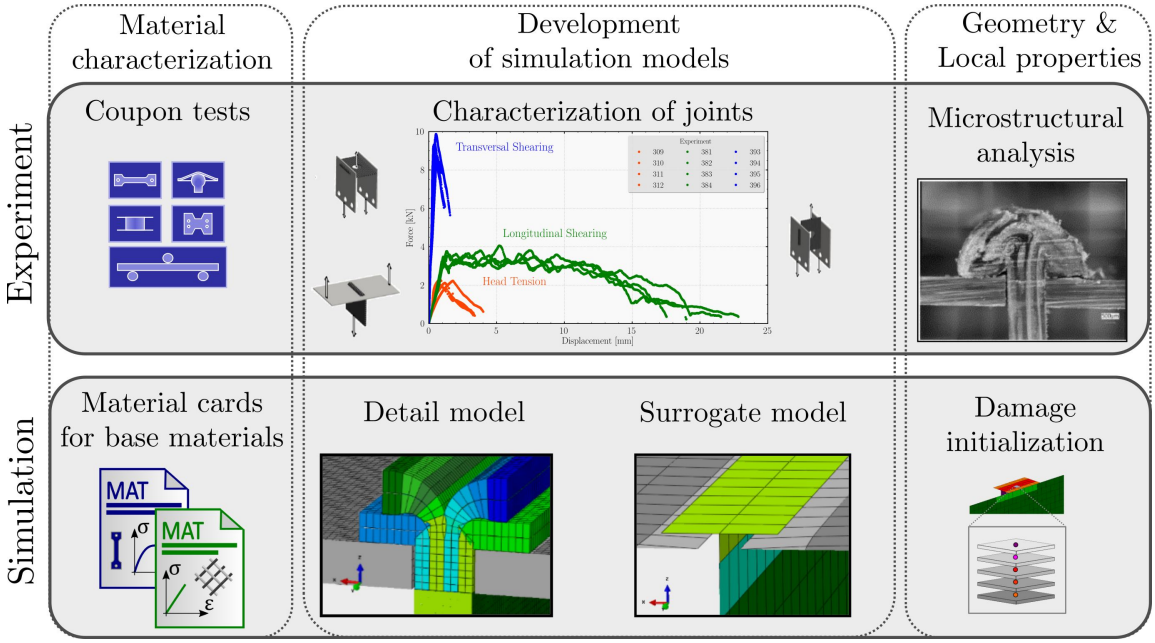

Figure 2.37.: Development scheme of surrogate sub-models for hybrid material pairings

Organic sheets are a semi-finished product consisting of a woven textile structure of endless fibers embedded in a thermoplastic matrix. Hence, they exhibit a complex material behavior under different loading conditions. This thesis addresses the aforementioned drawbacks of organic sheets by introducing a phenomenological material modeling concept for the organic sheet covering its deformation and failure behavior. All phenomena are analyzed on a multiscale approach and those relevant on a macroscopic level are identified. A material modeling approach adequate for simulating thin-walled structures under industrial conditions such as computational effort and resource efficiency is used as an expedient compromise between the necessary level of detail and computational cost. The approach is based on the user-defined material model MF GenYld+CrachFEM. Direct discretization is chosen based on an abstracted geometry of the joint with an emphasis on locally varied material properties due to the manufacturing and joining. Figure 2.37

displays the focus points of this work in its columns starting with the material characterization of the base materials, high-fidelity detail and low-fidelity surrogate models are developed by incorporating the geometrical dimensions and locally altered material properties of the joining zone. The two rows show how experiment and simulation relate to one another.

2.7. Outline

The advantages of not only multi-material design but also the application of organic sheets are outlined in Chapter 1. The theoretical fundamentals of continuum mechanic and the finite element method (FEM) as well as the application of different material models for metallic and composites materials are given in Chapter 2 and form the basis for the subsequent developments in the scope of this thesis.

In Chapter 3 the phenomenological material modeling of an organic sheet, representative for endless fiber reinforced composites by a smeared description on a macroscopic scale, is introduced. The subsequent Chapter 4 provides details of a material characterization in MF GenYld+CrachFEM exemplarily for a metallic and an organic sheet. Complementary to the exemplary material characterization, the material cards used within this thesis are visualized in Section A.6 of the Appendix.

Particularities for the modeling of hybrid material pairings are scrutinized in Chapter 5 and a method for the calibration of hybrid material pairings is introduced in its second part.

Surrogate models as a substitution for the mechanical behavior are hence developed for two different types of material pairings joined with a remote laser beam weld. In Chapter 6, a surrogate model is developed for hybrid material pairings for a dissimilar pairing of organic sheet Tepex® dynalite 102-RG600 and metal sheet S355. The development includes various bridge length of a thermo-mechanically formed bridge-deck panel joint using a form closed undercut. Adhesively bonded steel aluminum pairings are discussed in Chapter 7 with a two-step approach via a detail (high-fidelity) and surrogate model (low-fidelity).

Lastly, the results of this thesis are summarized and reflected in a critical discussion in Chapter 8 concluding in an outlook for future work.

3. Phenomenological material modeling of organic sheets

„Es lebe die [modulare] Phänomenologie"

Personal dedication from Julian Schöpfer to Matthias Vogler

Metallic sheets as well as fiber reinforced structures can be analyzed on multiple scales. The structural simulation in industry poses some requirements on the quality but also on the computational time and overall cost of the simulation results. The simulation of crystal plasticity on the micro-structure of metallic grains will hardly be completed within an acceptable range of time and effort on component level even when yielding promising simulation results. Therefore, phenomenological material models currently offer the best compromise between accuracy and computational cost and play hence an increasingly important role for simulation from specimen- to component-level up to a full-vehicle scale. While they are already well-established in industrial applications, for the simulation of metallic structures, they can also be applied to less homogeneous structures, such as wood and composite materials of glass or carbon fibers embedded in a thermo- or duroplastic matrix or copper windings (see also [72] and [118]). For a phenomenological material modeling of textile thermoplastics, so-called organic sheets, the effective material behavior is modeled treating the composite as if it were a homogeneous continuum. In this approach, the properties of its two constituents are described in a smeared manner on a macroscopic scale. In this Chapter 3, the proposed material modeling is described, i.e., it is explained how the smeared, phenomenological description relates to physical effects such as deformation and failure mechanisms occurring on lower scales. Then, in the subsequent Chapter 4 the material characterization based on a physical testing campaign is described. The proposed phenomenological material modeling for organic sheets (first published by the author of this thesis in [119]) allows modeling the full plasticity, a combination of a ductile, strain-based and a brittle, stress-based failure criterion while respecting the differently pronounced strain-rate sensitivities for fibers and matrix.

3.1. Deformation and fracture behavior of textile reinforced thermoplastics

Figure 3.1b demonstrates the force-displacement relation from in-plane uniaxial tensile tests for the off-axis angles 0°, 22.5°, and 45°. Due to the weaving of the fibers in weft direction their thickness ondulation[1] is slightly more pronounced than for the warp direction. This may result in small deviations in stiffness and strength between warp and weft direction which is neglected here [2]. For the organic sheet at hand it is supposed that the differences of the material weft and warp direction on the mechanical properties lay within the standard deviation of the experimental scatter [55]. Introducing an additional symmetry axis represented in green on the diagonal of textile displayed in the initial undeformed configuration in Figure 3.1a allows to further reduce the experimental campaign. The mechanical response for the off-axis angles 67.5° and 90° are therefore assumed to be the same as for the loadings in 22.5°- and 0°-direction.

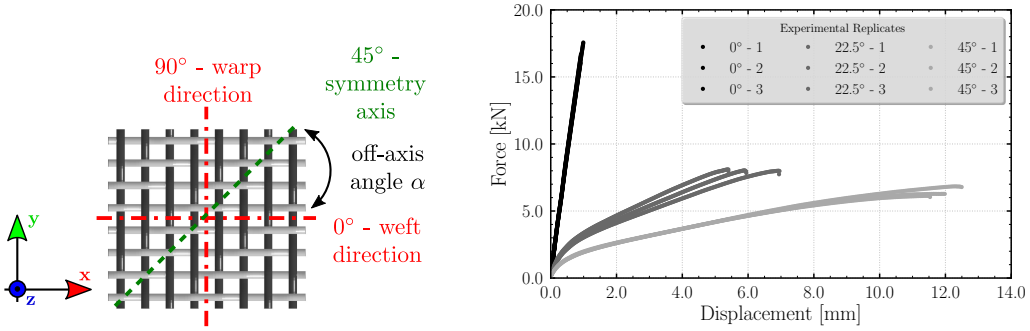

(a) Main orthotropy axis in 0°- for weft and 90°-direction for warp fibers and the off-axis angle α for the initial, undeformed configuration

(b) Force-displacement curves from uniaxial tensile test for off-axis loadings of $\alpha = 0°$, 22.5° and 45°

Figure 3.1.: Visualization of the initial configuration of the organic sheet (left) and force-displacement curves for various off-axis angles α (right)

A thorough analysis of the force-displacement curves for the different off-axis loadings in Figure 3.1b demonstrates the complex in-plane mechanical behavior of the textile reinforced thermoplastics. Its heterogeneous micro-structure with two different constituents, fiber and matrix, entails a complex mechanical behavior on a macroscopic scale. The force-displacement curves for the 0°-direction (black curves) are strongly linked to the properties of endless glass fibers and exhibit linear behavior until a brittle fracture by the fibers is initiated without any pronounced non-linearity. For the intermediate loadings in the off-axis angles α= 22.5° and 45°, the linear-elastic section is strongly reduced and a

[1] A measure for the waviness of endless fibers in thickness direction

pronounced non-linear strain hardening can be observed until fracture is initiated at very high deformation. Note that for the intermediate angles, the force stays approximately the same around 7.5 kN whereas the deformation at force peak at failure initiation changes significantly from 6.00 mm to 12.00 mm averaged across all experimental replicates. The reason for the drastic change in force-displacement is that there are three sources of material non-linearities in the textile composites. Besides the non-linear behavior of fiber and matrix itself the fiber weaving architecture is another source of non-linearity. On a macroscopic scale these non-linearities sum up and it is difficult or only feasible with enormous experimental effort to separate different phenomena occurring simultaneously on different scales [120, 121].

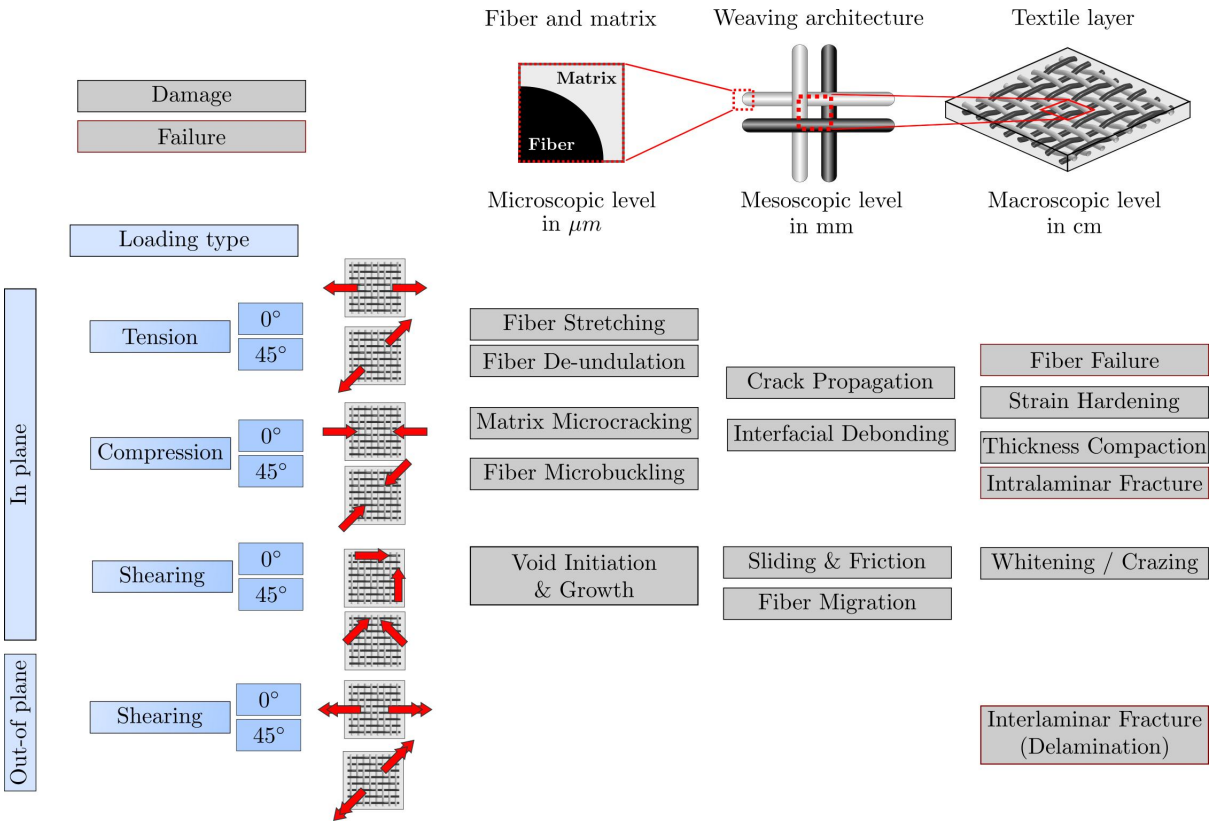

Figure 3.2.: Damage and failure phenomena on a multi-scale consideration [10, 54, 120]

Figure 3.2 classifies these different mechanisms with respect to the aforementioned scales (see Chapter 2.3.2) as well as to the type of loading for which they occur predominantly [122]. Therefore, the appropriate way proposed here, is to describe the effective material behavior on a macroscopic scale smeared across the singular properties of its two constituents and its architecture in a phenomenological manner but physically motivated. This approach allows relating the different mechanisms to one another. Fiber stretching and micro-buckling occurring on a microscopic scale for instance can be conceived macroscopically as plastic strain hardening and hence be respected as a characteristic of the plastic strain hardening. Therefore, different effects on the lower scales can be

summed up and put together to account for non-linearities prior to failure initiation. These non-linearities can then be modeled phenomenologically as the effective material behavior from the experiments.

Figure 3.3 illustrates how the different damage mechanisms relate to one another during a loading history represented on the regular twill-weave pattern of a textile architecture embedded in a thermoplastic matrix. A crack initiation starts either from a free edge or inner pores or voids in the thermoplastic matrix and grows depending on the remaining loading. By crossing one of the many endless glass fibers the fiber may stay intact (*Bridging*) or, if the fracture stress of the fiber is surpassed, it will cause a fiber failure. The latter may than force an interface debonding between the fibers and matrix or the interface and matrix.

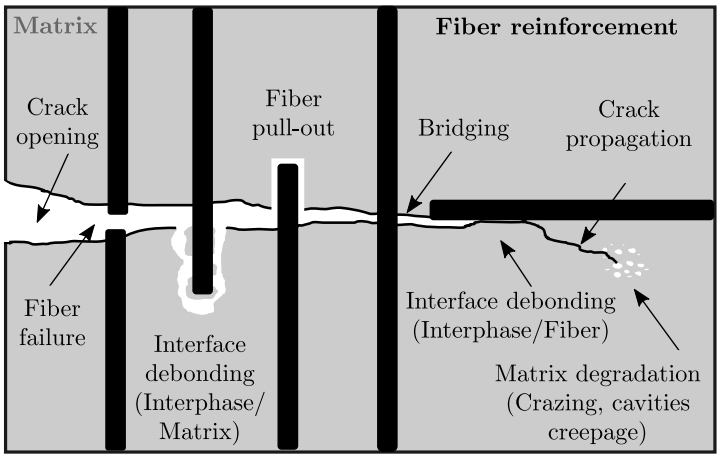

Figure 3.3.: Damage mechanisms of Endless Fiber Reinforced Thermoplastics (EFRT) adapted from [106]

This smeared approach allows summing up different mechanisms on lower scales and model them on a macroscopic scale as plastic strain hardening. Plastic strain hardening is assumed hence for the non-linearities prior to failure. It is modeled similarly to material models for ductile metals with a yield locus and a stress state and strain-rate $\dot{\varepsilon}$ dependent plastic strain hardening. Figure 3.4 illustrates the relation of a yield and fracture locus relative to one another for a textile composite. In the middle part of this figure, these two 3D concentric loci are displayed for the plane stress space spanned by the σ_1, σ_2 and τ_{12} components for the quasi-static regime. The inner yield locus represents the stress state dependent yield strength after which plastic strain hardening is assumed. The outer fracture locus represents the description of fiber failure in stress space. In between these two loci plastic strain hardening is assumed. The left and right part of Figure 3.4 display the traces of these two superimposed loci in the σ_1-σ_2-plane on the left and the σ_1-τ_{12}-plane on the right in green dashed lines for the yield and in red solid lines for the fracture locus. The traces in the σ_1-σ_2-plane illustrate that for the 0° and 90°, i.e. for weft and warp directions respectively, there is a significant elastic portion and very little plasticity until a brittle fracture mode is initiated by surpassing the stress threshold defined by the

fracture locus. For shearing however, displayed as the ordinate value in σ_1-τ_{12}-plane on the right, only a small portion is elastic when a huge deformation is reached until the fracture locus is reached.

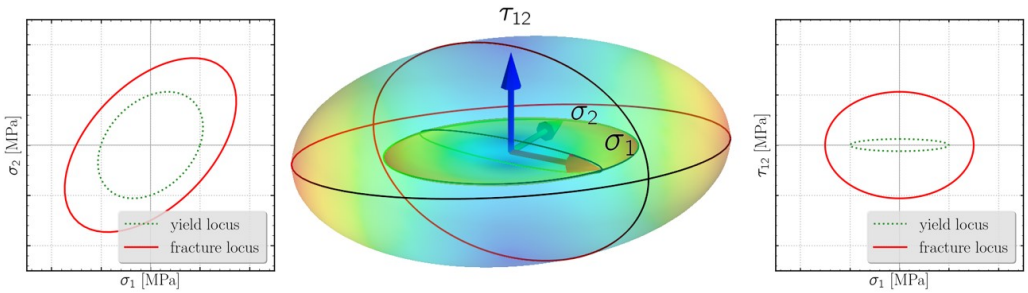

Figure 3.4.: Schematic representation of concentric yielding and fracture envelopes in 3D for plane stress state in the quasi-static regime (middle) and its traces in the σ_1-σ_2-plane (left) and σ_1-τ_{12}-plane (right)

Textile reinforced thermoplastics are woven from endless glassfibers, which combine the characteristic properties of a ductile and yielding matrix, as known from unreinforced thermoplastic or ductile sheet metals, and stiff and brittle fibers, which are usually characteristic for composites. Therefore, for the simulation of textile reinforced thermoplastics, it is crucial to cover not only the stress state dependent hardening after yielding but also the fracture initiation originating from both constituents, fiber and matrix.

3.2. Stress- and strain-based fracture criterion

Now, we address fracture recalling the in-plane material properties for different off-axis loadings under tension from Figure 3.1b. In Figure 3.5, true stress σ_{eq} - true strain ε_{eq} for the two extreme directions are displayed for $\alpha = 0°$ in red and 45° in green. This figure illustrates that from a material description point of view describing the fracture initiation of the ductile 45°-direction with a stress threshold may cause severe deviations in strain for only slightly different stress values. The same is true for characterizing the fracture initiation of the brittle 0°-direction with a strain-based threshold. Therefore, it is recommendable to use a more sensitive metric in the respective direction for a stable and robust description of the fracture initiation. Differentiating the fracture initiation for uniaxial tensile experiments in 22.5°- and 45°-orientation as displayed in Figure 3.1b is easier and more robust using a strain- rather than a stress-based threshold. Hence, a combination of two fracture criteria is proposed to complement one another. This means the approach uses a stress-based failure criterion for the brittle fracture mode primarily dominated by the fiber and a strain-based failure criterion for the comparatively softer matrix. Both need to be calibrated carefully with respect to one another in order to also correctly describe the fracture initiation for intermediate off-axis loadings. Figure 3.6a

and 3.6b display the critical fracture stress and strain in dependence on the off-axis angle α.
Failure initiation is hence considered as a macroscopic crack opening in the matrix material or a fiber failure. The drawback of this approach is that a clear allocation of the different mechanisms as introduced in Figure 3.2 is no longer possible. But it allows a clustering of the different phenomena for primarily matrix dominated failure modes as well as for fiber dominated failure modes [123].

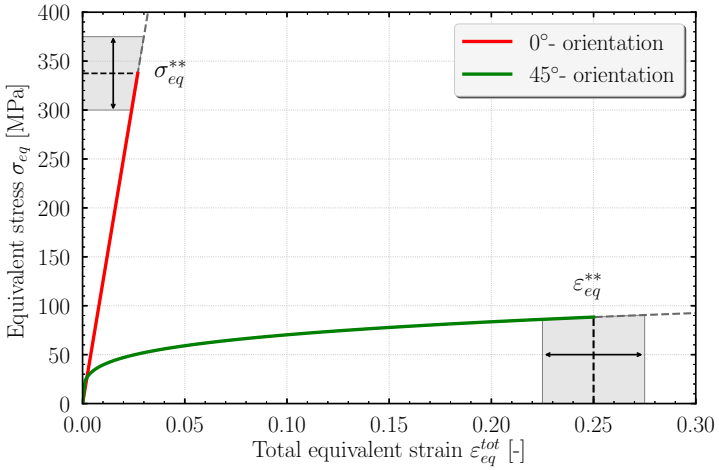

Figure 3.5.: Schematic representation of a stress- (red) and strain-based (green) failure criterion with respect to stress-strain-curves

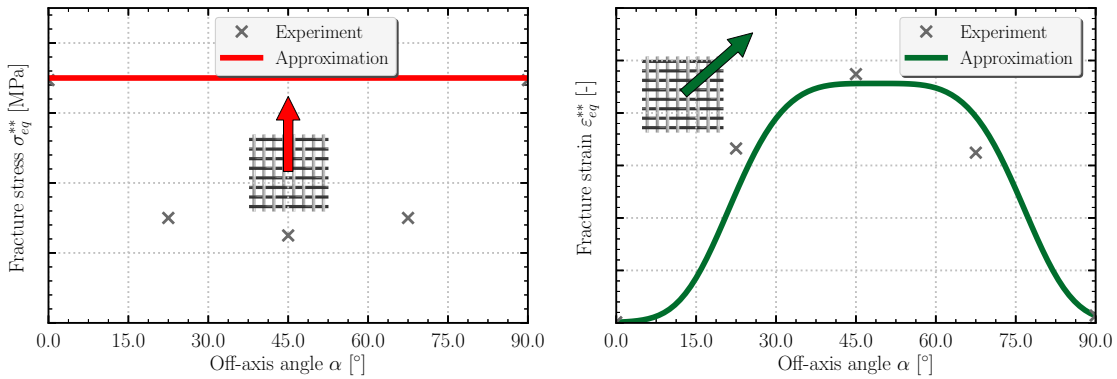

(a) Approximation of the stress-based failure criterion in dependence on the off-axis angle α

(b) Approximation of the strain-based failure criterion in dependence on the off-axis angle α

Figure 3.6.: Combination of a stress- and strain-based fracture criterion

The two fracture criteria serve in a complementary manner to one another using the more sensitive metric in the respective direction. In case an equally balanced twill weave

architecture is considered, a symmetry to the axis $\alpha = 45°$ is used. Therefore, the approximation of the stress-based criterion needs to be met for the stiff direction of weft and warp direction for $\alpha = 0°$ and 90°, respectively (see Figure 3.6a). Whereas the intermediate angles of $\alpha = 22.5°$, 45.0° and 67.5° are covered by the strain-based criterion (see Figure 3.6b).

3.2.1. Orthotropic strain-based fracture for ductile matrix

For the ductile strain-based failure criterion the aforementioned criterion for ductile normal fracture (DNF) originally developed and employed for metallic sheets (see Equation (2.71)) is adapted by a term to account for the planar orthotropy of the fracture strain by the function $c(\alpha)$ for organic sheets as given in Equation (3.1)

$$c(\alpha) = a_0 + a_1 \cdot \exp\left(-a_2 \left(|\alpha| - a_3\right)^n\right). \tag{3.1}$$

In order to ensure a smooth, horizontal plateau of the slope of c over α for α=0° and 45° as displayed in Figure 3.6b an exponent of $n = 4$ is recommended for modeling organic sheets. With α denoting the in-plane off-axis angle between the maximum strain-rate $\dot{\varepsilon}$ and the reference direction.

3.2.2. Orthotropic stress-based fracture for brittle fiber

The orthotropy of the stress-based failure criterion is defined implicitly by the formulation of the fracture locus. The trace displayed in Figure 3.6a represents an isotropic description under tension. In order to describe the orthotropy of the fracture locus, either an orthotropic formulation for a yield criterion can be used to define a non-isotropic threshold for initiating brittle as e.g. the Hill1948 formulation. Alternatively, a given yield locus can be adapted by the modules for biax-scaling, shearing or tension-compression asymmetry as described in Section 2.2.2 for anisotropic hardening. Concerning the description, e.g., of an unbalanced textile of an 80% fiber volume in weft and 20% in warp direction, the interested reader is referred to [124].

3.3. Strain-rate dependency of fiber and matrix

Another advantage of treating the failure initiation separately for fiber and matrix is that this allows incorporating a differently pronounced strain-rate sensitivity of the fracture for fiber and matrix. In accordance with [8] and [124], the trends of fiber and matrix dominated 0°- and 45°-orientation respectively are displayed for true strain-true stress

curves for various strain-rates in Figure 3.7. Non-linear effects in ramping up the strain-rate are neglected here. For a loading in fiber direction, a higher strain-rate has a positive impact, resulting in an increased strength and strain until rupture occurs [125]. In the matrix dominated 45°-direction however loading strength remains approximately on the same level while the critical strain until rupture increases. The latter negative strain-rate effect is consistent with strain-rate effects of unreinforced PP or PA-matrices [40, 48].

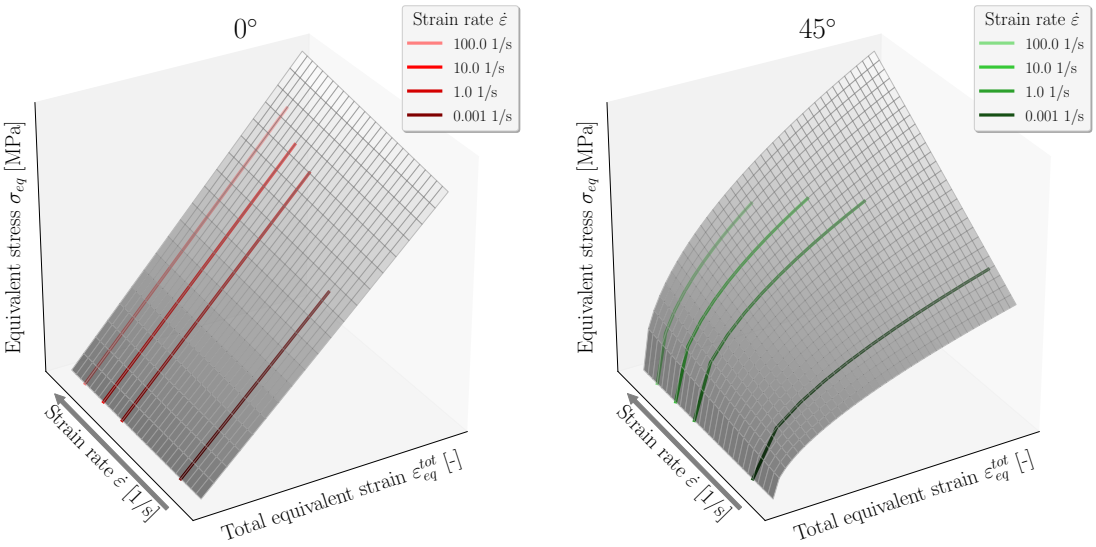

Figure 3.7.: Stress-strain curves displaying the influence of the strain-rate $\dot{\varepsilon}$ on the fiber dominated 0°- (left) and the matrix dominated 45°-orientation (right) of organic sheets in accordance with [124]

The positive strain-rate effect on the fiber failure initiated with a stress threshold can be modeled with enlarging the fracture locus for elevated strain-rates. The negative strain-rate effect on the fracture strain for the ductile matrix can be modeled by down-scaling the fracture curve for the dynamic strain-rate.

4. Material characterization of base materials for crashworthiness

Prerequisite for modeling deformation and failure behavior of similar and dissimilar material pairings in a structural simulation is a correct description of the two base materials to be joint together. For crashworthiness simulation this necessitates to cover not only the strain-rate dependency of the material, but also fracture. In dependence on the material properties, a comprehensive experimental program is required which covers all relevant aspects of the materials for multi-axial loading including a stress-state dependent plastic hardening and fracture behavior. On coupon level, physical tests are performed to obtain the structural response of the material under multiaxial, monotonously increasing loadings. The procedure of experimental characterization, derivation of material properties, translation in a material card, and final validation simulation is depicted schematically in Figure 4.1.

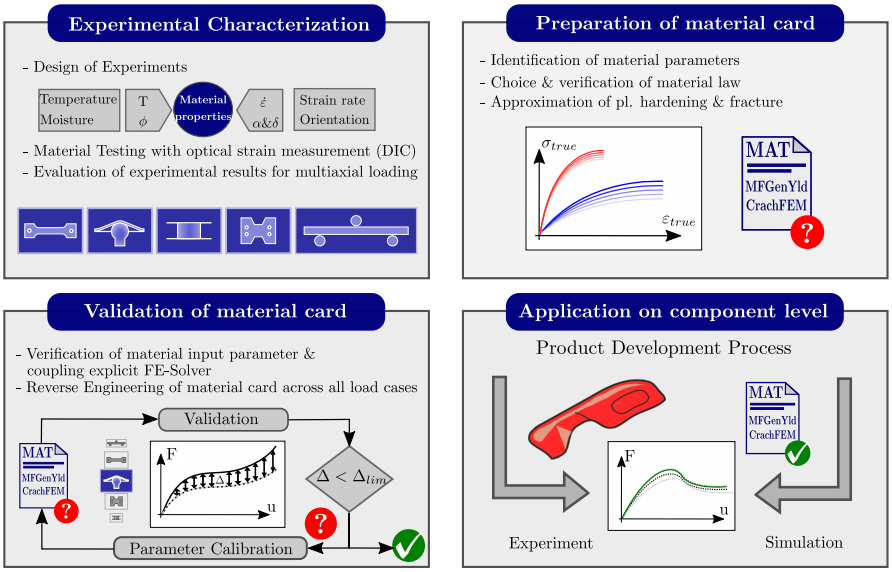

Figure 4.1.: Schematic depiction of deriving a material card including validation simulation on coupon level

On specimen level the distinction of effects, e.g. related to an elevated force level due to a pronounced positive strain-rate effect or to false thickness definition, can be unequivocally

scrutinized here. While on higher structural levels it is often difficult to separate the influence of different mechanisms occurring simultaneously. The comprehensive material characterization on specimen level allows to cover all relevant aspects of the material and integrate them in the physically motivated material card. The higher effort and cost for comprehensive material characterization pays off in the long run for a good prediction quality of the material card on a higher level as displayed in the building block approach (BBA) in Figure 4.2. With this approach, the amount of physical testing can be reduced for the higher levels where the complexity and associated costs increase. Hence, the forecast quality of the simulation is an essential step in not only reducing the costs but also accelerating the virtual design and development of components with increasingly stringent requirements.

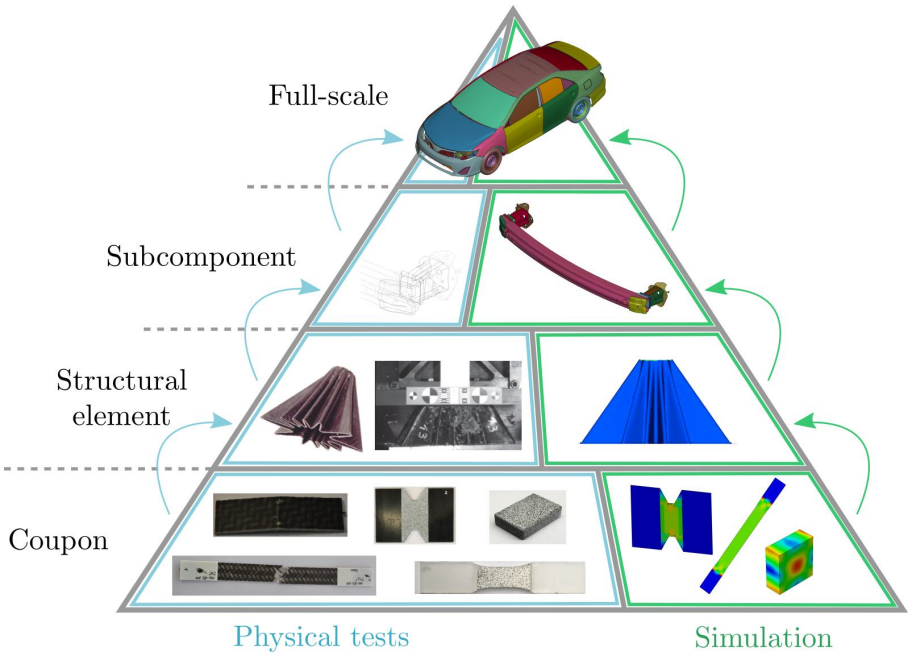

Figure 4.2.: Building block approach applied to automotive crash structures (adapted from [87, 126, 127])

In this chapter, the material characterization for crashworthiness is exemplarily shown for a steel sheet S355JR with 1.50 mm thickness in Section 4.2 and the organic sheet with 2.00 mm thickness from Bond Laminates under the tradename Tepex® dynalite 102-RG600 in Section 4.3. In the context of material characterization, only the essential information on the experiments is outlined for this thesis because it focuses on computational aspects. The visualization for a comparison between the different materials is given in the appendix under Sections A.6.1, A.6.2, and A.6.3 for the S355JR, the EN AW-6082 T6, and the 102RG600 representative for the material characterization of a steel sheet, an aluminum sheet, and a textile reinforced thermoplastics. The comparison between the different materials steel, aluminum, and organic sheets demonstrates the consistent material modeling with a target-oriented, precise combination of different phenomenological modules. This modeling strategy allows the CAE-engineer to thoroughly comprehend the

relevant material behavior beyond different material classes ranging from ductile metals over un- and reinforced thermoplastic to composites.

4.1. Framework of MF GenYld+CrachFEM

The acronym MF GenYld+CrachFEM is derived from MATFEM[1] (MF) Generalized Yield (GenYld) and Crach. The latter is the Russian word for instability and CrachFEM refers to a module for the prediction of instability of ductile metals, also known as necking.

The evaluation of failure risks for the aforementioned ductile and brittle failure models is integrated as an output of history variables of the material model MF GenYld+CrachFEM. These risks can be post-processed in a field plot in order to identify critical domains ranging from 0 to 1, with 1 representing elimination at 50% probability of failure [128]. Post-processing of history variables in MF GenYld+CrachFEM allows the evaluation of specific failure risks Ψ_{DNF} for ductile normal fracture (DNF), Ψ_{DSF} for ductile shear fracture (DSF), and Ψ_{Crach} for necking as a field plot and to identify critical regions in the simulation as well as the logarithmic strain-rate $\dot{\varepsilon}$. Finally, the general failure risk Ψ_{max} is determined via Equation (4.1) over all criteria for ductile failure models. Table 4.1 summarizes the important history variables (HVs) relevant in the scope of this thesis, which is a standard procedure but important in the context of this thesis [128]. Additionally to the ductile failure modes, the HV19 is used for the brittle failure model for brittle composites since instability and brittle fracture locus are mutually exclusive.

$$\Psi_{max} = \max\left\{\Psi_{DNF}, \Psi_{DSF}, \Psi_{Crach}\right\}. \tag{4.1}$$

Further the history variables s_{HV16}-s_{HV19} allow to account for locally altered material parameters by scaling the plastic hardening behavior as well as ductile fracture criteria. Since this can be done for each integration point in a simulation, this technique allows also to account for gradients of material properties across the thickness. An example for local modification of material properties is given later in Section 6.4 in the context of organic sheets.

4.2. Material characterization of the S355JR sheet

Exemplarily for the material characterization of metal sheets for a crashworthiness simulation using MF GenYld+CrachFEM, the experimental characterization and derivation of a material card is outlined in this chapter. In a crashworthiness simulation it is crucial

[1] www.matfem.de

Table 4.1.: History variables and their meaning in MF GenYld+CrachFEM

History variable (HV)	Description	Symbol
HV1	equivalent plastic strain	ε_{eq}
HV2	maximum failure risk	Ψ_{max}
HV3	ductile normal failure risk	Ψ_{DNF}
HV4	ductile shear failure risk	Ψ_{DSF}
HV5	accurate instability risk	Ψ_{Crach}
HV12	log. of equivalent strain-rate	$\dot{\varepsilon}$
HV16	Scaling factor for plastic strain hardening	s_{HV16}
HV17	Scaling factor for normal fracture	s_{HV17}
HV18	Scaling factor for shear fracture	s_{HV18}
HV19	Scaling factor for instability	s_{HV19}

to correctly assess the capacity to absorb energy which includes the initiation of failure under monotonous loading conditions covering velocities ranging from quasi-static to the elevated dynamic range. In order to cover these two aspects, besides a fully elasto-plastic description, the material model needs to account for strain-rate sensitivity and fracture across multiaxial loading conditions.

We regard a steel sheet with 1.5 mm thickness of the type S355JR, where the S stands for structural steel the 355 indicates a yield strength from at least 355 MPa and JR signifies an impact energy absorption capacity of at least 27 J at room temperature [129]. The chemical composition of the S355JR is given by Table 4.2.

Table 4.2.: Chemical composition in % determined by the ladle analysis for the S355JR steel in accordance with EN 10025-2 [129]

C	Si	Mn	P	S	Cu	N
0.24	0.55	1.60	0.035	0.035	0.55	0.012

The material characterization of S355JR is based on some assumption for metallic materials with regards of practicality. Firstly, the micro-structure of the grains exhibits a preferential direction referred to as the rolling direction (RD) for metallic sheets. Because this rolling direction has a minor influence in the elastic regime and elastic strains ε_{el} are significantly lower than plastic strains ε_{pl}, the anisotropy of the Young's modulus can be neglected. Hence, the metallic sheet is modeled as isotropic in the elastic but as planar orthotropic in the plastic regime. Further, after the onset of yielding plastic incompressibility is assumed. Lastly, for an accurate description of failure initiation in the simulation three-fold failure criterion needs to be included in the material characterization. Necking for a FLC, which will be predicted by the numerical algorithm Crach, combined with an isotropic $\beta-$ and $\theta-$ model to account for the separate failure mechanisms of ductile normal and ductile shear fracture.

4.2.1. Experimental characterization

Exemplarily for the material characterization of a metallic sheet the scope of the experimental matrix is summarized in Table 4.3. The orientation α in Table 4.3 gives the in-plane angle relative to the rolling direction. Here 0° denotes an orientation parallel, 45° diagonal, and 90° transversal w.r.t. the rolling direction. The uniaxial tensile tests at a different orientation relative to the rolling direction are necessary to measure in-plane the r-values and yield strength and at higher strain-rates to account for the strain-rate sensitivity of the plastic strain hardening behavior. All remaining specimens at the quasi-static strain-rate $\dot{\varepsilon} = 0.001$ serve to measure the critical fracture strain at different stress states. The experimental results for higher strain-rates are taken from *Thyssenkrupp Steel Europe* (TKSE) and the remaining experiments were done at the *Institure for Manufacturing Technology* (LFT) at the Friedrich-Alexander-Universität Erlangen-Nürnberg.

Table 4.3.: Overview of the experimental matrix for the material characterization of the S355JR with 1.50 mm thickness

Specimen	Orientation	Strain-rate	Norm
	α in °	$\dot{\varepsilon}$ in 1/s	
Uniaxial tension	0.0	0.001, 1.0, 10.0, 100.0, 250.0	DIN EN 6892
	45.0	0.001	DIN EN 6892
	90.0	0.001	DIN EN 6892
Tension with hole	0.0	0.001	-
Tension waisted	0.0	0.001	-
Tension grooved	0.0	0.001	-
Shearing	0.0	0.001	-
3-Point-Bending	0.0	0.001	ISO 7438
Erichsen	0.0	0.001	DIN EN ISO 20482

To evaluate the displacements in the experiments, local gauge lengths are used based on digital image correlation (DIC). For this method, a randomly distributed gray-scale scatter is applied to the surface of the specimens, which is filmed during the experiment. The deformation of this 2D or 3D gray-scale scatter is recorded throughout the experiment and allows to post-process superficial strains and displacements based on the recorded video. Figures of the specimen geometries used for this experimental characterization are given in the Appendix A.4.

4.2.2. Derivation of material card

In accordance with the experimental matrix, material parameters and stress-strain relations for the S355JR are identified. These parameters serve then as an input for the

approximation of analytical functions in MF GenYld+CrachFEM. Table 4.4 summarizes the elastic properties assuming an isotropic material.

Table 4.4.: Elastic parameters of the S355JR steel

Density	Young's modulus	Shear modulus	Bulk modulus	Poisson's ratio
ρ in t/mm^3	E in MPa	G in MPa	K in MPa	ν in -
7.80E-09	210,000.0	80,769.0	175,000.0	0.3

In general, the yield locus describes the onset of plastic strain hardening dependent on the stress state. In Figure 4.3 the trace of the yield locus in the σ_1-σ_2-plane is displayed for the Dell2006 formulation, which is found to be the best fit across all experiments. In order to display the orthotropic models in a unique manner, the σ_1-σ_2 are considered here to align with the material's principal directions. The Dell2006 yield locus, Equation (4.2) is the superposition of two different yield loci; one upper bound yield locus with a hexagonal, angular Tresca-like shape and the other one with a Hosford-type yield locus [25, 130]. It is applicable for a 3D stress state capturing r-values and yield strength with an associative plastic flow potential and was first published in [130].

$$k_1 \cdot (|X_1 - X_2|^{m_1} + |X_2 - X_3|^{m_1} + |X_3 - X_1|^{m_1})^{1/m_1} + k_2 \cdot (|Y_1|_2^m + |Y_2|_2^m + |Y_3|_2^m)^{1/m_2} = \sigma_{eq} \tag{4.2}$$

Anisotropy is defined by two transformation matrices with coefficients c_1-c_6 and d_1-d_6 defined in Equations (4.3), (4.4) and (4.5), (4.6). For plane stress states the number of coefficients of the transformation matrix can be reduced to 4.
The X_1, X_2, and X_3 are the principal components of the vector X_{ij}

$$\begin{pmatrix} X_{xx} \\ X_{yy} \\ X_{zz} \end{pmatrix} = \frac{1}{3} \cdot \begin{bmatrix} c_2 + c_3 & -c_3 & -c_2 \\ -c_3 & c_3 + c_1 & -c_1 \\ -c_2 & -c_1 & c_1 + c_2 \end{bmatrix} \cdot \begin{pmatrix} \sigma_{xx} \\ \sigma_{yy} \\ \sigma_{zz} \end{pmatrix}. \tag{4.3}$$

$$\begin{pmatrix} X_{xy} \\ X_{yz} \\ X_{zx} \end{pmatrix} = \frac{1}{3} \cdot \begin{bmatrix} c_4 & 0 & 0 \\ 0 & c_5 & 0 \\ 0 & 0 & c_6 \end{bmatrix} \cdot \begin{pmatrix} \sigma_{xy} \\ \sigma_{yz} \\ \sigma_{zx} \end{pmatrix}. \tag{4.4}$$

In a similar manner, Y_1, Y_2, and Y_3 are the principal components of the vector Y_{ij}

$$\begin{pmatrix} Y_{xx} \\ Y_{yy} \\ Y_{zz} \end{pmatrix} = \frac{1}{3} \cdot \begin{bmatrix} d_2 + d_3 & -d_3 & -d_2 \\ -d_3 & d_3 + d_1 & -d_1 \\ -d_2 & -d_1 & d_1 + d_2 \end{bmatrix} \cdot \begin{pmatrix} \sigma_{xx} \\ \sigma_{yy} \\ \sigma_{zz} \end{pmatrix}. \tag{4.5}$$

$$\begin{pmatrix} Y_{xy} \\ Y_{yz} \\ Y_{zx} \end{pmatrix} = \frac{1}{3} \cdot \begin{bmatrix} d_4 & 0 & 0 \\ 0 & d_5 & 0 \\ 0 & 0 & d_6 \end{bmatrix} \cdot \begin{pmatrix} \sigma_{xy} \\ \sigma_{yz} \\ \sigma_{zx} \end{pmatrix}. \tag{4.6}$$

The coefficients k_1 and k_2 depend on the weighting factor c $\in [0.0; 1.0]$.

$$k_1 = 3c \cdot (|c_2 + 2c_3|_1^m + |c_2 - c_3|_1^m + |2c_2 + c_3|_1^m)^{m_1} \tag{4.7}$$

$$k_2 = 3\,(1-c)\,(|c_2 + c_3|_2^m + |c_2|_2^m + |c_3|_2^m)^{m_2} \tag{4.8}$$

The parameters of the Dell2006 yield locus obtained for the S355JR are listed in Table 4.5. These parameters define the shape of the yield locus as displayed in Figure 4.3 normalized to the initial yield strength under tension. The absolute value for the yield locus is obtained by multiplication for the initial yield stress σ_y for uniaxial tension, which is defined as the first entry of the plastic hardening curves $\sigma_{eq}\left(\varepsilon_{eq}^{pl} = 0.0\right)$.

Table 4.5.: Parameters for the Dell2006 yield locus description [130]

c_1	c_2	c_3	c_4	c_5	c_6	d_1	d_2	d_3	d_4	d_5	d_6	m_1	m_2	C
1.779	1.067	0.917	1.192	1	1	0.2	1.071	0.941	0.796	1	1	2	2	0.5

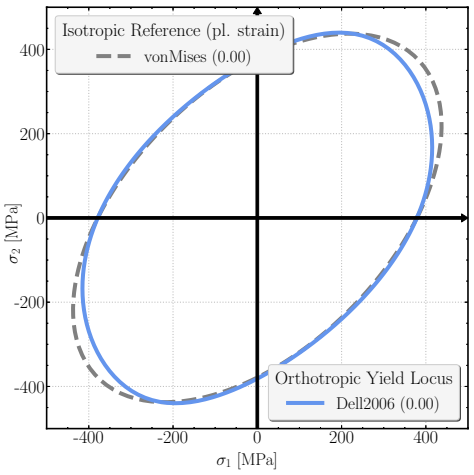

Figure 4.3.: Yield locus Dell2006

Figures 4.4a and 4.4b display the experimentally measured values at an angle of 0°, 45°, and 90° relative to the rolling direction for the yield stress and r-values respectively in comparison with the approximation of Dell2006 yield locus formulation.

Figure 4.5 displays the experimental measured relations of true stress vs. true plastic strain for uniaxial tensile tests under 0°, 45°, and 90° which are plotted until the point of uniform elongation. Beyond this point, the data is extended with the deformation of the bulge or Erichsen test for higher strains (see Section 2.2.2). The stresses from the bulge test are slightly scaled down to the level of uniaxial tension following the principle of plastic work hardening [31]. Besides the experimental results, shown in Figure 4.5, also the approximation of analytical plastic strain hardening laws is plotted. For the range of the experiments, a numerical optimization method is used to minimize the difference between the averaged experimental results and analytical descriptions by the method of least squares. Three different analytical laws are compared to one another and the

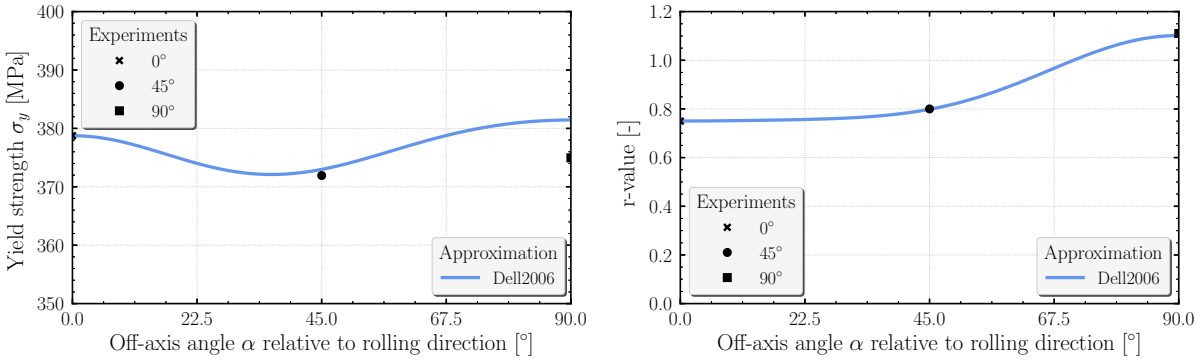

(a) In-plane yield stress over off-axis angle α (b) In-plane r-values over off-axis angle α

Figure 4.4.: Yield stress and r-value over the angle α for the yield locus Dell2006 for S355JR with 1.5 mm thickness

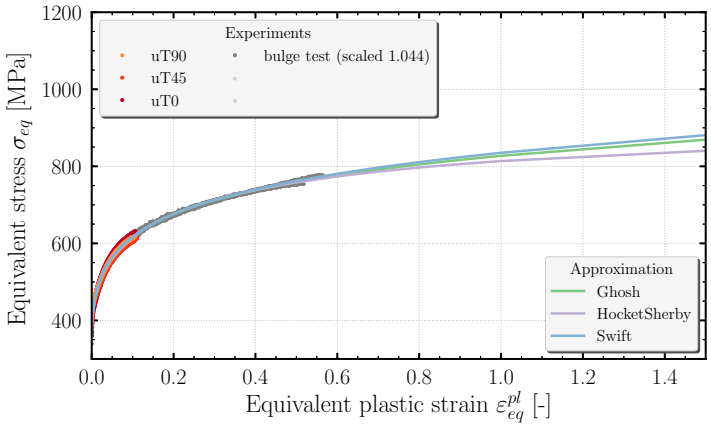

Figure 4.5.: Experimental curves of the plastic strain hardening behavior from multiple experiments, i.e. for uniaxial tension in 0° (uT0), 45° (uT45), 90° (ut90) complemented by bulge test and analytical approximation

best fitting is found for the approximation using the analytical law by Ghosh [33] (see Equation (2.58) in Section 2.2.2). The optimal set of parameters found for the analytical formulation according to Ghosh is summarized in Table 4.6.

Table 4.6.: Approximated parameters for the Ghosh formulation

a	ε_0	n	k
in MPa	in -	in -	in MPa
1,214.0	0.0043	0.0837	-387.1

The found Ghosh formulation can now be used as a reference hardening curve for a quasi-static strain-rate under the assumption of isotropic hardening. It can then be extrapolated for different strain rates to account for a positive strain-rate effect. In Figure 4.6a,

the plastic strain hardening behavior until the point of uniform elongation is given from uniaxial tensile tests for various strain rates. A positive strain-rate effect on the S355JR can be seen as for higher strain-rates the stress level increases. In the dynamic regime for the elevated strain-rates $\dot{\varepsilon} = 100.0$ and 250.0 1/s, noise is seen which is due to inertia effects in the dynamic experiments.
For the strain-rate dependency of the plastic hardening behavior for the S355JR displayed in Figure 4.6a, the best fit is found for the tanhyp formulation. Since the strain-dependency is not needed for metallic sheets, the tanhyp-formulation of Equation (4.9) suffices among all formulations outlined in Section 2.2.2. The equivalent stress σ_{eq} vs. plastic strain ε_{pl}^{eq} curves from Figure 4.6a in relation to the reference hardening curve translate into the scalar values used in Figure 4.6b which are taken here as supporting points. These values can be interpreted as scaling values for the quasi-static reference hardening curve. The gray line shows the best approximation results for the S355JR for the parameters of the tanhyp-formulation summarized in Table 4.7. The green dots represent the experimental supporting points used as the input for the approximation and the blue dots represent the obtained scaling factors for logarithmic, equi-distant strain-rates $\dot{\varepsilon}$ used later on as input for the material card. Taking the scaling factor for the strain-rate sensitivity from Figure 4.6b and multiplying it with the reference hardening curve yields the family of curves in Figure 4.7 which then serve as the input of multiple hardening curves for the corresponding strain-rates for the material card in MF GenYld+CrachFEM. Hence, a positive influence of the strain-rate effect is included in the material card assuming a constant characteristic of the plastic strain hardening behavior across all strain-rates.

$$\sigma\left(\dot{\varepsilon}\right) = \sigma_{ref}\left(\varepsilon\right)\left\{a_1 + a_2 \text{tanhyp}\left(a_3\left(\dot{\varepsilon} - a_4\right)\right)\right\}. \tag{4.9}$$

Table 4.7.: Approximated parameters for strain-rate dependent plastic hardening

a_1	a_2	a_3	a_4
in -	in -	in s	in 1/s
1.09	0.10	0.494	0.588

After the determination of the parameters for elasticity and for the yield locus and strain-rate dependent strain hardening the failure criteria need to be included in the material characterization. For ductile metals prone to necking, the forming limit curve (FLC) as well as the definition of the fracture envelopes is the last step to accurately describe all failure mechanisms in a crashworthiness simulation.

Table 4.8 summarizes the type of specimens used for the determination of the critical fracture strain under various multiaxial stress states. Based on the fracture surface of the tested specimen, the predominant failure mechanisms can be distinguished, which then allows to assign the fracture specimen to either ductile normal or shear fracture.

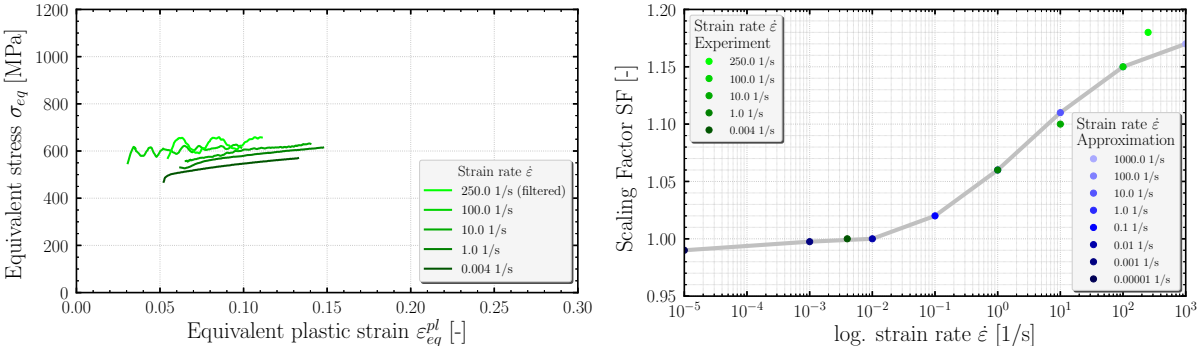

(a) Experimental plastic hardening behavior from uniaxial tensile tests for multiple strain-rates $\dot{\varepsilon}$ until uniform elongation

(b) Approximation of the strain-rate sensitivity

Figure 4.6.: Experimentally determined and approximated strain-rate sensitivity for the S233JR on the left and right hand side, respectively

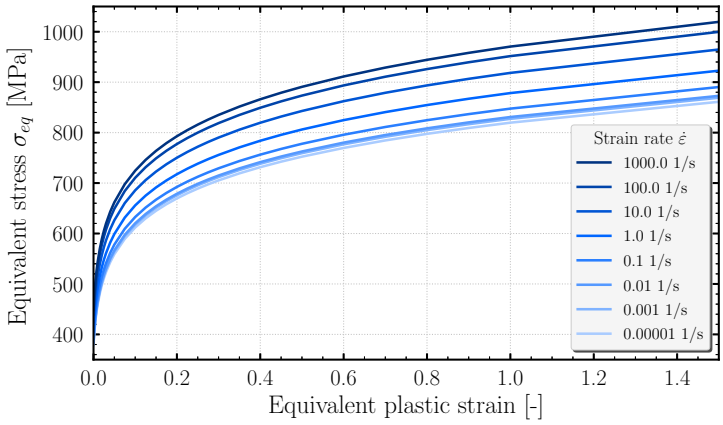

Figure 4.7.: Curves representing the strain-rate dependent plastic hardening behavior for the S355JR with 1.5 mm thickness

Occasionally, a mixture of failure types can be observed across multiple replicates of a type of experiment as can be seen in the last column of Table 4.8. Unfortunately, the S355JR material was too ductile for the chosen experimental setup of the three point bending test, so that no failure initiation was achieved here.
Similar to shear fracture parameter θ for DSF, the parameter β is introduced for the DNF. This allows to combine two stress state parameters, stress triaxiality η_{MF} and the ratio of σ_I/σ_{vM} with the use of a material specific constant s_{NF} (see Equation (4.10)). By introducing the normal fracture parameter β, the equivalent plastic strain ε^{**}_{eq} can be expressed as stated in Equation (4.11). Introducing s_{NF} facilitates the task of parameter fitting. However, since the parameters need to be determined individually for every material, the obtained parameters for β are no longer comparable between different materials [61]. In order to retain the comparability for different materials, the fracture curves are

Table 4.8.: Overview of the quasi-static fracture limit strains derived for different stress states for the S355JR with 1.50 mm thickness

Specimen	ε_{eq}^{**}	$\alpha = \frac{\varepsilon_2}{\varepsilon_1}$	$\eta_{MF} = \frac{p}{\sigma_{vM}}$	$\beta = \frac{\sigma_1}{\sigma_{vM}}$	$\theta = \frac{\tau_{max}}{\sigma_{vM}}$	Fracture type
	in -	in -	in -	in -	in -	
Uniaxial tension	0.356	-0.526	1.0	-	-	Necking
3-Point-Bending	-	-	-	-	-	No failure
Tension with hole	0.683	-0.5	1.0	0.835	1.8	Normal & Shear
Tension waisted	0.545	-0.063	1.673	0.6288	1.444	Normal & Shear
Tension grooved	0.584	0.0	1.73	-	1.432	Shear
Erichsen	0.581	0.953	2.0	0.665	1.588	Normal & Shear
Shearing	0.723	-1.0	0.0	-	1.732	Shear

commonly shown as a function of stress-state parameters η and α (see Appendix A.6.1-A.6.3). The β-failure model is an enhancement of the failure orthotropic criterion for ductile normal fracture first presented in Equations (2.69) and (2.71) in Section 2.2.3.

$$\beta = \beta\left(\frac{\sigma_I}{\sigma_{vM}}, \eta_{MF}\right) = \frac{1 - s_{NF} \cdot \eta_{MF}}{\frac{\sigma_I}{\sigma_{vM}}}; \tag{4.10}$$

$$\varepsilon_{eq}^{**} = de^{(q\beta)}. \tag{4.11}$$

For the fitting of the fracture envelopes described previously in Section 2.2.3, the stress states are translated into the stress state parameters β and θ (see Equations (4.10) and (2.72)) with the help of material specific parameters s_{NF} and k_{SF}. This allows to convert an initially 3D problem, i.e. the fitting of a fracture surface w.r.t. two stress state parameters, of the stress triaxiality η and the parameter of the Lode angle ξ, to a 2D problem of fitting a line w.r.t. the corresponding stress state parameter [36]. This reduces the effort for the fitting of the analytical description by one dimension. The approximated parameters for the S355JR are summarized in Table 4.9 for the normal fracture on the right and shear fracture on the left. The results of these two modes of ductile fracture, the normal and the shear mode, are visualized with the fracture surfaces over the stress state parameters β and θ in Figures 4.8a and 4.8b with experimental strains. The curve fitting is realized by the method of least squares using all experiments. To further facilitate the approximation task of fracture curves in 2D, an additional value is introduced for the fitting of ductile normal fracture. For incompressible metals under triaxial tension, failure will occur at very low strains. With this assumption another fictive supporting point is introduced for triaxial tension ($\beta = -3s_{NF}$ with $\varepsilon^{**} = 0.015$) resembles a numerical zero. In Figure 4.8a, for instance, the difference between the fracture curve and the experimental value for tension with a hole is the most pronounced. This point cannot be improved without reducing accuracy elsewhere; in addition, further the uniaxial tension with a circular hole tends to fail not from the free edge of the circular hole but in a small distance from it under a higher stress triaxiality. A good accordance throughout all

Table 4.9.: Approximated parameters of the failure envelopes for the β- and θ-model for the ductile normal and shear fracture respectively

Ductile normal fracture	Ductile shear fracture
$s_{NF} = 0.1650$	$k_{SF} = 0.1$
$d = 0.1078$	$\varepsilon^{+}_{SF} = 0.6013$
$q = 2.5117$	$\varepsilon^{-}_{SF} = 2.1545$
	$f = 2.0233$

experiments can be found for the approximation of the ductile shear fracture (DSF) as displayed in Figure 4.8b. The coloring of experiments in the legends of Figures 4.8a and 4.8b reflects the fracture type observed in the experiments; it is summarized in the last column of Table 4.9: black for a mixed fracture mode between normal and shear fracture used for the calibrations of DNF and light gray for the shear fracture.

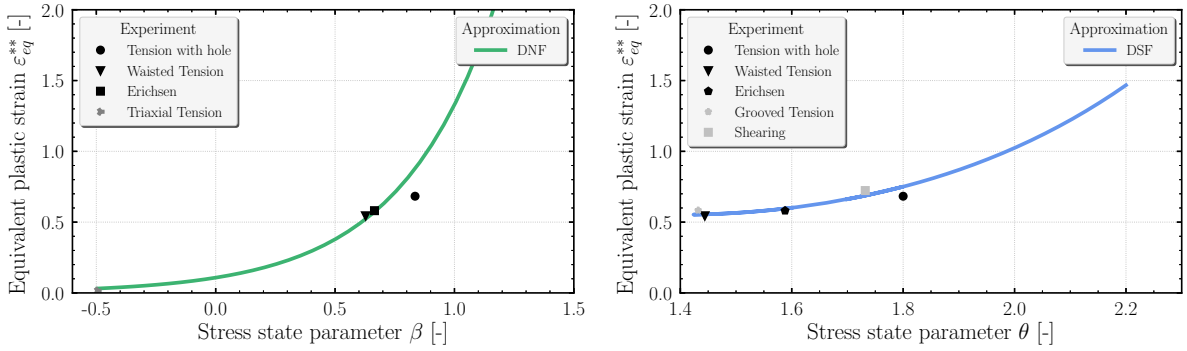

(a) β-model approximation for ductile normal fracture

(b) θ-model approximation for ductile shear fracture

Figure 4.8.: Comparison of experiments and approximation of analytical failure envelopes of the β and θ-model for the description of DNF and DSF respectively for S355JR with 1.5 mm thickness

The determined fracture curve can now be transformed back with the help of s_{NF} and k_{SF} into a 3D fracture surface related to the stress invariants stress triaxiality η_{MF} and Lode parameter ξ as displayed in Figure 4.9.

It is worth noting that most of the experimental points in Figure 4.10b populate a stress state between uni- and biaxial tension for η_{MF} ranging from 1.0 to 2.0. The shearing test is the only point outside this region. An additional uniaxial compression test would provide a supporting point for η_{MF} values smaller than zero. In the design of experiments for the material characterization, different specimens are chosen to explicitly evoke fracture under a certain stress state. These stress states are a-priori presumed for the geometry

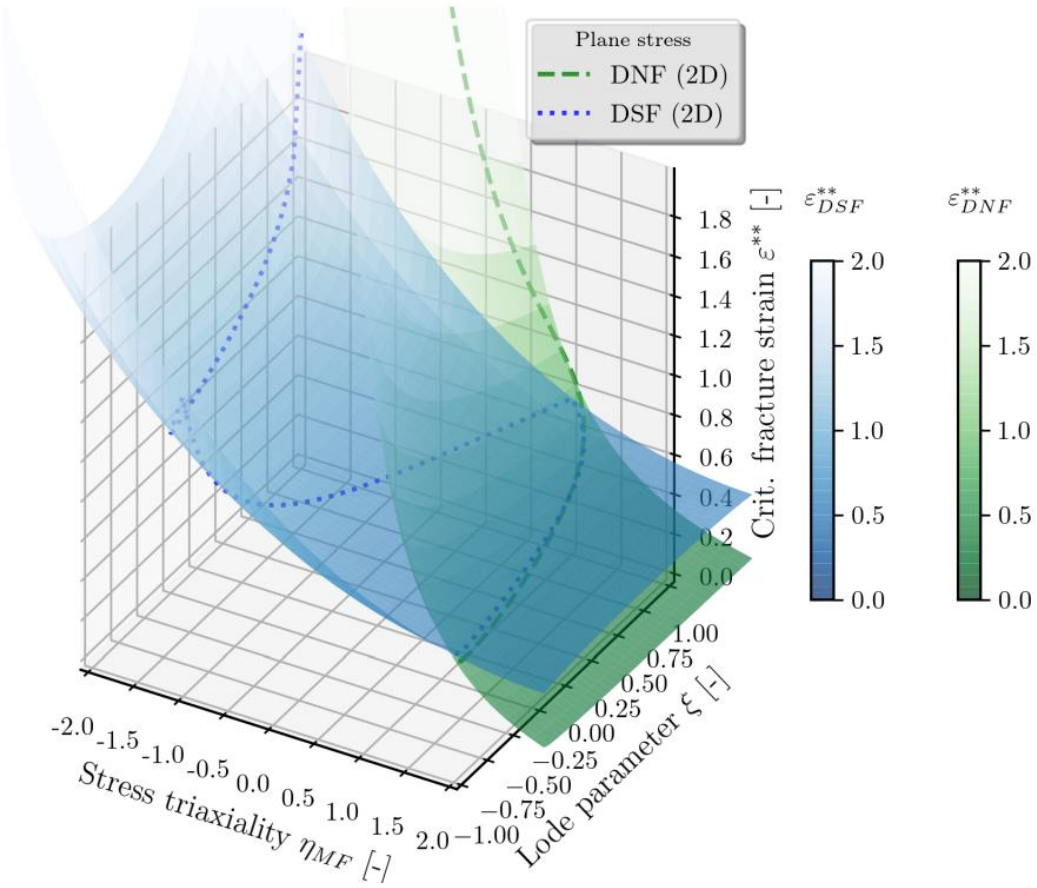

Figure 4.9.: Failure surfaces for ductile normal and ductile shear fracture over two stress invariants η_{MF} and ξ for S355JR with 1.5 mm thickness

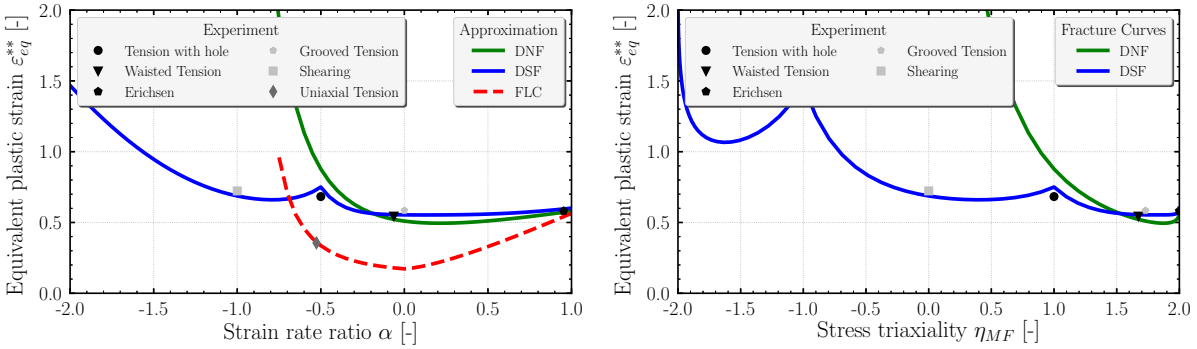

(a) Failure envelopes over strain-rate ratio α

(b) Failure envelopes over stress triaxiality η_{MF}

Figure 4.10.: Comparison of experiments and approximation of analytical failure envelopes of the β- and θ-model for the description of DNF and DSF respectively for S355JR with 1.5 mm thickness

but might drift strongly for higher deformation and very ductile materials throughout the loading history (see [131]).

The FLC is calibrated based on the experimental input of the uniaxial tensile tests as described in Section 2.2.3. It is displayed in a dashed red line together with the fracture curves and the experimentally measured supporting points in Figure 4.10a with respect to the strain-rate ratio α.

4.2.3. Simulation of material characterization tests

In the previous section, the material characterization is shown exemplarily for the S355JR. Based on physical experiments for different loading types and velocities material parameters are identified, which can be used either directly in the material card, as e.g. the elastic parameters, or for parameter fitting of different modules, e.g. plastic strain hardening or fracture limit curves. At the end of the material characterization, a material card for crashworthiness simulation is derived, which covers the full range of elasto-plastic material behavior including failure. In the last step, this material card is validated against the experimental force-displacement curves. A short summary which modules are activated for the simulation of the S355JR in MF GenYld+CrachFEM is given in Figure 4.11.

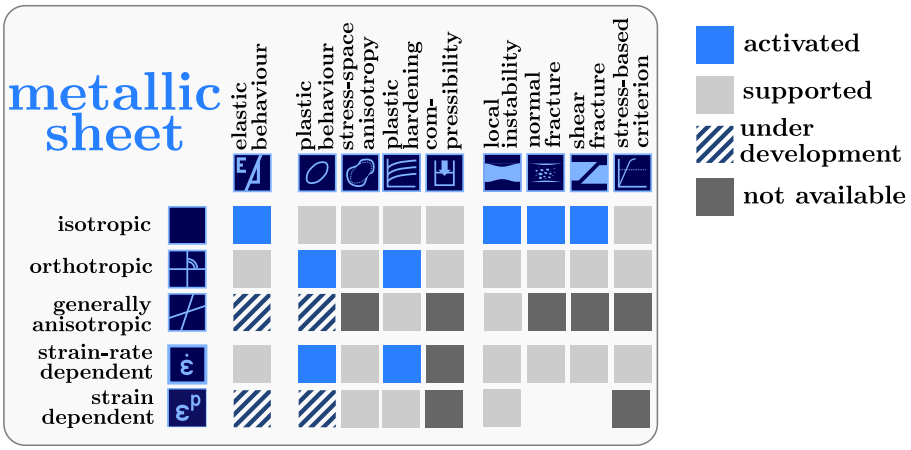

Figure 4.11.: Overview of the relevant modules in MF GenYld+CrachFEM for the simulation of thin-walled metallic sheets for the S355JR steel of 1.50 mm

In Figures 4.12a to 4.12d, the experimental force-displacement curves are displayed for different experiments. Two in-plane tensile tests with a waisted tension, as well as a tensile test with a groove under 90° and two out-of-plane loadings, a 3-point-bending and Erichsen test, are shown. Three replicates are conducted for every type of experiment which show little scatter considering a metallic material. For the validation, the force-displacement curves from the simulation are compared to those from experiments, as shown in Figures 4.13a to 4.13d. Technical drawings of the used specimens are provided

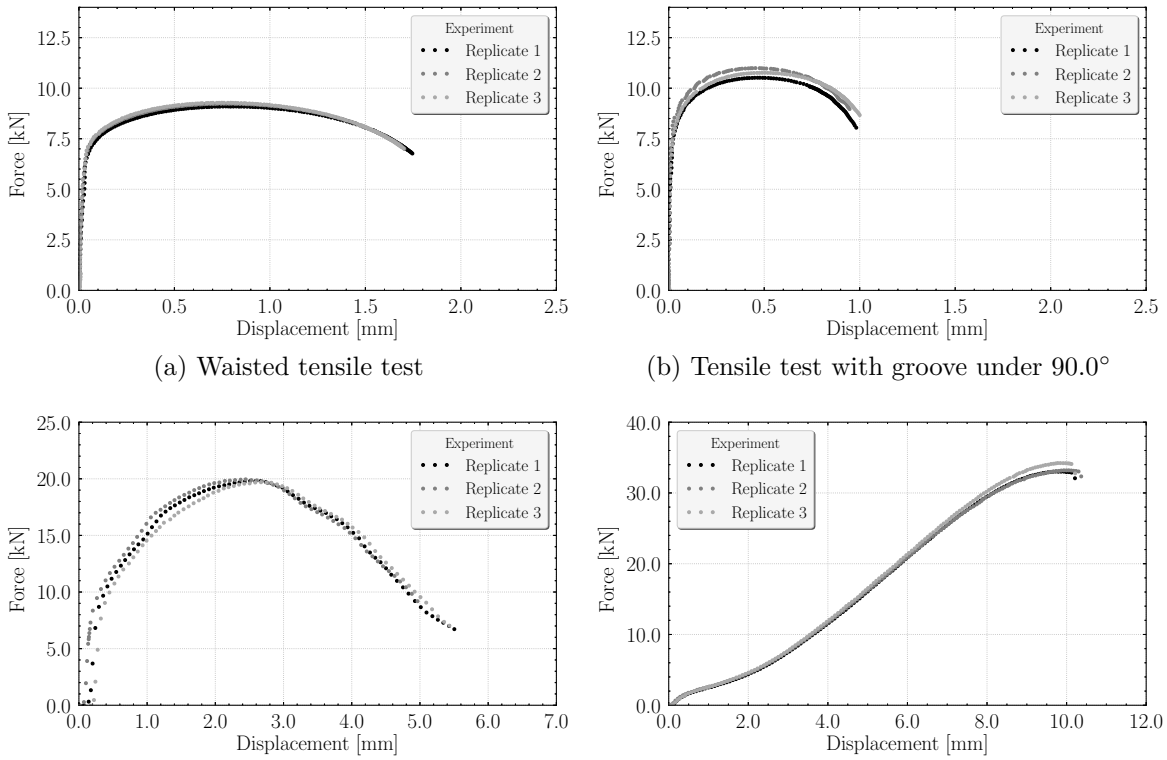

(a) Waisted tensile test

(b) Tensile test with groove under 90.0°

(c) 3-point bending test

(d) Erichsen test for biaxial tension under the pole

Figure 4.12.: Experimental force-displacement curves for multiple experiments of the S355JR steel with 1.50 mm thickness

in the Appendix A.4. The simulation uses not the nominal values but the measured dimensions of the specimens, e.g. thickness and width in the critical cross-section, averaged across all experimental replicates. For the simulation Abaqus Explicit Version 2018 is used in combination with the material model MF GenYld+CrachFEM Version 4.3.2. The specimens are discretized using the reduced integrated shell elements of type *S4R* with hourglass control and 5 integration points (IP) across the element thickness and continuum solid elements of type *C3D8R* with 5 elements across the critical cross-section. For the in-plane tension test the clamping on both sides is modeled as a rigid body. For the out-of-plane experiments the tools are modeled as a rigid body. Boundary conditions are applied to these rigid bodies via a velocity-time curve. Further, for the 3-point-bending test a contact formulation *pressure-overclosure=HARD* is used with a static and dynamic friction coefficient of a steel pairing of $\mu_{qs} = \mu_{dyn} = 0.15$. For the out-of-plane Erichsen test, a teflon tape is put between the plate and the punch to reduce friction and to assure a failure initiation at the pole, which is why in the simulation of this tests the friction coefficients are adapted accordingly to $\mu_{qs} = \mu_{dyn} = 0.05$. To reduce the simulation time, variable mass scaling for the most critical elements in the models is used. For the post-processing, nodes on the surface of the specimen representing the virtual gauge length

are used and a contact force or section force is evaluated for the out-of-plane or in-plane models, respectively.

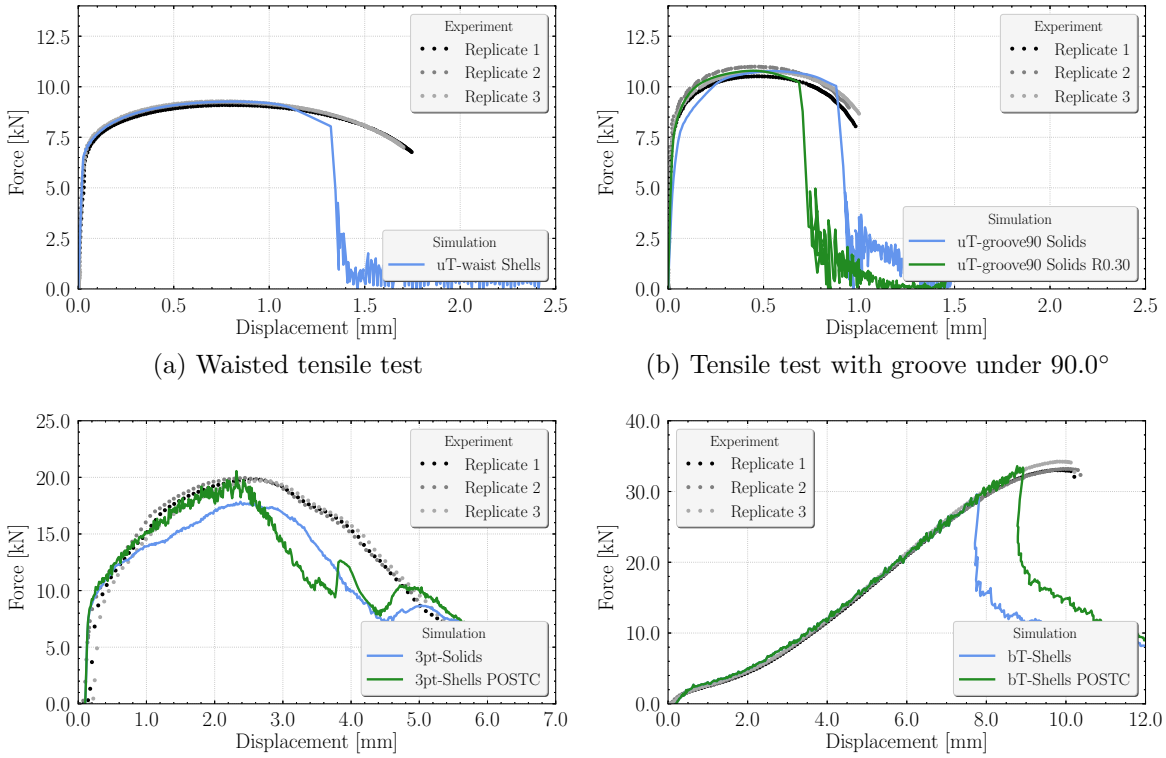

(a) Waisted tensile test

(b) Tensile test with groove under 90.0°

(c) 3-point bending test

(d) Erichsen test for biaxial tension under the pole

Figure 4.13.: Comparison of force-displacement-curves from experiment and simulation for the S355JR with 1.50 mm thickness.

The blue curves in Figures 4.13a to 4.13d display the simulation results of the previously described material card. For the simulation of the green curves for the out-of-plane experiments, 3-point bending and Erichsen, an additional post-critical module is activated emulating the crack propagation across the thickness by an excessive thinning of the shell thickness. This feature is only relevant for the out-of-plane experiments for which the critical element will be eliminated as soon as the extreme edge under tension reaches its failure limit.

For the evaluation, the force-displacement curves from the simulation are compared to the ones from the experimental replicates to assess the quality of the simulation results. Throughout the loading history of physical tensile and compression tests, the identified material parameters can be validated against the actual experiments for different stress states and loading velocities. Further, the most essential properties of the force-displacement curves relevant for the evaluation of crashworthiness load cases, like initial

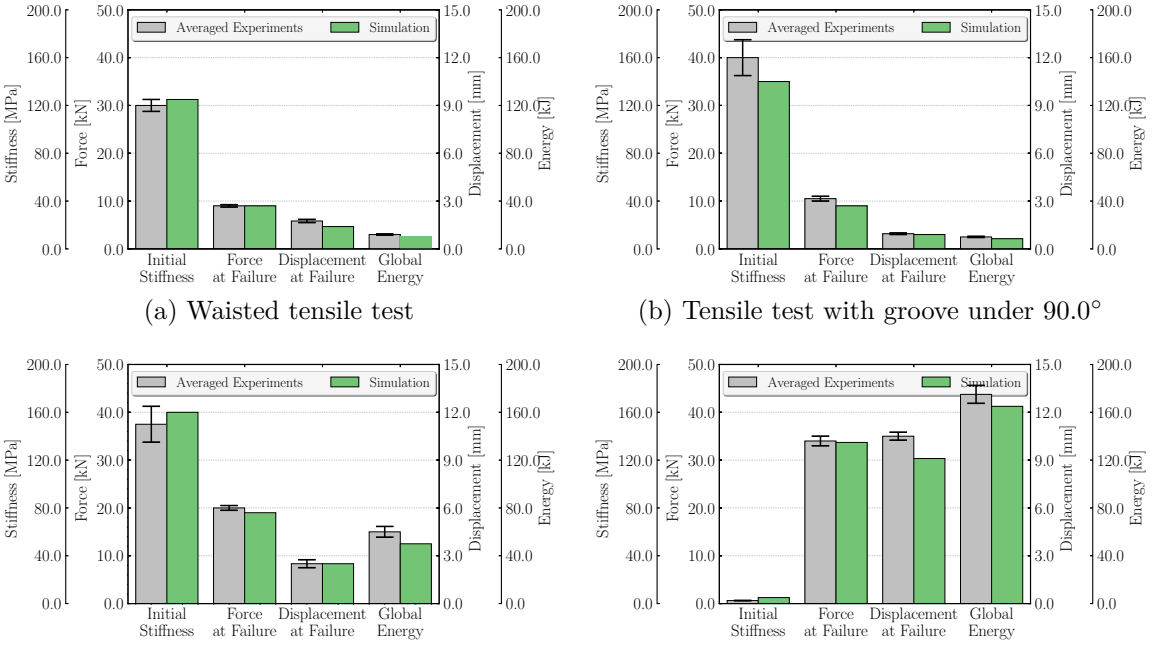

(a) Waisted tensile test

(b) Tensile test with groove under 90.0°

(c) 3-point bending test

(d) Erichsen test for biaxial tension under the pole

Figure 4.14.: Experimental validation of simulation results based on initial stiffness, failure strength and displacement at failure and global energy absorption

stiffness, force level, and displacement at failure initiation as well as the overall absorbed energy, are compared to the simulation results in the bar diagrams in Figures 4.14a and 4.14d. Here, the averaged values from the experimental replicates are displayed in gray together with the experimental scatter represented by the error bars in black and compared to the simulation results in green.

4.3. Material characterization of Tepex dynalite 102-RG600

In this section, the experimental material characterization and derivation of a material card is done exemplarily for an organic sheet. The organic sheet is an impregnated and consolidated semi-finished product which may consist of multiple laminae of 0.5 mm thickness each. For this characterization the product under the trade name Tepex® dynalite 102-RG600 from *Bond-Laminates* is considered in a set-up of 2.00 mm [2]. Embedded in a polyamide 6 matrix (PA6) are endless glass fibers of the E-type with a volume fraction of 47% (PA6-GF47). The architecture of the endless fibers is equally balanced in warp and weft direction with twill-weave bindings (see left side of Figure 4.15) without any additional reinforcement in the thickness direction. Table 4.10 summarizes the material properties of a single ply in accordance with the datasheet.

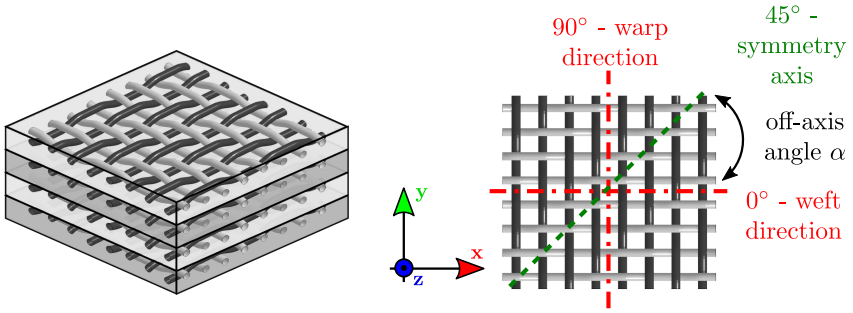

Figure 4.15.: Isometric view on a 4-layer stack-up (left) and schematic representation of the in-plane main axes of orthotropy and the off-axis angle α for the initial, i.e. undeformed configuration (right) for twill weaving structure

Table 4.10.: Material data of a single ply for Tepex® dynalite 102-RG600 for the thickness of $t = 0.5$ mm [2]

Laminate density	Fiber content	Tensile modulus	Tensile strength	Melting temperature	Glass transition temperature
ρ in t/mm^3	in % vol.	E_0 in GPa	σ_0^{**} in MPa	θ in °C	T_G in °C
1.80e-09	47.0	22.4	404.0	220.0	60.0

It is assumed here that the difference between strength in weft- and warp direction deviates by less than 2 %; this minor difference is considered negligible under the observed experimental scatter [55]. Assuming identical parameters in weft- and warp-direction for $\alpha = 0°$ or 90°, respectively, a symmetry axis at $\alpha = 45°$ allows to reduce the experimental characterization on loading for an in-plane off-axis angle between $\alpha = 0°$ and 45° (see right side of Figure 4.15).
For the material characterization four layers with a resulting thickness of t = 2.00 mm are used and it is assumed that the in-plane and out-of-plane stiffness are comparable. For

thinner layups of organic sheets this assumption may no longer be true because the Steiner contribution of fibre bundles no longer compensate one another and the kinematics of the cross section which no longer stay plane [124]. These effects necessitate a differentiation between in-plane and out-of-plane elasticity for layups thinner than t = 2.00 mm.

4.3.1. Experimental characterization of the organic sheet

The scope of the experimental characterization is summarized in Table 4.11 and small pictograms with the corresponding material orientation by an icon of the weaving structure are presented in Figure 4.16. Because of the symmetry for the fibers in weft- and warp-direction as displayed in Figure 4.15, the experimental scope for the characterization focuses on the off-axis loading in $\alpha = 0°$, 22.5°, and 45°. For the uniaxial tensile tests, oblique tabs are used at both ends of the rectangular specimen to avoid a superficial deterioration of the material due to clamping. Since the PA6-matrix shows significant dependency to moisture, the specimens were conditioned in a climate chamber prior to testing in order to account for the hygroscopic. An exposure of the specimen during 96 h at a relative humidity of 62% at a temperature of $T = 70°C$ in accordance with DIN EN ISO 1110 is supposed to simulate the exposure of composites for a single year after which the decrease in mechanical properties is saturated [132]. The elevated temperature ensures a relatively rapid water absorption. After conditioning, all experiments were conducted at room temperature (RT) $T = 23.0°C$ at relative humidity of approximately 50%.

Table 4.11.: Experimental scope for the material characterization of the organic sheet Tepex® dynalite 102RG600 with 2.00 mm thickness conditioned in accordance to DIN EN ISO 1110

Type of experiment	Off-axis angle α in °	Strain-rate $\dot{\varepsilon}$ in 1/s	Test standard	Dimension l in mm	w in mm	t in mm
Tension	0.0	0.001	ISO 527-4	250.0	15.0	2.0
Tension	22.5	0.001	ISO 527-4	250.0	25.0	2.0
Tension	45.0	0.001	ISO 527-4	250.0	25.0	2.0
Tension	0.0	0.025	ISO 527-4	250.0	15.0	2.0
Tension	45.0	0.025	ISO 527-4	250.0	25.0	2.0
3-Pt. Bending	0.0	0.001	ISO 178	80.0	25.0	2.0
3-Pt. Bending	45.0	0.001	ISO 178	80.0	25.0	2.0
Shearing	0.0	0.001	ASTM B831	100.0	60.0	2.0
Shearing	45.0	0.001	ASTM B831	100.0	60.0	2.0
Compression	0.0	0.001	ISO 604	10.0	10.0	4.0
Compression	45.0	0.001	ISO 604	10.0	10.0	4.0

The experiments were conducted at the facility of the project partner *Bosch* in Renningen and complimented by the shear specimen at partner laboratory *NewGenTechs* in Spain.

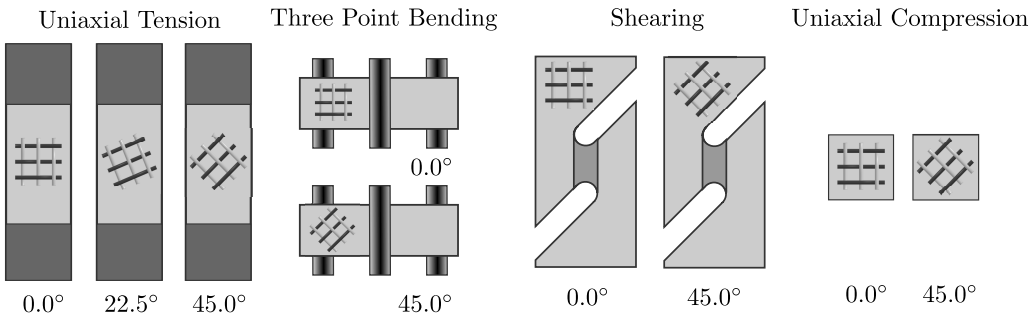

Figure 4.16.: Pictograms (not true to scale) for the experimental configurations including the textile orientation and the off-axis angle α.

The curves for all replicated experiments except of the 3-point bending the derived engineering stress s and strain e curves are displayed in Figures 4.17a - 4.17i with dots in different gray scales. An average curve across all replicates is further plotted together with the error bars for the force and displacement for the time of fracture initiation in the experiments in cyan color. For a lucid representation of the experimental replicates, pictograms of the type of experiment including orientation are added to the diagrams. In order to carve out the influence of fiber orientation on the type of experiment, the diagram axes are scaled uniformly. For obtaining engineering stress s the force normalized to the reference cross section of the notch. The biggest experimental scatter can be observed for the ASTM-type shear specimen in 0° orientation. For all other experiments, the scatter lays in a reasonable range across all experimental replicates without any remarkable outliers. Hence, the statistical average value also with only three experimental replicates is found to be a good representation for the different type of experiments. For the uniaxial tensile and shear test, the displacement is evaluated with tactile measures on the specimen and landmarks of the grayscale pattern, respectively. For the 3-point bending and uniaxial compression test, landmarks on the tools as close as possible to the specimen are used for the evaluation of the displacement. The local measure avoids to include the machine rigidity in the signal ensuring to capture only the mechanical response of the material. The ASTM-shear specimen, originally designed for ductile metals, is used in this study because it can be clamped and tested in a uniaxial tensile testing machine without any additional clamping devices. Due to the heterogeneous structure of the organic sheet, the deformation commenced in the designated notch of the shear specimen, represented as the dark gray area in the middle of the pictogram in Figure 4.16, but moved out of the notch for higher deformations. This explains also the pronounced experimental scatter of the shear specimen under 0° displayed in Figure 4.17f.
For the material characterization, local properties as the stress-strain relationship are derived. However for validation of the material card force-displacement curves from experiments represent a more global and stringent check-up. Not only is a precise definition of boundary condition for the clamping relevant here, but also local phenomena as e.g. strain localization in the matrix will be included.

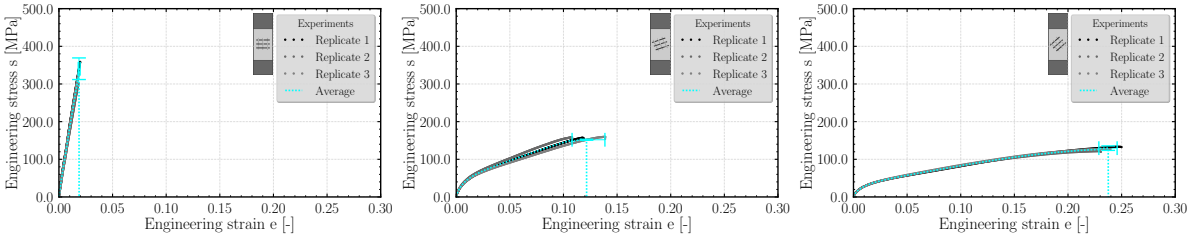

(a) Uniaxial tension 0.0° qs. (b) Uniaxial tension 22.5° qs. (c) Uniaxial tension 45.0° qs.

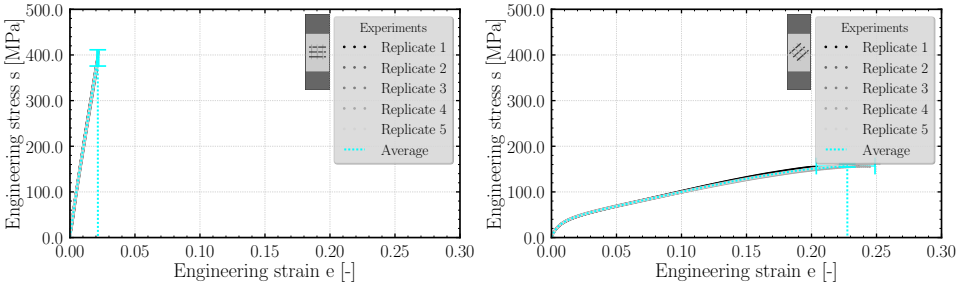

(d) Uniaxial tension 0.0° dyn. (e) Uniaxial tension 45.0° dyn.

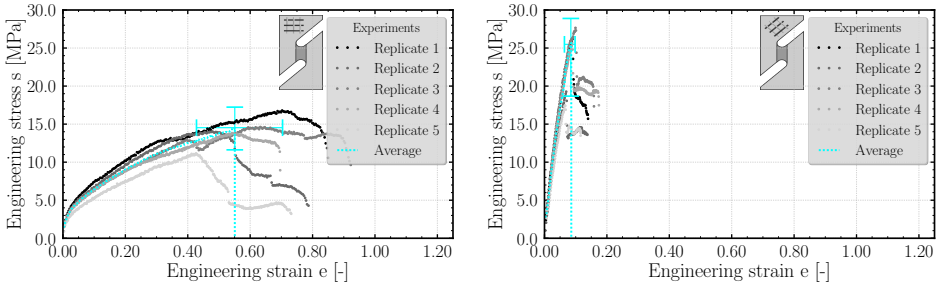

(f) Shearing 0.0° qs. (g) Shearing 45.0° qs.

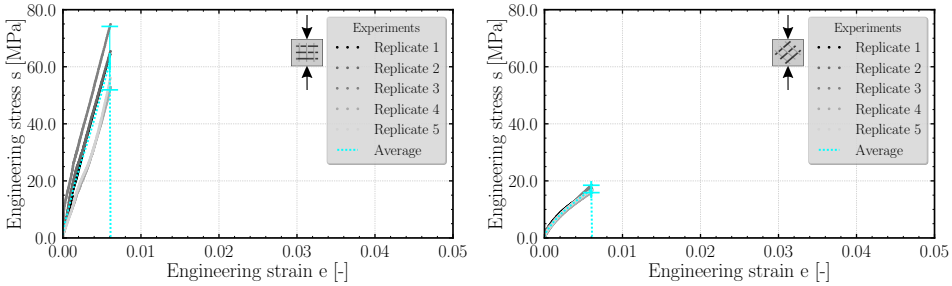

(h) Uniaxial compression 0.0° qs. (i) Uniaxial compression 45.0° qs.

Figure 4.17.: Engineering stress-strain curves of various quasi-static (qs.) and dynamic (dyn.) experiments including the averaged experimental curves (in cyan color)

For the uniaxial tensile experiments the testing velocity was increased by a factor of 25 between the slow experiments and the ones at elevated speed. Already with this small change an increase in the fracture strength under 0° can be observed by comparing the force-displacement curves from Figure 4.17a to 4.17d. An increase in the force level as well as a slight decrease in the fracture strain can also be observed in comparing the curves for the uniaxial tension under 45°. The three point bending tests were conducted in accordance with DIN EN ISO 178 with a punch radius of $r_p = 5.0\,\text{mm}$, a support radius of $r_s = 2.0\,\text{mm}$, and a free distance of $d = 64.0\,\text{mm}$ between the supports. Under 0°-orientation, failure can be initiated under tension as indicated by the drop of force in Figure **??**. Whereas the experimental set-up was not critical enough to also initiate failure under the ductile 45°-orientation, the specimen eventually slipped through the supports.

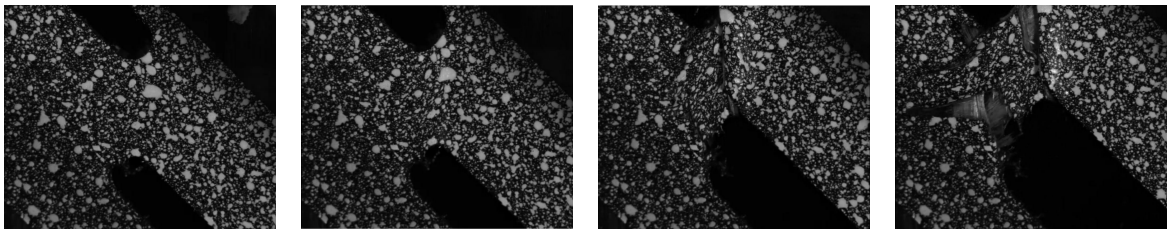

(a) Initial state x = 0.0 mm (b) Deformed state x = 1.63 mm (c) Deformed state x = 5.37 mm (d) After rupture x = 5.95 mm

Figure 4.18.: Sequence of the gray-scale pattern on the backside around the notch for different deformation states of the first replicate for shearing under 0°

For the shear specimens, failure initiated in the designated shear zone in form of a notch with half the thickness of the remaining specimen; but the deformation did not remain in this zone and started to propagate out of the notch. Figure 4.18 displays in a sequence of pictures the deformation state throughout the experiment for the first replicate of the shear specimen under $\alpha = 0°$. The displacement is measured on two landmarks outside the notch and corresponds to the force-displacement curves of Figure 4.17f. Upon loading, the deformation commences in the designated notch, but soon the endless fibers in the remaining cross-section move out of this zone of half sheet thickness into the rest of the specimen. Unfortunately, this specimen did not work as originally designed for a shearing of the organic sheet as the deformation did not remain within the notch. For future work the author recommends a V-notched rail shear (VNRS) specimen in accordance with the ASTM 7078 norm modified by a rectangular zone in the middle of the specimen with the smallest cross-section. This proposed geometry will allow not only to reduce the manufacturing influence, but will also result in a shear deformation in its middle upon loading.

Lastly, for the uniaxial compression test, small specimen dimensions were deliberately chosen to obtain the force-displacement curves until higher deformations. Even with the small geometrical dimensions listed in Table 4.11 the front faces for force application were ground plane-parallel and a lubrication using molybdenum disulphide was applied to

minimize the influence of friction. Despite these measures to ensure a stable deformation under compressive loading, the small samples failed pre-maturely under inter-laminar delamination between the four layers. To avoid this premature delamination in a compression test cube in the future, a higher width of the specimen is proposed, but with the same height, in order to keep the risk against buckling under compression as small as possible.
The proposed experimental campaign for the organic sheet focused on the in-plane properties and was realized to validate the structural simulation. Other experimental types which can be found in literature for the material characterization of textile reinforced semi-finished products are not as relevant in this context. With the bi-axial tension the mutual interference of weft and warp direction can be analyzed [55]. To record the compaction in thickness direction or the shear force over the shear angle during a picture frame test are relevant for forming simulation of textiles, for which shear deformation represents the main deformation mechanism [47, 81].

4.3.2. Derivation of material card

The experimental characterization proposed in Section 4.3.1 serves as an input to derive a material card in MF GenYld+CrachFEM for the organic sheet. This material card will be fully elasto-plastic with anisotropic hardening and combine a stress- and a strain-based failure criterion with a positive and negative strain-rate effect for the failure initiation of the fibers and matrix, respectively. The derivation of the material card is explained in detail in this Section 4.3.2 and an overview of the material card at hand is shown in Appendix A.6.3. The findings of the material modeling are also included in the publications [133, 119].

Table 4.12.: Elastic parameters of the Tepex® dynalite 102-RG600

Density	Young's modulus	Shear modulus	Bulk modulus	Poisson's ratio
ρ in t/mm^3	E_{00} in MPa	G in MPa	K in MPa	ν in -
1.80e-09	18,300.0	8,333.0	9,090.0	0.1

$$E(\alpha) = \frac{\sigma(\alpha)}{\varepsilon(\alpha)} = \left(\frac{\cos(\alpha)^2 \cos(2\alpha)}{E_{00}} - \frac{\sin(\alpha)^2 \cos(2\alpha)}{E_{90}} + \frac{\sin(2\alpha)^2}{E_{45}} \right)^{-1}. \tag{4.12}$$

The elastic properties for the organic sheet at hand are listed in Table 4.12 in fiber direction. The Young's modulus of the thermoplastic composite is dependent on the orientation and strain-rate. To account for the orientation dependency, the in-plane orthotropy of the Young's modulus will be approximated using Equation (4.12) based on three experimental supporting points E_{00}, E_{45}, and E_{90}. To further account for the strain-rate

dependency, a module for visco-elasticity[2] allows to define the in plane orthotropy for multiple strain-rates. For the organic sheets the characteristics in dependence on the off-axis angle α are displayed for two different strain-rates $\dot{\varepsilon} =$, 0.0001 1/s and 1000.0 1/s in polar diagrams in Figure 4.19.

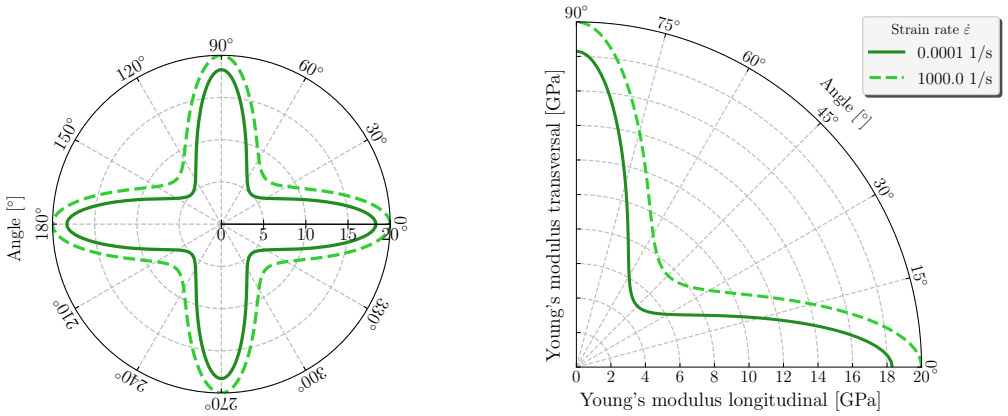

(a) In-plane orthotropy (b) Detailed view in the first quadrant

Figure 4.19.: Visualization of the viscoelasticity module defined using three supporting points in MF GenYld+CrachFEM for Tepex® dynalite 102-RG600 for two different strain-rates

The effective material behavior, as it can be measured in experiments, will be described in a smeared manner, homogenizing the properties of its two constituents, fiber and matrix, on a macroscopic scale. Originating from the ductile thermoplastic PA6-matrix, plastic strain hardening can be observed under multiple stress states and off-axis loadings. Therefore, a general 3D yield surface is used to model the onset of yielding depending on the stress state. In between the yield point and the point of fracture initiation, plastic strain hardening is assumed. This plastic strain hardening - also referred to as diffuse damage of textile reinforced composites [120] - describes the pre-failure non-linearities by accumulating the yielding of the matrix and damage mechanism on lower scales.
For the evaluated yield stresses for the organic sheets the yield criterion in accordance with Hill1948 showed the best agreement [134]; it is given for the plane stress state in Equation (4.13.2). σ_{eq} represents here the equivalent stress under uniaxial tension.

$$f(\sigma_{ij}) = 0. \tag{4.13.1}$$

$$(1 - a_x) \cdot \sigma_x^2 - 2 \cdot a_z \cdot \sigma_x \cdot \sigma_y + (1 - a_y) \cdot \sigma_y^2 + 2 \cdot a_{xy} \cdot \tau_{xy} - \frac{2}{3} \cdot \sigma_{eq}^2 = 0. \tag{4.13.2}$$

[2]This is a simplified module for visco-elasticity, approximating the strain-rate dependencies for monotonous loadings. In comparison with a full-fledged module for visco-elasticity, which includes the feedback of the strain-rate, viscous effect, e.g. for a stress relaxation during a springback cannot be accounted for.

Table 4.13.: Approximated r-values for the Hill1948 yield locus formulation

Longitudinal	Diagonal	Transverse
r_0 in -	r_{45} in -	r_{90} in -
0.482	564.589	0.482

$$a_x = \frac{r_0}{r_0 + r_{90} + r_0 r_{90}}, a_y = \frac{r_{90}}{r_0 + r_{90} + r_0 r_{90}}, \text{ and } a_{xy} = (a_x + a_y)(1/2 + r_{45}) \tag{4.14}$$

The anisotropy parameters a_x, a_y, and a_{xy} for the Hill1948 yield locus formulation (see Equation (4.13.2)) are calculated from the r-values r_0, r_{45} and r_{90} based on the Equations (4.14); because they must fulfill the condition $a_x + a_y + a_z = 1.0$, the missing value a_z can be determined.

Table 4.14.: Orthotropy values for Hill1948 yield locus

a_x	a_y	a_z	a_{xy}	a_{yz}	a_{zx}
in -	in -	in -	in -	in -	in -
0.4029	0.4029	0.1942	455.35	1.0	1.0

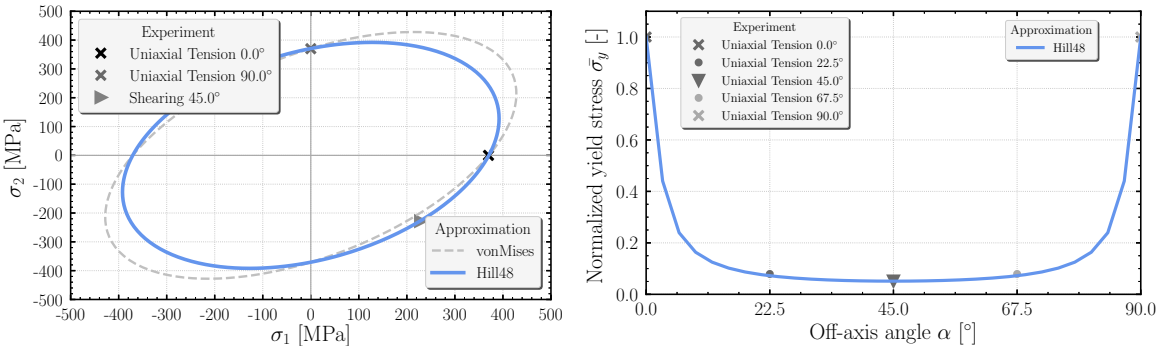

(a) Trace of the approximated yield locus and the measured yield strength for various stress states in the σ_1-σ_2-plane

(b) Normalized yield strength in dependence on the off-axis angle α

Figure 4.20.: Comparison of experimentally measured yield strength and the analytically approximated Hill1948 yield locus in dependence on the stress state (left) and off-axis angle (right)

Figure 4.20a displays the approximated values for the orthotropic Hill1948 yield locus formulation together with the experimentally measured yield stresses from uniaxial tensile tests under different orientations and an isotropic vonMises yield locus. The extreme drop of the yield stress from fiber direction $\alpha = 0$ to an off-axis orientation more dominated by the PA6-matrix is displayed in a normalized manner in Figure 4.20b. Hence, the yield stress is modeled as a function of the off-axis direction α and the plastic strain hardening depending on the stress state. The shape of the Hill1948 yield locus with the approximated r-values from Table 4.13 is visualized in Figure 4.21a. This flat shape of

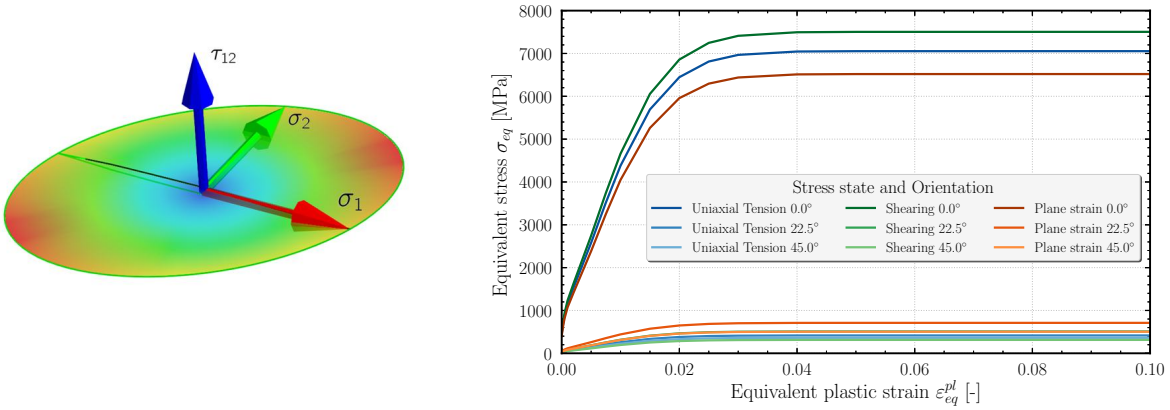

(a) 3D yield locus representation for plane strain stress state defined by σ_1, σ_2, and τ_{12}

(b) Plastic strain hardening behavior for stress states of uniaxial tension, shearing and plane strain off-axis orientation in $\alpha = 0°, 22.5°$, and $45.0°$ for strain-rate $\dot{\varepsilon} = 0.01$ 1/s.

Figure 4.21.: 3D-yield locus (left) and stress-state dependent plastic strain hardening (right)

the yield locus represents a relatively low yield stress under shearing τ_{12} compared to tension in one of the main axis σ_1 or σ_2 along the fibers. To illustrate the influence of the stress-state and the loading in an off-axis direction designated by α, the σ_{eq}-ε^{pl}_{eq} graphs are displayed for uniaxial tension, shearing, and plane strain for three different orientations $\alpha = 0°$, $22.5°$, and $45°$. For obtaining a plastic strain hardening curve, the measured force-displacement curves from uniaxial tensile tests in α= 0° and 45° are merged and approximated. The best approximation for the experimental input at hand is found for an extended formulation of Hocket-Sherby as given in Equation (4.15). The optimal parameters for the analytical approximation are summarized in Table 4.15.

$$\sigma_{eq}(\varepsilon) = a - (a - \sigma_0) \cdot \exp(-c\varepsilon^n_{eq}) + r\exp(-q\varepsilon_{eq}). \tag{4.15}$$

Table 4.15.: Parameters of the plastic strain hardening for the Hocket-Sherby formulation

a	σ_0	c	n	r	q
in MPa	in MPa	in -	in -	in MPa	in -
7,500.0	1,705.489	7,012.97	1.976	-1,303.81	750.0

The strain-rate sensitivity of the Tepex® dynalite 102-RG600 is evaluated based on uniaxial tensile experiments at two different strain-rates, $\dot{\varepsilon}$=0.001 and 0.025 1/s. Therefore, a constant m-value of $m = 0.035$ is found for the range between $\varepsilon^{pl}_{eq} = 0.001 - 0.015$. To obtain the plastic strain hardening behavior for all other strain rates as displayed

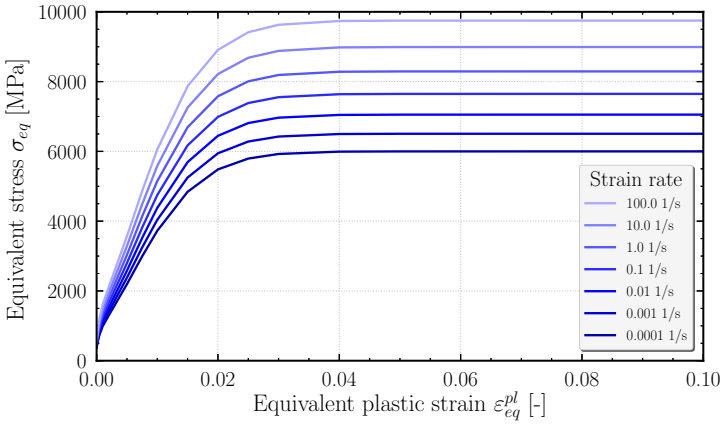

Figure 4.22.: Array of curves representing the strain-rate dependent plastic strain hardening behavior in reference direction for $\alpha = 0°$

in the array of curves in Figure 4.22, the found reference hardening curve is multiplied by a factor obtained from Equation (4.16). This factor is determined by the ratio of target ε to the reference strain-rate ε_{ref} to the power of m, where the reference strain rate $\varepsilon_{ref} = 0.0011/s$ equals the strain rate for which the quasi-static reference hardening curve is obtained by the Hocket-Sherby formulation. Using the natural logarithmic law expressed in Equation (4.16) supposes that the characteristic of the reference plastic strain hardening curve remains constant at different strain-rates. The strain-rate dependency of the plastic strain hardening is represented in this array of curves for the reference direction $\alpha = 0°$ extrapolated beyond the point of failure initiation. Because the elastic part of the strain is no longer negligible compared to the plastic part for reinforced thermoplastics, the total strain-rate is based on the sum of the two as represented in Equation (4.17).

$$\sigma_{eq}\left(\dot{\varepsilon}\right) = \sigma_{ref}\left(\varepsilon\right) \cdot \left(\frac{\dot{\varepsilon}}{\dot{\varepsilon_{ref}}}\right)^{m}; \tag{4.16}$$

$$\dot{\varepsilon}_{tot} = \dot{\varepsilon}_{el} + \dot{\varepsilon}_{pl}. \tag{4.17}$$

Depending on the load direction, organic sheets exhibit a linear elastic material behavior characteristic for brittle composites in $\alpha = 0°$ and a non-linear ductile behavior in $\alpha = 45°$ direction. In order to meet the needs of these differently pronounced material properties, a combination of a strain- and a stress-based failure criterion is proposed here. This allows to use the more sensitive metric as a threshold measure for the respective directions as displayed in Figure 3.2 in Section 3.5. The stress-based criterion is the more sensitive measure for the brittle fiber-dominated direction and the strain-based criterion the more sensitive one with respect to the ductile direction dominated by the thermoplastic matrix. The traces of the yield and fracture locus are plotted in the σ_1-σ_2-plane in Figure 4.23. For the loading under tension and shearing in the second and fourth quadrant, the yield locus is cloaking the fracture locus. This means that the critical fracture stress σ^{**} is met prior to yield stress σ_0 and fracture is initiated before plastic strain hardening takes

place. This is the case for tension under $\alpha = 0°$ initiating a brittle failure of fibers, as displayed exemplarily in Figures 4.17a and 4.17d.

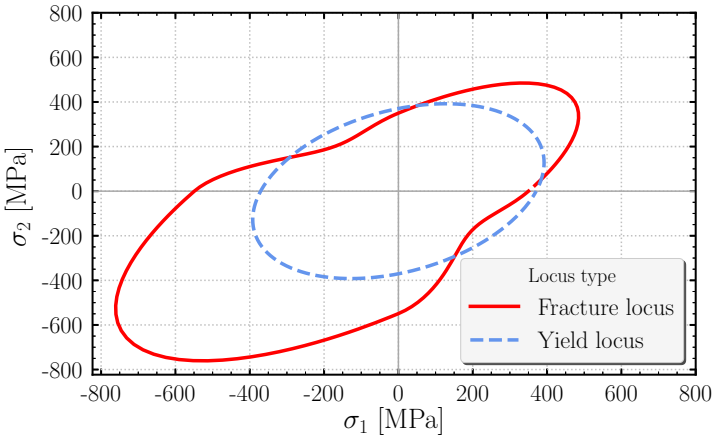

Figure 4.23.: Traces of an orthotropic yield locus Hill1948 and fracture locus based on a transverse isotropic Hill1948 formulation with a tension-compression asymmetry

For the fracture locus, a transverse isotropic Hill1948 formulation is used with a geometrically averaged r-value of $r_{avg} = 2.25$ and a tension-compression asymmetry of 0.5. The latter describes a fracture stress under compression by a factor two higher than under tension. The previously described shape of the fracture locus is scaled with a quasi-static fracture stress $\sigma^{**}(\dot{\varepsilon} = 0.01\,1/s) = 350\,\text{MPa}$ and displayed in red in Figure 4.23. To account for the positive strain-rate sensitivity the dynamic fracture stress is defined as $\sigma^{**}(\dot{\varepsilon} = 100.0\,1/s) = 675\,\text{MPa}$. In between these supporting points, fracture stresses are obtained via linear interpolation resulting in different sizes of the fracture locus with a constant shape as displayed in dashed red lines in Figure 4.24a.

Table 4.16 summarizes the experimentally measured fracture strain ε^{**} for different stress states and orientations. These values serve as supporting points for the approximation of the ductile fracture criterion as displayed in Figure 4.24b. The failure locus in stress-space is modeled isotropic assuming the same fracture stress for the fibers in weft- and warp direction as displayed in Figure 4.25a and the strain-based criterion orthotropic as displayed in Figure 4.25b. In both figures, the approximation in solid lines is compared to the experimental values used as supporting points for the parameter fitting.

Table 4.16.: Experimentally measured, quasi-static fracture strain ε^{**} for Tepex® dynalite 102-RG600 for different stress-states and off-axis loadings

Experiment			Tension	Shearing	Compression	3-Point Bending
Stress triaxiality η_{MF}		in -	-1.0	0.0	1.0	1.73
Orientation	$\alpha = 0.0°$	in -	0.01294	0.02745	0.0001	0.000087
	$\alpha = 45.0°$	in -	0.20448	0.577	0.1758	0.04052

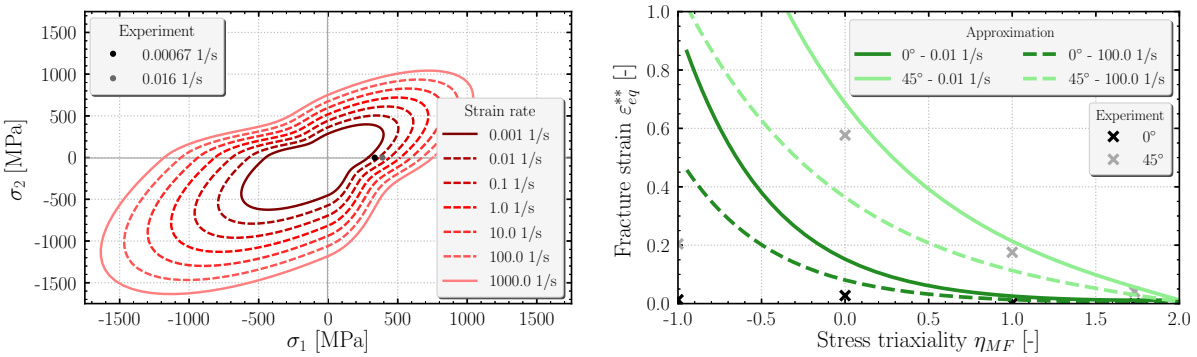

(a) Visualization of strain-rate dependent fracture locus in the σ_1-σ_2-plane.

(b) Ductile normal fracture limits depending on the stress triaxiality η_{MF} for the 0°- and 45°-directions.

Figure 4.24.: Comparison of the experiments and the analytical approximation for the stress-based (left) and strain-based (right) failure criteria in the fracture diagrams for Tepex® dynalite 102-RG600.

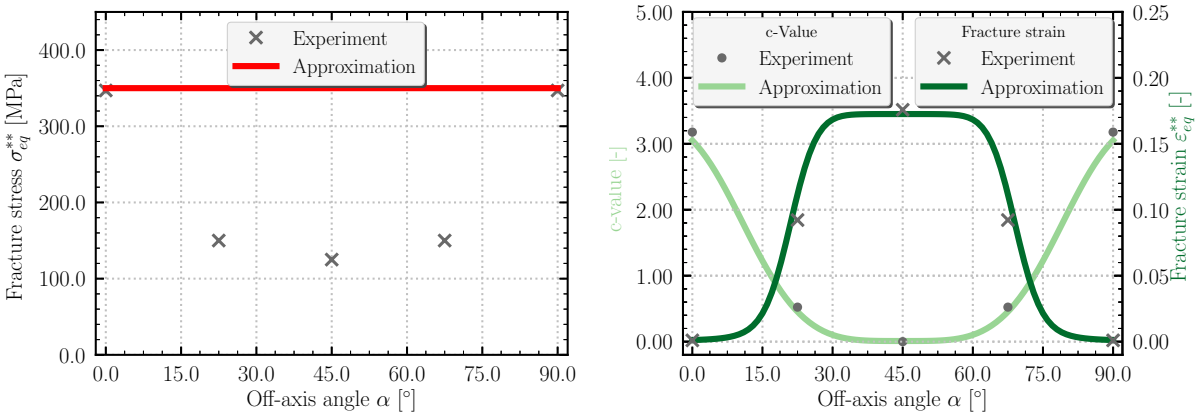

(a) Approximation of fracture stress for the stress-based failure criterion

(b) Approximation of fracture strain for the strain-based failure criterion

Figure 4.25.: Stress- and strain-based fracture criteria depending on the off-axis angle α

The different strain-rate sensitivities for the two constituents of organic sheets, fiber and matrix, are outlined in Section 3.3. They can be represented here with the definition of two separate failure criteria for the Tepex® dynalite 102-RG600. In order to account for the orthotropy of the strain-based failure criterion, an extension for ductile normal fracture, (Equation (2.71)), is used with a function $c(\alpha)$ (Equation (3.1)). Whereas the slope of the curve in Figure 4.24b displays the dependence of the fracture strain on the stress state, the Figure 4.25b shows the dependence of the value c and fracture strain ε_{eq}^{**} on the off-axis angle α. In both Figures 4.25a and 4.25b, which display the dependence of the stress- and strain-based failure criterion on the off-axis angle α, the geometrical

Table 4.17.: Parameters for the ductile normal fracture of Tepex® dynalite 102-RG600

Strain-rate $\dot{\varepsilon}$	ε_T^+	ε_T^-	a_0	a_1	a_2	a_3
in 1/s	in -	in -	in -	in -	in -	in -
0.01	0.02	0.5011	0.00	0.05711	-10.3952	0.7854
100.0	0.01	0.265	0.00	0.05711	-10.3952	0.7854

symmetry plane for the axis at $\alpha = 45°$ is evident. This symmetry axis is initially introduced at the beginning of this chapter on the right side of Figure 4.15.

4.3.3. Simulation of material characterization tests

Using the derived material card as described in Section 4.3.2, simulations are conducted to validate the material card on the experimental input. The force-displacement curves for all experimental replicates at hand are displayed in gray tones and the simulation results are plotted in green in the same diagrams in Figures 4.27a - 4.27k. All simulations are conducted with shell elements with reduced integration of type S4R with an average element length of 3.00 - 5.00 mm, except of the compression tests which are discretized using the reduced integrated hexahedron elements of type C3D8R with 1.00 mm length. The in-plane off-axis orientation of the endless fibers are defined using the keyword **Orientation* and passed to the **Shell section*. For the modeling of clamping with oblique tabs for the uniaxial tensile tests, there exists no robust and easy solution. Modeling the area of the specimen as a rigid body is too stiff compared to reality where minor deformations between the rectangular stripe of the specimen may occur depending on the pressure of clamping, adhesive, and type of material for the oblique tabs. Moreover, the rigid body may lead to a stress singularity between the clamping and deformable specimen which can trigger a premature failure of the stress-based criterion. To mitigate this effect, a velocity boundary condition in longitudinal direction is applied on all nodes in the clamping area and the transversal displacement is only prohibited for the last two rows. For the post-processing of the bending and compression force, the reaction forces of the tools are used and the section force for the tension and shearing. For all simulations, *Abaqus explicit* 2020 is used and coupled with MF GenYld+CrachFEM v.432. Figure 4.26 displays the combination of activated modules for the simulation of the organic sheet of type Tepex® dynalite 102RG600 in MF GenYld+CrachFEM.

The comparison of the force-displacement curves from experiment and simulation in Figures 4.27a - 4.27k show a good consistency not only for the initial stiffness but also for the deformation until failure initiation. A good accordance of the obtained material card can be seen across all considered off-axis angles and testing velocities for both in- and out-of-plane loadings. The markers on the force peak in the diagrams indicate whether the failure initiation is triggered by a fiber failure (○) or matrix failure (×).

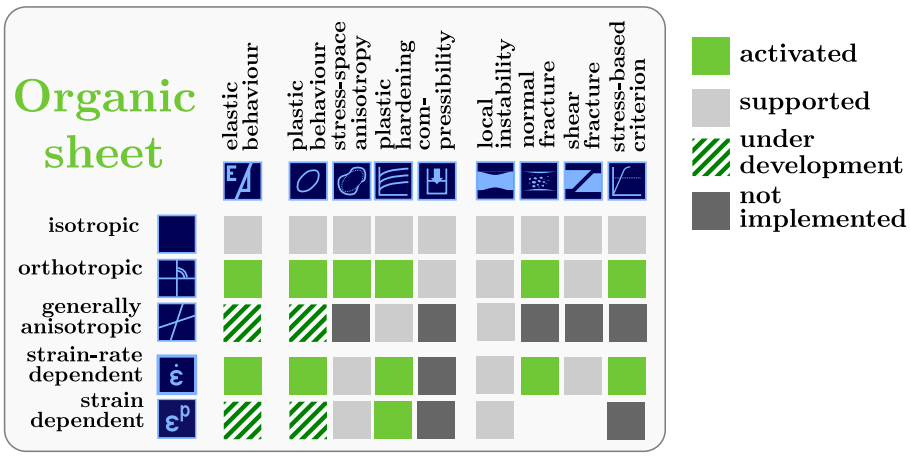

Figure 4.26.: Overview of the relevant modules in MF GenYld+CrachFEM for the simulation of organic sheets applied for the 102RG600 Tepex® dynalite of 2.00 mm

Across all simulations, the computational time is about 1.5 times higher than with an Abaqus internal IDS-material card averaged across all simulations on specimen level. Even though mainly in-plane experiments are used for the material characterization of the organic sheet, the material is fully compatible with a general 3D stress state meaning it can be used for the simulation of not only shell but also solid element formulations.

The fracture initiation by either one of the two envelopes in stress or strain space focuses on the in-plane fracture with the application for mainly thin-walled structures. After the failure threshold is reached for either one of the criteria at hand, the respective element can be eliminated from the simulation run to display the onset of failure. This procedure reaches its limits for the delamination occurring under uniaxial compression. Even though it would be possible to include also the experimentally measured strain under compression in the parameter fitting for the ductile normal fracture criterion, the degradation associated with the delamination failure can currently not be covered. An approach to incorporate the degradation on a macroscopic scale would be to reduce the out-of-plane shear stiffness correction term for shell elements. The delamination caused by either out-of-plane tension or shear stresses can currently not be accounted on the smeared, macroscopic level and requires to model the laminates and their interfaces on a mesoscopic scale. The phenomenological description of the failure envelopes in stress- and strain-space covers the onset of failure characterized by the force peak in the force-displacement curves. However, since the damage and failure mechanisms of endless reinforced thermoplastics are very complex, as outlined in Section 3.1, they can exhibit a pronounced post-critical behavior. This post-critical behavior is the domain between the failure initiation at the force peak on coupon level and the final collapse of the structure, representing a total rupture. Since this post-critical domain may have a significant contribution to the overall capacity of energy absorption, it would be beneficial to account for it as well.

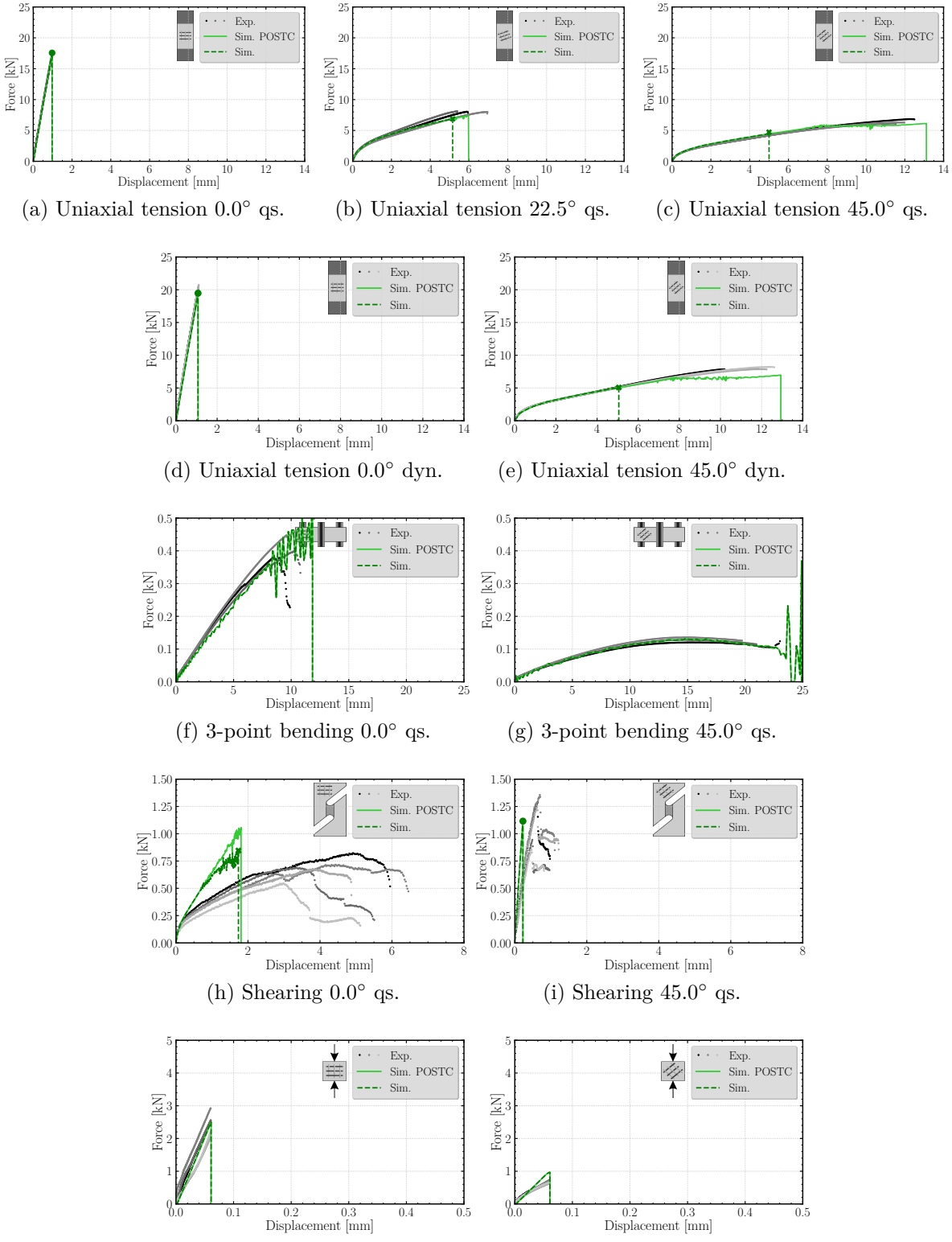

(a) Uniaxial tension 0.0° qs. (b) Uniaxial tension 22.5° qs. (c) Uniaxial tension 45.0° qs.

(d) Uniaxial tension 0.0° dyn. (e) Uniaxial tension 45.0° dyn.

(f) 3-point bending 0.0° qs. (g) 3-point bending 45.0° qs.

(h) Shearing 0.0° qs. (i) Shearing 45.0° qs.

(j) Uniaxial compression 0.0° qs. (k) Uniaxial compression 45.0° qs.

Figure 4.27.: Comparison of the force-displacement curves from experiment and simulation under various loading types for the Tepex® dynalite 102-RG600

5. Mechanical modeling aspects of hybrid joints

Hybrid material pairings entail several issues in the common interface because of the nature of the two dissimilar materials. The most commonly known is the delta-alpha problem displayed schematically in Figure 5.1a. The different thermal expansion coefficients may induce severe miss-fit stresses in the adhesive interface with elevated temperature gradients which may cause warpage, optically visible wrinkles or even ultimately failure. In a similar manner in the context of crash simulation, misfit stresses may be caused upon loading in the elastic as well as in the plastic regime for adhesive joints (see Figure 5.1b). Free edge stress singularities may originate at the common interface of the joint with two dissimilar materials with a high property mismatch in the elastic as well as the plastic region.

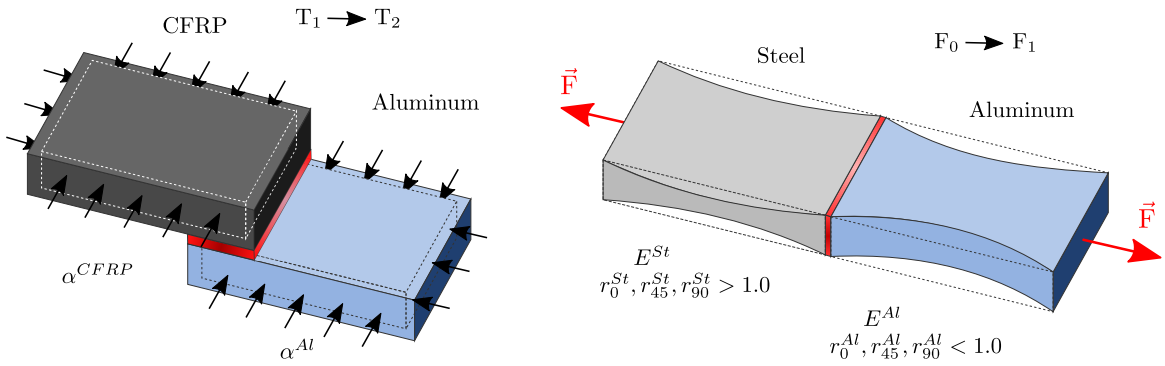

(a) Temperature induced residual stresses in an adhesive bond of a hybrid material pairing

(b) Loading induced misfit stresses for an adhesively bonded steel-aluminum pairing

Figure 5.1.: Display of misfit stresses for hybrid material pairings due to different thermal expansion coefficients (left) and different plastic yielding behavior (right)

These additional misfit stresses for an idealized adhesive joint may cause the common interface to fail. For a CAE assessment, the joint is often the bottleneck and the most crucial point to consider since the failure assessment of the base material can be handled well with an adequate failure model. Figure 5.1b displays the idealized adhesive joint for a steel and aluminum pairing for a butt joint. Upon loading the steel and aluminum sheet tend to yield differently. Whereas the steel sheet ($r^{St} > 1.0$) will flow from its thickness

direction, the aluminum sheet ($r^{Al} < 1.0$) will flow more from its width direction. These additional misfit stresses in the common interface are quantified and discussed in the following study.

Considering a perfect adhesive butt joint with an idealized interface will lead to a singularity in the stress field for a linear-elastic material behavior ($1/\sqrt{r}$) [18]. This stress singularity occurring only for purely elastic models is more of a theoretical nature; in real physical applications, plastic yielding or failure will take place. Nevertheless, this may serve as a good indicator for potential weak spots or predestined bottlenecks in a structure. While stress discontinuities occur due to either geometrical aspects (e.g. a notch) or material discontinuities (e.g. a hybrid joint), they are not as easy to detect as e.g. a stress singularity due to a point load.

5.1. Analysis of misfit stresses for adhesive joints

To examine the stress singularity in the interface collapsed iso-parametric quad-elements can be used for 2D applications. Collapsing a quad element is done by repositioning two nodes at the same location forming a triangular element and subsequently move the midside nodes on the sides to 1/4 of its length near the crack tip. In Abaqus these special purpose elements are available as type CPE8 to calculate the stress intensity factor (SFI) around a crack tip or an interface [22]. However they are limited to plane stress states and a $1/\sqrt{r}$ singularity suitable only for linear-elastic analysis.
Further scrutinizing stress distribution and stress state prevalent in the interface r-method of re-distributing nodes is not suitable since the problem at hand is fully 3D, we opt for the h-method by refining the mesh in order to examine the occurring stresses at the interface.

In this Section, we look at the problem of misfit stresses; hence, we simplify the other issue by regarding two materials who share a similar range in the hardening behavior from initial yield strength to the ultimate tensile strength. This means we focus on the misfit stresses originating from plastic anisotropy of the yield surfaces expressed by different r-values and avoid as much as possible a premature failure of the weaker partner.

$$R_{11} = 1.0; \tag{5.1a}$$

$$R_{12} = \sqrt{\frac{3r_{90}\left(1+r_0\right)}{\left(r_0+r_{90}\right)\left(1+2r_{45}\right)}}; \tag{5.1b}$$

$$R_{22} = \sqrt{\frac{r_{90}\left(1+r_0\right)}{r_0\left(1+r_{90}\right)}}; \tag{5.1c}$$

$$R_{13} = 1.0; \tag{5.1d}$$

$$R_{33} = \sqrt{\frac{r_{90}\,(1 + r_0)}{r_0 + r_{90}}}; \qquad (5.1e) \qquad R_{23} = 1.0; \qquad (5.1f)$$

The conversion of the in-plane r-values in different directions relative to the rolling direction is given in Equations (5.1a) - (5.1f). The parameters R_{11}, R_{12}, R_{22}, R_{13}, R_{33}, R_{23} are the input parameters to define the orthotropic yield criterion in Abaqus Standard in accordance with Hill1948 [22].

For the sensitivity study of the influence of discretization and the r-values on the misfit stresses two different alloys are chosen deliberately which share a common stress range in the plastic hardening behavior independent of the strain-rate $\dot{\varepsilon}$. For the simulation at hand the HX200 with a range of 240.76 - 501.54 MPa and EN AW-6082 T6 300.77 - 465.99 MPa are used. The slope of the plastic hardening behavior for these two materials is displayed in Figure 5.2. With their intersection at $\varepsilon_{eq}^{pl} = 0.50$ a equivalent plastic stress σ_{eq} 445.0 MPa this leaves an interval from 240.76 - 445.0 MPa.

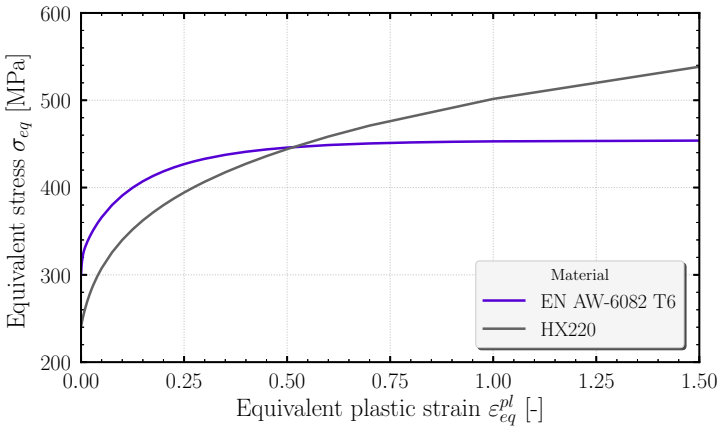

Figure 5.2.: Comparison of the plastic hardening behavior of EN AW-6082 T6 and HX220

Equation (5.2) gives the term for the geometrical averaging of the r-values in accordance with [135] to obtain the planar r-value r_{avg}. Using this planar r-value allows to reduce the geometrical complexity from an planar orthotropic to a transversal-isotropic one. While the transversal-isotropic material description represents an simplification compared to the orthotropic description its use does not require to define a material orientation.

$$r_{avg} = \frac{r_0 + 2r_{45} + r_{90}}{4} \qquad (5.2)$$

Table 5.1 summarizes the plastic material properties for the EN AW-6082 T6. The orthotropic r-values measured are given in the last row. Based on the geometrical averaging of the r-values given in Equation (5.2), they can be transformed for a transversal isotropic description, supposing a constant transverse isotropic r-value in-plane. Abaqus internal

Table 5.1.: r-values and yield stress ratios of Hill1948 yield locus for the EN AW-6082 T6 for an isotropic, transverse isotropic, and orthotropic material description

Material description	r-values			Stress ratios					
	r_0	r_{45}	r_{90}	R_{11}	R_{22}	R_{33}	R_{12}	R_{13}	R_{23}
isotropic	1.0	1.0	1.0	1.0	1.0	1.0	1.0	1.0	1.0
transverse isotropic	0.6575	0.6575	0.6575	1.0	1.0	0.910	1.036	1.0	1.0
orthotropic	0.545	0.73	0.625	1.0	1.044	0.908	1.003	1.0	1.0

IDS material model they need to be transferred into the yield stress ratios for the **Potential*-definition of the Hill48 yield locus description.

The influences of the different levels of material models for the EN AW-6082 T6 are displayed in Figures 5.3a to 5.3c for an isotropic, a transverse isotropic, and an orthotropic description using the vonMises, the Hilll1948 yield locus with constant r-values, and the Hill1948 yield locus formulations, respectively. As the trace of the yield locus is displayed only in the first quadrant and the off-axis angle α is given relative to the rolling direction (RD). For the visualization and discussion of the entire material card of the EN AW-6082 T6 in MF GenYld+CrachFEM the interested reader is referred to Section A.6.2 in the appendix.

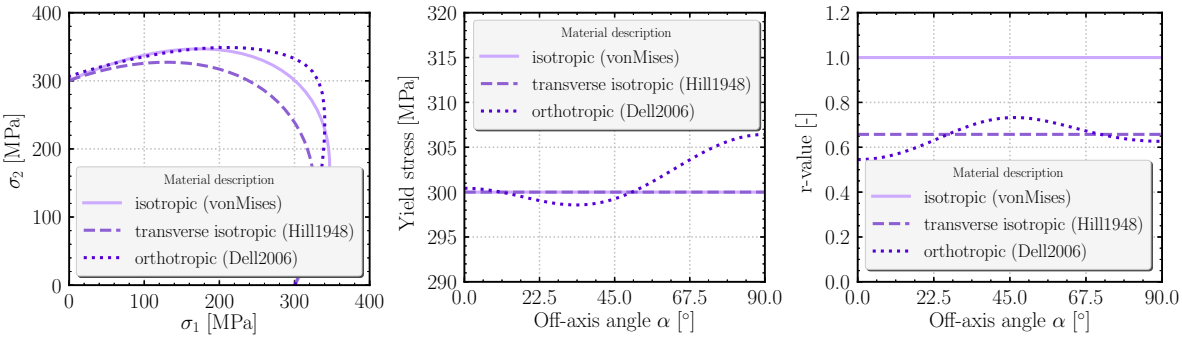

(a) Traces of yield loci (b) Yield stress (c) r-value

Figure 5.3.: Comparison of yield locus, yield strength and r-values for an isotropic, transverse isotropic and orthotropic modeling of the yield locus for EN AW-6082 T6

5.1.1. Parametric study on the discretization influence

While a stress singularity arises while using a linear-elastic material at either an interface of a hybrid material pairing or between a clamping and deformable part, the question is not sure if there is a plastic singularity or will the plastic strain saturate?

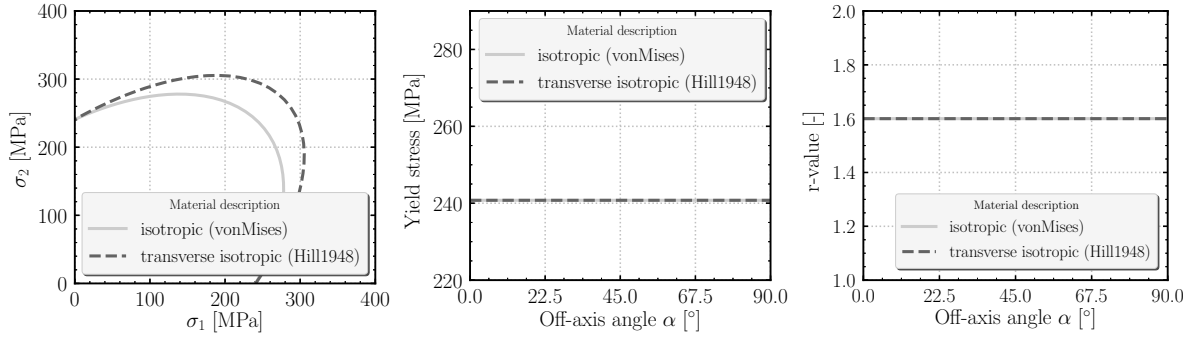

(a) Traces of yield loci (b) Yield stress (c) r-value

Figure 5.4.: Comparison of yield locus, yield strength and r-values for an isotropic and transverse isotropic modeling of the yield locus for HX220

For this study a flat dog-bone specimen is used with a width of 10.0 mm and a radius of r=10 mm and a parallel length of 60 mm. The interface between the aluminum and steel part is in the middle leaving 30 mm in the parallel length for both metals for free deformation. A virtual length of L_0=50.0 mm is chosen to capture a huge part of the deformation. The analysis are run run in AbaqusStandard v2020 using fully integrated solid elements of type C3D8 with 8 integration points. The reaction force from the rigid body of the clamping is evaluated as well as the displacement of two nodes in longitudinal direction of the specimen. Table 5.2 summarizes the average element length, number of elements and corresponding computational time of four CPUs.

Table 5.2.: Overview of mesh variants for parametric study

Variant	Avg. element	number of elements				CPU time
	size in mm	thickness	width	interface	total	in s
a.)	1.5	1	7	7	448	41
b.)	1.0	2	10	20	1760	84
c.)	0.75	2	13	26	4988	115
d.)	0.5	3	20	60	10596	397
e.)	0.3	5	33	165	48790	2113
f.)	0.15	10	66	660	408600	27426

Table 5.2 summarizes the number of elements used for the discretization study as well as the associated computational time.

Figures 5.5a and 5.5b show the vonMises equivalent stress σ_{vM} and the plastic strain ε_{eq}^{pl} of the dogbone specimen. The interface with the misfit in stresses is in the middle which can be inhomogeneous stress distribution in the middle. Force equilibrium at around ε_{eq}^{pl}=0.05 the slope of the aluminum hardening curve is steeper paired with its tendency to flow from width direction rather than thickness renders the HX220 the weaker part of

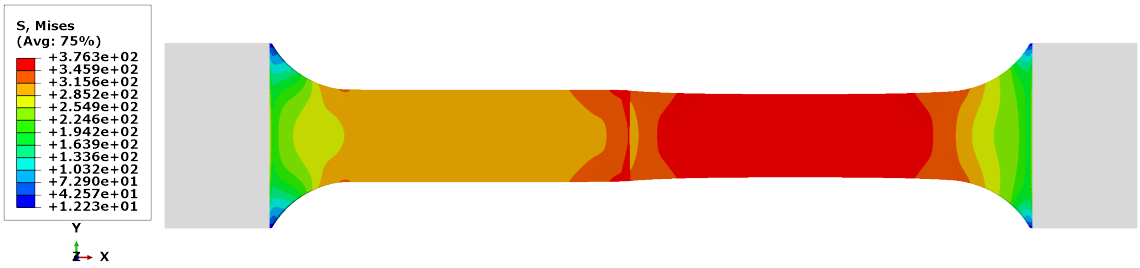

(a) vonMises equivalent stress σ_{vM} in MPa

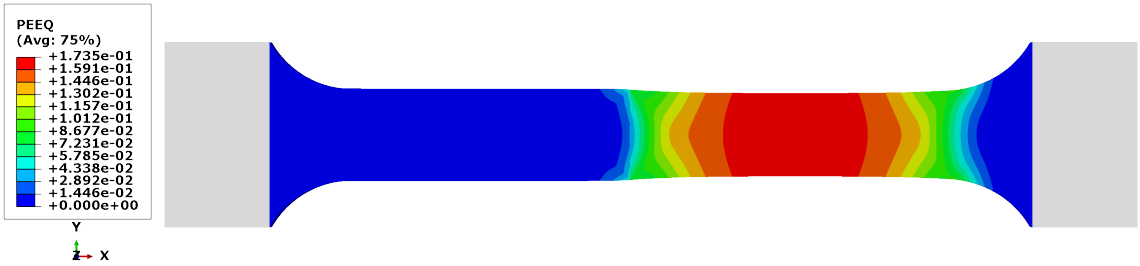

(b) Equivaent plastic strain ε_{eq}^{pl} in -

Figure 5.5.: Top view of the dogbone specimen with a aluminum EN AW-6082 T6 (orthotropic) on the top and steel HX220 (transverse isotropic) on the bottom for 0.3 mm solids of type C3D8

the hybrid joint where necking starts as can be seen on the right hand side on Figures 5.5a and 5.5b.

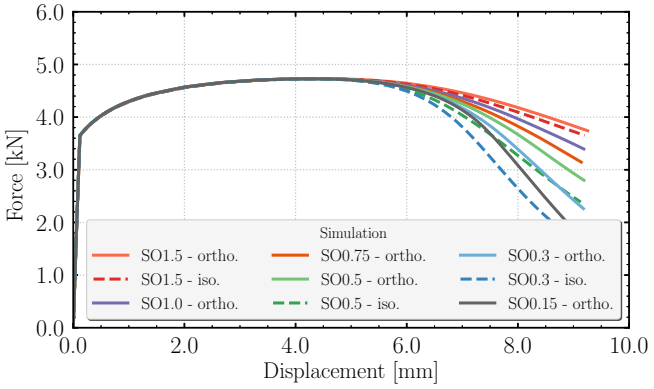

(a) Force-displacement curve for an uniaxial tensile test of a hybrid material pairing EN AW-6082 T6 and HX220

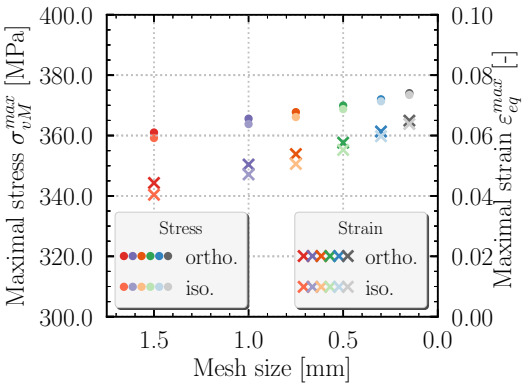

(b) Maximal vonMises equivalent stress and plastic strain of the critical element

Figure 5.6.: Discretization study on the critical element close to the interface of a hybrid material pairing of EN AW-6082 T6 and HX220

The force-displacement curves as well as the vonMises equivalent stress σ_{vM} and the plastic strain ε_{eq}^{pl} of the critical element in the interface are displayed in Figure 5.6a and 5.6b. The critical element is found at the outer edge of the aluminum part at the time of maximal force peak. The dots in Figure 5.6b represent the maximal stresses found at the force peak of the simulation of around 4.2 mm displacement and the crosses the critical stress. The darker dots display the simulation results of the orthotropic material description, while the lighter dots stand for the isotropic one. Comparing the results between the material description there is a small difference both in stress and strains which diminishes with increasing the mesh refinement. Further, it is found than rather than a strain singularity at the interface the critical strains follow the stress-strain relationship of the base materials for an elasto-plastic analysis. Hence no strain singularity occur at the interface of the idealized adhesive hybrid butt joint which is a prerequisite for using strain-based failure criteria for the high-fidelity detailed model.

5.1.2. Influence of the r-values

In order to get a qualitative representation of the misfit stresses, the joint interface of Figure 5.1b is thoroughly analyzed in the following. A simulation model of a rectangular tensile test is derived for an idealized butt joint connection between an aluminum and steel part. To resolve the stresses at the communal interface, the nodes are duplicated in the plane of the interface and the congruent nodes from both sides of the steel and aluminum butt are fused to one another with connector elements. For these connector elements, the force components CTF_1, CTF_2, and CTF_3 are outputted from the simulation and divided by the reference area of each node yielding the stress components of the interface σ_1, σ_2, and σ_3. Assuming that the change between the engineering strain and true plastic strain remains below 1 %, the change of the reference area due to the plastic deformation is neglected and the initial area A_0 associated to every node is used. Figure 5.7 displays schematically the FE mesh of the interface, the corresponding nodes which are connected from both sides, and the corresponding reference area for every node in dashed gray lines. Equation (5.3)-(5.5) define how the connector forces are summed up for the first components across the number of nodes n in the interface. In Abaqus the connector type "Join" is used for a kinematic coupling of the displacements of common nodes at the interface modeling an idealized adhesive interface.

$$F_x = \int\int \sigma_x dA = \int_0^t \int_0^w \sigma_x dy dz \approx \sum_{i=1}^{n} \frac{CTF_{1,i}}{A_{0,i}}; \tag{5.3}$$

$$F_y = \int\int \sigma_y dA = \int_0^t \int_0^w \sigma_y dy dz \approx \sum_{i=1}^{n} \frac{CTF_{2,i}}{A_{0,i}}; \tag{5.4}$$

$$F_z = \int\int \sigma_z dA = \int_0^t \int_0^w \sigma_z dy dz \approx \sum_{i=1}^{n} \frac{CTF_{3,i}}{A_{0,i}}. \tag{5.5}$$

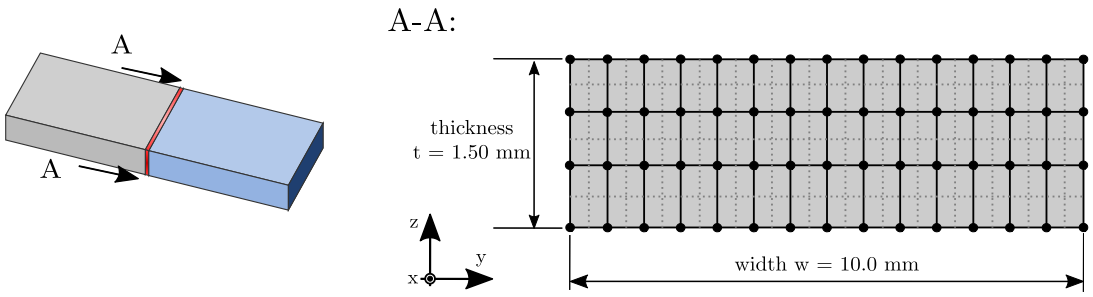

Figure 5.7.: Visualization of FEM mesh at the interface of the dissimilar material pairing of an idealized butt joint as displayed on the left

Continuum hexahedron elements of type C3D8R with a reduced integration are used. Because in Abaqus Explicit a numerical noise disturbs the signal of the connectors, the simulations are conducted in Abaqus Standard. The material cards are therefore converted to an Abaqus internal IDS material using the **Potential* keyword for defining an anisotropic Hill1948 yield criterion (see Equations (5.1)). Scrutinizing the interfacial stresses for an idealized adhesively bonded steel-aluminum pairing yields in a first step a qualitative statement on the discretization influence. Moreover, it outlines the influence while neglecting the σ_3-stress component in thickness direction which is appropriate for using shell elements for thin-walled joints in an industrial simulation. Since the interface itself cannot be accessed in an experiment, the analysis of the stresses and strains on the interface can only be investigated virtually. In order to observe interfacial stresses caused by a differently pronounced plastic anisotropy from width- ($r > 1.0$) and thickness-direction ($r < 1.0$), the two materials of the joint need to share a common range of the plastic hardening behavior defined between the yield stress and ultimate strength of the material. The interfacial stresses can be analyzed for a loading history until the weaker part of the joint - presumably the aluminum alloy - commences to exhibit necking.

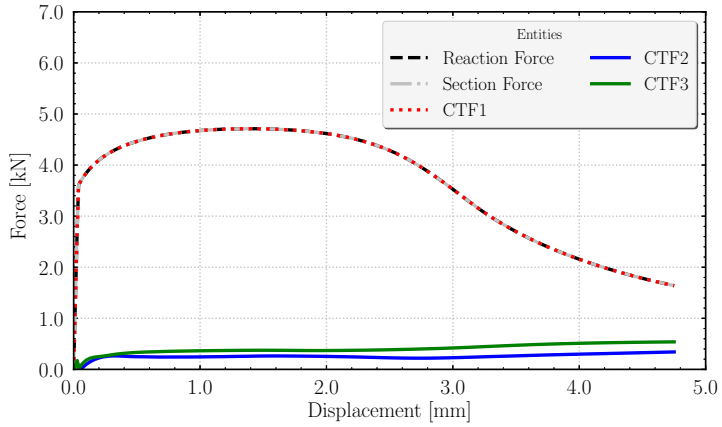

Figure 5.8.: Force-displacement curves from simulation with an average length of 0.3 mm of hexahedron type C3D8R

To verify the above assumption, the total sum of the connector forces is compared to a section force right next to the interface and a reaction force right next to the clamping of the tensile test. Figure 5.8 shows a constant behavior verifying that the force flow remains constant throughout the length of the specimen.

Table 5.3.: Elastic material parameters and r-values of different base materials

Material	Young's modulus	Shear modulus	Bulk modulus	Poisson's ratio	r-values		
	E in MPa	G in MPa	K in MPa	ν in -	r_0 in -	r_{45} in -	r_{90} in -
S355JR	210,000.0	80,769.0	175,000.0	0.3	0.775	0.80	1.1
HX220	210,000.0	80,769.0	175,000.0	0.3	1.60	1.60	1.60
AW-6082 T6	73,000.0	28,076.0	60,833.0	0.3	0.545	0.73	0.625

Figure 5.9 displays a vector plot of the σ_1 derived from the CTF_1 connector force of the deformed interface at the force peak prior to necking of the HX220.

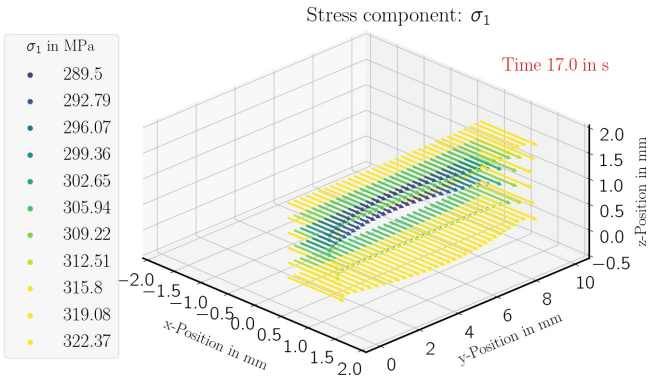

Figure 5.9.: Vector plots of the stress components in the interface of the hybrid steel-aluminum pairing

Because it is difficult to display the vector plots over time to compare the evolution of the stresses at the interface with one another, the traces of the connector forces on the interface edges are compared to one another over time in Figure 5.10. The onset of yielding in aluminum happens at 6 s (increment 22) and the force peak occurs at 22 s (increment 33).

Theoretical consideration of an idealized adhesive butt joint is relevant for the high-fidelity detail model and implies moreover the influence on simplifying the material description for an originally orthotropic material. Based on an adequate representation of the two base materials, the stresses at the interface can be examined with the proposed approach. Furthermore, the loading in the base material in the vicinity of the interface and the

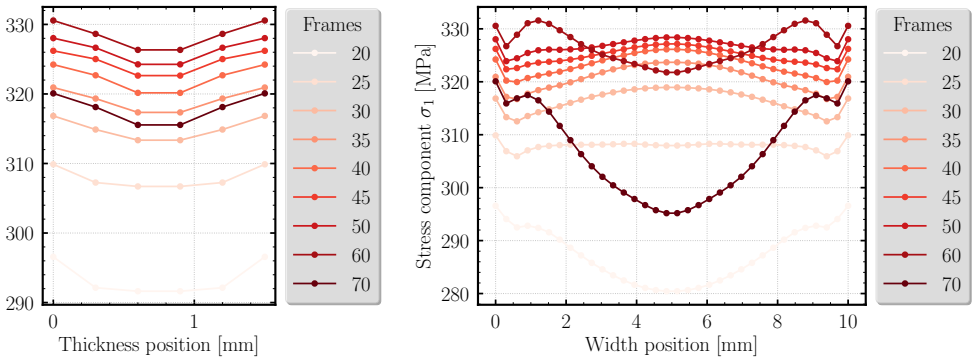

(a) Across the thickness on the left side of the interface at y=0.00 mm

(b) Across the width on top of the interface at z=1.50 mm

Figure 5.10.: Examination of stresses in the interfaces by line scans for different time frames across the thickness on the left and across the width of the interface on the right

influence of a potential confinement at the common interface can be analyzed using the underlying base material. Once the elasto-plastic material behavior is well covered by the simulation and shows a good accordance with experimental force displacement curves, the simulation model may serve as a virtual laboratory allowing with an indirect measurement inside the specimens of the joint to evaluate the fracture risk as well as the stress state as proposed by Schmeer [104]. Even though the theoretical consideration of a perfect adhesive joint for a hybrid steel-aluminum pairing with solid elements is idealized here, the occurring misfit stresses are influenced by the material description. Lastly, the misfit stresses in thickness direction cannot be covered in a surrogate model with shell elements and may lead to a premature prediction of failure. To compensate the shortcoming of the element formulation under plane stress, the introduction of knock-down factors for the neighboring elements quantified by a theoretical consideration as presented in this section can be a reasonable workaround.

The differences of stress distribution are compared for an isotropic and a orthotropic material model along the outer edge across the width and thickness in Figures 5.11a to 5.11d. The first frame 13 around of the non-linear hardening in the force-displacement curves and the second frame 33 of the force peak before diffuse necking commences.

To put the analysis of different material descriptions in a nutshell, the influence of the underlying material description yielded small differences in the stress distribution of the interface. The minor differences in the force displacement curves are negligible and the influence of the material description on the stress distribution of the interface has an subordinate role assuming a perfect adhesive joint of two materials sharing the same stress range in the plastic hardening regime. In reality most often the weaker part of a

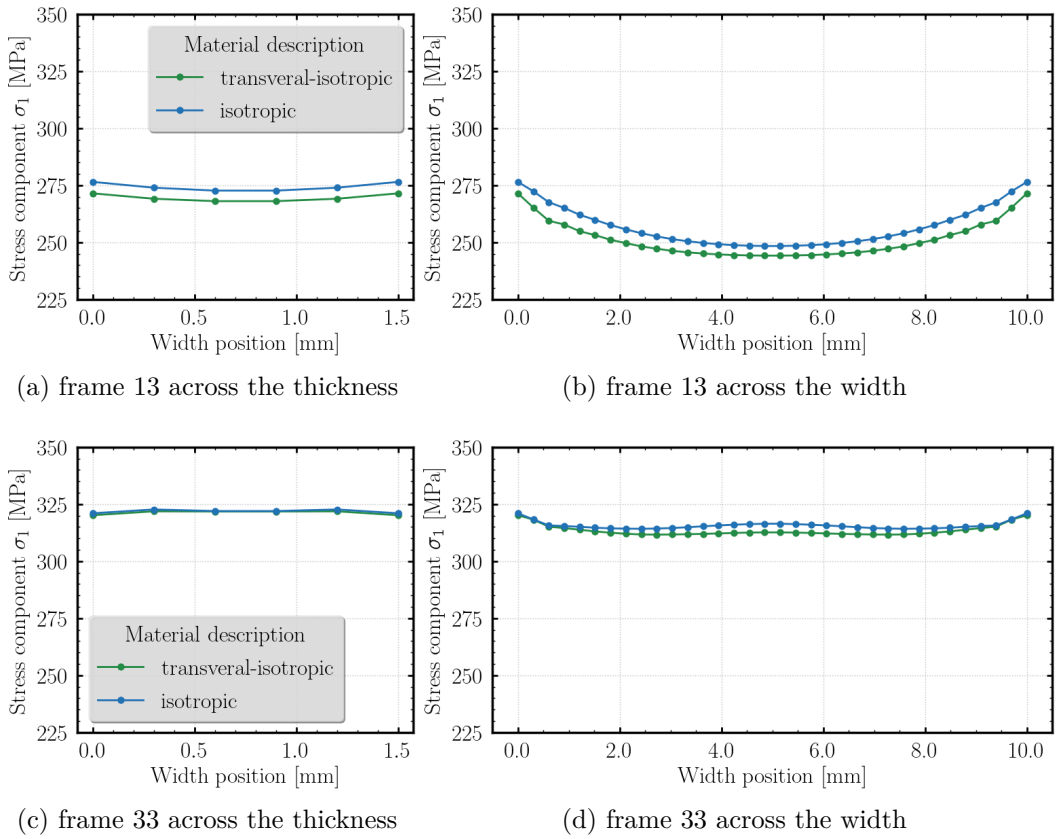

(a) frame 13 across the thickness

(b) frame 13 across the width

(c) frame 33 across the thickness

(d) frame 33 across the width

Figure 5.11.: Influence of the r-values on the σ_1-stresses in the interface for multiple states between the onset of yielding and necking

hybrid joint fails or failure is initiated at the interface by a pronounced scatter of material properties from e.g. a weld zone.

5.2. Abstracted, objectified assessment of quality

Because of the geometrical dimensions of the surrogate model as well as particularities of hybrid material pairings, none of the internal surrogate models of currently available solvers as presented in Section 2.4 can be used for hybrid joints. Therefore, a direct discretization using the material description of the base materials of the joint is applied here incorporating the particularities of the hybrid material pairing. Following the overall procedure presented in Figure 2.37, a detailed model with high accuracy and computational cost and a surrogate model with good accuracy but reduced computational cost are used in two consecutive steps. These two models, differing in their level of detail, are calibrated via the experimental force-displacement curves with a maximal mismatch of 5 % for the detailed model and approximately 15 % for the surrogate model. An overview

of the characteristics and modeling decisions of the detail and surrogate model is given in Table 5.4. For this calibration procedure, objectified quality criteria have to be used to assess the quality of the deformation and failure behavior of the model for the hybrid joint. Based on the experimental force-displacement curves, the detailed and surrogate model can be calibrated iteratively across all loading scenarios as displayed in Figure 5.12. To assess the model quality, the criteria can be clustered in two main groups, into local and global quality criteria. The low-fidelity surrogate model will serve in the following on

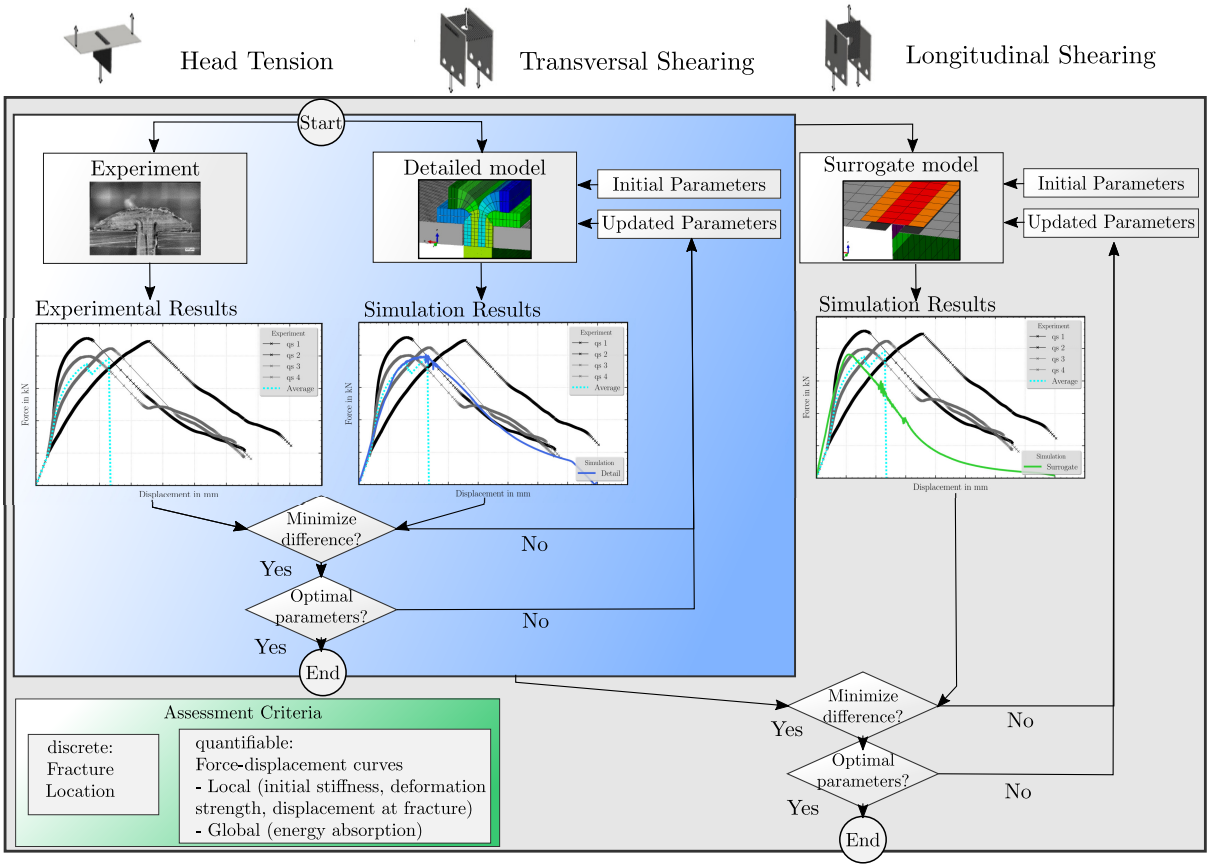

Figure 5.12.: Scheme for parameter identification for hybrid material joints across multiple loadings

higher component or sub-system level as a substitution for the mechanical deformation and failure behavior of the hybrid joint without hampering the overall critical time step and hence computational cost in an explicit simulation. The adequate way to calibrate both models is by comparison of the force-displacement curves from experiment and simulation. These curves can be read as a global measure on coupon-level. In the context of crashworthiness simulation, local and global quality criteria can be defined from these curves. For the experimental scatter may be pronounced for hybrid joints, including another curve with average experimental results may improve the modeling. For the evaluation of the model quality the goodness of fit is based on the following quantifiable properties:

Table 5.4.: Comparison of the attributes for the detailed and surrogate model

Entity	Detail model	Surrogate model
Level of detail:	high-fidelity	low-fidelity
Accuracy:	high	reduced
Element type:	Solids (3D)	mainly Shells (2D)
Computational cost:	high	low
Geometrical representation:	close	abstracted

- Initial stiffness;
- Deformation;
- Load-bearing capacity /strength;
- Failure behavior;
- Energy absorption.

All of the criteria listed above for the quality assessment of the model are local criteria except the last one which is considered a global criterion as the capacity to absorb energy of the joint is represented as the integral below the force-displacement curves. Hence, the total of the local criteria before defines implicitly the last global criterion. Additionally, to ensure that the physical failure behavior in the simulation corresponds to that of the physical coupon, a discrete criterion for the fracture location is introduced as well. These criteria for the optimal fitting of the hybrid material joint are visualized in the scheme of Figure 5.13 in blue in comparison to the averaged experimental results in cyan.

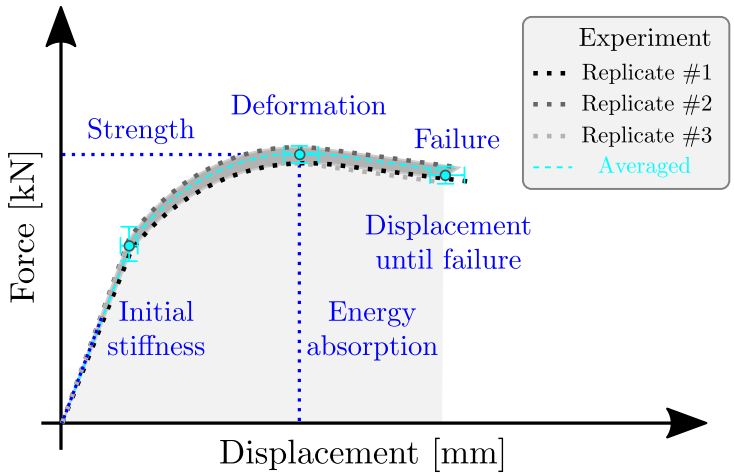

Figure 5.13.: Schematic representation of the relevant fitting criteria of a joint compared to the averaged experimental force-displacement curve

Another important aspect to differentiate between the detail and surrogate model is the type of element chosen as listed in Table 5.4. For surrogate model computational

efficiency shell elements are chosen. Whereas in the detail model a full 3D representation of the stress state is possible and also allows a close direct representation of the joint's geometry, the joint will be approximated by a plane stress assumption by transmitting only membrane stresses.

5.2.1. Local quality criteria

The tangent at the beginning of the slope is to be read as the initial stiffness of the joint. After trespassing the elastic regime and some non-linear plastic yield of the joint the force peak is reached. This is the point of failure initiation and the force-level and displacement until failure initiation constitutes the local quality criteria of the joint as displayed in the schematic representation in Figure 5.13. Only with a good approximation of these local quality criteria a good agreement between the experiment and simulation can be obtained for either the detailed or surrogate model. Further meeting these local quality criteria is prerequisite for global criteria.

5.2.2. Global quality criteria

After satisfying the local criteria as explained in Section 5.2.1, the global criterion can be considered as well. This is the overall capacity of load bearing and energy absorption. The overall capability for energy absorption is displayed as the light gray area below the curves in Figure 5.13. The load bearing capacity as well as the global capacity of energy absorption are met.

6. Surrogate models for hybrid bridge-deck panel joints including organic sheets

The joining concept of bridge-deck-panel joints was first developed by the *Fraunhofer Institut für Werkstoffe und Strahltechnik* (IWS) in Dresden/Germany for steel-aluminum pairings [89, 136]. It was then adapted for more general hybrid material pairings with metallic steel sheets serving as the deck panel and the organic sheets as the bridge [137]. For this concept, a slot is cut into a metallic sheet and a form-closed undercut is created on its backside creating a T-joint of the two sheets.
In a corresponding experimental study performed by the project partners in *LaserLeichter*, different material combinations were analyzed for the concept of the bridge-deck-panel joints [138]. Here, the deck panel was made of steel S355JR or of an aluminum alloy EN AW6082-T6 and the bridge panel of the organic sheet material Tepex® dynalite 102-RG600 or 104-RG600 with a thermoplastic PA6- or PP-matrix, respectively. Additionally, to cover also dissimilar metallic pairings, an aluminum sheet was used as the bridge panel. Enhancements of this concept, e.g. by increasing the adhesion between the rivet head of the organic sheet and the metallic sheet with a pre-structuring of the laser or by the use of an adhesion promoter, were also part of the comprehensive investigation by Fraunhofer IWS. As a representative of hybrid material pairing between an organic and metallic sheet, the combination of Tepex® dynalite 102-RG600 serving as the bridge panel and the S355JR as the deck panel is considered.

The development of the joining process as well as the experimental characterization of the hybrid material joints was done in the scope of the research project *LaserLeichter* by the *Fraunhofer* (IWS) in Dresden [138]. In the remaining part of this chapter experimental results from the IWS are summarized and the experimental characterization of the hybrid material joints serves as an input for the development of the surrogate modeling technique. Surrogate models are developed for a hybrid material pairing between steel and organic sheets using the bridge-deck panel concept by using the remote laser as a heat source for a thermo-mechanical forming to create a form closure in a geometrical undercut.

6.1. Thermo-mechanical forming of bridge-deck-panel joints

The basic concept is to create a form-closed undercut material. To achieve this, a rectangular hole is cut in the sheet, which will serve later on as the deck-panel. Then, the second joining partner, the organic sheet used as bridge as shown in Figure 6.1, is cut slightly smaller than the rectangular hole in the deck panel compensating for manufacturing tolerances (see exploded view on the left of Figure 6.1). Subsequently, the bridge of organic sheet material is put through the rectangular hole, which is heated up on the backside of the deck panel by a remote laser so that the glass transition temperature, T_g, of the thermoplastic matrix is reached. It is then reshaped by a roll to form a bulk material on the backside creating a form closure of these two semi-finished products (compare schematic representation in the middle and on the right of Figure 6.1). At the end of this process, the undercut form closure is obtained on the backside of the deck panel formed by an arbitrary shape. Figure 6.2 represents a side and front view of the bridge deck panel concept. Note that due to the rolling concept, the beginning and end of the rivet head have slightly different properties for the start-up and run-down phase. Further, the deposition of the fibers is not really perpendicular to the bridge length but directed under 45° due to the rolling process. Figure 6.3a displays the joining process for four

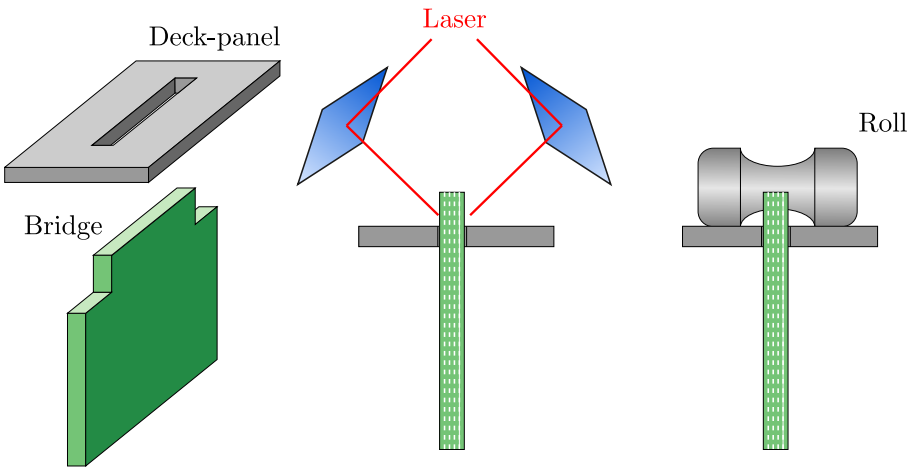

Figure 6.1.: Manufacturing process of bridge deck panel joints

bridge-deck-panel joints of 20.0 mm length. Towards the top of Figure 6.3a two mirrors reflecting the laser beam are visible ensuring an even distribution of the thermal input on both sides of the overlapping bridge material. This picture is taken right after the last bridge on the backside is heated up and immediately before the forming with the roll takes place. In this picture the left mirror is seen from behind and the right mirror is visible in light blue. Different geometries of the roll as displayed on the right side of Figure 6.2 were analyzed throughout the process investigation resulting in a different shape of the bulk material. A cross section cut of these different shapes is displayed

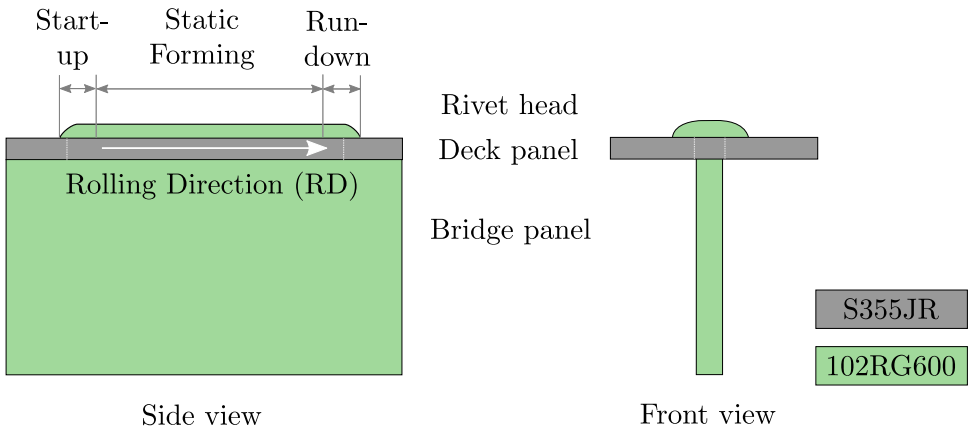

Figure 6.2.: Scheme of a hybrid material pairing between steel and organic sheet with front and side view

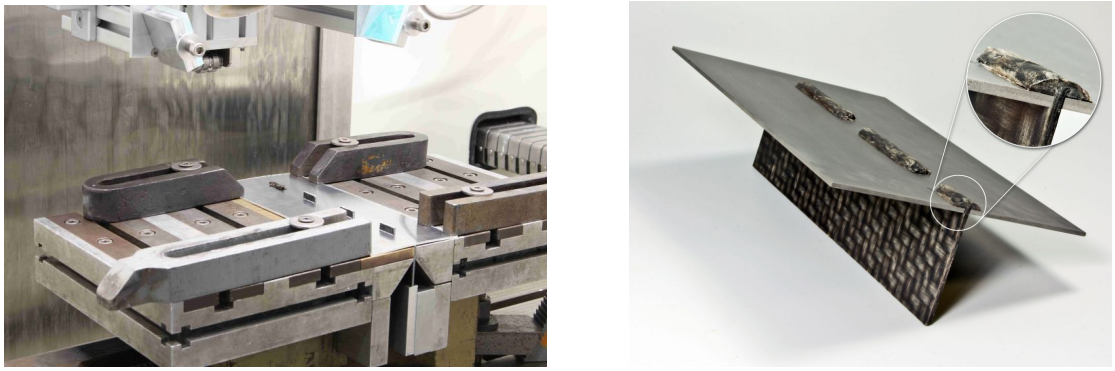

(a) Joining process of a deck panel with four bridges each of 20.0 mm length

(b) Sample of thermomechanically formed bridge-deck panel joint [137]

Figure 6.3.: Joining process on the left and a sample for head tension on the right [139]

in Figure 6.4. First experiments showed that the highest strength is achieved with the concept of the flat rivet head shown in Figure 6.4c which was then used throughout the comprehensive experimental study [139].

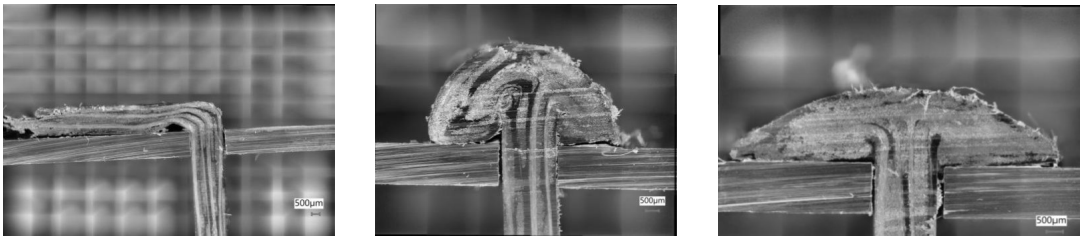

(a) Ship's bow (b) Rivet head (c) Rivet head flat

Figure 6.4.: Cross-section cuts with different forming types for the bulk material [140]

Since no technical term for the type of joining has currently been established, this concept is referred to, in the scope of this thesis, as bridge-deck panel joint. Another equivalent term which is used for this joining concept is web-slot joint.

6.2. Experimental characterization

The bridge-deck panel joints were manufactured and tested at the Fraunhofer IWS in Dresden with three different variations of 10.0, 20.0, and 40.0 mm length of the bridge to account for non-linear influences. For the experimental characterization, the set-up as displayed in Figure 6.5 was employed. For the head tension depicted on the left an additional mount is used, which is not displayed in Figure 6.5. For shearing in longitudinal and transversal direction, the symmetrical set-up containing two bridge-deck panel joints is used [140].

(a) Head tension (b) Transversal shearing (c) Longitudinal shearing

Figure 6.5.: Loading types for the experimental characterization of the bridge-deck-panel joints [139]

Figure 6.6 displays the force-displacement curves for the three loading types in every row, i.e. head tension as well as longitudinal and transversal shearing. Experimental results are given for varying bridge lengths in the different columns. Additionally, bar diagrams are displayed with the averaged experimental value for the maximal force and displacement at failure initiation as well as vertical error bars are displayed for the experimental scatter across all four replicates. Comparing the absolute values of the forces, the loading in head tension is the most critical exhibiting the lowest force level. A load-case of pure head tension results in a compression loading of the material in the so-called rivet head. The other two load-cases of transversal and lateral shearing are defined by the edge-to-edge contact of the organic and metallic sheet serving as the bridge and deck panel, respectively. Here, the material in the rivet-head has more of a supporting function.

In the following section, the experimental force-displacement curves are discussed in detail for the different loadings. The influence of the bridge length is studied with the help of bar

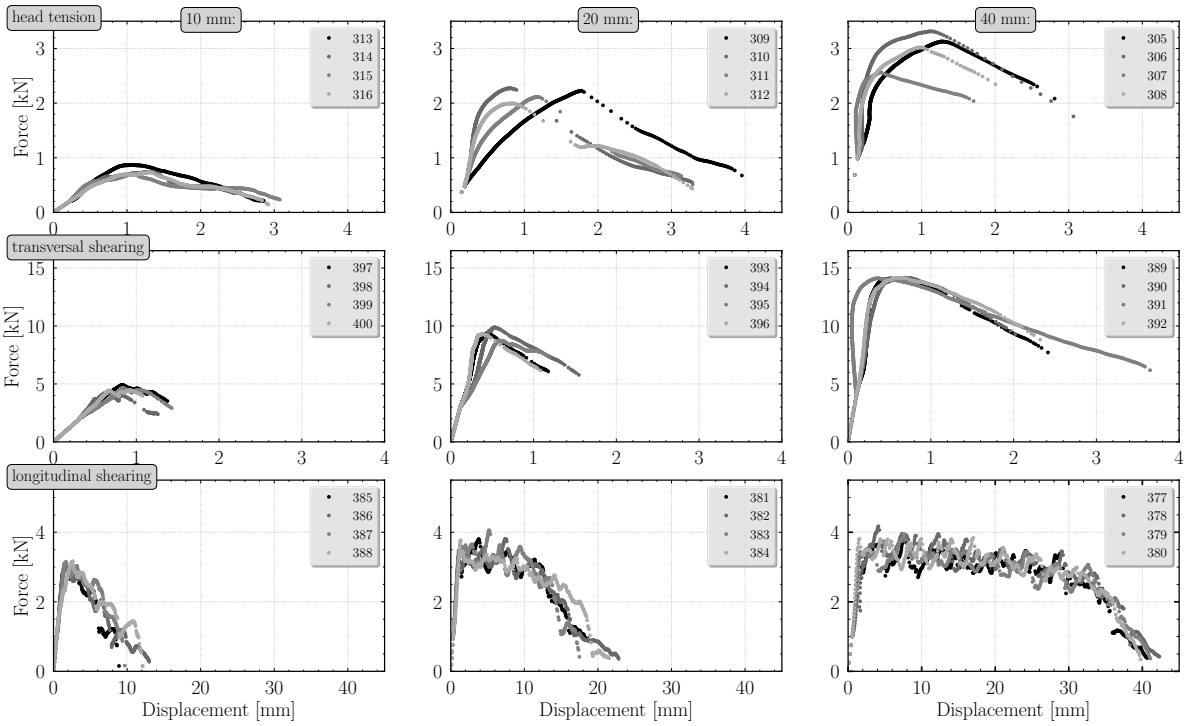

Figure 6.6.: Experimental force-displacement curves of the bridge-deck-panel joint for a varying bridge length of 10.0, 20.0, and 40.0 mm - results are given for all four experimental replicates indicated by the 3xx-numbering [139]

diagrams. For these diagrams, the displacement and force levels for failure initiation are analyzed for the averaged values across all four replicates. Four bridge-deck panel joints were joint at the same time as displayed in Figure 6.3a and all four of them were tested. An uneven number of experimental replicates is used deliberately to ensure a meaningful statistical average. So for the sake of completeness, all four replicate experiments are used in the following section. The experimental scatter for the hybrid bridge-deck panel joints is higher than for the experiments of the base materials and more pronounced for the displacement until failure than for the force level. The displacement measurements were performed on the horizontal traverse bars including not only the compliance of the mounting but also that of the machine itself. In order to remove the influence of the mounting and machine stiffness on the measured displacement signal their proportion is removed from the displacement measurement[1].

6.2.1. Head tension

The head tension is the most critical loading of a bridge-deck-panel joint. The tension on the bridge panel will result directly in a compressive loading of the so-called rivet head

[1]Detailed information is given in Appendix Section A.3.

where the material underwent severe alterations during the thermo-mechanical forming. The compression of the rivet heads forces the edges to move towards one another. As shown by the results in Figure 6.7, the length of the bridge has a linear influence on the force level until failure initiation whereas the displacement until failure remains on a constant level.

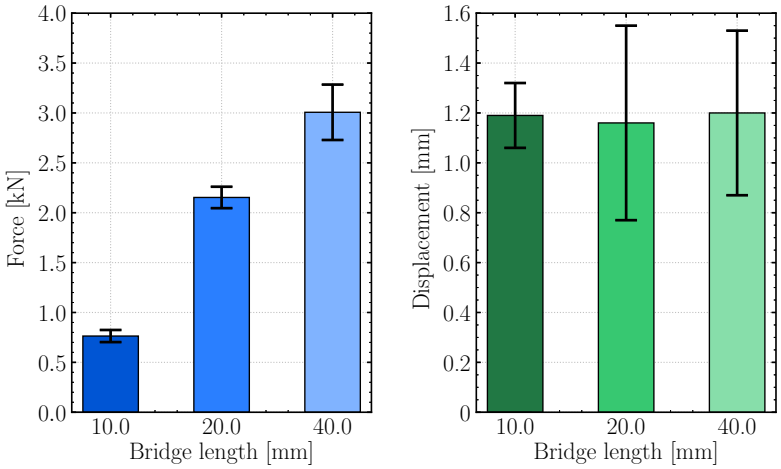

Figure 6.7.: Bar diagrams of the experimental evaluation of force and displacement until failure initiation for head tension

The following two shear loading scenarios are slightly more favorable for the simulation because their failure behavior is not affected as much by the joining process and closer to the deformation and failure behavior of the base material. From a design point of view this is favorable because not only the influence of the joining process on the failure behavior is reduced but the failure mechanism itself is more reproducible and predictable by the characteristics of the base material.

6.2.2. Shearing in transversal direction

An exemplary experimental set-up for the transversal shearing in a mounting for a uniaxial tensile test machine including two bridge-deck-panel joints is shown in Figure 6.8b. The deformation and failure of the bridge-deck panel joint under transversal shear loading is displayed in the second row in Figure 6.5 and relates directly to the length of the bridge. In Figure 6.8a, the influence of the varying bridge length is analyzed with respect to the force and displacement at failure initiation. The force level increases with a linear relation to the bridge length. For the displacement until failure, the shortest bridge length resembles an outlier since the length is so short; the behavior of the rivet head is primarily dominated by a start-up and roll-down process from the forming process with the roll. Therefore, the bulk material of the rivet head poses little resistance and

is continuously torn out of the rectangular hole resulting in a much higher displacement for the bridge length of 10.0 mm than for the others. For the higher length of 20.0 and 40.0 mm, the rivet head has enough support to ensure that the failure initiates in the bridge itself, resulting in an almost constant failure displacement.

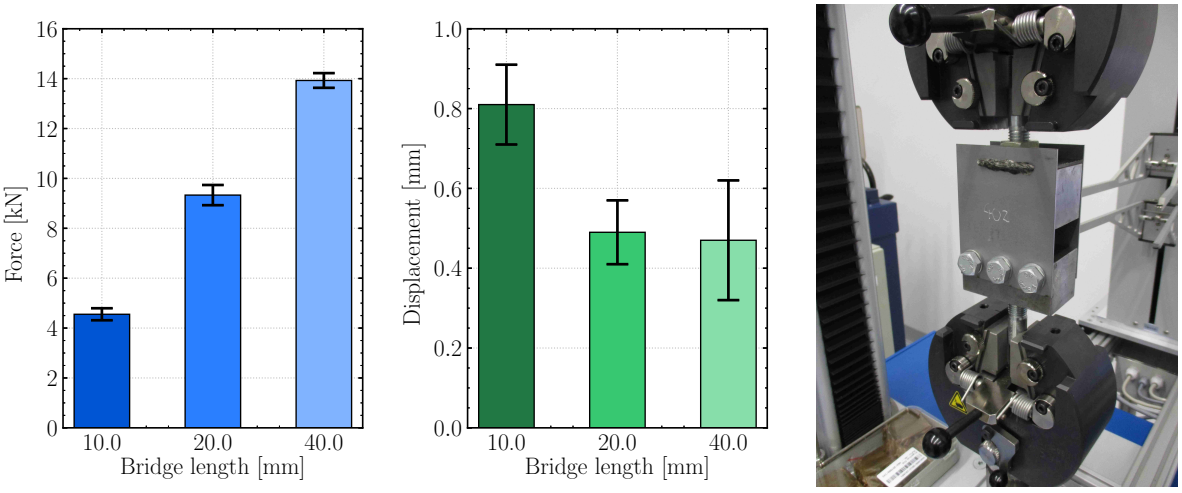

(a) Bar diagrams (b) Experimental setup [139]

Figure 6.8.: Bar diagrams of the experimental evaluation of the force and displacement at failure on the left and photography of the experiment on the right for transversal shearing

6.2.3. Shearing in longitudinal direction

The loading alongside the longitudinal direction of the bridge is characterized by a linear elastic behavior up to the point of fracture in the force-displacement curves as shown in the last line in Figure 6.6. After initial failure, the organic sheet of the bridge panel being the weaker material is continuously sheared off across the metallic deck panel as can be seen in the photograph of the experiment with 40 mm bridge length in Figure 6.9b. The fracture strength for the longitudinal shear loading is hence characterized by the thickness dimensions of the two edges of the metallic and organic sheet. This results in a nearly constant fracture force and displacement until failure across the three different bridge lengths in Figure 6.9a. The slight decrease of the fracture strength with decreasing bridge length can be explained by the missing supporting effect which ensures a constant off-shearing. The smaller the bridge length, the less support the bridge panel has during the shearing. After the fracture strength is reached for the first time, a jagging in the force signal can be observed, which is best visible for the 40.0 mm bridge length on the bottom right of Figure 6.6. These repetitively occurring force peaks in the experiment are due to the textile weaving structure of the organic sheet and the distance between these peaks directly represents the mesh size of the textile of approximately 4.00 mm.

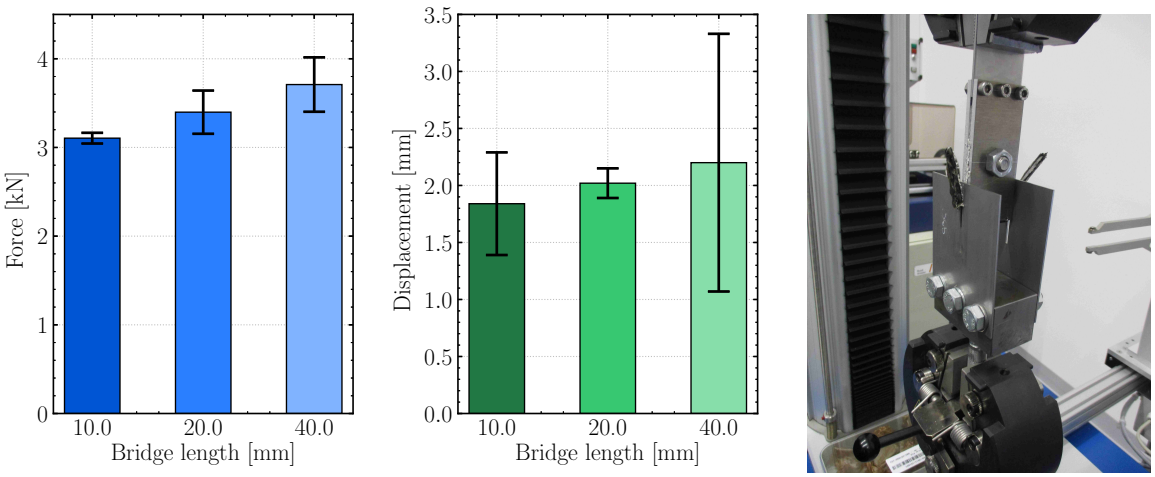

(a) Bar diagrams

(b) Experimental setup [139]

Figure 6.9.: Bar diagrams for experimental evaluation of force and displacement at failure on the left and photography of the experiment on the right for longitudinal shearing

6.3. Discretization of the surrogate model

In order to meet the mesh requirements of a surrogate model discussed in Section 2.4.3, the geometry of the bridge-deck-panel joint needs to be abstracted. To avoid high computational effort, the mesh size should be as large as possible respecting still the main geometric features of the bridge-deck panel joint. Shell elements of the type S4R (*Abaqus explicit*) using 5 integration points across the thickness are chosen here.

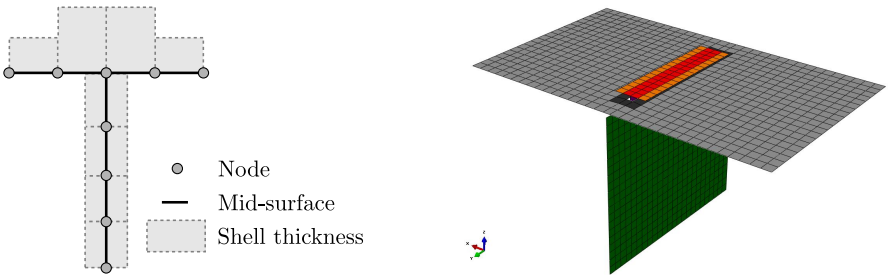

(a) Cross-section of surrogate discretization

(b) Isometric view of the surrogate model with 40.0 mm bridge length

Figure 6.10.: Proposed shell discretization for the low-fidelity surrogate simulation model of the rivet head

Considering the shape in the cross-section from Figure 6.4c, we see that the thermo-mechanical bulk material on the backside constituting the rivet-head is of slender geometrical dimensions justifying a shell discretization. Based on the polished section-cut

of Figure 6.4c, different discretizations are abstracted. The best matching between the simulation results with the behavior observed in the experiments is obtained with the shell discretization displayed in Figure 6.10. In Figure 6.10a the mid-surface and shell thickness are displayed in a cross-section cut for the proposed discretization using shell elements with an average element length of 3.00 mm. The rivet head itself is modeled with four rows of shell elements using a thickness offset so that the shell thickness represents the bulk material. The varying shell thickness allows to represent the flattening of the rivet head towards its outer ends. For the discretization of the rivet head, the shell elements are locally slightly refined to 2.50 mm length so that a symmetrical set-up of the rivet head of elements to both sides of the bridge can be achieved constituting an overall length of the rivet head of 10.00 mm.

The first simulation runs using only the base material card showed quickly that the force level in the simulation with the proposed shell modeling techniques is overestimated by a factor of three compared to the experiments for the most crucial load case, i.e. the head tension. In addition, it can be assumed that the thermo-mechanical forming of the rivet head causes a re-alignment of the fibers from initially 0° to 45° of rotation around the normal of the shell; considering this, the factor could only be reduced to 2.

6.4. Damage induced by the joining process

Due to the thermo-mechanically forming of the organic sheet material in the rivet head, the material properties are significantly altered - recalling the thermal heat-up by the remote laser and the mechanical forming into a shape like a rivet head bulk material by the roll discussed in Section 6.1. It is possible to account for locally altered material properties, as discussed for example in [141] for the heat-affected zone (HAZ) in welded joints of metallic materials, which can be characterized or rather calibrated with the use of micro-tensile tests of the material in the area of the HAZ. For the material in the rivet head, the realization of such micro-tensile tests is hardly feasible. Therefore, an analysis of the material with the use of a cross-section cut and a μ computed tomography scan (CT) was conducted as displayed in Figure 6.11a. For these μCT-scans, the metallic sheet was carefully cut-off leaving only the organic sheet material formed like a rivet head. In addition, the position of extraction along the bridge length was carefully chosen with a distance from 4.00 mm to the start and end to avoid the influence of the start-up or run-down phase. The μCT-scans were conducted by the BTU Cottbus with a resolution of 5 μm to ensure the visibility of fibers within the project *LaserLeichter* [138]. In the lower part of Figure 6.11a one can clearly see the four fiber bundles of the organic sheet. Figure 6.11a displays a detailed view of the material of the rivet head, which previously underwent the thermo-mechanical forming during the joining process for a more thorough analysis. With respect to the base material, two major changes can be observed. Firstly, due to the small bending radius on the edge of the deck panel, the endless glass fibers

tend to break, which can be seen on the left side. Secondly, below the bulk material indicated by the green circles an imperfect adhesion of the PA6-matrix can be found in the transition between the bridge and the rivet head constituting another weak spot.

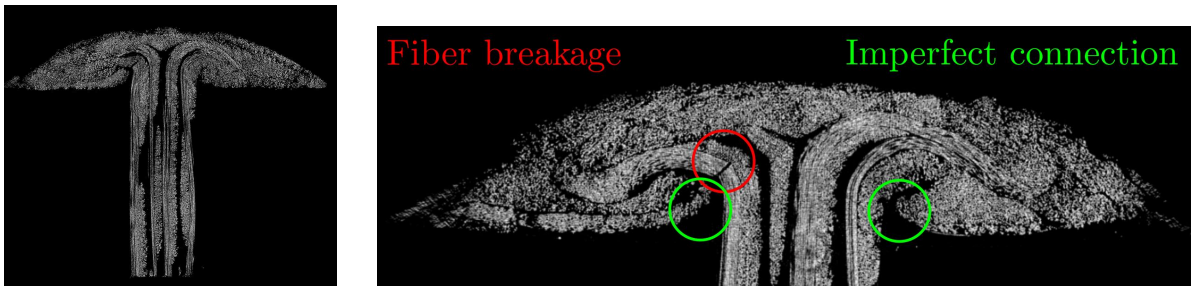

(a) Cross-section cut

(b) Detailed view of the rivet head including fiber breakage and imperfect re-connection of the PA6-matrix

Figure 6.11.: μCT-scan of the bridge panel from BTU Cottbus [142]

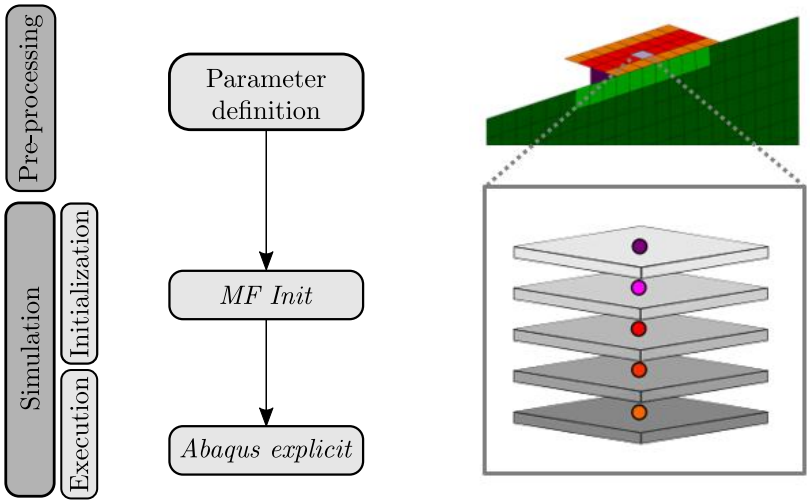

(a) Scheme of initialization routine

(b) Detailed view on shell element in the rivet head

Figure 6.12.: Initialization of history variables for the damage induced by the joining process for every integration point through the shell thickness

After identifying the damage induced by the thermo-mechanical forming process in the rivet head, an initialization routine in MF GenYld+CrachFEM for the history variables (HVs) called MF Init is developed by MATFEM. At the very beginning of the simulation, scaling factors for the plastic hardening and ductile failure mechanisms are read-in to modify the properties of the base material as displayed in Figure 6.13. This initialization routine is coupled as a shared object to the material model. Using MF Init allows to account for locally altered material properties, e.g. metallurgical notch effects due to

cold forming after a punching process or a thermal alteration as it is the case for the heat affected zone (HAZ) around spot welds, while using only a single material card of the base material [143].

Based on the initialization routine MFInit, the material properties can be altered individually for every element or integration point. In accordance with Figure 6.13 the material properties of the base material are adapted by scaling the history variables for plastic hardening behavior (HV16), ductile normal, and ductile shear fracture (HV17 and HV18) as well as the FLC. A down-scaling of the plastic hardening behavior as displayed in the left diagram of Figure 6.13 decreases the yield strength as well as the plastic hardening behavior while keeping the same slope or characteristic of the plastic strain hardening curve behavior of the base material. Similarly, the fracture curves as well as the FLC can be locally adapted. Scaling HV19 for the FLC causes a change from a previous dynamic calculation of the FLC based on the prior strain history of every element to a static calculation.

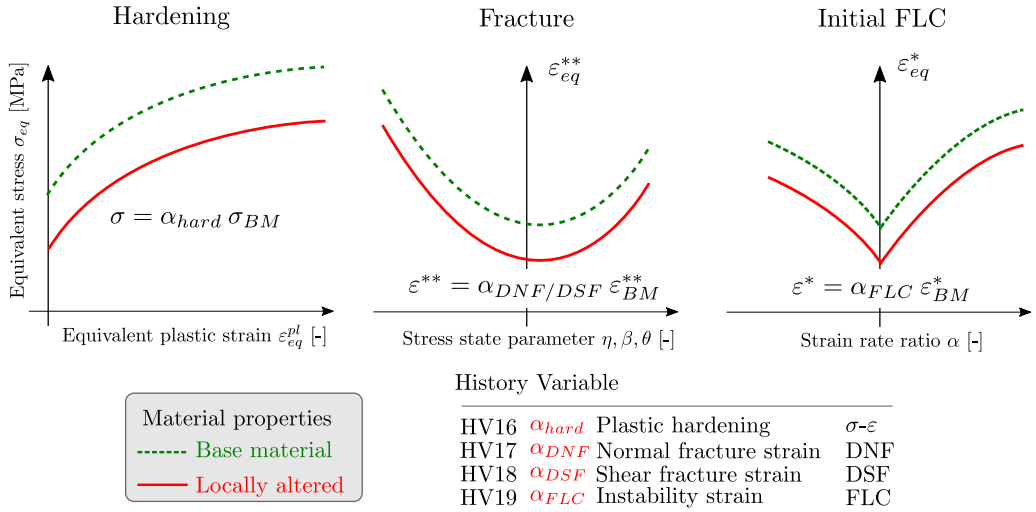

Figure 6.13.: Scaling of history variables HV16 - HV19 in MF GenYld+CrachFEM

Figure 6.12b shows an exemplary initialization of a single shell element representing the bulk material in the rivet head. With the initialization routine MF Init, the values of the history variables of every single integration point across the thickness can be changed with respect to the base material (BM). The individual assignment of specific values for every single integration point across the thickness of a shell element allows to integrate gradients of material properties in the respectively coarse discretization. A series of elements can be addressed either individually or by a range of numbers. The initialization routine MFInit hence represents an enhancement of the interface in Abaqus to initialize solution dependent variables (SDV) of a user-defined material model defined by the keyword **Initial Condition, type=Solution*. The use of MFInit allows the individual initialization of every integration point (IP) [144].

6.5. Parameter identification for a single loading

The damage identified in the previous section using μCT-scans of the thermo-mechanical joining process is integrated in the simulation by altering the history variables of the inner shell elements representing the rivet head. The damage originated from fiber breakage, imperfect re-connections of the matrix and voids is best represented by decreasing the plastic hardening behavior of history variables 16 (HV16). The HV16 will be adapted for every section point following the gradient of damage found in Figure 6.11b. For the beginning, this is done for every load case individually in order to find the best agreement in force-displacement curves for the different loading scenarios, head tension and shearing in transversal, and longitudinal direction. The found scaling parameters representing the damage induced by the joining process are displayed in Tables 6.1-6.3 and are obtained individually for every load case. The scaling is done for the inner row of shell elements right next to the T-joint in the cross-section as indicated by the gray element in Figure 6.12b.

6.5.1. Head tension

Table 6.1 summarizes the optimal set of parameters for the head tension across the thickness for all integration points across the thickness and their respective position. In Abaqus, integration points (IP) are referred to as section points (SP). The gradient of factors across the thickness resembles an extensive down-scaling for the section points on the bottom representing fiber breakage and imperfect connections or cavities on the bottom of the rivet head. Further, a pronounced gradient of the HV16 across the thickness can be seen from quasi zero at the bottom to 1.0 resembling the intact material behavior of the base material on the top of the rivet head.

Table 6.1.: Optimal parameters for load case head tension

Position	Number of SP	HV16	HV17	HV19
Upper side	5	1.0	1.0	1.0
-	4	1.0	1.0	1.0
Membrane	3	0.75	1.0	1.0
-	2	0.15	1.0	1.0
Lower side	1	0.01	1.0	1.0

The initialization of the damage in the lower section points 1-3 allows not only a good correlation in the force-displacement curves between experimental replicates and simulation results, but it also assures that both sides of the rivet head can pivot around the intersection where the horizontal and vertical elements share common nodes.

6.5.2. Shearing in transversal direction

Table 6.2 summarizes the scaling parameters obtained for the transversal shear loading. A strong gradient of the scaling factors can be observed here; the HV16 value for the upper integration points saturates around a value of 0.65.

Table 6.2.: Optimal parameters for load case transversal shearing

Position	Number of SP	HV16	HV17	HV19
Upper side	5	0.65	1.0	1.0
-	4	0.65	1.0	1.0
Membrane	3	0.65	1.0	1.0
-	2	0.03	1.0	1.0
Lower side	1	0.01	1.0	1.0

6.5.3. Shearing in longitudinal direction

Table 6.3 lists the parameters for the longitudinal shear loading. As for both loading scenarios, the strength of the rivet head has a supportive role; these scaling parameters ensure a stable deformation throughout the In order to simulate shearing-off of the bridge

Table 6.3.: Optimal parameters for load case longitudinal shearing

Position	Number of SP	HV16	HV17	HV17
Upper side	5	0.65	1.0	1.0
-	4	0.65	1.0	1.0
Membrane	3	0.65	1.0	1.0
-	2	0.03	1.0	1.0
Lower side	1	0.01	1.0	1.0

across the metallic deck panel properly, an additional edge-to-edge contact has to be defined in Abaqus. This is best done by defining the edges of both shearing parts as free edge using the keyword **Surface property assignment, property=feature edge criteria.*

Figure 6.14 displays the averaged experimental results in cyan color across all experimental replicates as well as corridors of experimental scatter in gray color. For the development of the surrogate model the averaged experimental results are used as the reference curve.

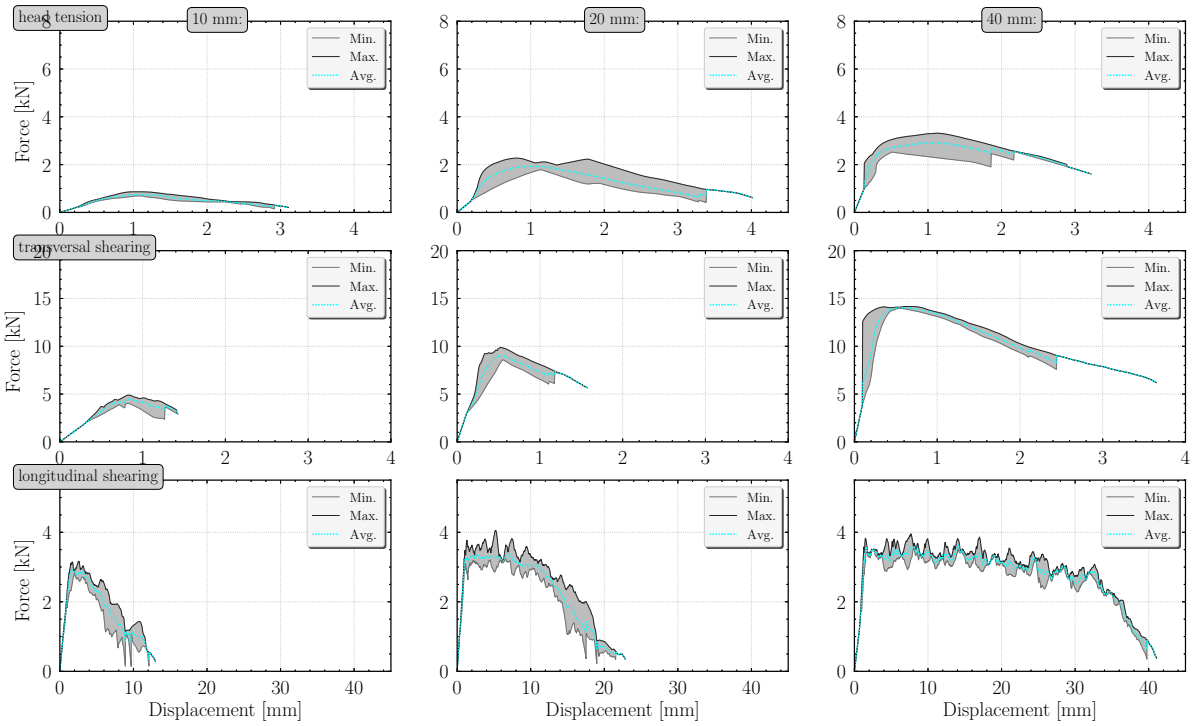

Figure 6.14.: Comparison of the minimal, maximal, and averaged force-displacement curves across all experimental replicates and the simulation results for the two sets of parameters

6.6. Iterative parameter identification of multi-axial loading

The different scaling factors found individually for a single loading type summarized in Tables 6.1, 6.2, and 6.3 represent the best accordance of the deformation and failure behavior between experiment and simulation for a single loading, e.g. shearing in longitudinal direction. As these parameters deviate from one another, a global compromise across all loading types and bridge lengths needs to be found. Head tension is the most crucial load case because the force flux goes directly through the rivet head which underwent thermo-mechnical forming during the joining process. For both shearing types, the rivet head has a supportive effect to keep the bridge in the open hole of the deck panel while the failure behavior is mainly triggered in the base material of the organic sheet.

Figure 6.15 displays the force-displacement curves for the optimal set of parameters across all loading types and variations of bridge length. Displayed in gray colors are the experimental replicates displayed with equidistant points over time and in green are the simulation results for the optimum. For a lucid representation of the bridge length influence, the scales of abscissa and ordinate are uniform for every line.

Table 6.4.: Optimal parameters across all load-cases

Position	Number of SP	HV16	HV17	HV19
Upper side	5	0.65	1.0	1.0
-	4	0.65	1.0	1.0
Membrane	3	0.65	1.0	1.0
-	2	0.04	1.0	1.0
Lower side	1	0.01	1.0	1.0

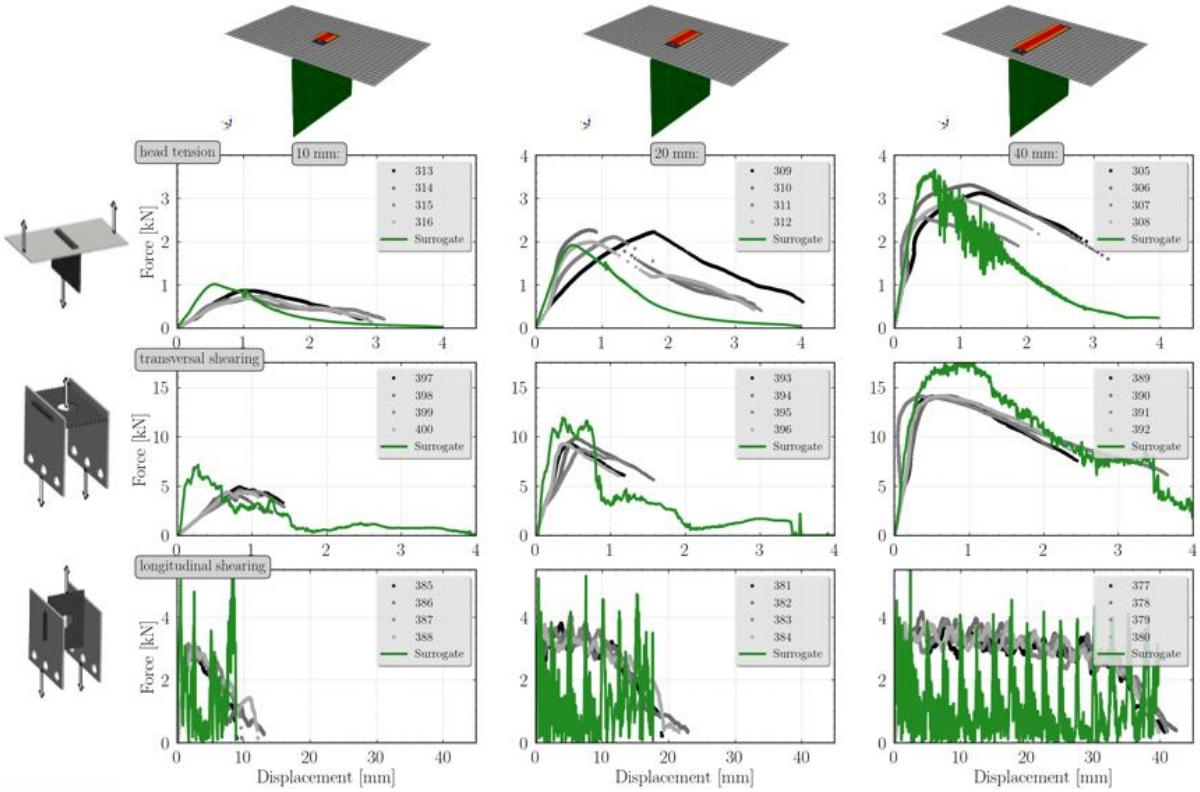

Figure 6.15.: Comparison of the force-displacement curves from experiments and simulations using the surrogate model

The smallest bridge length is dominated by start-up and ramp-down phases, which can be seen by a deviation already in the linear elastic range. This phases constitute also the biggest geometrical deviations in the shape of the rivet head between the physical joint and the FEM mesh. Further, the transversal shearing for higher bridge length showed plastification in the deck panel as well. Hence, the focus for the calibration of the damage parameter in the rivet head lies on the head tension of 20.0 and 40.0 mm bridge length while complying with the transversal shearing as much as possible. The biggest difference between the experiments and simulation results using the low-fidelity surrogate model is observed for the continuous shearing in longitudinal direction along the bridge. The abrupt elimination of shell elements as soon as they reach the critical threshold of either

failure criterion does currently not account for the post-critical behavior as outlined in Section 4.3.3.

The optimal set of global parameters are summarized in Table 6.4. With this set of parameter the simulation results as displayed in Figure 6.15 can be achieved across three different loading types and bridge lengths. These parameters are found by a semi-automatic approach running all simulation at the same time. In this procedure 60 sets of parameters, with 9 single simulation runs are conducted, to compare the influence on the parameters across all relevant loading types and bridge lengths. Besides an initial change of the orientation in the rivet head and a reduction of the Young's modulus at the beginning and the end, the main parameters which were subject of the analysis are the damage values across the thickness for every single integration point. In order to obtain the best result, the local and global quality criteria for comparing the force-displacement curves from experiment and simulation introduced in Section 5.2 are used.

6.7. Concluding remarks

The development of low-fidelity, surrogate mechanical models is successfully demonstrated for the hybrid material pairing of Tepex® dynalite 102-RG600 serving as the bridge panel and the S355JR as the deck panel. The proposed solution is further capable to cover also multiple bridge lengths for the bridge-deck panel concept. Incorporating the damage induced by the thermo-mechanical forming process using a remote laser has a pivotal role for assuring a good quality of the surrogate model.
These parameters are obtained by an iterative simulation of all load-cases and lengths of the joint. By automation of the simulation runs and the assessment of the quality of fit between the experimental replicates and simulation results obtained with the surrogate model, the procedure can also be used in the future for a numerical optimization.

The proposed and envisaged approach by deducting a high-fidelity detail model of the joint in a first step and then by deriving a low-fidelity surrogate model in a consecutive step is difficult to achieve for the organic sheet being involved. A more refined approach for the detailed model would necessitate to move from a macroscopic to a mesoscopic scale for the material model and hence model the four layers individually. To represent the influence of cavities and fiber breakage due to the forming process would need a statistical scatter of these properties, which were not obtained experimentally.

Since the failure behavior of the bridge-deck panel joints is mainly dominated by the material of the rivet head, which underwent thermo-mechanical forming, the failure assessment of the hybrid material joint focused primarily on the failure behavior of the organic sheet. For the in-plane failure analysis of the metallic deck panel it was assumed

that the stress raising effect of the geometrical notch by the rectangular hole is well-covered with the material description of the base material and the mesh. Additional stress raisers to account not only for the geometrical but also the metallurgical notch effect due to the hole or a heat-affected zone due to the cutting out of the rectangular hole with a remote laser are not further analyzed.

Even though moderate strengths are obtained, the joining concept can be enhanced in the future by adding either adhesive promoter at the interface or introducing a structuring using a laser on the metallic deck panel for enhancing the bonding surface. From a process point of view, different concepts for joining metallic and organic sheets have been developed which reduce the damage and destruction of fibers and hence yield higher strengths for this hybrid material pairing. Integration of thin metal pins in the interface allows the endless fiber to wind around them, reducing the fiber destruction and can hence ensure an elevated force flux throughout the hybrid material pairing proposed e.g. by [145, 146].

7. Surrogate models for hybrid steel-aluminum weld lines

„The easiest solution may not necessarily be the worst one"

Harry Dell

The welding of hybrid steel-aluminum pairings poses some challenges due to the different melting temperatures θ, thermal conductivities λ, and lattice structures, which cause a reduced solubility between the material pairings. However, the laser beam is a very fine beam and allows very precise steering to control the thermal input in the joining zone. The different lattice structures normally allow only for a limited solubility of 18 % of aluminum in iron while compositions with a higher degree of aluminum in iron lead to the formation of hard and brittle intermetallic phases (BIP) [100].

The development of the joining process as well as the experimental characterization of the hybrid material joints were conducted in the scope of the research project *LaserLeichter* by the *Laserzentrum Hannover e.V.* (LZH) [147]. In the remaining part of this chapter experimental results from the LZH are summarized and the experimental characterization of the hybrid material joints serves as an input for the developments presented here, i.e. for the proposed surrogate modeling technique of hybrid material pairing between a steel and aluminum sheet welded directly in a lap joint by a remote laser beam source. The experimental and metallographic analyses were discussed and coordinated between the *LZH* and *MATFEM*.

7.1. Remote laser welding of hybrid steel-aluminum pairings

For the experimental analysis, the energy per unit length was varied by changing both, the power as well as the feed speed of the laser beam. Apart from the energy per unit length other influences on the obtainable strength of the hybrid steel-aluminum pairing in a lap joint were investigated such as:

- material grade,
- sheet thickness,
- weld type (lap weld and fillet weld),
- irradiation (aluminum- and steel-sided).

a lap joint with a lap weld for the steel-sided irradiation and a fillet weld for the aluminum-sided irradiation [101] Figure 7.1 displays the different weld types for steel-sided irradiation on the left and aluminum-sided irradiation on the right.

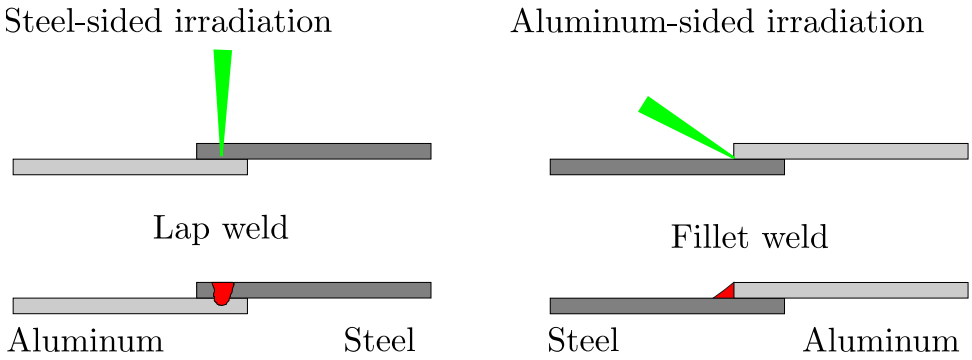

Figure 7.1.: Schematic setup for the laser beam welding of different dissimilar lap welds and fillet welds for steel and aluminum with steel-sided and aluminum-sided irradiation on the left and right, respectively [101]

Besides metallographic analysis, the strength of the hybrid material pairings was analyzed using a single lap shear specimen under tension in accordance with DIN EN ISO 14273 and the optimal sets of parameters were identified for different material combinations. More detailed information on the welding process can be found in the final report from *LZH* [147] and the corresponding publications [101, 148].

7.2. Characterization of hybrid steel-aluminum weld lines

Because of the high experimental effort for the comprehensive characterization of the joint as an input for the development, it was conducted exemplarily for the hybrid material pairing of HX220LAD+Z100 in 1.00 mm thickness and EN AW-6016 T4 in 1.15 mm thickness. The optimal set of parameters for the joining process defines a narrow process window for the welding of hybrid steel-aluminum weld lines by means of a remote laser beam [149]. Already small deviations in feed speed can cause significant changes in the geometrical dimension and mixture of the adhesion. In addition, even with the optimal parameters for joining, significant experimental scatter occurred, which can be explained by two independent effects:

- Formation of brittle intermetallic phases and potential micro-cracks. Such a weak imperfection is located directly in a heavily loaded zone, e.g. directly under the punch for a three-point bending test, which will result in an immediate failure even for relatively low loads.
- Different solidification in the melting pool. Taking this into account, the cross-section of the metallographic cut resembles only a small snapshot of the welding and approximates the depth and width of the adhesion momentarily.

Because of the pronounced experimental scatter of the material properties in the area of the weld (weld metal and heat affected zone), the weld line has to be over-dimensioned for safety-relevant components. This assures a failure initiation in the base material where materials properties can be obtained in a precise and reproducible manner [61].

Even though aluminum alloys were welded in the T4-condition, they were submitted to natural aging at RT before the mechanical testing was performed. Therefore, the material behavior of the aluminum alloys corresponds well to the solution annealed and artificially aged (T6) heat treatment condition rather than to the solution annealed and naturally aged (T4) condition. For structural parts, which are later submitted to the cathodic dip painting (CDP) process in the manufacturing of the BIW, the T4-condition is favorable to conduct welding and deep drawing processes for its lower yield stress and higher fracture toughness, which render it more suitable for forming while reducing the wear of tooling [135].

7.2.1. Experimental characterization

Based on the experimental findings of the process analysis, an experimental program was conceived for the specimens now welded with the optimal parameters. The welded specimens of the hybrid material connection need to be characterized experimentally to obtain the parameter values for the FEM simulations and the development and calibration of surrogate models. The experimental program includes a head tension, a three point bending with the weld seam in longitudinal direction under two different orientations, and a double lap shear specimen (see Figure 7.2). The double lap shear specimen bears the advantage compared to the single lap shear specimen of reducing the bending component ensuring a predominant shear loading of the weld seam. For a single lap shear test, the specimen commences to pivot around the joint, such that the local loading is gradually changed from an initial pure shear loading to a combined loading with an increasing proportion of head tension. Therefore, the single lap shear specimen is more a technological test usable for validation but inappropriate for experimental characterization of the joint under pure shear loading.
Further bonded cross tests were conducted for investigating the deformation and failure behavior under local head tension of the joint. However, the bonded cross test as displayed on the top right of Figure 7.2 has two drawbacks resulting in very low strengths.

Firstly, due to the long metal stripes, a lot of energy is dispersed in elastic deformation before the weld seam commences to bear significant loading. Secondly, for the bonded cross tests, the start-up and ramp-down phases are both included in the weld seam, which are also the areas where the highest stress distribution is observed in the interface (see stress distribution along the length of the weld seam on the top right of Figure 7.2). The last setup is a 3-point bending test as displayed on the bottom of Figure 7.2. This test evokes an out-of-plane loading of the weld seam under conditions that are representative for a real load case. Because of the different Young's moduli of the steel $E^{St} = 210\,\text{GPa}$ and aluminum $E^{Al} = 70\,\text{GPa}$, the neutral axis under 3-point bending shifts from the geometrical middle towards the stiffer, steel part, resulting in a local loading dominated by tension for the root sided bending and compression for the top sided configuration. Even though the proposed characterization scheme deviates from the discussed state of the art, the set-up of these experiments constitutes the best practice of effects discussed in Section 2.4 for the characterization of the hybrid steel-aluminum joint.

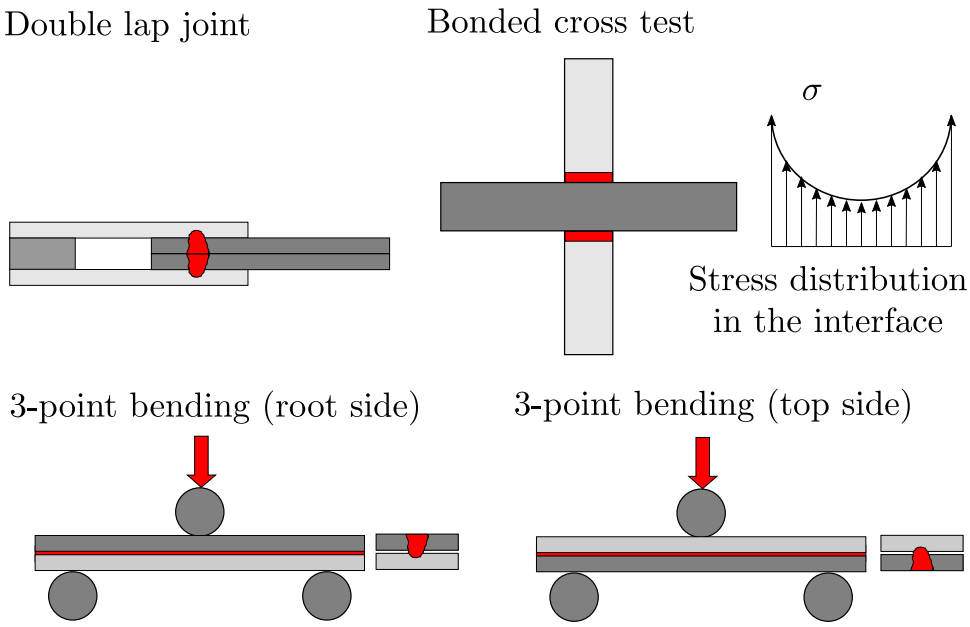

Figure 7.2.: Experimental characterization of the steel-sided irradiated joints for aluminum in light gray and steel in dark gray

7.2.2. Metallographic analysis

Complementary to the mechanical tests under different loadings metallographic analyses were conducted. Micro-cuts of the weld line were realized in longitudinal and transversal direction w.r.t. the weld line as well as the penetration depth and adhesion width of the weld line. Etching of the surface in the micro-cuts was done to identify the different metallurgical grain structures of base material (BM), heat-affected zone (HAZ) and the

weld metal itself.[1] Additional line scans on the transversal micro-cuts with micro-hardness measurements of Vickers $HV_{0.1}$ were used to back these findings.
The chemical composition of the binary system was scrutinized using an energy dispersive X-ray spectroscopy (EDX) to detect the brittle intermetallic phases with their strength reducing influence on the mechanical properties of the joint. The occurrence of BIP is found in a zone with higher aluminum content on the bottom of the weld seam.

7.2.3. Brittle intermetallic phases

The findings of the analysis are that the optimal strength for hybrid material pairings is obtained via a compromise between the geometrical dimensions of the weld seam (welding penetration depth and adhesion width) and the occurrence of brittle intermetallic phases (BIP) [147]. A too deep welding penetration will result in a high mixture of the melting pool causing the formation of brittle intermetallic phases, which tend to fail under a brittle fracture mode and therefore reduce the strength of the weld line tremendously [100, 101].

Moreover, since no additional material is used for the laser beam welding, e.g. a welding wire, it is assumed that the representation of the alteration of the base material due to the heat input by the laser will suffice. The geometrical dimensions and influence of the joining process will be scrutinized with microstructural analysis.

7.3. Simulation for multi-axial loading

Due to the occurrence of the brittle intermetallic phases in the lower part of the weld seam, the hybrid steel-aluminum weld lines are prone to brittle fracture and hence very little ductility compared to the base materials is seen. For the development of a detailed and surrogate model, hybrid material pairings are chosen here deliberately, which show the highest amount of ductility prior to failure initiation. For this reason the first material pairing is chosen among the potential hybrid steel-aluminum pairings joint in a lap weld with steel-sided irradiation:

- HX220ZE+LA 1.00 mm & EN AW-6016 T4 1.15 mm,
- X5CrNi18-10 (1.4301) 1.50 mm & EN AW-6082 T6 1.50 mm.

[1] weld seam = HAZ + weld metal

Prior to the development of the surrogate model, a detailed model with a fine discretization using only solid elements is constructed. In a consecutive step, a surrogate model is deducted using a hybrid mesh containing both shell and solid-elements. The discretization of the surrogate model is chosen so that the actual geometry of the joint is approximated as closely as possible, while bearing in mind that the objective for the surrogate model is not to reduce the overall critical time step in the explicit simulation. For the development of the surrogate model, the experimental results are used; in addition, the detailed model is used serving as a virtual laboratory. Based on the metallurgical analysis in cross-section cuts of the weld in longitudinal and transversal direction to the weld line, it is assumed that the geometrical deviation along the weld line lies in a small range for the chosen hybrid material pairings. For the discretization of the detailed model, the cross-section cut transverse to the weld line can be used as a blueprint. In doing so the different areas and characteristics of the base material, HAZ, and the weld metal can be depicted exactly.

A particularity of the steel-aluminum hybrid weld lines is the transition zone between the two metals in the weld seam. Not only BIP as well as micro-cracks can occur here, but also a blending of the metals can partially take place leading to an island effect. Because of the heterogeneity of the weld seam area together with the imperfections (BIP and micro-cracks), the manufacturing of miniature tensile specimens for a characterization of the local material properties of the weldline is not feasible. Further, the assumption to scale the hardening behavior in correlation with the local distribution of micro-hardness reaches its limit, since with the occurrence of BIP, micro-hardness measurements become five times higher compared to those of the base material. In the macroscopic material description, this area is described here in a smeared manner, with a plastic strain hardening curve using a linear interpolation scheme linking the micro-hardness measurements to the plastic strain hardening behavior of the base materials from steel and aluminum. The thus obtained material card provides a correct depiction of the material behavior in the weld seam across all scrutinized loading scenarios. In order to account for the pronounced experimental scatter, different approaches realized via MF GenYld+CrachFEM are proposed here. The material specific scatter of the fracture curves can be captured by a probabilistic design. In the study, a thorough analysis of the 3-point bending for the upper- and root-sided orientations clarified that due to the re-alignment of the neutral fiber from the geometrical center towards the stiffer steel part, the critical weld seam is loaded locally under tension and compression. This different local loading can also be observed in the experimental results. The BIP and micro-pores and -cracks in the weld seam have a strength reducing influence under tensile loading (root sided orientation), while under compressive loading (top sided orientation) higher force levels can be obtained. To account for this asymmetrical behavior under tension and compression, two different approaches are implemented and compared with one another. The first approach in MF GenYld+CrachFEM originates from the simulation of high pressure die casts (HPDC), in which pores arise in an in-homogeneous manner across the wall thickness. These pores from the cast material can be initialized as a type of damage in the simulation model and behave differently under tension and compression, which can

be quantified with an evolution law. A different evolution under tension and compression dominated loadings influences indirectly the curve for the ductile normal fracture (DNF). The second approach to take into account the different strength under tension and compression is the implementation of a stress-based fracture locus. Analogously to the definition of a yield locus, the fracture locus can be differently scaled for tension and compression or modified with a waist function (see Figure 2.7 in Section 2.2.2). Depending on the stress state, the fracture locus in stress space hence defines a threshold for the onset of failure. Stress-based failure criteria are commonly used for the description of fracture of composites (see Section 2.3.4) or for metals under very low temperatures (see Section 2.2.3). The use of a stress-based fracture criterion harbors the danger, that the stress-based threshold might be surpassed due to an overshoot in the system leading to a premature triggering of the stress-based criterion. To counteract this effect, the stresses can be filtered in MF GenYld+CrachFEM either over the number of time increments or based on drag pointer. The second approach discussed above is used in this thesis because of its universality. All welded hybrid material pairings manufactured at the LZH in the scope of the process analysis, showed very little ductility prior to failure. To keep the approach as generally applicable as possible, the stress-based failure criterion resembles the most promising approach to account for the failure of brittle phases in steel-aluminum hybrid material pairings. As soon as a discretization is fixed based

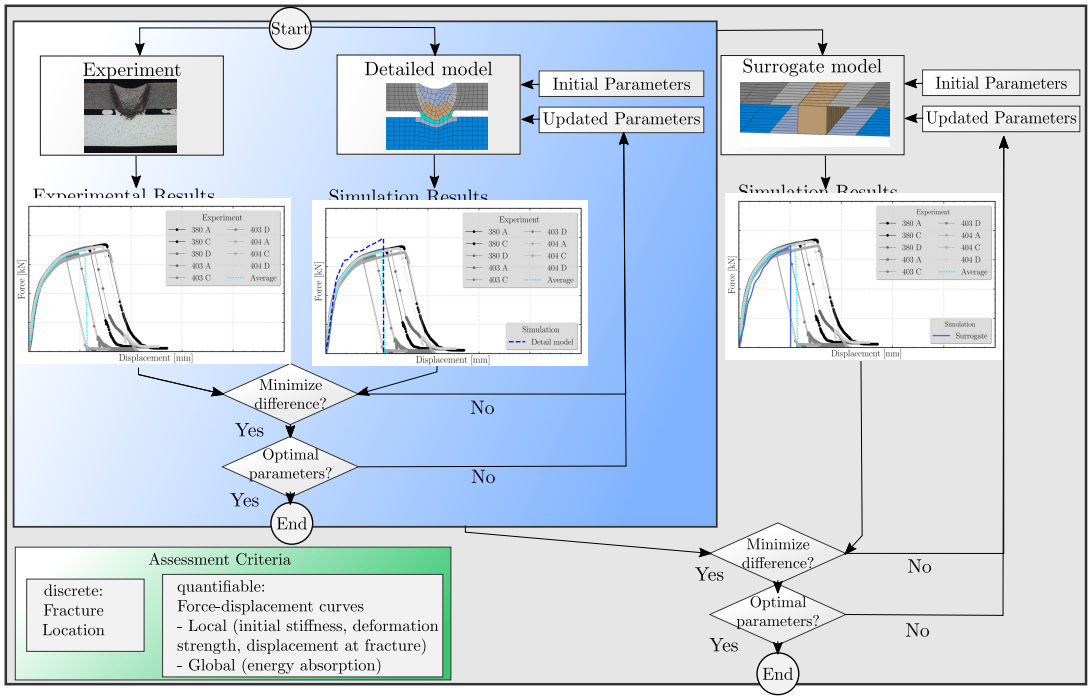

Figure 7.3.: Schematic representation for the parameter identification for a 3-point bending of a hybrid steel-aluminum weld line

on an abstracted geometry of the joint, the material parameters for the hybrid material pairing can be calibrated iteratively following the scheme in Figure 7.3. This allows to

account for the local alteration of material properties due to the thermal input by the laser beam by only using the material cards of the base materials. This parameter calibration is done in two consecutive steps; first for the detailed model and then for the surrogate model for every single load case. All parameters identified for a single load case define hence a parameter corridor within which the global optimum can be found. The global optimum includes all load cases, in order to fit a preferably versatile model across a wide range of load cases. For the iterative calibration of parameters, distinct and quantifiable criteria are introduced. An example of a discrete criterion is the correction depiction of the location of failure initiation. In case the location of the experiments and the simulations do not longer coincide after the latest iteration, the set of parameters is declared not valid. All other remaining quantifiable criteria rely on the comparison of the force-displacement curves between the averaged experiments and simulation and depend on one another. This approach aims to gradually meet all the properties of the compound along the loading history: starting with the stiffness, followed by the strength and failure until displacement of the joint, which eventually all accumulate in the global energy absorption capacity of the joint (area below the force-displacement curves). Stringing together local and global criteria allows not only a clear allocation of parameters to properties of the joint, but also to objectify the parameter identification. A weighting of these criteria for the optimization or a weighting of load cases has an immediate impact on the desired effect representation or in fact it is a prioritization of the load cases relative to one another. For the analyzed load cases and material combinations a single shear test of the lap joint and 3-point bending under two different orientations is regarded. The simulation of head tension is deliberately not used, because due to the manufacturing the start-up and run-down phase of the laser cannot be excluded from examination and these are exactly the same critical spots for the highest stresses under head tension.
For all analyzed hybrid material pairings, material cards for MF GenYld+CrachFEM were characterized covering the elasto-plastic material behavior including strain-rate dependency and a stress-state dependent fracture curve. Only for the material card of the HX220LAD+Z100, a transverse isotropic (transv.-iso.) Hill1948 yield locus is chosen together with a strain-rate dependent plastic hardening behavior with the analytical strain-hardening law of Gosh. For the other materials an isotropic (iso.) vonMises plasticity is used; modeling of hardening as well as fracture behavior in the quasi-static (qs.) case was found to be sufficient. The forming limit curves (FLC) for all materials are calibrated based on the quasi-static strain hardening behavior using the algorithm Crach in the software CrachLab (see paragraph Instability in Section 2.2.3 and [36]).

Table 7.1.: Overview of material cards derived for the hybrid steel-aluminum pairings

Material	Yield locus	Plastic Hardening	Failure		
			DNF	DSF	FLC
22MnB5+AS150	iso. vonMises	qs. Ghosh	qs.	qs.	CrachLab
HX220LAD+Z100	transv.-iso. Hill1948	Ghosh	qs.	qs.	CrachLab
EN AW-6016 T6	iso. vonMises	qs. Ghosh	qs.	qs.	CrachLab

The material modeling and derivation of material cards follow the same principle as outlined in Section 4.2 and in Appendix A.6. Due to confidentiality reasons, numerical values for the material properties cannot be published in more detail in the scope of this thesis. The material card for the HX220LAD+Z100 is hence based here on literature values taken from [150].

7.3.1. Simulation of load cases with a detailed model

For discretization of the detailed model, the cross-section cut of the steel-aluminum hybrid pairing displayed in Figure 7.4 serves as a blueprint for a correct and close follow-up of the geometrical details. The discretization of the detailed model is displayed in Figure 7.5. In the detailed model, the different colors represent zones for which a fairly homogeneous progression of the micro-hardness measurements is obtained. For these zones, a homogeneous material behavior is assumed for the simulation by scaling the plastic strain hardening behavior in accordance with the ratio of the micro-hardness measurements between the base material and the heat-affected zone (HAZ). By linear scaling of the plastic strain hardening behavior, which is represented by the history variable 16 (HV16) in *MF GenYld+CrachFEM*, the characteristic of the hardening curve remains constant. For the mixed zones of the binary systems, for which the occurrence of brittle intermetallic phases is detected by EDX, the material properties are averaged between the base materials; they are derived by scaling a plastic strain hardening behavior of the heat affected zones (HAZ) with the ratio of the micro-hardness measurements [151]. This proposed procedure yields a strong plastic strain hardening of the weld seam in Figure 7.5 ranging from the uniaxial tensile strength of the aluminum EN AW-6016 T4 to the saturation of the steel HX220LAD+Z100.

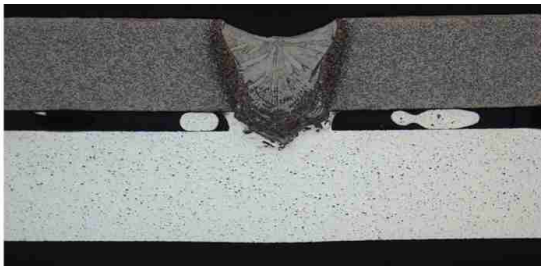

Figure 7.4.: Photograph of the transversal cross-section cut of the steel-aluminum-pairing for a steel-sided irradiation of HX220LAD+Z100 and EN AW-6016 T4 material pairing [152]

Using the derived discretization realizing the subdivision in different zones, the elasto-plastic behavior including failure of the base materials (BM) is assumed. Instead of conducting a separate material characterization using micro-tensile tests extracted from the HAZ, a linear correlation between the micro-hardness measurement and the plastic hardening behavior is assumed [141]. Pavlina et al. showed a linear correlation between

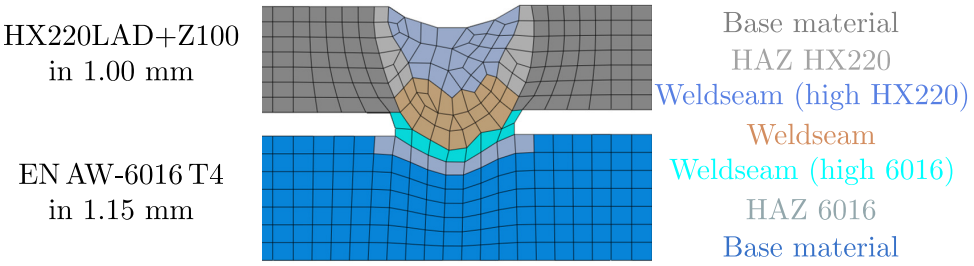

Figure 7.5.: FE mesh of detailed model including different zones

the micro-hardness measurement and yield strength and ultimate tensile strength for a variety of non-austenitic, hypoeutectoid steel grades [153]. The same type of correlation is assumed for aluminum. Therefore, scaling of the plastic hardening behavior of the BM is done with a quotient of the Vickers micro-hardness from BM and HAZ. Firstly, this up-scaling of the plastic hardening curve (HV16) correlates best with the yield strength and ultimate tensile strength (UTS) and secondly an additional adaption of the fracture criteria is not necessary for the HAZ and weld seam rich phase. An up-scaling of the HV16 will move the location of failure initiation to a different zone of BM and a down-scaling of, e.g., the HAZ will trigger a localization of the strains within the HAZ and therefore lead to a sudden increase of strains which renders an additional scaling of the fracture strain subordinate.
A plastic strain hardening for a hybrid material card, based on the mixture detected in the weld seam, and the corresponding micro-hardness measurements are created for the weld seam. Lastly, the failure initiation of the weld seam remains an unknown quantity. Because very little plasticity is observed in the experiments of the joint, a fracture initiation using the isotropic vonMises fracture locus is calibrated based on the experiments of the joint. The other diagrams in Figure 7.6 display the force-displacement curves for a single lap shear specimen and a three-point bending with weld seam either on the top side or root side. All force-displacement curves from the experimental replicates are compared to the simulation results with and without failure. Because of the pronounced experimental scatter due to the aforementioned dynamic of the melting pool, the average experimental results across all replicates are displayed additionally. A direct comparison of the simulation results with the averaged experimental curves shows good accordance across all load cases. Not only the initial stiffness of the welded hybrid material pairing is captured well but also the plastic hardening and the displacement until failure initiation are reproduced correctly in the simulation with the detailed model. Only for the single lap shear tests some deviations remain in the strength of the joint and the drop of force after the failure initiation is not as pronounced in the simulation as for the experiments. In the simulations, the failure initiation is reproduced correctly but too few elements will be eliminated leaving more material of the weld seam intact in the interface.

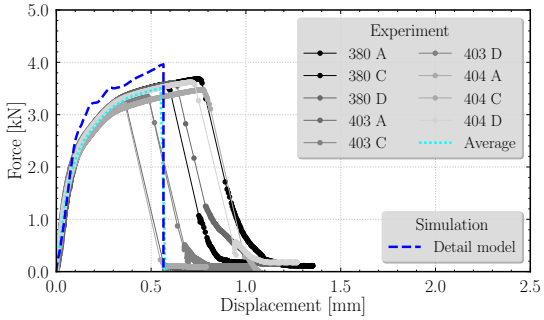

(a) Shear lap specimen

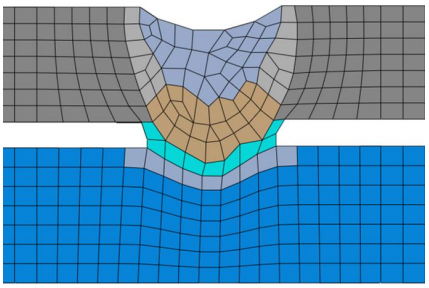

(b) FE mesh of the detailed model

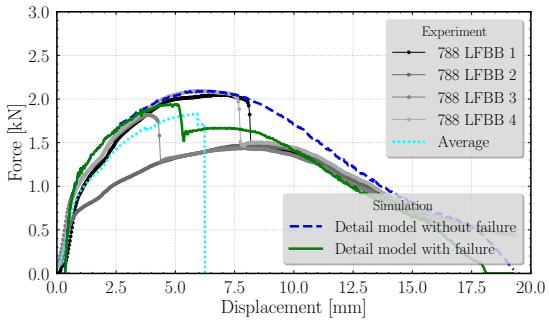

(c) 3-Point Bending upper side

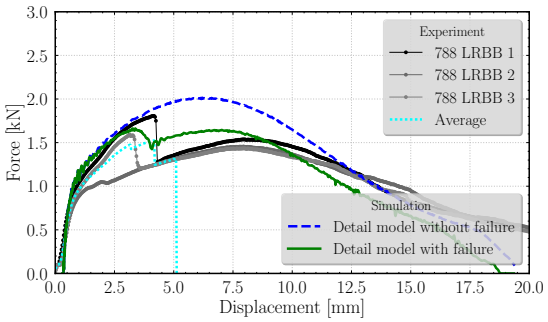

(d) 3-Point Bending root side

Figure 7.6.: Comparison of force-displacement curves from experiment and simulation using a detailed model

7.3.2. Simulation of load cases with a surrogate model

A special challenge is to transfer the results from the examination of the joints and the simulation using a detailed model onto the surrogate model. In order to account for the small geometrical dimension of the laser weld line of approximately 1.20 mm, the FE mesh needs to be refined in the vicinity of the weld line from originally 3.00 mm from industrial mesh requirements. This concerns only a small number of elements and the local refinement of the mesh and a concomitant reduction of the critical time step is deliberately accepted knowing that it can be compensated by a selective mass scaling of these elements. Further, the element in the middle serving as the connecting link between the two metallic sheets is discretized by solid elements because a full stress state allows also to transmit shear forces in the interface. In Figure 7.7, a schematic sketch of the cross-section for the proposed surrogate model is displayed using a solid element for the representation of the weld seam connecting the two metal sheets. The thickness of the shell elements below and above the solid element is reduced to half the sheet thickness using an offset in order to avoid an artificially higher mass due to overlapping elements.

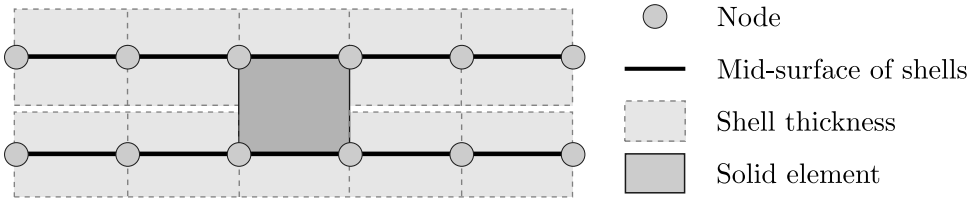

Figure 7.7.: Low-fidelity surrogate model for steel-aluminum pairing with steel-sided irradiation

The calibration of the surrogate model is based on the same distribution of micro-hardness measurements for the scaling of the plastic hardening behavior as for the detailed model. In the next step, the limits for the failure locus need to be calibrated. Because of the coarser discretization of 1.20 mm in the area of the weld seam and 3.00 mm in the rest of the surrogate model, the stress peaks are not dissolved in the same way and are displayed in a smeared manner using the surrogate model.

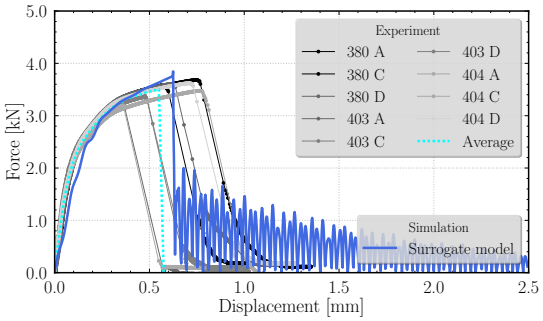

(a) Shear lap specimen

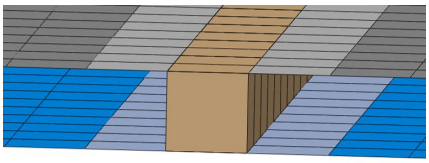

(b) FE mesh of the surrogate model

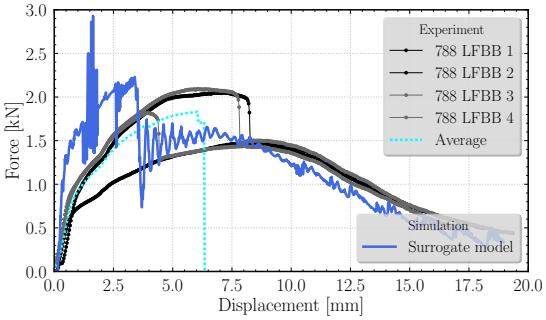

(c) 3-Point Bending upper side

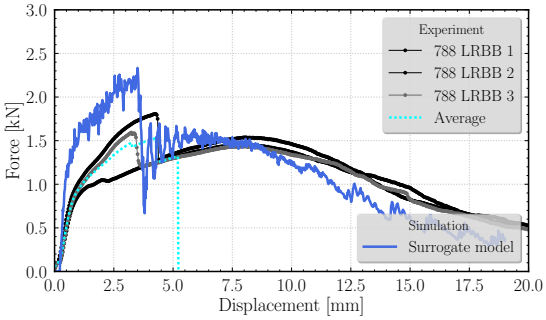

(d) 3-Point Bending root side

Figure 7.8.: Comparison of force-displacement curves from experiment and simulation using a surrogate model

Figure 7.8 shows, besides the discretization of the surrogate model, the force-displacement curves from experiment and simulation for the surrogate model. In the area of the weld seam, solid elements are used with shared nodes in both sheets. The shell discretization

of the sheets is continuous throughout the entire sheet. For all analyzed load cases not only the additional stiffness of the joint but also the failure initiation are accurately represented. The only deviation is the force level for the three-point bending tests which is overestimated in the simulation. This overestimation of the force level is due to a coarser shell discretization. Firstly, the results with a coarser shell discretization behave slightly stiffer. Secondly, because of the coarser discretization the heat affected zone is overestimated and the adaption of the plastic strain hardening behavior covers a broader area in the range of the HAZ than in reality. Besides, the stress states differ no longer as pronounced under tension and compression as for the detailed model because of the local scaling around the weld seam as for the detail model, which is why a compromise between the tension and compression dominated loading needs to be found. Still, with the restriction discussed above, the behavior in the force-displacement curves can be represented in good agreement with the experiment as well as the location of failure initiation can be accurately captured.

Table 7.2.: Comparison of the parameters and computational expense for the detailed and surrogate model

Model type	Level of detail in -	Average element size l_{avg} in mm	Computational time t in h	Fracture stress σ^{**} in MPa
Detailed model	High-fidelity	0.15	23.0	435
Surrogate model	Low-fidelity	1.20	0.5	350

Table 7.2 summarizes the main features of the detailed and surrogate model outlining the main differences as well as the computational costs for the different levels of detail. The brittle failure mode was modeled with a stress-based criterion for fracture initiation for the material representing the weld seam. The critical threshold for fracture initiation σ^{**} amounts to 435 MPa for the detailed model. Exchanging the detailed solid mesh (Figure 7.5) with the mesh of the surrogate model (Figure 7.7) it becomes evident that the fracture peaks are not resolved with the same accuracy, which is why the fracture stress σ^{**} is adapted in the material card. At the same time the computational cost for running the simulation of all three load cases is reduced from 23 h to under 30 min reducing the overall computational time to 2.17 %. Inserting the surrogate model into a component allows to represent the deformation and failure behavior of the hybrid material joint well without compromising the computational cost on component level.

7.4. Validation on component level

The weld lines analyzed and characterized above, are transferred to a generic validation structure. This validation structure is derived from an automotive B-pillar and comprises a hat profile made of press hardened boron steel 22MnB5+AS150 in 1.5 mm, a striking

plate from a galvanized higher strength steel HX220LAD+Z100 in 1.00 mm, and a cover plate made from aluminum EN AW-6016 T4 in 1.15 mm. The striking and cover plate are welded with the aforementioned parameters developed at the LZH. For the steel-steel joint between the hat profile and the striking plate welding parameters from LZH are used.

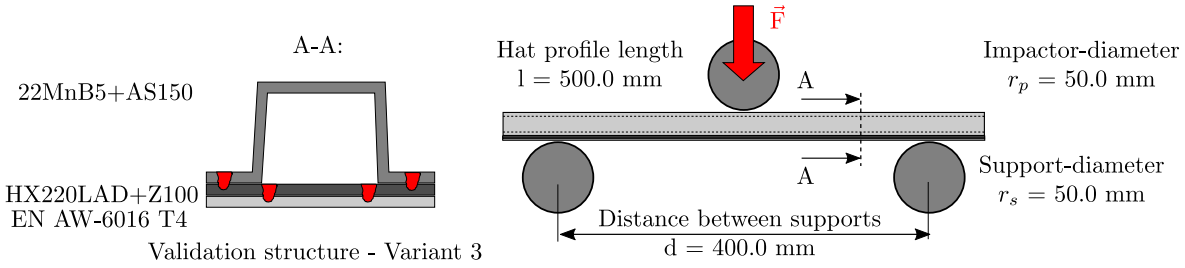

Figure 7.9.: Schematic representation of the joining on the left and experimental setup of the 3-point bending test on the right

An experimental program on the validation structure is subcontracted by Volkswagen AG (VW) to the *Forschungsgesellschaft Kraftfahrtwesen Aachen* (FKA) in the scope of the research project *LaserLeichter* and covers five replicates of a quasi-static and a dynamic 3-point bending load case. Firstly, the quasi-static 3-point bending tests are conducted and based on the measured force-displacement curves and the overall capacity of energy absorption was evaluated. Based on this calculated energy, mass and height of the drop tower test were calibrated, to ensure a comparable energy absorption for the quasi-static and dynamic test.

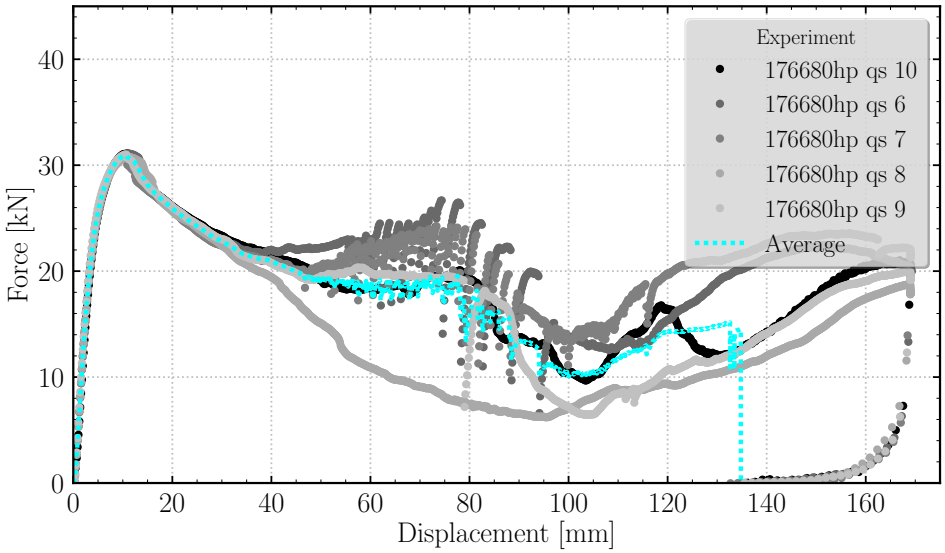

Figure 7.10.: Experimental force-displacement curves for the quasi-static 3-point bending

Based on the derived material cards for the steel sheets (see Table 7.1) and the experimental characterization of the hybrid pairings in the precedent chapters, the validation struc-

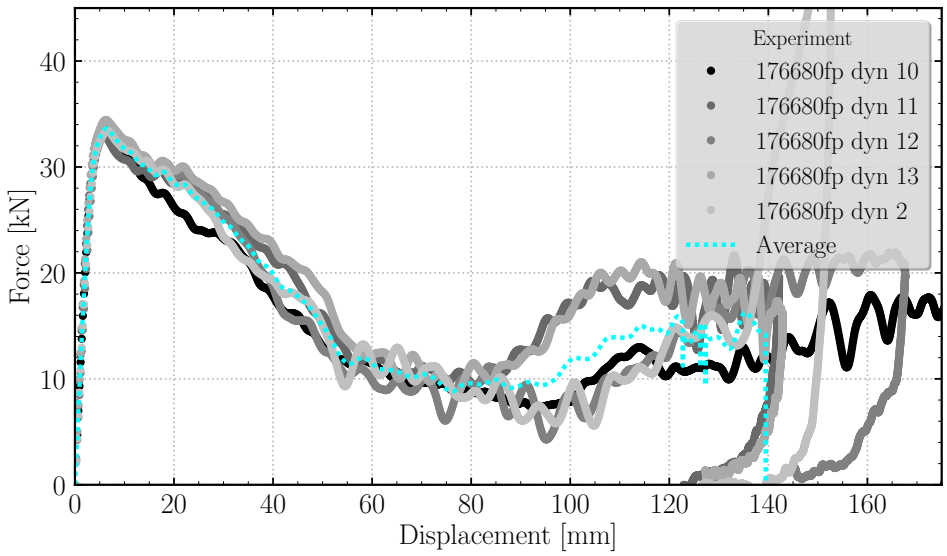

Figure 7.11.: Experimental force-displacement curves for the dynamic 3-point bending

ture can be simulated. Figures 7.10 and 7.11 show the experimental force-displacement results for all five replicates of the component test for a quasi-static and dynamic experiment, respectively. Comparing these two diagrams, very little scatter for each experiment can be observed and a pronounced influence of the experimental velocity on the stiffness and strength is visible. The oscillation of the measured force originates from a slipping of the structure from the supports. This stick-slip effect was eliminated in the following experiments by reducing the friction with the application of graphite spray on the supports. In surpassing the force peak, the validation structure commences to buckle in the hat profile. The failure of the weld seam between the striking and cover plates plays only a subordinate role in the characteristics of the force-displacement curves. For the experiment, only the hybrid material pairing of HX220LAD+ZE with 1.00 mm and EN AW-6016 T4 with 1.15 mm thickness is simulated with the surrogate model outlined above. For the weld lines of the similar material pairing between the boron steel 22MnB5+AS150 with 1.50 mm and the galvanized steel HX220LAD+ZE with 1.00 mm, no experimental input is available. Because this material pairing of two steel sheets does not include any brittle intermetallic phases, the joint will be modeled without failure in the simulation. Further, the punch and supports are modeled as rigid bodies. The supports are fixed. For the quasi-static load cases a constant velocity is applied to the structure. For the dynamic load case all other degrees of freedom are fixed and in the direction of the testing, a mass and initial velocity are defined for the punch, with which the punch hits the structure in the experiment of the drop tower test. Figures 7.12 and 7.13 show the simulation results of the generic validation structure from VW using the developed surrogate models for the quasi-static and dynamic 3-point bending. Comparing the force-displacement curves between experiment and simulation it can be stated that with the use of the surrogate

model the initial stiffness and the displacement and force at failure initiation as well as the global energy absorption of the structure are accurately represented.

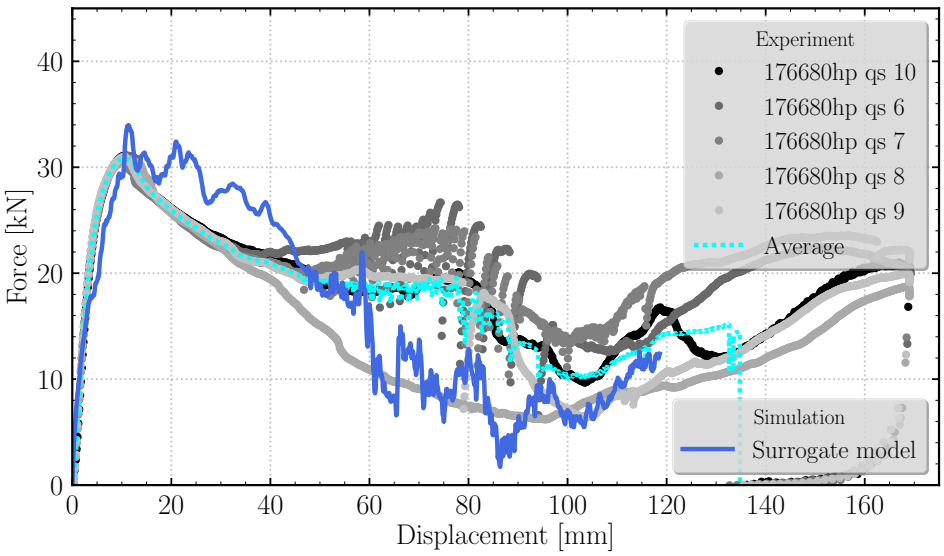

Figure 7.12.: Comparison of force-displacement curves for the quasi-static 3-point bending from experiment and simulation for the component

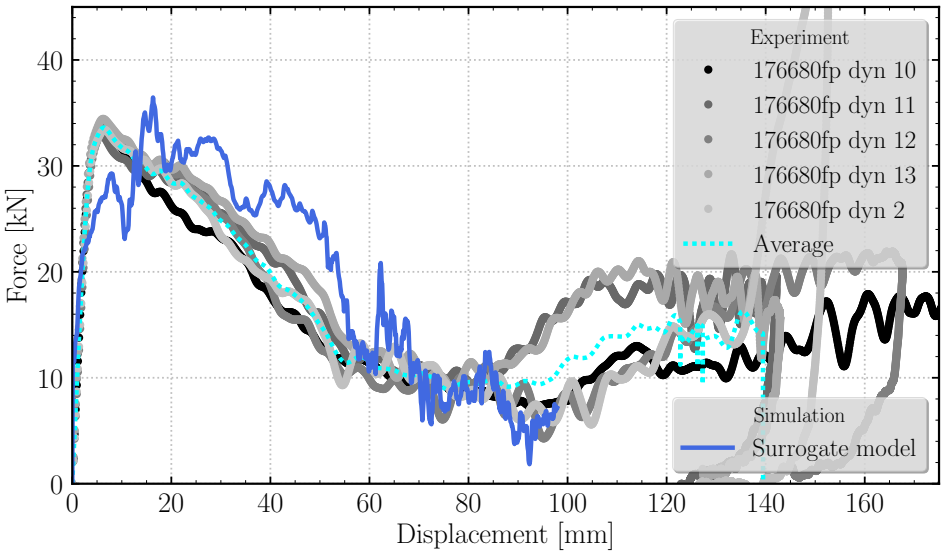

Figure 7.13.: Comparison of force-displacement curves for the dynamic 3-point bending from experiment and simulation for the component

Improvements in the correct depiction of the buckling behavior are found via including the waviness of the hat profile as an imperfection in the simulation model compared to the perfect dimensions of a FEM model based on the nominal geometrical dimensions. The slight underestimation of the force level in the simulation can be explained by the

imperfections of the validation structure which could not be captured in the simulation model. The FE mesh for the validation structure uses the nominal dimensions. In reality, the flanks of the hat profile are slightly inclined due to the springback behavior of the forming; in addition, the thickness distribution of the hat profile varies between 1.50 and 1.60 mm. The spread of the flanks could be integrated in the simulation model but the inhomogeneous thickness distribution could not be accounted for. Further, the development of the surrogate models is solely based on a quasi-static experimental characterization. Because of the force oscillation for higher testing velocities, only quasi-static experiments could be conducted. Hence, the strain-rate dependency in the surrogate model is only accounted for in the base material, but not for the properties of the joint. This can explain the good forecasting quality of the simulation for the quasi-static three-point bending as well as the slightly increased deviation for the dynamic testing.

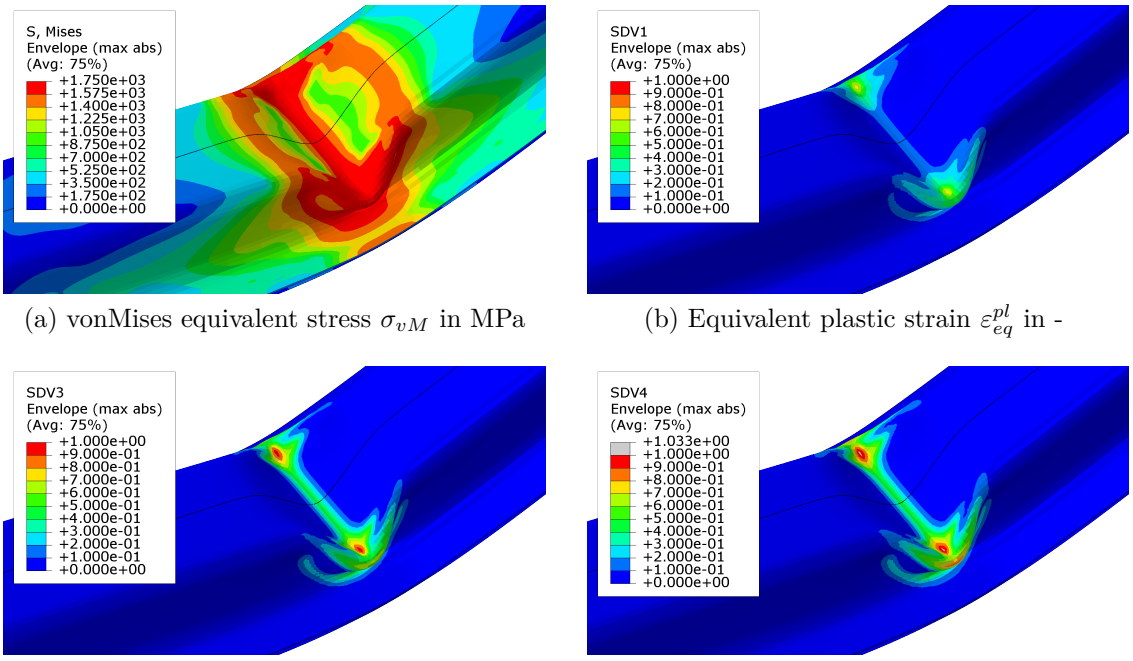

(a) vonMises equivalent stress σ_{vM} in MPa

(b) Equivalent plastic strain ε_{eq}^{pl} in -

(c) Normal failure risk Ψ_{DNF} in -

(d) Shear failure risk Ψ_{DSF} in -

Figure 7.14.: Simulation results of the deformed hat profile on the area below the impactor in an isometric view prior to failure initiation

Figure 7.14a through 7.14d display the deformed state of the hat profile prior to the failure initiation. The drop of force in the experiment is primarily dominated by the buckling of the hat profile and the joints play a subordinate role. In good accordance with the experiments, partial ablation of the weld seam between striking and cover plate can be observed in the simulation using the surrogate model. In Figure 7.14b a contour plot of equivalent plastic strain ε_{eq}^{pl} is displayed as well as the failure risk for normal Ψ_{DNF} and shear fracture Ψ_{DSF} in Figures 7.14c and 7.14d.

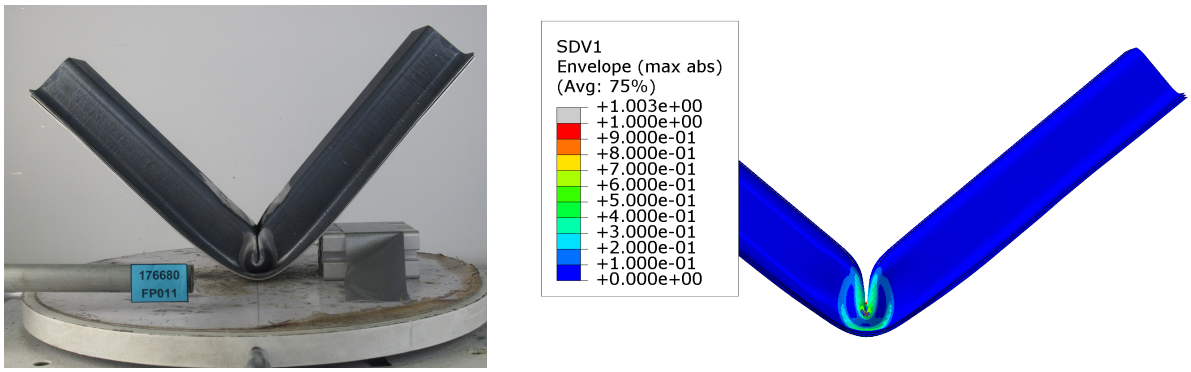

(a) The component after dynamic impact

(b) Equivalent plastic strain ε_{eq}^{pl} in -

Figure 7.15.: Comparison of the deformed component between experiment on the left and simulation results in Abaqus on the right at the end of the simulation

The qualitative comparison of Figures 7.15a and 7.15b displays that the deformed hat profile after the dynamic experiment is well-captured in the simulation with a buckling.

7.5. Concluding remarks

The proposed two-folded modeling strategy for surrogate models is successfully used here for the hybrid material combination of HX220LAD+Z100 and EN AW-6016 T4 for a steel-sided irradiation by a remote laser beam weld. While the high-fidelity, detailed model is computationally expensive it offers a high level of detail. The underlying material experimental input is used as a virtual laboratory for further analysis and calibration of the hybrid joint model. In a second step, the experimental characterization as well as the detailed model are used to develop a surrogate modeling technique. Even though the level of detail was reduced to lower fidelity for the very same joint, the surrogate model yields reasonable results in comparison with the experimentally measured force-displacement curves while reducing the overall computational time strongly to 2.17 % compared to the detailed model. Lastly, the surrogate model is successfully validated on component level.

The unsteady weld seam of the hybrid steel-aluminum pairing including imperfections such as the BIP culminates in a pronounced experimental scatter best observable in the characterization of the joints. Currently, this experimental scatter is not taken into account, neither in the detailed nor surrogate model. Future work could incorporate this scatter e.g. by imposing a randomly distributed scatter of the fracture stress σ^{**} for every single element in the area of the weld seam in the detailed model. With this approach, a transition from a deterministic to a probabilistic design is possible enabling robustness investigations of the material-based scatter.

Even though the detailed and surrogate modeling of the hybrid joint are successfully used here for the hybrid material pairing of HX220LAD+Z100 and EN AW-6016-T4, the restricted solubility of the aluminum in iron due to the different binary systems remains a challenge. The overall shear strength obtained for the joint is relatively low compared to the shear strength of the base material.
Further, on a component level it is found that using the nominal dimension of the hat-profile, the buckling prior to failure is wrongly predicted. Introducing imperfections as the waviness of the hat profile measured on the actual components can significantly improve the simulation. This outlines the necessity in the current state of the art for crashworthiness simulation to also account for the manufacturing history of the component. Usually, the pre-strain history and thickness distributions can be mapped in an integrative simulation approach from the deep-drawing simulation onto the mesh for the subsequent structural simulation.

8. Summary and outlook

„A chain can only be as strong as its weakest link"

8.1. Summary

Multi-material design combines the materials for their locally stipulated properties and efficient use of resources. For use of multi-material design, a material combination needs to be joined in a reliable and reproducible manner. Dissimilar material pairings such as the pairing of a textile reinforced composite (organic sheet) with metal or steel and aluminum are of special importance for their employment. Because of its high flexibility and high degree of automation the joining is achieved by remote laser beam welding.
For the virtual design in an early phase of a component possessing dissimilar joints mechanical surrogate models, which correctly depict the behavior of the joint in a simulation, are indispensable. The use of the virtual design allows to reduce cost- and time-consuming hardware tests on prototypes. However, because of the limitations of the model size in an industrial application, the joint cannot be modeled in detail and has to be represented by a substitute model. This surrogate model has to be capable of fully depicting the deformation and failure behavior of the joint under different loading scenarios.
Basis for the development of surrogate models is a comprehensive material characterization of the base materials, here proposed via the software MF GenYld+CrachFEM, in order to correctly depict not only the elasto-plastic but also the fracture behavior phenomenologically. Using the consistent, modular material model model allowed to obtain material cards for both monolithic steel sheets and for organic sheets. With the use of parameters determined throughout the process investigation, specimens are joined and examined experimentally under different loadings. On the basis of experimentally determined force-deflection curves, metallographic analysis, microhardness measurements, and μCT-Scans of the joint, a detailed model is created. This model enables with a fine discretization a thorough look at the behavior of the joint and once calibrated in good accordance can serve as a virtual laboratory for further numerical investigations of the joint. The joint behavior needs to be abstracted in a consecutive step for the development of the surrogate model, so that an industrial discretization level can be realized, for which

the material parameters are calibrated. The quantity of damage stemming from the joining process will be assessed with metallographic analysis, microhardness measurement and μCT-Scans of the joint. With the use of the user-defined material model it is further possible to initialize the locally induced damage by the joining process at the beginning of the simulation individually for every single integration point. This allows the surrogate model to include gradients of material properties and to account for local material alteration while using only a single material card for the base material and an industrial discretization. The surrogate model is designed as a sub-model to substitute the mechanical behavior on a component level without compromising the overall critical time step in an explicit time integration scheme. As it is the industrial standard for thin-walled structures to use only shell elements this means that the behavior of the detailed model using fine discretized solid elements needs to be abstracted that it can also be captured under the assumption of a plane stress state for shell elements. Because simplifications need to be made for the calibration of the surrogate model in comparison with the detailed model, not all joints can be modeled with the same precision across all loading scenarios. This is why quantifiable criteria for the evaluation of the model accuracy are introduced and weighted in accordance with the requirements of the model. With this procedure, an objective measure and target-oriented calibration of the substitute model is feasible for the considered loadings. Although the proposed workflow for the calibration of hybrid material joints is exemplarily developed for bridge-deck panel joints of organic and steel sheets as well as for hybrid steel-aluminum pairings, this procedure is universally applicable to dissimilar material pairings accounting for the irregularities. The simulation results provide a good approximation of the deformation and failure behavior, without a strong increase of the computational cost.

8.2. Outlook

The mesoscopically smeared elasto-plastic material modeling shows promising simulation results for crashworthiness load-cases while keeping the computational cost low. But the full elasto-plastic material modeling may also serve as the basis for localization phenomena in matrix rich phases of a multilayered EFRT resulting in both inter and intra laminar failure modes.
The material characterization presented in this thesis is based on a testing campaign with physical experiments. The critical cross-sections of these experiments are supposed to be large enough to be representative of the composite structure as a whole. In the future, material parameters of the composite can be derived from virtual experiments. Based on the material properties of fiber and matrix, the heterogeneous micro-structure of the composite can be modeled in an RVE. These homogenization schemes currently show promising results in a linear-elastic regime. However, for crash simulations, with highly pronounced material non-linearities and scatter afflicted properties for the fiber-matrix interface, covering pre-failure, non-linear yielding, and failure itself still remains

a challenge. Homogenization techniques based on RVE and RUC can in the future serve in a complementary manner for the substitution of physical experiments and provide macroscopic material parameters for the phenomenological description without rendering it obsolete. Nonetheless, future enhancements for the phenomenological material models can still improve the current state of the art. Phenomenological material modeling is a suitable and reliable method in other applications of various disciplines such as the material modeling of lamination stacks for asynchronous machines [72] or for the heterogeneity of timber and glulam[1] materials [118]. Especially in the context of composites and organic sheets, failure initiation is well described. However, the post-critical behavior ranging from failure initiation to the final complete collapse of the composite is currently covered only rudimentarily. The state of the art of an isotropic weakening across the thickness is derived from metallic materials. Future approaches should cover an in-plane anisotropic weakening of the composite after the onset of failure so that a pronounced fracture toughness can also be accounted for. This anisotropic weakening after the failure initiation entails a mesh regularization to compensate the pathological mesh dependency of material softening.
Both, the detailed and surrogate model are focused on failure initiation in the comparatively weaker material of the hybrid joint while neglecting a failure purely in the stronger joint partner. For the hybrid bridge-deck panel joints for instance a failure can originate from the notch of a geometrical hole in the deck panel. Enhancements could be developed here to also incorporate the geometrical and metallurgical notch effects via an initialization of the damage for boundary elements around the hole of the deck-panel as stress raisers.
The simulation quality for the surrogate model has been shown for two different material pairings across multiple loading scenarios representative for miscellaneous loading conditions. However, integrating the mechanical surrogate models in a component still requires some additional effort in the model preparation. This model integration could be subject of an automated routine to facilitate the use of the surrogate model as a sub-model in simulation on bigger scales.

Last but not least, a lot of discussion in this thesis focuses on the nature of different materials primarily for the material groups of ductile sheet metals and organic sheets. However, for the future there are some promising new technologies that can be used to further exploit the lightweight potentials of metallic structures for a more load-adapted design. Firstly, the use of a remote laser beam allows to increase the micro-hardness for martensite transformation hardenable non-austenitic steel sheets. Including traces of this locally strengthened zones enhances the crash performance [154]. This technique can be easily integrated into already existing designs and improve the formerly monolithic, overdimensioned design by a load-adapted texture. Further, in a broader sense the selective laser melting (SLM) of metallic structures allows to locally vary process parameters for a target-oriented and load-adapted design of parts, which can be conceived in an entirely new manner.

[1] abbreviation for glued laminated timber

References

Books:

[4] Klaus Dilger. *Kontiniuierliche kraftflussgerechte Textiltechnologien für Leichtbaustrukturen in Großserie - Ergebnisse aus dem BMBF-Verbundprojekt KonText*. Springer, 2020. ISBN: 978-3-662-61002-2.

[14] Wilfried Becker and Dietmar Gross. *Mechanik elastischer Körper und Strukturen*. Springer Verlag, 2002. ISBN: 978-3-540-43511-2.

[15] Ted Belytschko, Wing Kam Liu, and Brian Moran. *Nonlinear Finite Element for Continua and Structures*. John Wiley and Sons Ltd., 2000. ISBN: 0-471-98773-5.

[16] Peter Wriggers. *Nichtlineare FEM*. Springer Berlin, 2001. ISBN: 978-3-5406-7747-5.

[17] Wolfgang A. Wall and S. Tinkl. *Nichlineare Finite-Elemente-Methoden*. Lehrstuhl für numerische Mechanik - TU München, 2011.

[18] Dietmar Gross and Thomas Seelig. *Bruchmechanik - Mit Einführung in die Mikromechanik*. Springer Berlin, 2011. ISBN: 978-3-642-10195-3.

[21] Markus Stommel, Marcus Stojek, and Wolfgang Korte. *FEM zur Berechnung von Kunststoff- und Elastomerbauteilen*. Carl Hanser Verlag GmbH, 2018. ISBN: 978-3-4464-4714-1.

[24] Jacob Lubliner. *Plasticity theory*. Dover Publications, 2008. ISBN: 978-0-486-46290-5.

[26] Juan C. Simo and Thomas J. R. Hughes. *Computational Inelasticity*. Springer Science and Business Media, 2006. ISBN: 978-0-387-22763-4.

[34] Jean Lemaitre and Jean-Louis Chaboche. *Mechanic of Solid Materials*. Cambridge University Press, 1994. ISBN: 978-0-521-47758-1.

[37] Percy Williams Bridgman. *Studies in Large Plastic Flow and Fracture*. Harvard University Press, 1964. ISBN: 0-674-73133-6.

[41] Gottfried Wilhelm Ehrenstein. *Handbuch Kunststoff-Verbindungstechnik*. Carl Hanser Verlag, 2004. ISBN: 978-3-446-22668-5.

[42] Helmut Schürmann. *Konstruieren mit Faser-Kunststoff-Verbunden*. Springer Verlag, 2007. ISBN: 978-3-540-72189-5.

[43] Elmar Witten and Volker Mathes. *Handbuch Faserverbundkunststoffe/Composites*. Springer Verlag, 2013. ISBN: 978-3-658-02754-4.

[47] Chokri Cherif. *Textile Materials for Lightweight Construction*. Springer, 2016. ISBN: 978-3-642-17991-4.

[135] Friedrich Ostermann. *Anwendungstechnologie Aluminium*. Springer-Verlag, 2007. ISBN: 978-3-662-43806-0.

[166] Manfred Flemming, Gerhard Ziegmann, and Siegfried Roth. *Faserverbundbauweisen - Fasern und Matrices*. Springer, 1995. ISBN: 978-3-642-63352-2.

[167] Georg H. Michler. *Kunststoff-Mikromechanik: Morphologie, Deformations- und Bruchmechansimen von polymeren Werkstoffen*. Hanser Fachbuch, 1992. ISBN: 978-3446170681.

[168] Carlos Felippa. *Advanced Finite Element Methods*. University of Colorado Boulder, 2000.

PhD thesis:

[3] Théo Baumard. *Modelling the influence of infrared preheating and temperature uniformity in forming of powder-impregnated thermoplastic composites*. PhD thesis. Belfast, Northern Ireland, UK, 2019.

[6] Ulf Paul Breuer. *Beitrag zur Umformtechnik gewebeverstärkter Kunststoffe*. PhD thesis. Kaiserslautern, Germany, 1997.

[7] Andreas Dehn. *Experimentelle Untersuchung und numerische Simulation des Crashverhaltens gewebeverstärkter Thermoplaste unter Temperatureinfluss*. PhD thesis. Kaiserlautern, Germany: Institut für Verbundwerkstoffe (IVW), 2001. ISBN: 3-934930-18-2.

[9] Matthias Vogler. *Anisotropic material models for fiber reinforced polymers*. PhD thesis. Hannover, Germany: Institut für Statik und Dynmaik (ISD), 2014.

[19] Ilya Peshekhodov. *Experimentell-numerische Methode zur Charakterisierung des Versagensverhaltens hochfester Stahlbleche*. PhD thesis. Hannover, Germany: Institut für Umformtechnik und Umformmaschinen (IFUM), 2018.

[29] Patrick Larour. *Strain rate sensitivity of automotive sheet steels: influence of plastic strain, strain rate, temperature, microstructure, bake hardening and pre-strain*. PhD thesis. Aachen, Germany: Insitut für Eisenhüttenkunde, 2010.

[32] David Jocham. *Bestimmung der lokalen Einschnürung nach linearer und nichtlinearer Umformhistorie sowie Ermittlung dehnungs- und geschwindigkeitsabhängiger Materialkennwerte*. PhD thesis. Munich, Germany: Chair of Metal Forming and Casting, 2018.

[40] Michael Junginger. *Charakterisierung und Modellierung unverstärkter thermoplastischer Kunststoffe zur numerischen Simulation von Crashvorgängen*. PhD thesis. Freiburg, Germany: Universität der Bundeswehr München, 2002. ISBN: 3-8167-6339-1.

[46] Thomas Senner. *Methodik zur virtuellen Absicherung der formgebenden Operation des Nasspressprozesses von Gelege-Mehrschichtverbunden*. PhD thesis. Erlangen, Germany, 2016. ISBN: 978-3-87525-414-3.

[48] Florian Becker. *Entwicklung einer Beschreibungsmethodik für das mechanische Verhalten unverstärkter Thermoplaste bei hohen Deformationsgeschwindigkeiten*. PhD thesis. Halle-Wittenberg, Germany, 2009.

[49] Jochen Peter. *Experimentelle und numerische Untersuchungen zum Crashverhalten von Strukturbauteilen aus kohlefaserverstärkten Kunststoffen*. PhD thesis. Freiburg, Germany: Universität der Bundeswehr München, 2004.

[50] Roland Kryvachi. *Charakterisierung und Modellierung kurzfaserverstärkter thermoplastischer Kunststoffe zur numerischen Simulation von Crashvorgängen*. PhD thesis. Freiburg, Germany: Universität der Bundeswehr München, 2007.

[51] Julian Schöpfer. *Spritzgussbauteile aus kurzfaserverstärkten Kunststoffen: Methoden der Charakterisierung und Modellierung zur nichtlinearen Simulation von statischen und crashrelevanten Lastfällen*. PhD thesis. Kaiserlautern, Germany, 2011.

[55] Bernhard Maron. *Beitrag zur Modellierung und Simulation des Thermoumformprozesses von textilverstärkten Thermoplastverbunden*. PhD thesis. Dresden, Germany, 2016.

[56] Benjamin Kaiser. *A generalised interface for multi-level coupling of beam unit cell mesomodels to macro finite elements in draping simulation*. PhD thesis. 2020.

[57] Andreas Rösner. *Beschreibung des viskoelastischen und viskoplastischen Deformationsverhaltens von kontinuierlich faserverstärktem Polyamid-6*. PhD thesis. Karlsruhe, Germany, 2015.

[64] Matthias Zscheyge. *Zum temperatur- und dehnratenabhängigen Deformations- und Schädigungsverhalten von Textil-Thermoplast-Verbunden*. PhD thesis. Dresden, Germany: Institut für Leichtbau und Kunststofftechnik (ILK), 2015.

[69] Silvestre Taveira Pinho. *Modelling failure of laminated composites using physically based failure models*. PhD thesis. London, UK, 2005.

[70] Matthias Hörmann. *Nichtlineare Versagensanalyse von Faserverbundstrukturen*. PhD thesis. Stuttgart, Germany: Institut für Baustatik, 2002. ISBN: 3-00-010896-3.

[71] Markus Kober. *Ein Beitrag zur strukturmechanischen Optimierung realer Bauteile in metallischer und Faserverbundbauweise unter Verwendung von wirkebenenbasierten Bruchkriterien*. PhD thesis. Cottbus, Germany, 2011.

[72] Daniel Loos. *Werkstoffbasierter Festigkeitsnachweis für elektrische Antriebskomponenten*. PhD thesis. Darmstadt, Germany: Fraunhofer Institut für Betriebsfestigkeit und Systemzuverlässigkeit (LBF), 2019.

[87] Michael Dlugosch. *Zur Methodenentwicklung im Entwurf automobiler Strukturkonzepte in FVK-Metall-Hybridbauweise unter Crashbelastung*. PhD thesis. Freiburg, Germany, 2018.

[88] David Hummelberger. *Hybride Werkstoffsysteme - Systematische Betrachtung und Bewertung der physikalischen Wirkmechanismen*. PhD thesis. Karlsruhe, Germany: Institut für Fahrzeugsystemtechnik, 2019. ISBN: 978-3-7315-0901-1.

[93] André Heckert. *Oberflächenstrukturierung von Aluminium mittels gepulster Laserstrahlung für das thermische Fügen an endlosfaserverstärkte Thermoplaste*. PhD thesis. Munich, Germany: Institut für Werkzeugmaschinen und Betriebswissenschaften (IWB), 2019.

[97] Dustin Flock. *Wärmeleitungsfügen hybrider Kunstoff-Metall-Verbindungen*. PhD thesis. Aachen, Germany, 2011.

[100] Peter Kallage. *Laserschweißen von Mischverbindungen aus Aluminium und verzinktem sowie unverzinktem Stahl*. PhD thesis. 2014.

[103] Silke Sommer. *Modellierung des Verformungs- und Versagensverhaltens von Punktschweißverbindungen unter monoton ansteigender Belastung*. PhD thesis. Karlsruhe, Germany, 2009.

[104] Sebastian Schmeer. *Experimentelle und simulative Analyse von induktionsgeschweißten Hybridverbindungen*. PhD thesis. Kaiserslautern, Germany, 2009.

[105] Niels Pasligh. *Hybride formschlüssige Strukturverbindungen in Leichtbaustrukturen aus Stahlblech und Aluminiumdruckguss*. PhD thesis. Aachen, Germany: Gießerei-Institut, 2011.

[106] Hanna Paul. *Bewertung von langfaserverstärkten Kunststoff-Metall-Hybridverbunden auf der Basis des Verformungs- und Versagensverhaltens*. PhD thesis. Karlsruhe, Germany: Fraunhofer Institut für Werkstoffmechanik IWM, 2013.

[108] Frank Burbulla. *Kontinuumsmechanische und bruchmechanische Modelle für Werkstoffverbunde*. PhD thesis. Kassel, Germany, 2015. ISBN: 978-3-86219-582-4.

[109] Sebastian Burget. *Modellierung des Verformungs- und Versagensverhaltens punktgeschweißter Mischverbindungen zwischen mikro-legierten und pressgehärteten Stählen*. PhD thesis. Karlsruher, Germany: Fraunhofer Verlag, 2015. ISBN: 978-3-8396-1087-9.

[110] Alexander Nelson. *Modellierung und Finite-Elemente-Berechnung form- und stoffschlüssiger Fügeverbindungen*. PhD thesis. Kassel, Germany, 2019.

[111] Matthias Reil. *Connections between steel and aluminium using adhesive bonding combined with self-piercing riveting: Testing, modelling and analysis*. PhD thesis. Trondheim, Norway: CASA, 2019.

[113] Tony Porsch. *Ersatzmodellentwicklung zur Prognose des kerbinduzierten Fügeteilversagens von Halbhohlstanznietverbindungen unter Crashbelastung*. PhD thesis. Paderborn, Germany: Laboratorium für Werkstoff- und Fügetechnik (LWF), 2020.

[114] John Frederick Berntsen. *Testing and modelling of multi-material joints*. PhD thesis. Trondheim, Norway, 2020. ISBN: 978-82-326-5083-5.

[118] Ani Sarnaghi Khaloian. *Development of a numerical method for the strength prediction of timber*. PhD thesis. Munich, Germany, 2020.

[126] Thomas Bru. *Material characterisation for crash modelling of composites*. PhD thesis. Gothenburg, Sweden, 2018. ISBN: 978-91-7597-805-5.

[145] Ludwig Eberl. *Mechanical Performance of pinned composite/metal joints under tension*. PhD thesis. Munich, Germany: Lehrstuhl für Carbon Composites (LCC), 2018.

[155] Tim Bergmann. *Beitrag zur Charakterisierung und Auslegung zugbelasteter Energieabsorptionskonzepte mittels experimenteller, analytischer und numerischer Methoden*. PhD thesis. Kaiserslautern, Germany, 2017.

[156] Sascha Fliegener. *Micromechanical finite element modeling of fiber reinforced thermoplastics*. PhD thesis. Karlsruhe, Germany, 2015.

[157] Nico Feindler. *Charakterisierungs- und Simulationsmethodik zum Versagensverhalten energieabsorbierender Faserverbundstrukturen*. PhD thesis. Munich, Germany: Lehrstuhl für Carbon Composites (LCC), 2012.

[158] Sascha Hell. *Beiträge zur Analyse und Bewertung von 3D-Spannungssingularitäten mittels einer angereicherten Skalierte-Rand-Finite-Element-Methode*. PhD thesis. Darmstadt, Germany, 2018.

[159] Frank Kunkel. *Zum Deformationsverhalten von spritzgegossenen Bauteilen aus talkumgefüllten Thermoplasten unter dynamischer Beanspruchung*. Magdeburg, Germany, 2017.

[160] A. Langkamp. *Bruchmodebezogene Versagensmodelle von faser- und textilverstärkten Verbundwerkstoffen mit polymeren, keramischen sowie metallischen Matrices*. PhD thesis. 2002.

[161] Markus Kästner. *Skalenübergreifende Modellierung und Simulation des mechanischen Verhaltens von textilverstärktem Polypropylen unter Nutzung der XFEM*. PhD thesis. 2009.

[162] Martin Knops. *Sukzessives Bruchverhalten von Faserverbundlaminaten*. PhD thesis. Aachen, Germany, 2003.

[163] Hannes Körber. *Mechanical Response of Advanced Composites under High Strain Rates*. PhD thesis. Porto, Lisbon, 2010.

[164] Ulrich Mandel. *Mechanism based constitutive model for composite laminates*. PhD thesis. Munich, Germany: Lehrstuhl für Carbon Composites (LCC), 2017.

[165] Christian Mildner. *Numerische und experimentelle Untersuchungen des Crashverhaltens von FVK-verstärkten Metallbaustrukturen*. PhD thesis. Munich, Germany: Lehrstuhl für Carbon Composites (LCC), 2013.

MSc or Diploma thesis:

[131] Yijun Zhou. *Numerical Shape Optimization of Fracture Specimens for Material Characterization*. MSc thesis, 2019.

[140] Matthias Stubbe. *Entwicklung eines Laserstrahlfügeverfahrens für Steg-Schlitz-Verbindungen in Metall-Faser-Kunststoff-Verbund-Mischbauweisen*. MSc thesis, 2016.

[189] Muhammad Khalid. *A new material concept for Simulation of Crushing of Fiber Reinforced Plastics*. MSc thesis, 2016.

[190] Dora Schoof. *Kalibrierung eines Materialmodells für die numerische Simulation eines unverstärkten thermoplastischen Kunststoffs auf der Basis von Versuchsdaten*. MSc thesis, 2017.

Publications:

[10] Matthias Vogler. “New material modeling approaches for thermoplastic, composites and organic sheet”. In: 9th European LS-Dyna conference, 2013, pp. 859–874.

[20] Harry Hooputra et al. “A comprehensive failure model for crashworthiness simulation of aluminium extrusion”. In: *International Journal of Crashworthiness* 9, No. 5 (2004), pp. 449–463. DOI: 10.1533/ijcr.2004.0289.

[23] Richard Courant, K. Friedrichs, and H. Lewy. “Über die partiellen Differenzengleichungen der mathematischen Physik”. In: *Mathematische Analen* 100 (1928), pp. 32–74. DOI: 10.1007/BF01448839.

[30] Patrick Larour et al. “Influence of strain-rate, temperature, plastic strain and microstructure on the strain-rate sensitivity of automotive sheet steels”. In: *Steel research* 84(5) (2013), pp. 426–442. DOI: 10.1002/srin.201200099.

[33] Amit K. Ghosh. “Tensile instability and necking in materials with strain hardening and strain-rate hardening”. In: *Acta Metallurgica* 25 (1977), pp. 1413–1424. DOI: 10.1016/0001-6160(77)90072-4.

[38] Lutz Kessler et al. “An approach to model sheet failure after onset of localized necking in industrial high strength steel stamping and crash simulations”. In: *SAE International Journal Passenger Cars - Mechanical Systems* 1(1) (2009), pp. 361–370. DOI: 10.4271/2008-01-0503.

[39] Tomasz Wierzbicki et al. “Calibration and evaluation of seven fracture models”. In: *International Journal of Mechanical Sciences* 47 (2005), pp. 719–743. DOI: 10.1016/j.ijmecsci.2005.03.003.

[45] Jan Striewe et al. “Manufacturing and crashworthiness of fabric-reinforced thermoplastic composites”. In: *Thin-Walled Structures* 123 (2018), pp. 501–508. DOI: 10.1016/j.tws.2017.11.011.

[52] Benjamin Kaiser, Thomas Pyttel, and Fabian Duddeck. “A generalised method for the coupling of a parallelogram-like unit cell with a macroscopic finite element to simulate the behavior of textiles”. In: *International Journal of Material Forming* (2019). DOI: 10.1007/s12289-019-01472-9.

[53] Oliver Döbrich, Thomas Gereke, and Chokri Cherif. “Modelling of textile composite reinforcements on the micro-scale”. In: *AUTEX Research Journal* 14 (2014), pp. 28–33. DOI: 10.2478/v10304-012-0047-z.

[54] Raimund Rolfes et al. “Exploiting the structural reserve of textile composite structures by progressive failure analysis using a new orthotropic failure criterion”. In: *Computers and Structures* 89 (2011), pp. 1214–1223. DOI: 10.1016/j.compstruc.2010.09.003.

[58] Volker Ulbricht et al. “Modelling of the effective material behavior of textile reinforced composites”. In: *Journal of Plastics Technology* 32 (2008), pp. 2532–2544.

[59] Lars Greve and Anthony Pickett. “Modelling damage and failure in carbon/epoxy non-crimp fabric composites including effects of fabric pre-shear”. In: *Composites: Part A* 37 (2006), pp. 1983–2001. DOI: 10.1016/j.compositesa.2005.12.012.

[60] Matthias Vogler, Stefan Kolling, and André Haufe. “A constitutive model for plastics with piecewise linear yield surface and damage”. In: Dynamore, 2007.

[65] Markus Kästner, Sebastian Müller, and Volker Ulbricht. “XFEM modelling of inelastic material behaviour and interface failure in textile-reinforced composites”. In: *Material Science* 2 (2013), pp. 43–51. DOI: 10.1016/j.mspro.2013.02.006.

[66] Olivier Cousigne et al. “Development of a new nonlinear numerical material model for woven composite materials accounting for permanent deformation and damage”. In: *Composite Structures* 106 (2013), pp. 601–614. DOI: 10.1016/j.compstruct.2013.07.026.

[67] Bilad Ahmad and Xiangfan Fang. “Modeling shear behavior of woven fabric thermoplastic composites for crash simulations”. In: *Applied Composites Materials* 27 (2020), pp. 739–765. DOI: 10.1007/s10443-020-09844-0.

[68] Ralf Cuntze. “Strength and failure conditions of the various structural materials: Is there some common basis existing?” In: *SDHM* 74 (2008), pp. 1–19.

[73] Zvi Hashin. “Failure criteria for unidirectional fiber composites”. In: *Journal of Applied Mechanics* 47 (1980), pp. 449–463. DOI: 10.1115/1.3153664.

[74] P. Soden, A. Kaddour, and M. Hinton. “Recommendations for designers and researchers resulting from the world-wide failure exercise”. In: *Composites Science and Technology* 64 (2004), pp. 589–604. DOI: 10.1016/S0266-3538(03)00228-8.

[75] Alfred Puck and Helmut Schürmann. “Failure analysis of FRP laminates by means of physically based phenomenological models”. In: *Composites Science and Technology* 58 (1998), pp. 1045–1067. DOI: 10.1016/S0266-3538(01)00208-1.

[78] Pierre Ladevèze and E. LeDantec. “Damage Modelling of the elementary ply for laminated composites”. In: *Composites Science and Technology* 43(3) (1992), pp. 257–267. DOI: 10.1016/0266-3538(92)90097-M.

[81] Jian Cao et al. “Characterization of mechanical behavior of woven fabrics: Experimental methods and benchmark results”. In: *Composites: Part A* 2 (2008), pp. 1037–1053. DOI: 10.1016/j.compositesa.2008.02.016.

[82] Anton Matzenmiller, Jacob Lubliner, and Robert L. Taylor. “A constitutive model for anisotropic damage in fiber composites”. In: *Mechanics of Materials* 20 No. 2 (1995), pp. 125–152. DOI: 10.1016/0167-6636(94)00053-0.

[83] Silvestre Pinho, Lorenzo Iannucci, and Paul Robinson. “Physically based failure models and criteria for laminated fibre-reinforced composites with emphasis on fibre kinking Part I: Development”. In: *Composites Part A* 37(5) (2006), pp. 766–777. DOI: 10.1016/j.compositesa.2005.04.016.

[84] Lorenzo Pinho Silvestre Iannucci and Paul Robinson. “Physically based failure models and criteria for laminated fibre-reinforced composites with emphasis on fibre kinking Part I: FE implementation”. In: *Composites Part A* 37(5) (2006), pp. 766–777. DOI: 10.1016/j.compositesa.2005.06.008.

[85] Pere Maimí et al. “A continuum damage model for composite laminates: Part I - constitutive model”. In: *Mechanics of Materials* 39(10) (2007), pp. 897–908. DOI: 10.1016/j.mechmat.2007.03.005.

[86] Pere Maimí et al. “A continuum damage model for composite laminates: Part I - computational implementation and validation”. In: *Mechanics of Materials* 39(10) (2007), pp. 909–919. DOI: 10.1016/j.mechmat.2007.03.006.

[90] Gerson Meschut, Vitalij Janzen, and Thomas Offermann. “Innovative and highly productive joining technologies for multi-material lightweight car body structures”. In: *Journal of Materials Engineering and Performance* 23 (2014), pp. 1515–1523. DOI: 10.1007/s11665-014-0962-3.

[91] E. Moldovan, M.H. Tierean, and E.M. Stanciu. “Overview of joining dissimilar materials: metals and polymers”. In: *Engineering Sciences* 10 (2017).

[92] Jean Pierre Bergmann and Martin Stambke. “Potential of laser-manufactured polymer-metal hybrid joints”. In: *Physics Procedia* 39 (2012), pp. 84–91. DOI: 10.1016/j.phpro.2012.10.017.

[94] André Heckert and Michael Zäh. “Laser Surface pre-treatment of aluminium for hybrid joints with glass fibre reinforced thermoplastics”. In: *Physics Procedia* 56 (2014), pp. 1171–1181. DOI: 10.1016/j.phpro.2014.08.032.

[95] Tilo Köckritz et al. “Improving the bond strength at hybrid-yarn textile thermoplastic composites for high-technology applications by laser radiations”. In: *International Journal of Adhesion and Adhesives* 46 (2013), pp. 85–94. DOI: 10.1016/j.ijadhadh.2013.06.004.

[98] Eva Rodríguez-Vidal et al. “Laser joining of different polymer-metal configurations: analysis of mechanical performance and failure mechanisms”. In: *Physics Procedia* 83 (2016), pp. 1110–1117. DOI: 10.1016/j.phpro.2016.09.002.

[101] Oliver Seffer et al. “Investigations on laser beam welding of different dissimilar joints of steel and aluminum for automotive lightweight construction”. In: *Physics Procedia* 83 (2016), pp. 383–395. DOI: 10.1016/j.phpro.2016.08.040.

[102] Andreas Roesner et al. “Laser Assisted Joining of Plastic Metal Hybrids”. In: *Physics Procedia* 12 (2011), pp. 370–377. DOI: 10.1016/j.phpro.2011.03.146.

[107] Hanna Paul, Michael Luke, and Frank Henning. “Kunststoff-Metall-Hybridverbunde - Experimentelle Untersuchungen zum Verformungs- und Versagensverhalten”. In: *Journal of Plastics Technology* 17(6) (2014), pp. 117–141.

[112] Matthias Reil et al. “Connections between steel and aluminum using adhesive bonding combined with self-piercing riveting”. In: vol. 183. 2018. DOI: 10.1051/epjconf/201818304010.

[119] Michael Richter et al. “Phenomenological material modeling of thermoplastic textile composites for crashworthiness simulation combining a strass- and strain-based failure criterion”. In: *Thin Walled Structures* submitted (2022).

[120] Robert Boehm, Maik Gude, and Werner Hufenbach. “A phenomenologically based damage model for 2D and 3D-textile composites with non-crimp reinforcement”. In: *Materials and Design* 32 (2011), pp. 2532–2544. DOI: 10.1016/j.matdes.2011.01.049.

[121] Werner Hufenbach et al. “Theoretical and experimental investigation of anisotropic damage in textile-reinforced composite structures”. In: *Mechanics of Composite Materials* 40 (2004), pp. 519–532. DOI: 10.1007/s11029-005-0022-z.

[122] Robert Boehm and Werner Hufenbach. “Experimentally based strategy for damage analysis of textile-reinforced composites under static loading”. In: *Composites Science and Technology* 70 (9) (2010), p. 1130. DOI: 10.1016/j.compscitech.2010.04.008.

[123] R. M. Christensen. “Stress based yield/failure criteria for fiber composites”. In: *International Journal of Solid Structures* 34 (1997), pp. 529–543. DOI: 10.1016/S0020-7683(96)00038-8.

[125] Werner Hufenbach et al. “Characterization of strain rate dependent material properties of textile reinforced thermoplastics for crash and impact analysis”. In: *Procedia Material Science* 2 (2013), pp. 204–211. DOI: 10.1016/j.mspro.2013.02.025.

[134] Rodney Hill. “A theory of the yielding and plastic flow of anisotropic metals”. In: *Proceedings of the Royal Society A* A193 (1948), pp. 281–297. DOI: 10.1098/rspa.1948.0045.

[141] D. P. Norman. “Modelling spotweld fracture using CrachFEM”. In: vol. 9th. 2013.

[146] Holger Seidlitz et al. “Advanced Welding Technology for highly stressable multi-material designs with fiber-reinforced plastic and metals”. In: *Open Journal of Composite Materials* 7 (2017), pp. 166–177. DOI: 10.4236/ojcm.2017.73010.

[148] Oliver Seffer, André Springer, and Stefan Kaierle. “Remote laser beam welding of different, dissimilar steel and aluminum alloys with varying sheet thicknesses for automotive lightweight construction”. In: *Journal of Laser Applications* 29 (2017). DOI: 10.2351/1.4983241.

[149] Anton Evdokimov et al. “Mechanical properties of dissimilar steel-aluminum welds”. In: *Materials Science and Engineering: A* 722 (2018), pp. 242–254. DOI: 10.1016/j.msea.2018.03.019.

[153] E.J. Pavlina and Chester van Tyne. “Correlation of yield strength and tensile strength with hardness of steels”. In: *Journal of Materials Engineering and Performance* 10 (2008), pp. 888–893. DOI: \10.1007/s11665-008-9225-5.

[154] Axel Jahn et al. “Local Laser Strengthening of Steel Sheets for Load Adapted Component Design in Car Body Structures”. In: *Physics Procedia* 12 (2011), pp. 431–441. DOI: 10.1016/j.phpro.2011.03.054.

[169] Pedro Camanho et al. “Three-dimensional invariant-based failure criteria for fibre-reinforced composites”. In: *International Journal of Solids and Structures* 55 (2015), pp. 92–107. DOI: 10.1016/j.ijsolstr.2014.03.038.

[170] Ulrich Mandel, Robin Tauber, and Roland Hinterhölzl. “Mechanism based nonlinear constitutive model for composite laminates subjected to large deformations”. In: *Composites Structures* 132 (2015), pp. 98–108. DOI: 10.1016/j.compstruct.2015.04.029.

[171] W. Stieglbauer and J. Kazmaier. “Innovative, multifunctional, form-locked joining technology for dissimilar material combinations”. In: *Die Verbindungsspezialisten* 258 (2009), pp. 100–103.

[172] Felipe Viana, Christian Gogu, and Tushar Goel. “Surrogate modeling: tricks that endured the test of time and some recent developments”. In: *Structural and multidisciplinary optimization* (2021), pp. 2881–2908. DOI: 10.1007/s00158-021-03001-2.

Manuals:

[22] ABAQUS version 2016. *ABAQUS Theory manual*. Dassault Systèmes - Simulia, 2016.

[25] Gernot Oberhofer, Martin Gross, and Martin Oehm. *MF GenYld+CrachFEM Theory Manual*. MATFEM Partnerschaft, 2016.

[62] R11. *LS-DYNA Keyword User's Manual - Volume II Material Models*. Livermore Software Technology Corporation (LSTC), 2018.

[115] ABAQUS version 2016. *Getting Started with ABAQUS*. Dassault Systèmes - Simulia, 2016.

[116] R11. *LS-DYNA Keyword User's Manual - Volume I*. Livermore Software Technology Corporation (LSTC), 2018.

[128] H. Gese et al. *MF GenYld+CrachFEM Manual for Abaqus, v4.2.0*. MATFEM Partnerschaft, 2016.

Conference Proceedings:

[27] Fabian Duddeck, Duo Zeng, and Michael Richter. "Material model dependency of optimal topologies for crashworthiness". In: *4. MATFEM Conference*. 2017.

[28] Helmut Gese et al. "Weiterentwickeltes Materialmodell zur Bewertung von Mg-Extrusionsprofilen". In: *5. Nordmetall Kolloquium*. 2009.

[31] Helmut Gese et al. "Ermittlung von Fließwiderstandskurven bei großen Formänderungen für die Blechumformsimulation". In: *Proceedings DVM-Tagung Werkstoffprüfung 2002 - Kennwertermittlung für die Praxis*. Wiley-VCH Verlag, 2002.

[35] Heinz Werner and Helmut Gese. "Zur Bedeutung von dehnratenabhängigen Werkstoffkennwerten in der Crashsimulation". In: *DVM-Tagung Werkstoffprüfung, Bad Nauheim*. 2002.

[36] Harry Dell, Helmut Gese, and Gernot Oberhofer. "CrachFEM - A comprehensive approach for the prediction of sheet metal failure". In: *Conference Proceedings of 9th International Conference on Numerical Methods in Industrial Forming Processes (Numiform)*. Vol. 908. American Institute of Physics, 2007. DOI: 10.1063/1.2740806.

[44] Sascha Müller et al. "Integrative Prozess- und Bauteilsimulation für kurzfaserverstärkte Spritzgußbauteile". In: *9. SAXON SIMULATION MEETING*. 2017. URL: http://nbn-resolving.de/urn:nbn:de:bsz:ch1-qucosa-225813 (visited on 01/08/2021).

[63] Andre Haufe et al. "A semi-analytical model for polymers subjected to high strain rates". In: vol. 5. Dynamore, 2005.

[76] Marcel Brandt. "Berechnungsmöglichkeiten für gewebeverstärkte thermoplastische Composites". In: *Kunststoffe und Simulation*. Hanser Verlag, 2016.

[77] Jérôme Coulton. "CAE of organo-sheet material (Thermoplastic woven glass composites)". In: *LS-Dyna Forum*. 2012. URL: https://www.dynamore.de/dynamore/de/download/papers/ls-dyna-forum-2012/documents/crash-2-1 (visited on 03/11/2021).

[80] Werner Hufenbach et al. "Experimental and numerical evaluation of crash and impact loaded textile reinforced thermoplastic components". In: *15th European Conference on composite materials*. 2012. URL: http://www.escm.eu.org/eccm15/data/assets/962.pdf (visited on 08/08/2019).

[89] Markus Wagner et al. “Innovative joining technologies for multi-material lightweight car body structures”. In: *International Automotive Body Congress (IABC), Dearbon, Michigan*. 2014.

[96] Hanna Paul, Michael Luke, and Frank Henning. “Evaluation of the joining mechanisms of polymer metal components”. In: *15th European Conference on composite materials (ECCM)*. 2012. URL: http://www.escm.eu.org/eccm15/data/assets/955.pdf (visited on 02/09/2021).

[117] Frank Burbulla and Anton Matzenmiller. “Crashsimulation von Klebeverbindungen des Rohkarosseriebaus”. In: *LS-Dyna Anwenderforum*. Dynamore, 2013.

[124] Gernot Oberhofer et al. “Current solution and open challenges in modelling organic sheets”. In: *automotive CAE Grand Challenge*. 2016.

[127] Joachim Hausmann et al. “Mechanik und Simulation von Verbundwerkstoffstrukturen”. In: *Dresdner Werkstoffwoche*. 2015.

[130] Harry Dell, Helmut Gese, and Gernot Oberhofer. “Advanced yield loci and anisotropic hardening in the material model MF GenYld+CrachFEM)”. In: *Conference Proceedings of 9th International Conference on Numerical Simulation of 3D Sheet Metal Forming Processes (Numisheet)*. Interlaken, Swizterland, 2008.

[133] Michael Richter et al. “Material modelling of textile reinforced composites with respect to fracture initiation and strain rate sensitivity”. In: *8th ECCOMAS Thematic Conference on Mechanical Response of Composites*. 2021.

[143] Lacy Heather et al. “Notch stress raiser detection and handling in automotive body structure - An approach at Jaguar Land Rover”. In: *4. MATFEM Conference*. 2017.

[144] Michael Richter et al. “Surrogate modeling of hybrid material pairings including organic sheets”. In: *Hybrid Materials and Structures*. 2020. URL: https://hybrid2020.dgm.de/the-conference/proceedings/ (visited on 02/03/2021).

Internet sources:

[1] pixabay. *Leaf of a walnut tree*. URL: https://pixabay.com/de/photos/laub-blatt-nussbaumblatt-fr%C3%BChling-3420078/ (visited on 10/24/2020).

[2] Bond Laminates. *Material data sheet for Tepex®dynalite 102-RG600(x)/47%*. 2017. URL: http://bond-laminates.com/fileadmin/user_upload/MDS_102-RG600_x_-47__SSe_170706.pdf (visited on 10/27/2019).

[129] Weltstahl. *Data sheet for S355JR from Weltstahl*. URL: https://www.weltstahl.com/werkstoff-stahl-s355-datenblatt/ (visited on 10/27/2020).

[136] R. Schedewy. *Laser beam welded slot-tab joints*. URL: http://publica.fraunhofer.de/documents/N-100675.html (visited on 01/11/2021).

[137] Jens Standfuß. *Weniger ist mehr - Leichtbau durch Hybridverbindungen*. URL: https://www.iws.fraunhofer.de/de/newsundmedien/pres%5C-se%5C-in%5C-for%5C-ma%5C-tio%5C-nen/2016/presseinformation_2016-13.html (visited on 01/11/2021).

[138] Federal Ministry of Education and Research. *Photonik Forschung Deutschland*. URL: https://www.photonikforschung.de/projekte/lasertechnik/projekt/la%5C-ser%5C-lei%5C-chter.html (visited on 12/12/2020).

[150] Thyssen Group Steel Europe AG. *Produktinformationen höherfeste IF-Stähle HX*. URL: https://www.thyssenkrupp-steel.com/media/content_1/pub%5C-li%5C-ka%5C-tio%5C-nen/pro%5C-dukt%5C-in%5C-for%5C-ma%5C-ti%5C-o%5C-nen/if_hx/thyssenkrupp_if-hx_produktinformation_steel_de.pdf (visited on 12/12/2017).

[173] Bernd Klein. *Einführung in numpy*. 2014. URL: https://www.vda.de/de/arbeitsgebiete/leichtbau/index.html (visited on 06/22/2014).

[174] VDA. *Klimaschutz durch Fahrzeugleichtbau*. Oct. 2012. URL: https://www.vda.de/de/arbeitsgebiete/leichtbau/index.html (visited on 10/19/2014).

[175] Hubert Pelc. *Optimierung von Hybridverbindungen*. URL: https://www.sprin%5C-ger%5C-pro%5C-fess%5C-io%5C-nal.de/verbindungstechnik/optimierung-von-hybridverbindungen/18938128 (visited on 03/11/2021).

[176] Clemens Doriat. *Crashtüren, Bio-Kindersitze und Schweizer Finnen*. URL: https://www.kunststoffe.de/a/news/crashtueren-bio-kindersitze-und-schweize-325385 (visited on 06/06/2021).

[177] Daniel Häfelein, Sascha Majic Neven andBockelkamp, and Hermann Fischer. *Series Production of Fiber Composite Safety Components for Automotive Industry*. URL: https://www.m-a-i.de/en/blog-post/boge-leichtbauartikel/ (visited on 07/02/2021).

Final reports:

[5] M. Stegelmann, K. Demnitz, and M. Müller. *Forel Studie 2018 - Ressourceneffizienter Leichtbau für die Mobilität*. Ed. by M. Gude et al. 2018. URL: https://plattform-forel.de/studie/ (visited on 03/12/2021).

[8] D. Bonefeld. *Kombination von Thermoplast-Spritzguss und Thermoformen kontinuierlich faserverstärkter Thermoplaste für Crashelemente (SpriForm) - Gemeinsamer Schlussbericht zum BMBF-Verbundprojekt*. BMBF, 2012. URL: https://www.tib.eu/de/suchen/id/TIBKAT%3A739340360/Kombination-von-Ther%5C-mo%5C-plast-Spritzguss-und-Thermoformen/ (visited on 09/23/2017).

[11] M. Stegelmann and G. Just. *Chancen und Herausforderungen im ressourceneffizienten Leichtbau für die Elektromobilität*. Ed. by M. Gude et al. 2015. URL: https://plattform-forel.de/studie/ (visited on 03/12/2021).

[12] M. Stegelmann. *Forel Wegweiser 2020 - Handlungsempfehlungen für den ressourceneffizienten Leichtbau*. Ed. by M. Gude et al. 2020. URL: https://plattform-forel.de/wegweiser/ (visited on 03/12/2021).

[13] Brett Smith et al. *Technology Roadmaps: Intelligent Mobility Technology, Materials and Manufacturing Processes and Light Duty Vehicle Propulsion*. Center for Automotive Research (CAR), 2017. URL: https://www.cargroup.org/publication/technology-roadmaps-intelligent-mobility-technology-materials-and-manufacturing-processes-and-light-duty-vehicle-propulsion/ (visited on 07/04/2017).

[79] Ralf Cuntze. *Neue Bruchkriterien, und Festigkeitsnachweise für unidirektionalen Faserkunststoffverbund unter mehrachsiger Beanspruchung - Modellbildung und Experimente*. VDI, 1997. DOI: http://publications.rwth-aachen.de/record/90193.

[147] Oliver Seffer et al. *Entwicklung von laserbasierten Fügetechnologien für artungleiche Leichtbaukonstruktionen, Teilvorhaben: Prozessentwicklung für das 3D-Laserstrahlschweißen von Stahl-Aluminium-Mischverbindungen*. Laserzentrum Hannover (LZH), 2018. DOI: 10.2314/GBV:1032236116.

[178] Philipp Scheiner. *Entwicklung von laserbasierten Fügetechnologien für artungleiche Leichtbaukonstruktionen, Teilvorhaben: Rechnergestützte Entwicklung von laserbasierter Fügeprozesse für leichtbauoptimierte Gehäusekonzepte in Hybridbauweise*. Robert Bosch GmbH, 2018. DOI: 10.2314/GBV:1040933017.

[179] Anton Evdokimov, Katrin Springer, and Ralf Ossenbrink. *Entwicklung von laserbasierten Fügetechnologien für artungleiche Leichtbaukonstruktionen, Teilvorhaben: Simulationsmodelle für das 3D-Laserstrahlschweißen von Stahl/Aluminium Mischverbindungen*. Lehrstuhl für Füge- und Schweißtechnik (LFT) der Brandenburgischen Technischen Universität Cottbus-Senftenberg (BTU), 2018. DOI: 10.2314/GBV:1024520161.

[180] Jens Standfuß et al. *Entwicklung von laserbasierten Fügetechnologien für artungleiche Leichtbaukonstruktionen, Teilvorhaben: Prozessentwicklung Steg-Schlitz-Verbindung, Fügen Metall-Organoblech und lokale Laserverfestigung*. Fraunhofer-Institut für Werkstoff- und Strahltechnik (IWS), 2018. DOI: 10.2314/GBV:1024819094.

[181] Michael Richter and Helmut Gese. *Entwicklung von laserbasierten Fügetechnologien für artungleiche Leichtbaukonstruktionen, Abschlussbericht zum Teilvorhaben mechanische Modelle für hybride Verbindungen im Verbundprojekt LaserLeichter*. MATFEM Partnerschaft, 2018. DOI: 10.2314/KXP:1823491332.

[182] Daniel Lezock. *Entwicklung von laserbasierten Fügetechnologien für artungleiche Leichtbaukonstruktionen, Teilvorhaben: Leichtbau-Lehnenstruktur Fond mit Rückwand*. Scherdel Marienberg GmbH, 2018. DOI: 10.2314/GBV:1024199118.

[183] Dieter Päthe, Meinulf Hinz, and Thorge Hammer. *Entwicklung von laserbasierten Fügetechnologien für artungleiche Leichtbaukonstruktionen, Teilvorhaben: Laserstrahlschweißen von Aluminium/Stahlverbindungen für den Karosseriebau*. Volkswagen AG, 2018. DOI: 10.2314/GBV:1024535878.

[184] Leif Ickert et al. *Beitrag zum Fortschritt im Automobilleichtbau durch belastungsgerechte Gestaltung und innovative Lösungen für lokale Verstärkungen von Fahrzeugstrukturen in Mischbauweise)*. Vol. 244. Forschungsvereinigung Automobiltechnik (FAT), 2020. URL: https://www.vda.de/de/services/Publikationen/fat-schriftenreihe-244.html (visited on 07/04/2017).

[185] Oliver Seffer and Ronny Pfeifer. *Laserstrahlschweißen von anwendungsnahen Stahl-Aluminium-Mischverbindungen für den automobilen Leichtbau*. Vol. 288. Forschungsvereinigung Automobiltechnik (FAT), 2020. URL: https://www.vda.de/de/services/Publikationen/fat-schriftenreihe-288.html (visited on 05/15/2017).

[186] Gerson Meschut et al. *Lebensdauerberechnung hybrider Verbindungen (Lifetime prediction of hybrid joints)*. Vol. 326. Forschungsvereinigung Automobiltechnik (FAT), 2020. URL: https://www.vda.de/de/services/Publikationen/fat-schriftenreihe-326.html (visited on 01/05/2021).

[187] Peter Gumbsch, Lila Schuster, and Silke Sommer. *Charakterisierung und Meta-Modellierung von ungleichartigen Punktschweißverbindungen für die Crashsimulation*. Vol. 333. Forschungsvereinigung Automobiltechnik (FAT), 2020. URL: https://www.vda.de/de/services/Publikationen/fat-schriftenreihe-333.html (visited on 01/05/2021).

[188] Peter Gumbsch, Lila Schuster, and Silke Sommer. *Charakterisierung und Modellierung des Versagens von Laserstrahlschweißverbindungen von Stahlblechen für die Crashsimulation*. Vol. 237. Forschungsvereinigung der Arbeitsgemeinschaft der Eisen und Metall verarbeitenden Industrie e.V. (AVIF), 2009.

Standards:

[99] *Prüfung von Verbindungseigenschaften; Prüfung der Eigenschaften mechanisch und kombiniert mittels Kleben gefertigter Verbindungen*. Deutscher Verband für Schweißen und verwandte Verfahren; Europäische Forschungsgesellschaft für Blechverarbeitung, 2007.

[132] *Kunststoffe - Polyamide - Beschleunigte Konditionierung von Probekörpern*. Deutsches Institut für Normung e. V., 2019. DOI: 10.31030/3083554.

Miscellaneous:

[61] Michael Richter. *Notes of a personal communication with Dr. Helmut Gese (MATFEM)*. unpublished, 2018.

[139] Michael Richter. *Notes of a personal communication and exchange of data within the research project LaserLeichter with Dipl.-Ing. Frieder Zimmermann (IWS)*. unpublished, 2017.

[142] Michael Richter. *Notes of a personal communication and exchange of data within the research project LaserLeichter with Dr.-Ing. Ralf Ossenbrink (BTU)*. unpublished, 2017.

[151] Michael Richter. *Notes of a personal communication with Prof. Dr. Harry Dell (MATFEM)*. unpublished, 2017.

[152] Michael Richter. *Notes of a personal communication and exchange of data within the research project LaserLeichter with Dipl.-Ing. Oliver Seffer (LZH)*. unpublished, 2017.

List of Figures

List of Tables

A. Appendix

A.1. Assigning specimens to stress states

Table A.1.: Overview of characteristic stress states define by the stress triaxiality η and the corresponding experimental specimens

Stress state	Stress triaxiality η	Stress components	Specimen
hydrostatic pressure	- ∞	$\sigma_I = \sigma_{II} = \sigma_{III} < 0$	-
biaxial compression	$-\frac{2}{3}$	$\sigma_I = \sigma_{II} < 0, \sigma_{III} = 0$	biaxial compression test
uniaxial compression	$-\frac{1}{3}$	$\sigma_I < 0, \sigma_{II} = \sigma_{III} = 0$	uniaxial compression test
shearing	0.0	$\sigma_I = -\sigma_{II}, \sigma_{III} = 0$	ASTM-shear specimen, Ioscipecu
uniaxial tension	$+\frac{1}{3}$	$\sigma_I > 0, \sigma_{II} = \sigma_{III} = 0$	uniaxial tensile test
plain strain	$\frac{1}{\sqrt{3}} = +0.577$	$\sigma_I > 0, \sigma_{II} = \sigma_{III} = 0$	waisted tensile test
biaxial tension	$+\frac{2}{3}$	$\sigma_I = \sigma_{II} > 0, \sigma_{III} = 0$	biaxial or notched tensile test
hydrostatic tension	+ ∞	$\sigma_I = \sigma_{II} = \sigma_{III} > 0$	-

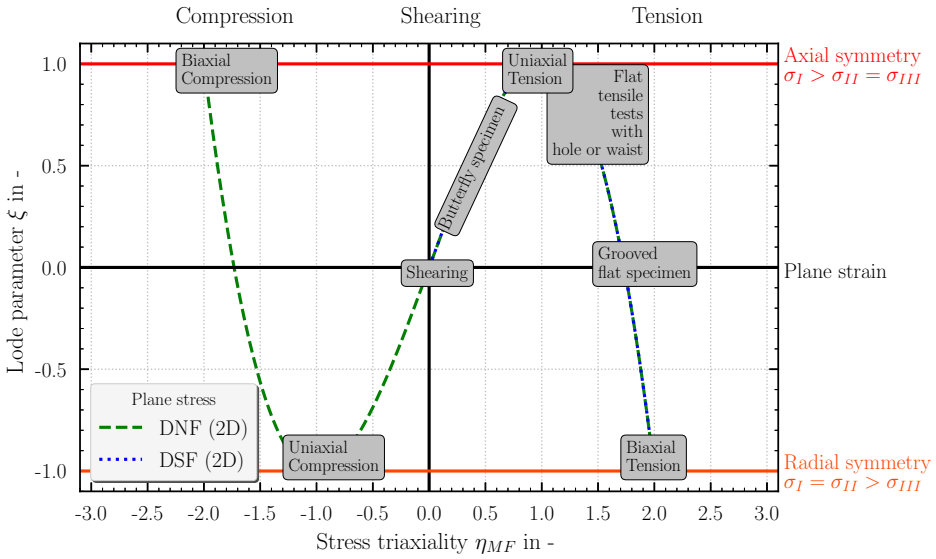

Figure A.1.: Assignment of specimens to stress space defined by the invariants triaxiality η_{MF} and Lode parameter ξ

A.2. Fracture criteria for metals

Table A.2.: Comparison of different failure models for ductile sheet metals and their capabilities

Model	Plasticity model with damage	Localized necking			Fracture				
		Initial FLC	Transient FLC	Post necking	Ductile normal fracture (DNF)	Ductile shear fracture (DSF)	Integral damage accumulation	Orthotropy of fracture	Applicable for shells and solids
Gurson (GTN)	Yes	No	No	No	Yes	No	Scalar	No	No
Xue-Wierzbicki	No	No	No	No	Yes		Scalar	No	Yes, 3D with Triax&Lode
GISSMO-type	No/Yes	ECRIT (experiment)[a]	Damage accumulation	FADEXP	Yes, no analytical model for fitting of experiments		Scalar	eGISSMO (only 2D for DNF)	Yes, 3D with Triax&Lode
DIEM- or IDS-type	No	MSFLC (experiment)	No	ΔL; energy	Yes	Yes	Scalar	No	DNF (only 2D)
CrachFEM	No/(Yes)[b]	MSFLC (virtual)	orthotropic Crach	PIS	Yes	Yes	Yes	2D&3D	Yes

[a] limited to isotropic and transversal isotropic materials

[b] regularization needed due to mesh dependent solution

A.3. Compensating machine stiffness

The displacement measurements of the bridge-deck-panel joints was done on transversal bars of the tensile test machine including not only the compliance of the mounting itself but also of the machine set-up. Preferably would be to measure the displacement signal directly on the specimen with a local device such as tactile sensors or DIC-system. In order to compensate these additional proportion of displacement in the signal a detailed FE-model of the mounting were built up to determine the compliance for

$$\vec{F} = C\vec{u} \tag{A.1}$$

$$C = C_{ma} + C_{mo} + C_s \tag{A.2}$$

$$\vec{u}_{loc} = \vec{u}_{glob} - \vec{u}_{ma} - \vec{u}_{mo} = \vec{u}_{glob} - \frac{\vec{F}}{C_{ma}} - \frac{\vec{F}}{C_{mo}} \tag{A.3}$$

machine stiffness is based on other 10.000 N and remains the same across all loadings. The compliance of the mounting is individual for every mounting and can be derived from the detailed FE-models and validated against renewed experiments of 40.0 mm bridge length with stiff mounting.

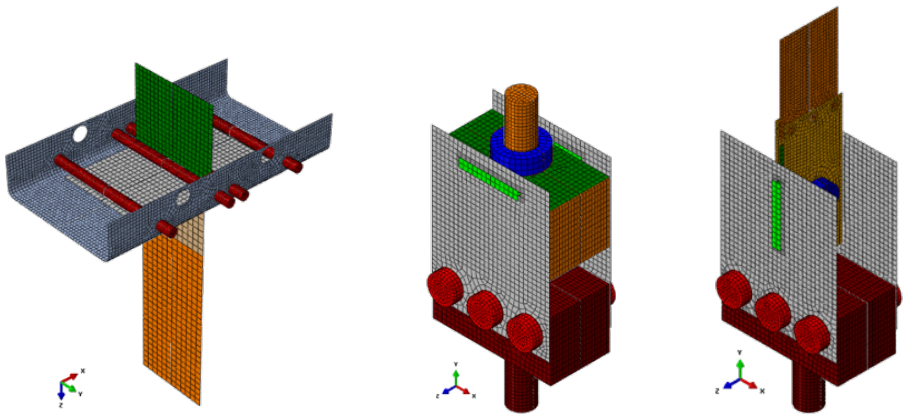

(a) Head tension (b) Transversal shearing (c) Longitudinal shearing

Figure A.2.: Detailed FE-model of the mounting for different loading types of the bridge-deck-panel joint

A.4. Specimen for material characterization

For material characterization small specimens or coupons are used for an experimental characterization which allow to extract material properties from continuous loading until

fracture initiation. Loading velocity, multi-axial loading results in a multi-axial stress state, anisotropy of the material due to metallurgical micro-structure, temperature etc.

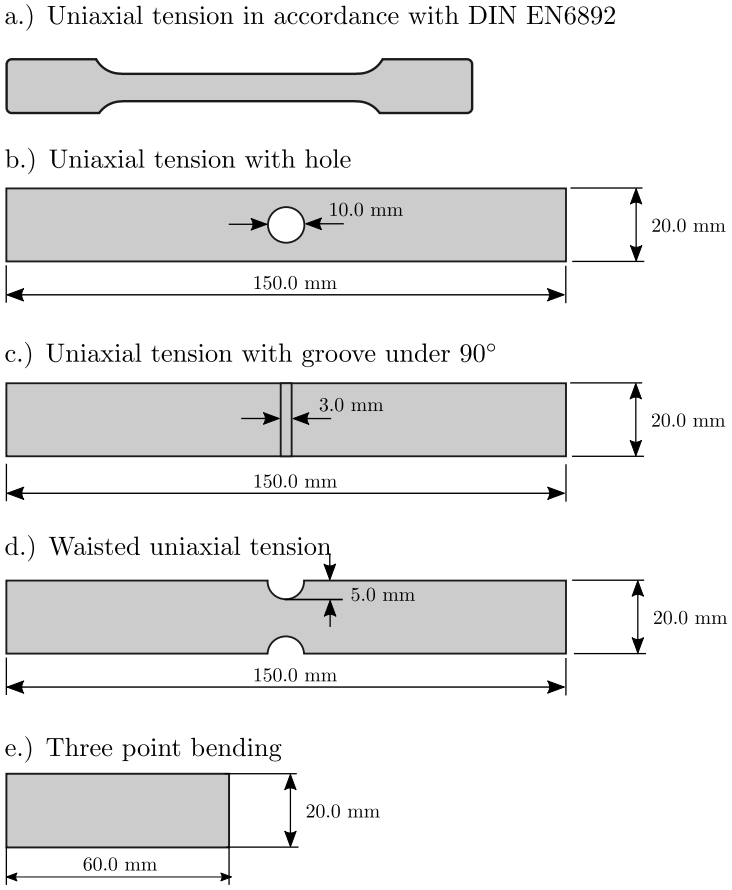

Figure A.3.: Schematic of specimen including dimension for material characterization of thin-walled, ductile metal sheets

A.5. Numerical optimization

Based on the experimentally obtained material properties a material card can be deducted by either using the material paremters directly as input or by means of parameter fitting. Based on the model assumptions of the material behavior mathematical equations for these models can be approximated using the aforementioned experimental properties as supporting points. The parameter fitting for analytical equations, as e.g. the plastic strain hardening laws (See Equations 2.55-2.60 in Section 2.2.2) or the equations for the fracture curves (See Equations 2.71,4.10, 2.72 and 2.73 in Section 2.2.3), can be stated as numerical optimization. The parameters for the material card will be obtained by minimizing the

difference between the experimental supporting points v_{exp} and the continuous analytical solution v_{app} by the method of least squares. The minimization problem states:

- Objective function:

$$min\left\{y(\boldsymbol{x})|g_j\left(\boldsymbol{x}\right) \leq \mathbf{1}; h_1\left(\boldsymbol{x}\right) = 1\right\} \tag{A.4}$$

$$with \qquad y\left(\boldsymbol{x}\right) = \sum_{i=1}^{n}\left(v_{exp} - v_{app}\left(x_j\right)\right)^2 \tag{A.5}$$

- Design variables:
  Respective model parameter of the underlying analytical functions

The material card hence contains the optimal set of material and model parameters across all loadings. To ensure that the optimal fit is found across multiple analytical laws the optimal parameter fit for different laws will be compared with one another and evaluated for their goodness of fit.

Further points to be discussed here:equality/ inequality constraints, e.g. point of uniform elongation is met, ensuring a global optimum with different starting points or systematic search with a serial optimization of evolutionary based algorithms and gradient-based analyitcal algorithms

A.6. Material Cards for MF GenYld+CrachFEM

A.6.1. Steel sheet S355JR in 1.50 mm

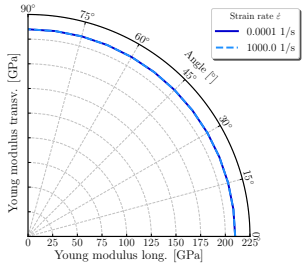

(a) Definition of elasticity

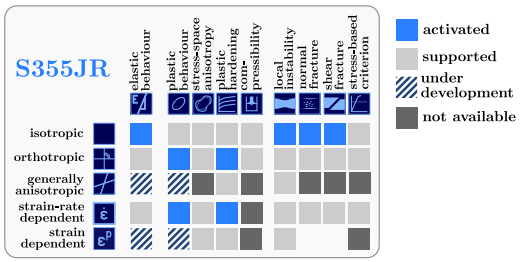

(b) Modular material modeling

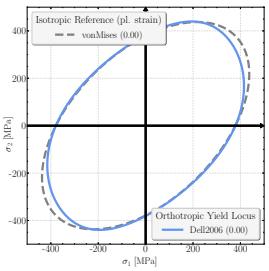

(c) Trace of yield locus

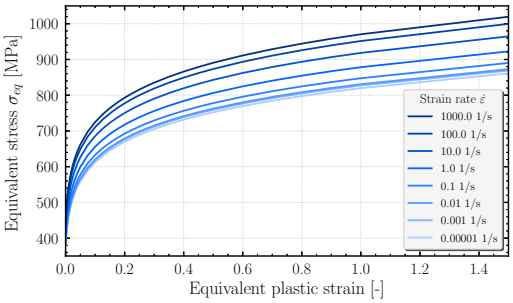

(d) Strain-rate dependent plastic hardening

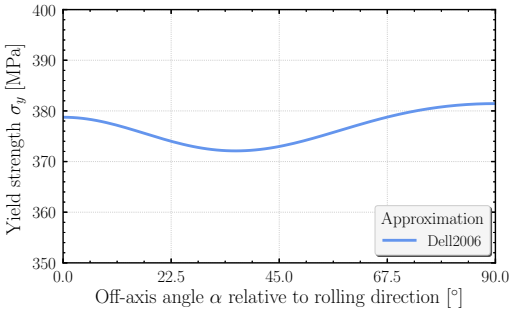

(e) Yield strength over α

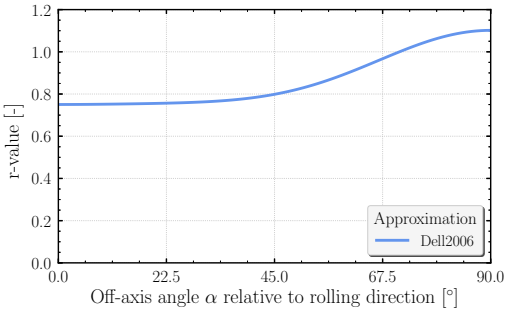

(f) R-value over α

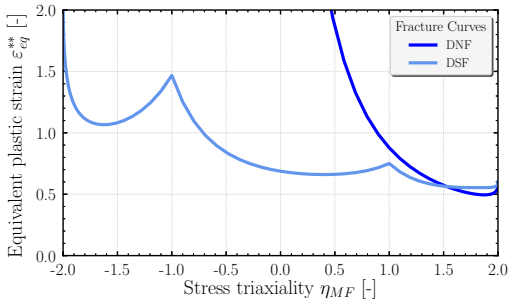

(g) Fracture curves DNF and DSF

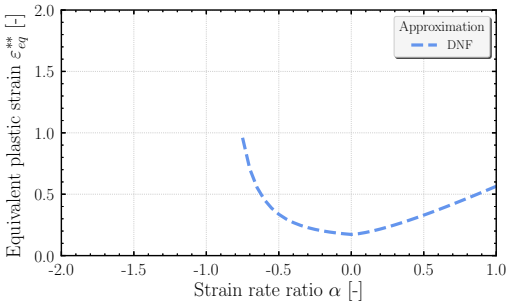

(h) FLC over strain rate ratio α

Figure A.4.: Visualization of activated modules in MF GenYld+CrachFEM material card for S355JR in 1.50 mm

A.6.2. Aluminum sheet EN AW-6082 T6 in 1.50 mm

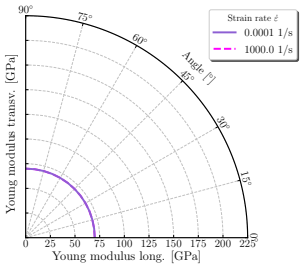

(a) Definition of elasticity

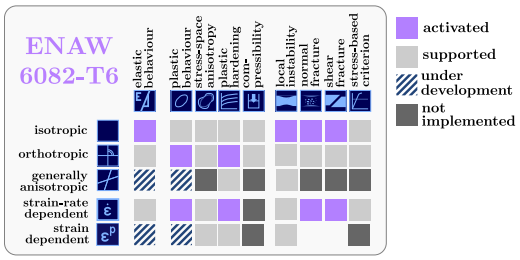

(b) Modular material modeling

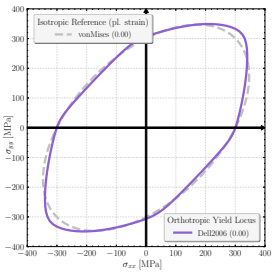

(c) Trace of yield locus

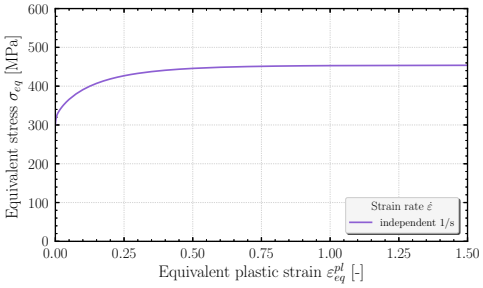

(d) Plastic hardening

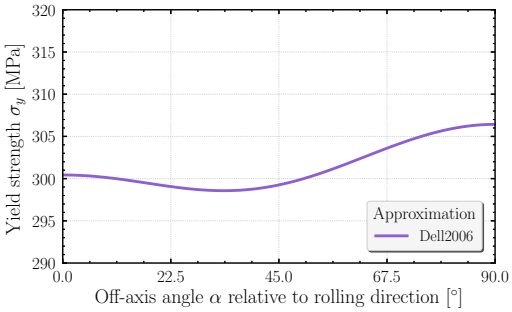

(e) Yield strength over α

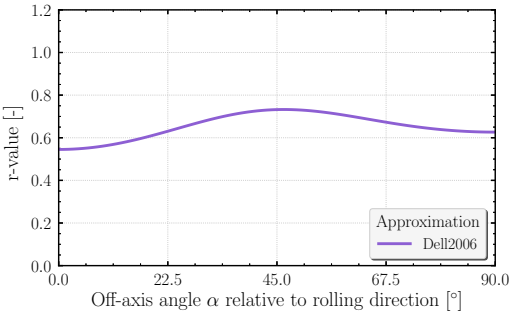

(f) R-value over α

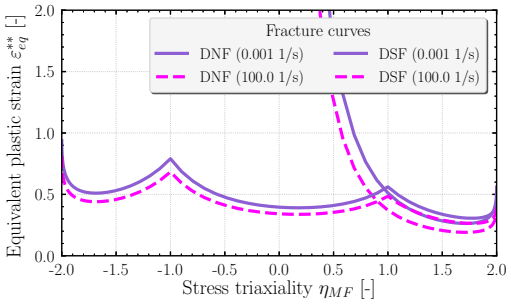

(g) Fracture curves DNF and DSF

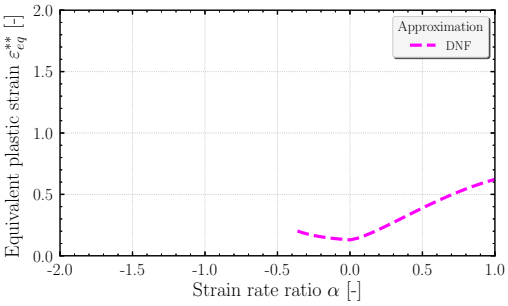

(h) FLC over strain rate ratio α

Figure A.5.: Visualization of activated modules in MF GenYld+CrachFEM material card for ENAW6082-T6 in 1.50 mm

A.6.3. Tepex® dynalite 102-RG600 in 2.00 mm

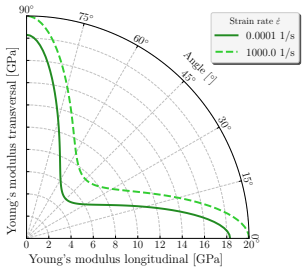

(a) Visco-elasticity

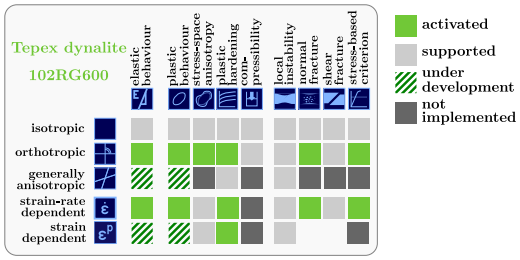

(b) Modular material modeling

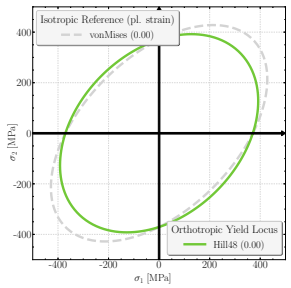

(c) Trace of yield locus

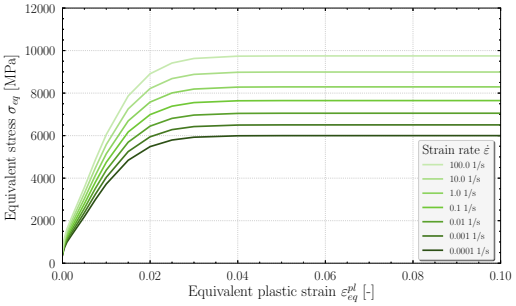

(d) Strain-rate dependent plastic hardening

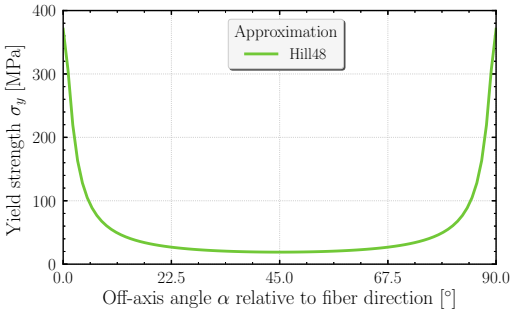

(e) Yield strength over α

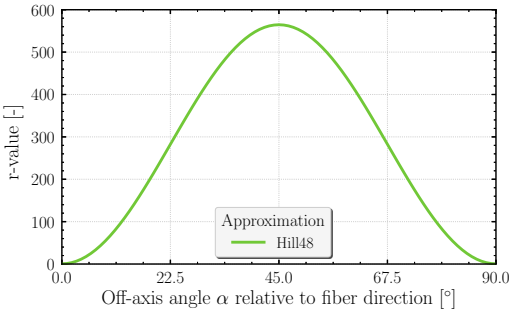

(f) R-value over α

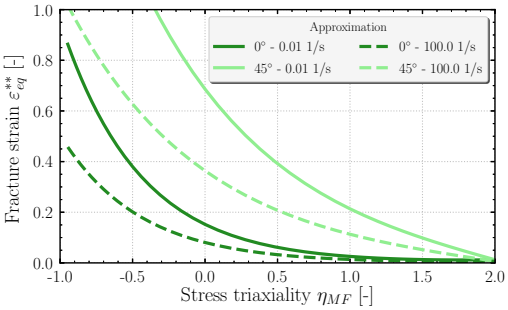

(g) DNF over stress triaxiality η_{MF}

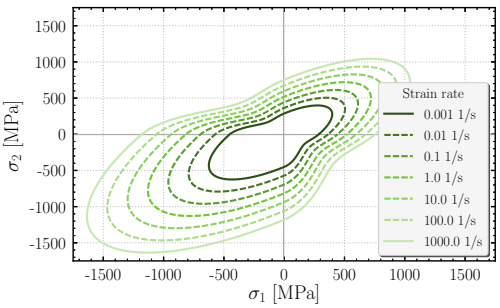

(h) Traces of fracture locus σ_1-σ_2-plane

Figure A.6.: Visualization of activated modules in MF GenYld+CrachFEM material card for Tepex® dynalite 102-RG600 in 2.00 mm